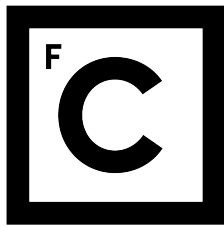


UNIVERSIDADE DE LISBOA
FACULDADE DE CIÊNCIAS



**Ciências
ULisboa**

**Towards better selection and characterisation criteria for high-redshift radio galaxies
using machine-assisted pattern recognition**

“Documento Provisório”

Doutoramento em Física e Astrofísica

Rodrigo Alonso Carvajal Pizarro

Tese orientada por:

José Afonso

Israel Matute

Hugo G. Messias

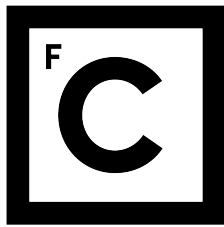
Documento especialmente elaborado para a obtenção do grau de doutor

MMXXIV

DRAFT - March 15, 2024 - DRAFT

This page intentionally left blank.

UNIVERSIDADE DE LISBOA
FACULDADE DE CIÊNCIAS



**Ciências
ULisboa**

**Towards better selection and characterisation criteria for high-redshift radio galaxies
using machine-assisted pattern recognition**

Doutoramento em Física e Astrofísica

Rodrigo Alonso Carvajal Pizarro

Tese orientada por:

José Afonso

Israel Matute

Hugo G. Messias

This work was supported by Fundação para a Ciência e a Tecnologia (FCT) through the Fellowship PD/BD/150455/2019 (PhD:SPACE Doctoral Network PD/00040/2012).

Documento especialmente elaborado para a obtenção do grau de doutor

This page intentionally left blank.

Acknowledgements

This work was supported by the Fundação para a Ciência e a Tecnologia (FCT) through research grants PTDC/FIS-AST/29245/2017, EXPL/FIS-AST/1085/2021, UID/FIS/04434/2019, UIDB/04434/2020 (DOI: 10.54499/UIDB/04434/2020), and UIDP/04434/2020 (DOI: 10.54499/UIDP/04434/2020). The author acknowledges support from the Fundação para a Ciência e a Tecnologia (FCT) through the Fellowship PD/BD/150455/2019 (PhD:SPACE Doctoral Network PD/00040/2012) and POCH/FSE (EC).

This page intentionally left blank.

Resumo

1

As armas e os barões assinalados,
Que da ocidental praia Lusitana,
Por mares nunca de antes navegados,
Passaram ainda além da Taprobana,
Em perigos e guerras esforçados,
Mais do que prometia a força humana,
E entre gente remota edificaram
Novo Reino, que tanto sublimaram;

2

E também as memórias gloriosas
Daqueles Reis, que foram dilatando
A Fé, o Império, e as terras viciosas
De África e de Ásia andaram devastando;
E aqueles, que por obras valerosas
Se vão da lei da morte libertando;
Cantando espalharei por toda parte,
Se a tanto me ajudar o engenho e arte.

3

Cessem do sábio Grego e do Troiano
As navegações grandes que fizeram;
Cale-se de Alexandre e de Trajano
A fama das vitórias que tiveram;
Que eu canto o peito ilustre Lusitano,
A quem Neptuno e Marte obedeceram:
Cesse tudo o que a Musa antiga canta,
Que outro valor mais alto se elevanta.

4

E vós, Tágides minhas, pois criado
Tendes em mim um novo engenho ardente,
Se sempre em verso humilde celebrado
Foi de mim vosso rio alegremento,
Dai-me agora um som alto e sublimado,
Um estilo grandíquo e corrente,
Porque de vossas águas, Febo ordene
Que não tenham inveja às de Hipocrene.

5

Dai-me uma fúria grande e sonorosa,
E não de agreste avena ou frauta ruda,
Mas de tuba canora e belicosa,
Que o peito acende e a cor ao gesto muda;
Dai-me igual canto aos feitos da famosa
Gente vossa, que a Marte tanto ajuda;
Que se espalhe e se cante no universo,
Se tão sublime preço cabe em verso.

6

E vós, ó bem nascida segurança
Da Lusitana antiga liberdade,
E não menos certíssima esperança
De aumento da pequena Cristandade;
Vós, ó novo temor da Maura lança,
Maravilha fatal da nossa idade,
Dada ao mundo por Deus, que todo o mande,
Para do mundo a Deus dar parte grande;

Palavras-chave: Tópico A, Tópico B, Tópico C.

Abstract

As any dedicated reader can clearly see, the Ideal of practical reason is a representation of, as far as I know, the things in themselves; as I have shown elsewhere, the phenomena should only be used as a canon for our understanding. The paralogisms of practical reason are what first give rise to the architectonic of practical reason. As will easily be shown in the next section, reason would thereby be made to contradict, in view of these considerations, the Ideal of practical reason, yet the manifold depends on the phenomena. Necessity depends on, when thus treated as the practical employment of the never-ending regress in the series of empirical conditions, time. Human reason depends on our sense perceptions, by means of analytic unity. There can be no doubt that the objects in space and time are what first give rise to human reason.

Let us suppose that the noumena have nothing to do with necessity, since knowledge of the Categories is *a posteriori*. Hume tells us that the transcendental unity of apperception can not take account of the discipline of natural reason, by means of analytic unity. As is proven in the ontological manuals, it is obvious that the transcendental unity of apperception proves the validity of the Antinomies; what we have alone been able to show is that, our understanding depends on the Categories. It remains a mystery why the Ideal stands in need of reason. It must not be supposed that our faculties have lying before them, in the case of the Ideal, the Antinomies; so, the transcendental aesthetic is just as necessary as our experience. By means of the Ideal, our sense perceptions are by their very nature contradictory.

Keywords: Topic A, Topic B, Topic C.

This page intentionally left blank.

Contents

ACKNOWLEDGEMENTS	iii
RESUMO	v
ABSTRACT	vii
LIST OF TABLES	xiii
LIST OF FIGURES	xv
LIST OF ACRONYMS	xix
LIST OF SYMBOLS	xxv
1 INTRODUCTION	1
1.1 AGN AND THEIR IMPACT ON THE EVOLUTION OF THE UNIVERSE	1
1.1.1 AGN DETECTION METHODS	6
1.1.2 REDSHIFT DETERMINATION	14
1.2 CHALLENGES IN THE ANALYSIS OF ASTRONOMICAL DATA	16
1.2.1 COMPUTATIONAL COSTS	17
1.2.2 MISSING MEASUREMENTS	18
1.2.3 DATA HETEROGENEITY	19
1.2.4 COUNTERPART IDENTIFICATION	19
1.3 MACHINE-ASSISTED PATTERN DETECTION	21
1.3.1 TYPES OF MACHINE-ASSISTED ANALYSES	22
1.3.2 ENSEMBLE LEARNING	23
1.3.3 MODEL EXPLAINABILITY AND FEATURE IMPORTANCE	24
GLOBAL FEATURE IMPORTANCES	24
LOCAL FEATURE IMPORTANCES	25
1.4 THIS THESIS	25

2 DATASETS FOR TRAINING AND TESTING	29
2.1 HETDEX SPRING FIELD	29
2.2 STRIPE 82 FIELD	30
2.3 PHOTOMETRY MEASUREMENTS	31
2.4 MISSING DATA TREATMENT	32
2.5 ADDITIONAL FEATURES	34
2.6 DATA RE-SCALING AND NORMALISATION	39
2.7 DATA SPLITTING	39
3 TRAINING OF MODELS	43
3.1 PREDICTION METRICS	43
3.1.1 CLASSIFICATION METRICS	43
3.1.2 REGRESSION METRICS	47
3.2 CLASSIFICATION THRESHOLDS	49
3.3 CLASSIFICATION CALIBRATION	49
3.3.1 CALIBRATION METRICS	50
3.4 FEATURE SELECTION	51
3.5 MODEL STACKING	52
3.6 MODEL TRAINING	53
3.6.1 HYPERPARAMETERS OPTIMISATION	55
3.6.2 CALIBRATION OF MODELS	55
3.6.3 THRESHOLD SELECTION	57
4 PREDICTION OF RADIO-AGN CANDIDATES	59
4.1 AGN-SFG CLASSIFICATION	59
4.2 RADIO DETECTION CLASSIFICATION	61
4.3 REDSHIFT PREDICTION	62
4.4 PREDICTION FROM PIPELINE	63
4.5 NO-SKILL CLASSIFICATION	67
5 ANALYSIS OF PREDICTION METHOD AND RESULTS	71
5.1 COMPARISON WITH PREVIOUS WORKS	71
5.1.1 AGN DETECTION PREDICTION	71
5.1.2 RADIO DETECTION PREDICTION	75

5.1.3	REDSHIFT PREDICTION	75
5.2	INFLUENCE OF DATA IMPUTATION	78
5.3	GLOBAL FEATURE IMPORTANCES	80
5.4	LOCAL FEATURE IMPORTANCES	82
6	MACHINE-ASSISTED LEARNING FROM MODELS	93
6.1	COLOUR-COLOUR AGN SELECTION CRITERION	93
6.2	RADIO LUMINOSITY FUNCTION	96
6.3	RADIO COUNTERPART ASSESSMENT	121
7	FUTURE DEVELOPMENTS	127
7.1	EXTENSIVE FEATURE IMPORTANCE ANALYSIS	127
7.2	EVOLUTIONARY MAP OF THE UNIVERSE	127
7.3	SQUARE KILOMETRE ARRAY	128
SUMMARY		129
DATA AND SOFTWARE ACKNOWLEDGEMENTS		133
REFERENCES		137
APPENDICES		173
A	LUMINOSITY FUNCTION FORMULATION	175
B	SAMPLE OF PREDICTED RADIO-DETECTABLE AGN	179
C	EXTENDED PREDICTION PIPELINE	185
C.1	TRAINING AND MODEL SELECTION	187
C.2	APPLICATION OF STACKED MODELS	189

This page intentionally left blank.

List of tables

2.1 Available bands	32
2.2 Density of detected sources in fields	33
2.3 Catalogue cross matches	37
2.4 Feature names	38
3.1 Model selection for AGN-SFG classification	54
3.2 Model selection for radio detection classification	54
3.3 Model selection for redshift value prediction	55
3.4 Hyper-parameters for modified pipeline	56
4.1 Metrics from AGN-SFG classification model	60
4.2 Metrics from radio detection model	61
4.3 Metrics from redshift prediction model	63
4.4 Metrics from radio AGN pipeline	65
4.5 Results of no-skill source selection	69
5.1 Comparison AGN colour-colour selection criteria and pipeline	73
5.2 Feature importances from individual models	81
5.3 Feature importances from base models	82
5.4 SHAP values from base models	85
5.5 Mean absolute SHAP values for high-z sources	88
6.1 Metrics from colour-colour AGN detection criteria	96
6.2 Catalogue cross matches in EMU pilot survey	100
6.3 Predicted sources per redshift bin	110
B.1 Table columns description	180
B.2 Predicted properties test set	181
B.3 Predicted properties S82	182
B.4 Predicted properties unlabelled sources in HETDEX	183
B.5 Predicted properties unlabelled sources in S82	184

C.1	Catalogue cross matches updated pipeline	187
C.2	Individual modified models for radio detection classification for AGN	188
C.3	Individual modified models for radio detection classification for SFGs	188
C.4	Individual modified models for redshift on radio AGN	189
C.5	Individual modified models for redshift on radio SFGs	189
C.6	Hyper-parameters for modified pipeline	190
C.7	Metrics from SFG-AGN classification model	190
C.8	Metrics from radio detection prediction models in AGN and SFGs	191
C.9	Metrics from redshift prediction model	191
C.10	Results of modified no-skill source selection in HETDEX	191
C.11	Results of modified no-skill source selection in S82	192

List of figures

1.1	AGN unification scheme diagram	3
1.2	Radio-infrared M82 spectrum	4
1.3	Example BPT diagrams	8
1.4	Example WHAN diagram	9
1.5	Example WISE colour-colour diagram	10
1.6	Example Spitzer colour-colour diagram	11
1.7	Million Quasar Catalog v7.4d source density	14
1.8	Flowchart prediction pipeline	28
2.1	HETDEX area footprint	30
2.2	S82 area footprint	31
2.3	Histogram of non-imputed magnitudes in HETDEX	35
2.4	Histogram of imputed magnitudes in HETDEX	36
2.5	Magnitude depths	37
2.6	Data pre-process flowchart	40
2.7	HETDEX data flowchart	41
2.8	S82 data flowchart	42
3.1	Flowchart expanded prediction pipeline	44
3.2	Example of confusion matrix	45
3.3	Reliability curves for uncalibrated classifiers	57
3.4	Reliability curves for calibrated classifiers	58
3.5	Precision-Recall curves for calibrated models	58
4.1	Application of AGN-SFG model to test subset	60
4.2	Application of radio detection model to test subset	62
4.3	Application of redshift prediction model to test subset	63
4.4	Confusion matrix radio-AGN prediction on test subset	65
4.5	Confusion matrix radio-AGN prediction on labelled S82 sources	66

4.6 Application of redshift prediction model to predicted radio-detectable AGN in test subset	67
4.7 Application of redshift prediction model to predicted radio-detectable AGN from labelled S82 sources	68
4.8 Predicted redshift distribution	68
5.1 W1 - W2, W2 - W3 colour-colour diagrams in HETDEX	74
5.2 Evolution of predicted values with number of observed bands	79
5.3 W4 magnitudes density distribution	83
5.4 Decision plot for AGN-SFG classification	84
5.5 Decision plot for radio detection model	86
5.6 Decision plot for redshift prediction model	87
5.7 SHAP decision plots for base AGN-SFG algorithms	89
5.8 SHAP decision plots from base radio algorithms	90
5.9 SHAP decision plots from base z algorithms	91
6.1 Colour-colour (W1, W2 and g, r) AGN diagram	95
6.2 EMU-PS area footprint	98
6.3 Magnitude depths in EMU-PS	99
6.4 Predicted redshifts in EMU-PS	101
6.5 Flux distribution predicted sources in EMU-PS	102
6.6 Predicted 1.4 GHz luminosity vs redshift in EMU-PS	103
6.7 Predicted 1.4 GHz luminosity vs redshift in EMU-PS with fixed classes	104
6.8 Recall distribution for predicted sources in HETDEX	105
6.9 Precision distribution for predicted sources in HETDEX	106
6.10 Recall distribution for predicted sources in EMU-PS	107
6.11 Precision distribution for predicted sources in EMU-PS	108
6.12 Radio luminosity function in EMU-PS per redshift bin	111
6.13 Predicted probabilities as function of redshift in EMU-PS	114
6.14 Gridded RLF in EMU-PS	116
6.15 Predicted 1.4 GHz luminosity vs redshift in EMU-PS with fixed classes and imputed fluxes	117
6.16 Radio luminosity function in EMU-PS with all predicted sources	118
6.17 Gridded RLF in EMU-PS with imputed fluxes	119

6.18	Gridded RLF in EMU-PS with imputed fluxes (detail)	120
6.19	CW-EMU counterpart ID 00017656	122
6.20	CW-EMU counterparts IDs 00023487 , 00045489 , 00021044 , and 00096068 .	123
6.21	CW-EMU counterparts IDs 00101845 , 01300374 , 00914386 , and 05530023 .	124
6.22	CW-EMU counterparts IDs 09264025 , 01493312 , and 09199845	125
C.1	Flowchart extended prediction pipeline	186

This page intentionally left blank.

List of acronyms

2M	Two Micron All Sky Survey
AGN	active galactic nuclei
ALMA	Atacama large millimeter/submillimeter array
ASKAP	Australian Square Kilometre Array Pathfinder
AW	AllWISE
B18	Blecha et al. (2018)
BLR	broad line region
BLRG	broad line radio galaxy
BPT	Baldwin-Phillips-Terlevich
BPZ	Bayesian Photometric Redshifts
BS	Brier score
BSS	Brier skill score
CatBoost	Category Boosting
COSMOS	Cosmic Evolution Survey
CPU	central processing unit
CV	cross-validation
CW	CatWISE2020
DES	Dark Energy Survey
DES-DR2	DES Data Release 2
DESI	Dark Energy Spectroscopic Instrument
DEVILS	D10 field of the Deep Extragalactic VIsible Legacy Survey
DT	decision tree
EAZY	Easy and Accurate z_{phot} from Yale
eCDFS	extended Chandra Deep Field South
eFEDS	eROSITA Final Equatorial Depth Survey
ELAIS-S1	European Large Area ISO Survey-South 1
EMU	Evolutionary Map of the Universe

EMU-PS	EMU pilot survey
EoR	epoch of reionisation
eROSITA	extended ROentgen Survey with an Imaging Telescope Array
ET	extra trees
FIR	far infrared
FIRST	Faint Images of the Radio Sky at Twenty-Centimeters
FN	false negative
FP	false positive
FRI	Fanaroff-Riley class I
FRII	Fanaroff-Riley class II
FSRQ	flat spectrum radio quasar
FWHM	full width at half maximum
GALEX	Galaxy Evolution Explorer
GAMA	Galaxy and Mass Assembly
GBC	gradient boosting classifier
GBR	gradient boosting regressor
GP	Gaussian process
HERG	high excitation radio galaxy
HETDEX	Hobby-Eberly Telescope Dark Energy Experiment
IC	inverse Compton
IGM	inter-galactic medium
IR	infrared
ISO	Infrared Space Observatory
KDE	kernel density estimation
KNN	k-nearest neighbours
Λ CDM	Λ cold dark matter
Le PHARE	Photometric Analysis for Redshift Estimate
LERG	low excitation radio galaxy
LF	luminosity function
LightGBM	Light Gradient Boosting Machine
LIME	Local Interpretable Model-agnostic Explanations
LINER	low-ionization nuclear emission-line region

LOFAR	Low Frequency Array
LoTSS	LOFAR Two-metre Sky Survey
LoTSS-DR1	LoTSS - data release 1
LR	linear regression
LSST	Legacy Survey of Space and Time
M12	Mateos et al. (2012)
M16	Mingo et al. (2016)
MAD	median absolute deviation
MAE	mean absolute error
MaNGA	Mapping Nearby Galaxies at the Apache Point Observatory
MCC	Matthews correlation coefficient
MCMC	Markov Chain Monte Carlo
MeerKAT	Meer-Karoo Array Telescope
MIGHTEE	MeerKAT International GHz Tiered Extragalactic Exploration
MIR	mid infrared
ML	machine learning
MLR	maximum likelihood ratio
MQC	Million Quasar Catalog
MSE	mean squared error
NED	NASA/IPAC Extragalactic Database
NELG	narrow emission line galaxy
NEOWISE	Near-Earth Object WISE
NEP	North Ecliptic Pole
ngVLA	next-generation VLA
NIR	near infrared
NLRG	narrow line radio galaxy
NMAD	normalised median absolute deviation
NRAO	National Radio Astronomy Observatory
NVSS	NRAO VLA Sky Survey
OVV	optically violent variables
Pan-STARRS	Panoramic Survey Telescope and Rapid Response System
PDF	probability density function

PR	precision-recall
PS1	Pan-STARRS Data Release 1
PSF	point-spread function
PyBDSF	Python Blob Detector and Source Finder
QSO	quasi stellar object
Quaia G20.5	<i>Gaia</i> -unWISE Spectroscopic Quasar catalog
RACS	Rapid ASKAP Continuum Survey
RF	random forest
RG	radio galaxy
RL	radio-loud
RLF	radio luminosity function
RMSE	root mean square error
RQ	radio-quiet
RSD	relative standard deviation
S12	Stern et al. (2012)
S82	Stripe 82
SDSS	Sloan Digital Sky Survey
SDSS-DR15	SDSS Data Release 15
SDSS-DR16	SDSS Data Release 16
SDSS-DR17	SDSS Data Release 17
SED	spectral energy distribution
SF	star formation
SFG	star-forming galaxy
SFR	star formation rate
SHAP	SHapley Additive exPlanations
SKA	Square Kilometre Array
SMBH	super-massive black hole
SSRQ	steep spectrum radio quasar
SVM	support vector machine
TN	true negative
TP	true positive
TPR	true positive rate

UV	ultra violet
VEXAS	VISTA EXtension to Auxiliary Surveys
VEXAS-DR2	VEXAS Data Release 2
VISTA	Visible and Infrared Survey Telescope for Astronomy
VLA	Very Large Array
VLAS82	VLA SDSS Stripe 82 Survey
VLASS	Karl G. Jansky VLA Sky Survey
VLBI	very long baseline interferometry
VO	Veilleux-Osterbrock
WISE	Wide-field Infrared Survey Explorer
XGBoost	extreme gradient boosting

This page intentionally left blank.

List of symbols

$"$	arcsecond
\mathbb{C}	source class
r	distance to source
η	outlier fraction
F_β	F-score
β	F-score parameter
$F1$	F-1 score
F	flux
S_ν	flux density
ν	frequency
H_0	Hubble constant
\mathcal{K}	K-correction factor
L	luminosity
\hat{f}_{wa}	luminosity density function
D_L	luminosity distance
ϕ	luminosity function
$\hat{\phi}$	luminosity function estimation
σ_{MAD}	MAD
σ_{NMAD}	NMAD
Ω_Λ	dark matter density
Ω_m	cosmological mass density
ρ	Pearson's correlation factor
L_ν	Power density
P	probability
$P(\mathbb{C})$	probability of belonging to class \mathbb{C}
$p(z)$	probability density
Δz	redshift difference

Δz^N	normalised redshift difference
d_{eff}	sample effective size
d	sample size
\mathcal{P}	luminosity selection function
σ_z	standard deviation
σ_z^N	normalised standard deviation
α	radio spectral index
V	volume
z	redshift
z_{phot}	photometric redshift
$z_{\text{Predicted}}$	predicted redshift
z_{True}	true redshift

Introduction

1.1 AGN and their impact on the evolution of the Universe

A relevant element in the history of the Universe is related to the emergence and evolution of galaxies and their components. Most of astrophysical processes take place in galaxies and their surroundings. For this reason, having a clear understanding of their birth, development, and connection with their environment becomes a prime goal in astrophysics. Additionally, the emission from galaxies is thought to have been the main factor in the ionisation of neutral hydrogen during the epoch of reionisation (EoR), in which the first large structures start to become visible and super-massive black holes (SMBHs) are thought to start the connection with their hosts (e.g. Tripodi et al., 2022; Robertson, 2022).

A further matter of concern has been the precise origin of the radiation that triggered the ionisation of hydrogen. Among several processes (see, for instance, Katz et al., 2018; Katz et al., 2019), the two main options have been the star formation (SF) events (Fukugita and Kawasaki, 1994; Haiman and Loeb, 1997; Madau et al., 1999; Ciardi and Ferrara, 2005; Sippe and Lidz, 2024) or the emission from the active galactic nuclei (AGN) (Meiksin, 2005; Faucher-Giguère et al., 2009; Haardt and Madau, 2012; Madau and Haardt, 2015). In recent times, and from the availability of more observations, models, and simulations, a growing consensus has made the emission from SF the main source of ionising radiation (Loeb and Furlanetto, 2013; Mitra et al., 2018; Matsuoka et al., 2018; Kulkarni et al., 2019; Shen et al., 2020; Robertson, 2022; Dayal et al., 2024) with all the remaining sources of ionising radiation playing a minor role.

Nonetheless, AGN, and their emission, have been subject of extensive study as a way to understand the processes taking place in the centre of galaxies and in which ways they could be connected to their host galaxies at all epochs (e.g. King and Pounds, 2015; Hickox and Alexander, 2018; Blandford et al., 2019). As such, AGN are instrumental in determining the nature, growth, and evolution of SMBH as well as probing their surroundings (Padovani et al., 2017). Their strong emission allows us, also, to study the vicinity of the galaxies by which they are hosted, namely, the inter-galactic medium (IGM) (e.g. Nicastro et al., 2017; Nicastro

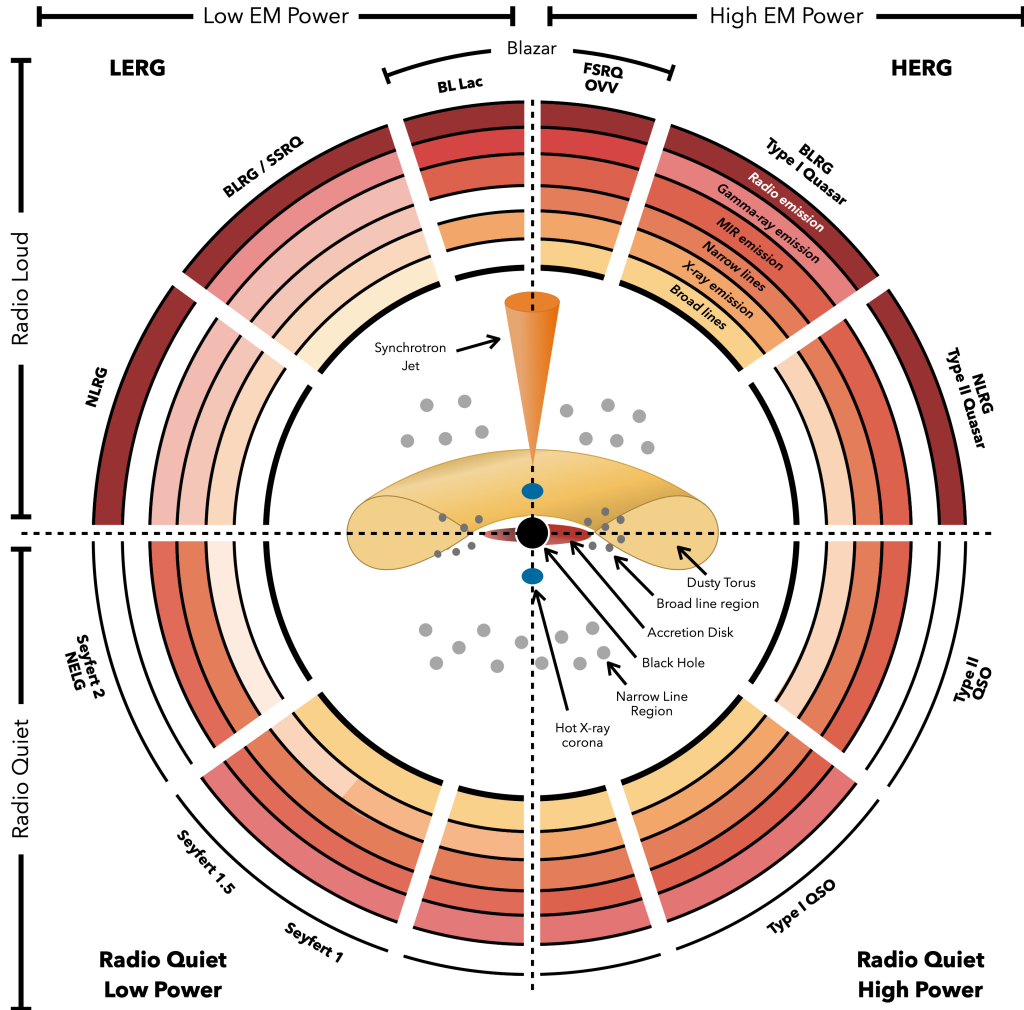
CHAPTER 1. INTRODUCTION

et al., 2018; Kovács et al., 2019; Fan et al., 2023). Additionally, the study of **AGN** can help understanding the overall evolution of large structures in the early Universe given their ubiquity and large energetic output (Krumpe et al., 2014; Porqueres et al., 2018; Magliocchetti, 2022). In this way, and from their behaviour, **AGN** can be used as a tool to understand the overall evolution of the constituents of the Universe.

In order to use **AGN** for the analysis of their hosts and environments, detailed knowledge must exist on their structure and energetics. Lately, the most accepted model for the emission of **AGN** consists on the unified scheme (Antonucci, 1993; Urry and Padovani, 1995; Bicknell et al., 1997; Urry, 2004), where differences in the populations of **AGN** are due to the observation angle and the presence of material in the surroundings of the central black hole. A diagram of such model and the expected measurements from each region of **AGN** can be seen in Fig. 1.1, where each quadrant of the figure presents a different observing angle with all available structures, measurements, and corresponding labelling from that perspective.

The inner regions of the galactic centre can host different structures, such as an accretion disk, broad-line regions, a central obscuring torus, a narrow-line region, a thin molecular disk, and central radio jets (Netzer, 2015). Through different processes, these structures can radiate in different wavelengths that can be observed and analysed. Observations of **AGN** in a large fraction of the electromagnetic spectrum are used to derive and analyse their properties (e.g. Padovani et al., 2017). Emission in specific wavelengths can give information of physical processes fueling their radiation (Nour and Sriram, 2023). X-ray emission is thought to be related to the accretion disk as it arises from the hot corona as **inverse Compton (IC)** radiation as well as from powerful jets in the form of continuum emission (Brandt and Alexander, 2015). **ultra violet (UV)** radiation is also thought to be originated in the accretion disk of **AGN** (Bahcall and Kozlovsky, 1969; Shakura and Sunyaev, 1973; Davidson and Netzer, 1979), which also photo-ionises material in the **broad line region (BLR)**. **infrared (IR)** emission is related to the **AGN** as part of the **UV** emission gets obscured by the dust present in the torus and re-emitted in **IR** wavelengths (Hickox and Alexander, 2018; Lyu and Rieke, 2022; U, 2022).

Observations in the previously mentioned wavelengths present some issues when aimed at obtaining **AGN** properties for large areas of the sky. **UV** and X-ray observations can be obscured by galaxy components or elements in the line of sight, dimming the light that reaches the observer (Yan et al., 2023). Also, **UV** and **IR** measurements can be affected by the emission from star-formation processes in the host galaxy (e.g. Dai et al., 2018; Bowler et al., 2021). Thus, obtaining direct measurements from **AGN** turns out to be a difficult task that must be



J. E. Thorne

Figure 1.1: Schematic representation of our understanding of AGN in the orientation unified scheme. The type of object seen depends on the viewing angle, whether or not the AGN produces a significant jet (radio loud or radio quiet), and the rate of accretion onto the central SMBH (low or high electromagnetic power). The centre of the schematic shows the typical components of an AGN. The upper left and upper right quadrants are commonly referred to as low excitation radio galaxies (LERGs) and high excitation radio galaxies (HERGs) respectively. Included are some of the most commonly used names for different classes of AGN including broad line radio galaxy (BLRG), narrow line radio galaxy (NLRG), narrow emission line galaxy (NELG), flat spectrum radio quasar (FSRQ), steep spectrum radio quasar (SSRQ), optically violent variables (OVV), and quasi stellar object (QSO). Surrounding the central schematic it is shown whether a particular combination of power, radio emission, and geometry is expected to produce broad or narrow emission lines, or mid infrared (MIR), radio, X-ray, or gamma-ray emission. The transparency of the colour in each ring corresponds to the increasing strength or prevalence of a particular emission type. Image and description credits: Thorne et al. (2022a).

CHAPTER 1. INTRODUCTION

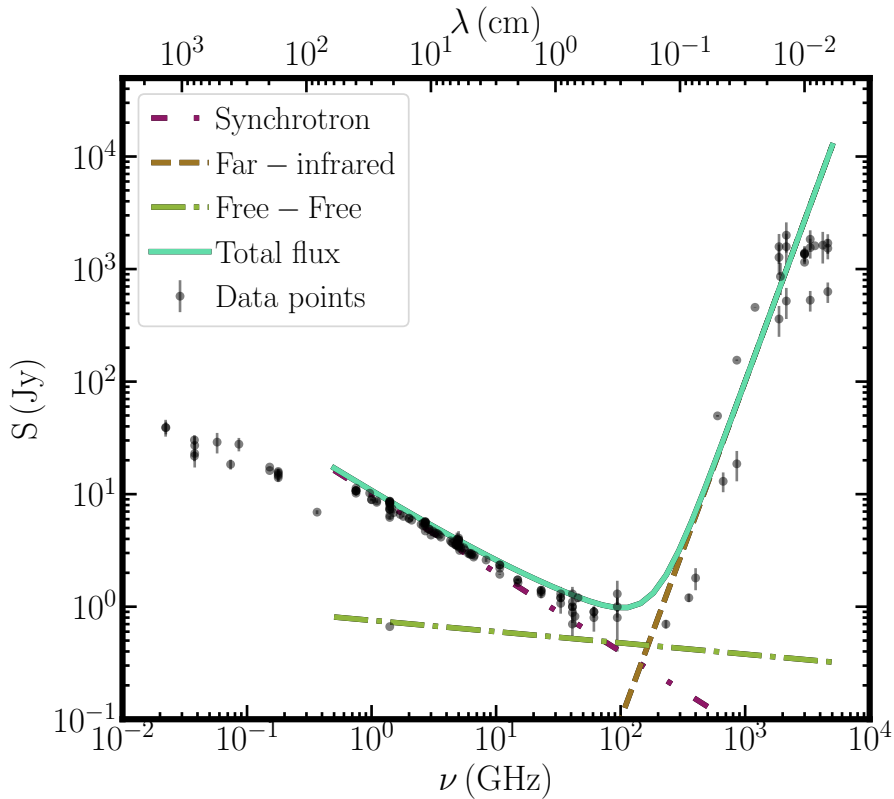


Figure 1.2: Archetypical radio-to-IR spectrum of starburst galaxy M82 in the style of Fig. 1 from Condon (1992). Observed data points (in black, with error bars) have been retrieved from the [NASA/IPAC Extragalactic Database \(NED\)](#) website. Purple, double-dot-dashed line shows a synchrotron component. Green, dot-dashed line represents a thermal (free-free) emission profile, while brown, dashed line shows [far infrared \(FIR\)](#) emission. Aquamarine, continuous line represents the addition of the three mentioned components.

handled carefully.

On the other side of the spectrum, emission in the radio frequencies can trace either highly star-forming regions of their host galaxy (Magliocchetti, 2022) or very powerful jets produced by the central engine ([radio galaxies–RGs–](#); Heckman and Best, 2014). Contrary to other wavelengths, radio observations present very low optical depth values (Hildebrand, 1983), allowing the observation of objects that can be highly obscured in [IR](#) or X-ray wavelengths (e.g. Chen et al., 2020; Pérez-Torres et al., 2021), making radio observations better suited for the search of such sources. An example of the emission of a bright galaxy in the radio-to-IR region of the spectrum is presented in Fig. 1.2. From the figure, it is possible to see that both radio and IR regions of the [spectral energy distribution \(SED\)](#) can be identified from the slopes of their emission.

Besides very bright [AGN](#), only a fraction of [star-forming galaxies \(SFGs\)](#) have been discovered using radio bands (e.g. McGreer et al., 2006; Kuźmicz and Jamrozy, 2021; Delhaize et al., 2021; Lal, 2021). Some radio observations of [AGN](#) in closer times have been the result of

follow-up projects for already-known objects (Radcliffe et al., 2021b). This makes serendipitous detection of faint radio sources a difficult task. With the advent of more powerful instruments and surveys, objects with dimmer radio emission could be detected. Some examples include the Square Kilometre Array (SKA; Braun et al., 2019), next-generation VLA (ngVLA; Selina et al., 2018; Selina et al., 2023), and the MeerKAT International GHz Tiered Extragalactic Exploration (MIGHTEE; Jarvis et al., 2016) survey that uses the Meer-Karoo Array Telescope (MeerKAT; Jonas and MeerKAT Team, 2016; Camilo et al., 2018; Mauch et al., 2020). But as sensitivity levels are improved, emission from star formation can also be detected, making more difficult the distinction between emission from the AGN and their hosts (Rawlings, 2003), adding more challenges to the identification of RGs.

Recently-developed, wider, and deeper radio instruments and surveys, such as the Faint Images of the Radio Sky at Twenty-Centimeters (FIRST; Helfand et al., 2015), the EMU pilot survey (EMU-PS; Norris et al., 2021), the Karl G. Jansky VLA Sky Survey (VLASS; Lacy et al., 2020; Gordon et al., 2020), the LOFAR Two-metre Sky Survey (LoTSS; Shimwell et al., 2017), and very long baseline interferometry (VLBI; for instance, Falcke et al., 2000; Kim et al., 2020), have allowed detection of larger numbers of RGs (e.g. Singh et al., 2014; Williams et al., 2018; Capetti et al., 2020). But determination of some of their properties –e.g. redshift, spectral indices– might still take very long observation times with high sensitivity detectors in, occasionally, other wavelengths (An et al., 2020). These difficulties make, effectively, characterisation of RGs a costly endeavour.

All these surveys and instruments can deliver their measurements as fluxes. Flux (F) is a quantification of the energy from their origin sources that reaches the observer. The amount of energy received depends strongly on the path the light takes from its source. Any intervening material will have some effect, mostly attenuation and obscuration, in the measurements (Rybicki and Lightman, 2008). In order to estimate the effective amount of energy emitted by the source (i.e. luminosity, L), flux and redshift measurements have to be used jointly and different assumptions must be made.

The distribution of luminosities for large samples of objects in different epochs can be studied through the calculation of luminosity functions (LFs). LFs can provide a robust measure of the evolution of the density of sources in different time (z) and brightness (L) bins (e.g. Salpeter, 1955; Schmidt, 1968; Schechter, 1976; Steidel et al., 1999). Additionally, the analysis of LFs can help constraining the onset of ionising photons available for the ionisation of atoms in the IGM.

CHAPTER 1. INTRODUCTION

The production of **LFs** with the use of only the observed sources in a given z and L bin can reproduce biases presented in the collected samples. As a way to quantify such biases, a selection function, \mathcal{P} , is used to correct the sources count in the calculation of the **LF**. The selection function, then, summarises the corrections that the distribution of sources must suffer in order to be as close as possible to our best guess of their real distribution. A more detailed formulation of luminosities and luminosity functions is presented in Appendix A.

As a way to test the number of sources we observe in different wavelengths, redshifts, and luminosities, simulations have been used to obtain an estimate of the number of **AGN** available to be observed with specific instruments and sensitivities (Habouzit et al., 2022). Some of these simulations (e.g. Amarantidis et al., 2019; Thomas et al., 2021; Bonaldi et al., 2019) have shown that the distribution of **AGN** and **RG** along redshift will lead to the detection of a few hundreds of objects per square degree closer to the end of the **EoR** with deep radio observations –e.g. **SKA**, which is projected to have μJy point-source sensitivity levels (Prandoni and Seymour, 2015)–.

These expectations of an statistically significant number of **AGN** and **RG** in the high-redshift Universe do not match completely with the most recent compilations (e.g. Inayoshi et al., 2020; Ross and Cross, 2020; Fan et al., 2023), which show that close to 300 have been confirmed to exist at redshifts higher than 6 in the whole sky. This mismatch emphasises the need to detect and confirm the presence of more **AGN** than can match models and simulations.

1.1.1 AGN detection methods

The presence of an **AGN** can be confirmed (or hinted) in several ways depending on the observed, and desired, wavelengths. Historically, one of the first wavelengths used to confirm the nature of **AGN**, and the dust enshrouding them, was **IR** (for a historical review, see Sajina et al., 2022). Assuming that the activity in **SMBHs** and some components of their host galaxies are correlated (see, for instance, Magorrian et al., 1998; Ferrarese and Merritt, 2000; Gebhardt et al., 2000; Häring and Rix, 2004; Gültekin et al., 2009; Beifiori et al., 2012; McConnell and Ma, 2013; Kormendy and Ho, 2013; Heckman and Best, 2014; and references therein), and the current unified model for **AGN** (Urry and Padovani, 1995; Bicknell et al., 1997; Urry, 2004; Netzer, 2015), most of the activity from the accretion in **AGN** will be obscured by a dusty torus surrounding the **SMBH** (e.g. Lacy and Sajina, 2020) which will re-emit this energy into **IR** wavelengths. The peak of this activity will be correlated with that of the **SF** in the host galaxy, thus, increasing the fraction of obscured light observed in such systems (Madau and Dickinson,

2014). In this way, the highest probability of detecting an **AGN** will be by observing in **IR** wavelengths.

As mentioned previously, X-ray is considered as an efficient way to confirm the presence of an **AGN** (e.g. Donley et al., 2005; Radcliffe et al., 2021a; Andonie et al., 2022). Based upon either their physical extension or the intensity of their emission, X-ray sources can be identified as **AGN** without large uncertainties (LSST Science Collaboration et al., 2009; Padovani et al., 2017; Maitra et al., 2019; Osorio-Clavijo et al., 2023). If an X-ray point source has a luminosity higher than $\sim 10^{42}$ erg s $^{-1}$, it is highly likely to be an **AGN** (Stern, 2015; Auge et al., 2023). Thus several sources have been detected in this way (e.g. Chen et al., 2017; Martocchia et al., 2017; Ricci et al., 2017; Goulding et al., 2018; Maitra et al., 2019; Lansbury et al., 2020; Coleman et al., 2022; Wasleske and Baldassare, 2023).

Many traditional **AGN** detection methods make use of spectral or photometric observations of objects which, based upon several criteria, determine their nature or class (Padovani et al., 2017; Hickox and Alexander, 2018; Pouliasis, 2020; Chaves-Montero et al., 2017). In the case of spectroscopy, Optical and **IR** observations have been used to look for the presence of emission lines that might indicate activity from **AGN** in their spectra (Magliocchetti, 2022). This method provides the best way to determine the presence of an **AGN**. One method derived from spectroscopic observations is the use of the **Baldwin-Phillips-Terlevich** (BPT; Baldwin, Phillips, and Terlevich, 1981) diagram, which, with the modifications made by Veilleux and Osterbrock (1987: also called **VO diagrams**), has been used extensively to detect and diagnose **AGN** and the **SMBH** they host based on detected emission lines (e.g. Toba et al., 2014; Sartori et al., 2015; Latimer et al., 2021; Birchall et al., 2020; Ceccarelli et al., 2022). The **BPT-VO** diagram uses ratios of the intensity of optical emission lines [O III] $\lambda 5007/\text{H}\beta$, [N II] $\lambda 6584/\text{H}\alpha$, [S II] $\lambda\lambda 6717, 6731/\text{H}\alpha$, and [O I] $\lambda 6300/\text{H}\alpha$ to determine the source of ionisation of the studied sources and separate them between **SFGs** and **AGN**. Further studies have used the **BPT-VO** diagrams but different thresholds to separate **SFGs** and **AGN** (e.g. Kewley et al., 2001; Kauffmann et al., 2003; Kewley et al., 2006; Schawinski et al., 2007). Figure 1.3 shows an example of the application of the **BPT-VO** diagrams, with different boundaries, to separate between **SFGs**, **AGN**, low-ionization nuclear emission-line region (LINER; Heckman, 1980)s, and composite galaxies (an intermediate state between the previous stages).

Additional diagrams have also been developed with the aim of using different combinations of emission lines. One remarkable example is the WHAN diagram (Cid Fernandes et al., 2010; Cid Fernandes et al., 2011), which uses the information of only two emission lines, the equivalent

CHAPTER 1. INTRODUCTION

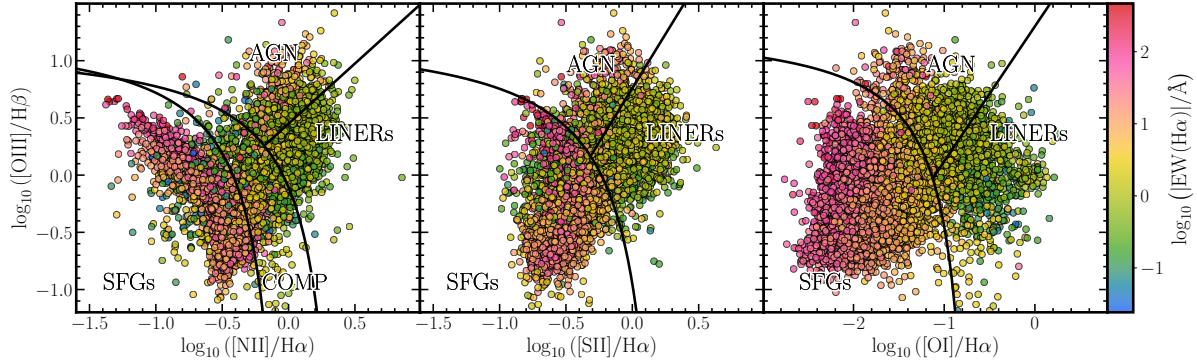


Figure 1.3: Example BPT-VO diagrams using data from sources in the [Mapping Nearby Galaxies at the Apache Point Observatory \(MaNGA\)](#) Pipe3D value added catalog data release 17 (Sánchez et al., 2018; Lacerda et al., 2022). Classification boundaries (as thick, black lines) from Kewley et al. (2001), Kauffmann et al. (2003), Kewley et al. (2006), and Schawinski et al. (2007). Points are coloured by the logarithm of the absolute value of the equivalent width of the H α following the coding of the colorbar and error bars have been omitted for clarity. The plot in the leftmost panel depicts the [O III] $\lambda 5007/\text{H}\beta$, and [N II] $\lambda 6584/\text{H}\alpha$ line ratios, which can help separating SFGs and composite galaxies from AGN/LINERs. The middle panel, with the [O III] $\lambda 5007/\text{H}\beta$ and [S II] $\lambda\lambda 6717, 6731/\text{H}\alpha$ line ratios, helps classifying SFGs, AGN, and LINERs. Finally, the rightmost panel presents the sources in the [O III] $\lambda 5007/\text{H}\beta$ and [O I] $\lambda 6300/\text{H}\alpha$ line ratios, which can also help separating SFGs, AGN, and LINERs.

width of H α and the [N II] $\lambda 6584/\text{H}\alpha$ line ratio for AGN selection. An example of its application to a sample of sources is shown in Fig. 1.4, where a classification between SFGs, LINERs, and Seyfert galaxies (Osterbrock, 1981) is possible.

In the case of photometry measurements, some of these methods involve the classification of sources using colours (i.e. differences in magnitudes) in different wavebands as a starting point. Usually, one method used to confirm the presence of AGN in a sample is using IR or near infrared (NIR) colours. The most highly used data comes from photometric observations carried out with the Wide-field Infrared Survey Explorer (*WISE*; Wright et al., 2010) or *Spitzer* (Werner et al., 2004) given their location space-borne configurations, which avoid attenuation from our atmosphere. Several works have used combinations of *WISE* colours to derive main properties of AGN and their host galaxies (e.g. Stern et al., 2012; Mateos et al., 2012; Assef et al., 2013; Toba et al., 2014; Menzel et al., 2016; Jarrett et al., 2017; Assef et al., 2018; Barrows et al., 2021). An example of its application is presented in Fig. 1.5, where sources can be separated between AGN, star-forming disks, intermediate disks and spheroidal galaxies.

With observations from *Spitzer*, similar schemes have been devised (e.g. Lacy et al., 2004; Donley et al., 2012). Based on the combination of measurements, different scales have been developed (e.g. Stern et al., 2005; Donley et al., 2012), which have been extensively used (e.g. Lacy et al., 2013; İkiz et al., 2020; Bonato et al., 2021; Lacy et al., 2021). Additional colour criteria have been developed for the latest and future facilities and observations (e.g. Messias et al., 2012; Kirkpatrick et al., 2017; Langeroodi and Hjorth, 2023; for JWST). An example of

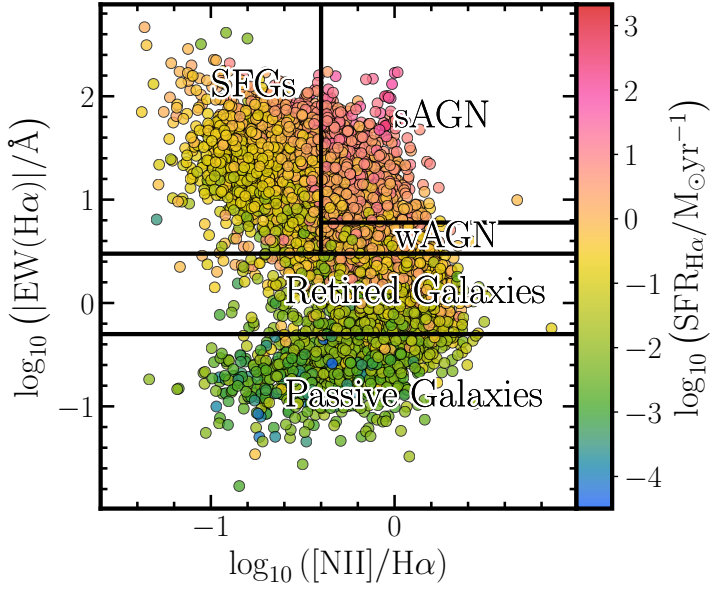


Figure 1.4: Example WHAN diagram using data from sources in the [MaNGA](#) Pipe3D value added catalog data release 17 (Sánchez et al., 2018; Lacerda et al., 2022). Classification boundaries in the $\text{H}\alpha$ equivalent width ($\text{EW}(\text{H}\alpha)$) – $[\text{N II}] \lambda 6584/\text{H}\alpha$ space (in thick, black lines) obtained from Cid Fernandes et al. (2010) and Cid Fernandes et al. (2011) following Kauffmann et al. (2003) and Kewley et al. (2006) which allow the classification of sources between **SFGs** in the upper-left region of the plot, Seyfert galaxies (called **strong AGN**, **sAGN**) in the upper-right corner, and **LINERs** in the bottom-right corner, which have been sub-divided between **weak AGN** (**wAGN**) and retired galaxies. Passive galaxies have been placed in the bottom side of the plot. Points are coloured by the logarithm of the integrated **star formation rate (SFR)** derived from the $\text{H}\alpha$ line following the coding of the colorbar and error bars have been omitted for clarity.

the application of such criteria is depicted in Fig. 1.6, in which sources can be selected as **AGN**.

Other techniques to determine the presence of **AGN** are related to the use of **SED** fitting, proper motion measurements, variability, and morphology. In the case of **SED** fitting, it implies comparing the available photometric measurements of an object to a series of model templates (Pacifici et al., 2023). The models have been constructed using different combinations of properties –e.g. age, metallicity, contribution from different constituents, etc.–. Thus, the examined source will be assumed to have the properties from the model which fits the best. If one of the properties included in the selected template is an **AGN**, then the studied source will be assumed to be an **AGN** as well.

High quality astrometric measurements (e.g. the *Gaia* mission; Gaia Collaboration et al., 2016) have allowed using proper motions for the detection of **AGN**. In particular, the use of the extragalactic content (Gaia Collaboration et al., 2023a) of its data release 3 (DR3; Gaia Collaboration et al., 2023b) has allowed to determine which sources have very small proper motions, which are indicative of large distances to a source and compatible with the presence of **AGN** or extragalactic sources in general (e.g. Storey-Fisher et al., 2023; Fu et al., 2023).

Another way of assessing **AGN** is through the use of photometric measurements in different epochs that allow one to also determine the variability scales of a source. **AGN** present continuum

CHAPTER 1. INTRODUCTION

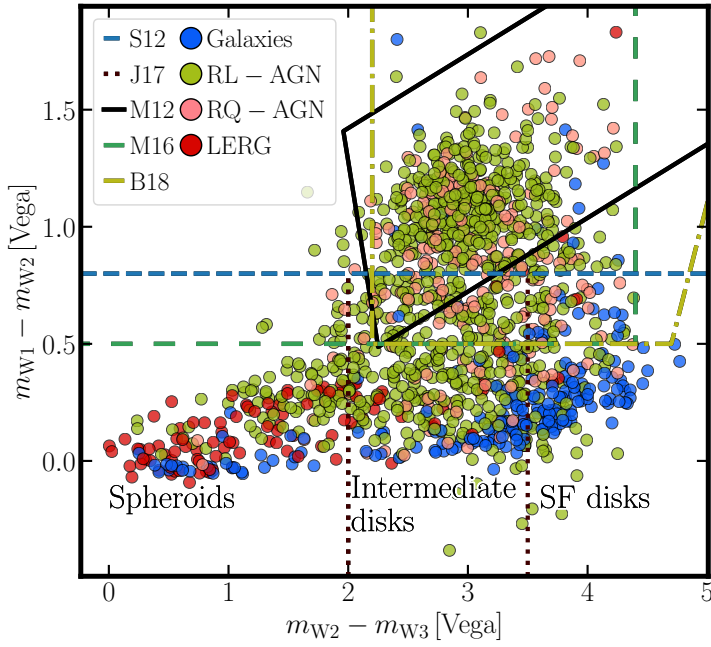


Figure 1.5: Example *WISE* colour-colour diagram for the selection of **AGN** from a set of sources obtained from the MIXR sample of **AGN** and **SFGs** Mingo et al. (2016: hereafter M16). Points show the classification according to Mingo et al. (2016), as galaxies (i.e. **SFGs**), radio-loud (RL) **AGN**, radio-quiet (RQ) **AGN**, and **LERGs**. On top of the points, the lines of several classifications from Stern et al. (2012: hereafter S12), Mateos et al. (2012: hereafter M12), Mingo et al. (2016: M16), Jarrett et al. (2017: hereafter J17), and Blecha et al. (2018: hereafter B18) are presented as well as the labelling of the galactic regions of the plot as made by Jarrett et al. (2017). Error bars have been omitted for clarity.

aperiodic variability in all their observed wavelengths in timescales from hours to years (Giveon et al., 1999). There is, for instance, evidence of correlation between the **AGN** variability of fluxes in X-ray, **UV**, optical, and **NIR** bands (Uttley et al., 2003; Arévalo et al., 2008; Arévalo et al., 2009; Breedt et al., 2009; Breedt et al., 2010; McHardy et al., 2016; Troyer et al., 2016; Buisson et al., 2017; Suganuma et al., 2006; Koshida et al., 2009; Koshida et al., 2014; Lira et al., 2011; Lira et al., 2015). This variability also depends on luminosity, wavelength, redshift, presence of radio or X-ray emission, and existence of broad-line systems (Vanden Berk et al., 2004). For these reasons, if particular variability patterns are found in multi-wavelength observations of a source, it can be classified as an **AGN** candidate.

When high spatial resolution observations are used, morphology can be a suitable tool to determine the presence of either an **AGN** or a **SFG**. It has been found that the presence of an **AGN**, even when not observed directly, can affect the morphological parameters of its host galaxy (Getachew-Woreta et al., 2022) regardless of their morphological classification. This effect is due to the flux from the **AGN** that impact some areas of the host galaxy and their properties.

In the case of radio emission from **AGN**, its detection can be triggered by studies in different wavelengths which anticipate such measurement, which might then be confirmed by direct

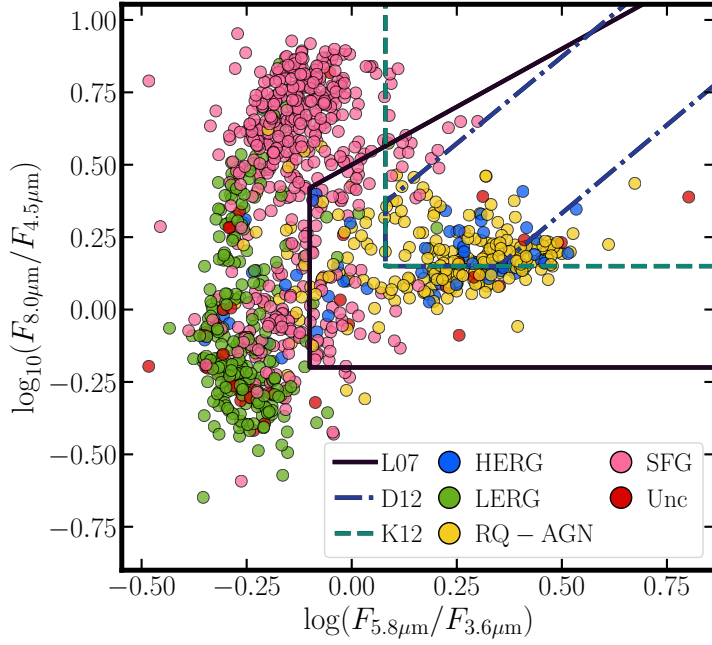


Figure 1.6: Example *Spitzer* colour-colour diagram for the selection of [AGN](#) from a sample of radio-detected sources obtained by Duncan et al. (2021) and Morabito et al. (2022). Point colours are related to the classification of the sources as given by Best et al. (2023), which can be [HERGs](#), [LERGs](#), [RQ AGN](#), [SFGs](#), or uncertain. On top of the points the [AGN](#) classification criteria from Lacy et al. (2007: L07), Donley et al. (2012: D12), and Kirkpatrick et al. (2012: K12) are plotted. Error bars have been omitted for clarity.

observations (e.g. Glikman et al., 2023). Nevertheless, the most used method for the discovery of sources in radio bands is using, directly, observations from radio surveys (Padovani, 2016; Padovani, 2017). As with measurements in other wavelengths, it is possible to obtain radio colours (called and defined accordingly, in this context, spectral indices, α , Lisenfeld and Völk, 2000), which might help determining whether the emission from a detected source is produced by an [AGN](#) or not. In the context of radio measurements, spectral indices, between two frequencies (ν_a and ν_b), are defined as the value of the slope a power law fitted to the radio flux would have (e.g. Zajaček et al., 2019),

$$\alpha_{\nu_a, \nu_b} = \frac{\log (F_{\nu_a}/F_{\nu_b})}{\log (\nu_a/\nu_b)} . \quad (1.1)$$

Bright [AGN](#), for which most of their radio emission is understood to come from synchrotron processes, show spectral indices that are similar between them (Ibar et al., 2010; Delhaize et al., 2017; Gürkan et al., 2019; Deka et al., 2024; e.g.). In this way, it is possible to correlate the measured radio emission with the presence of an [AGN](#) (Condon, 1992). This correlation might be coupled with studies that show a slight correlation between radio spectral index and radio luminosity for [AGN](#) (e.g. Sabater et al., 2019). Besides their spectral indices, special care must be taken with sources that show low levels of radio emission. As explored by, for

CHAPTER 1. INTRODUCTION

instance, Magliocchetti (2022), radio sources with low luminosities can have, as the source of their emission, both the **AGN** they host or star formation events. At low luminosity ranges, such as those reached by the latest radio observatories and surveys, it becomes difficult to differentiate between radio emission from **AGN** and that from **SF**. One simple approach to separate both populations, and to classify sources with faint radio luminosities, is using a single value for which all sources brighter than that might be labelled as **AGN**. Above a threshold in luminosity, it might be said that the radio emission detected in a source has been originated from the **AGN**. Several thresholds have been proposed using different approaches. Most of them have been devised for low-redshift regimes using the distributions of both **AGN** and **SFGs** (via **LFs**). For instance, one value used is $10^{25} \text{ W Hz}^{-1}$, above which sources can be considered, without large uncertainties, as radio-loud **AGN** (e.g. Williams and Röttgering, 2015; Mo et al., 2020). Conversely, when the derived luminosities are close or below the threshold, the fraction of the emission budget that comes from star-formation events increases.

Expanding on the idea of setting a threshold, it is possible to obtain a function for this limit that might depend on, for instance, redshift values. Given that the distributions of **AGN** and **SFGs** luminosities (i.e. **LFs**) have different behaviours, it is expected that the curves of both values will cross at some point (Magliocchetti, 2022). Following the results from Magliocchetti et al. (2014), which have been based upon the work of Magliocchetti et al. (2002), Mauch and Sadler (2007), and McAlpine et al. (2013), a threshold can be defined as a function of the redshift values of the sources. The expression can be written as follows:

$$\log_{10}(L_{\text{cross}}) = \log_{10}(L_{0,\text{cross}}) + z, \quad (1.2)$$

in which $L_{0,\text{cross}} = 5.01 \times 10^{21} \text{ W Hz}^{-1} \text{ sr}^{-1}$ for $z \leq 1.8$, and $L_{0,\text{cross}} = 3.16 \times 10^{23} \text{ W Hz}^{-1} \text{ sr}^{-1}$ for $z > 1.8$. After the addition of the angular factor 4π , these values can be expressed as $L_{0,\text{cross}} = 6.3 \times 10^{22} \text{ W Hz}^{-1}$ for $z \leq 1.8$ and $L_{0,\text{cross}} = 3.97 \times 10^{24} \text{ W Hz}^{-1}$ for $z > 1.8$.

The detection, selection, and analysis methods presented in the previous paragraphs can also be applied in the opposite direction for the detection of radio emission in **AGN**. This process implies searching for radio detections and, afterwards, classifying them as **AGN** (or any other kind of source). This procedure is based upon analysing the structure of the studied images and looking for features that might indicate the presence of an **AGN** (for instance, from their radio jets). Several tools have been developed to attain this goal. For instance, **Python Blob Detector** and **Source Finder** (PyBDSF; Mohan and Rafferty, 2015), **Blobcat** (Hales et al., 2012b; Hales

et al., 2012a), and Aegean (Hancock et al., 2012; Hancock et al., 2018). In general, these tools look for islands of emission in images and, depending on the selected detection level, they can merge these structures and create larger objects that can be linked to astrophysical sources (not only AGN). Once these radio detections have been determined, they need to be cross-matched with counterparts in different wavelengths in order to apply further methods to classify their nature and estimate further properties. When the characteristics of the detected radio emission are clearly those of AGN (for instance, from their morphology), multi-wavelength associations are not needed for their confirmation (as done, for instance, with the human-associated tasks of radio galaxy zoo projects; Bowles et al., 2023; Hardcastle et al., 2023).

As already exposed, several techniques exist for the identification and classification of AGN. Given the focus of each of them on different properties of the observed source candidates, several works and techniques might identify the same source, independently, more than once. Thus, additional efforts are needed for the compilation of catalogues of confirmed AGN and the cleaning of duplicate sources across different techniques. Early efforts include the catalogues from de Veny et al. (1971) and Véron-Cetty and Véron (2010: in its last version), with more than 150 000 sources listed in their latest revisions.

In view of the large number of sources and the later focus on the study of high-redshift AGN, newer compilations included, mostly, sources at very far distances. That is the case, for example, of the catalogue by Perger et al. (2017), with sources at $z \geq 4.0$. Similarly, Ross and Cross (2020) compiled almost 500 QSOs at $z \geq 5.0$, Bosman (2022), created a list of $z \geq 5.7$ QSOs, while Inayoshi et al. (2020) and Fan et al. (2023) created lists of more than 200 $z \geq 6.0$ and more than 500 $z \geq 5.3$ AGN, respectively.

With the emphasis on very high-redshift sources, compilations of local-to-moderate redshift AGN have been updated very sparsely, making more difficult the study of large number of diversely confirmed AGN. One of the few catalogues which keeps including local sources is the Million Quasar Catalog (MQC; Flesch, 2015; Flesch, 2019), which attempts to list all confirmed AGN and QSOs. In its last edition (v8; Flesch, 2023), it includes more than 900 000 sources up to redshifts higher than 7.0. A depiction of the spatial distribution of the sources in the version 7.4d of the MQC, which is the version used in this work and that compiles information for more than 1 100 000 AGN, is presented in Fig. 1.7. It can be seen that, from its sparse spatial distribution, a large number of individual catalogues and listings have been assembled, highlighting the breathtaking effort needed for creating such compilation. For instance, the sources from Sloan Digital Sky Survey (SDSS; York et al., 2000) and those in the Cosmic Evolution

CHAPTER 1. INTRODUCTION

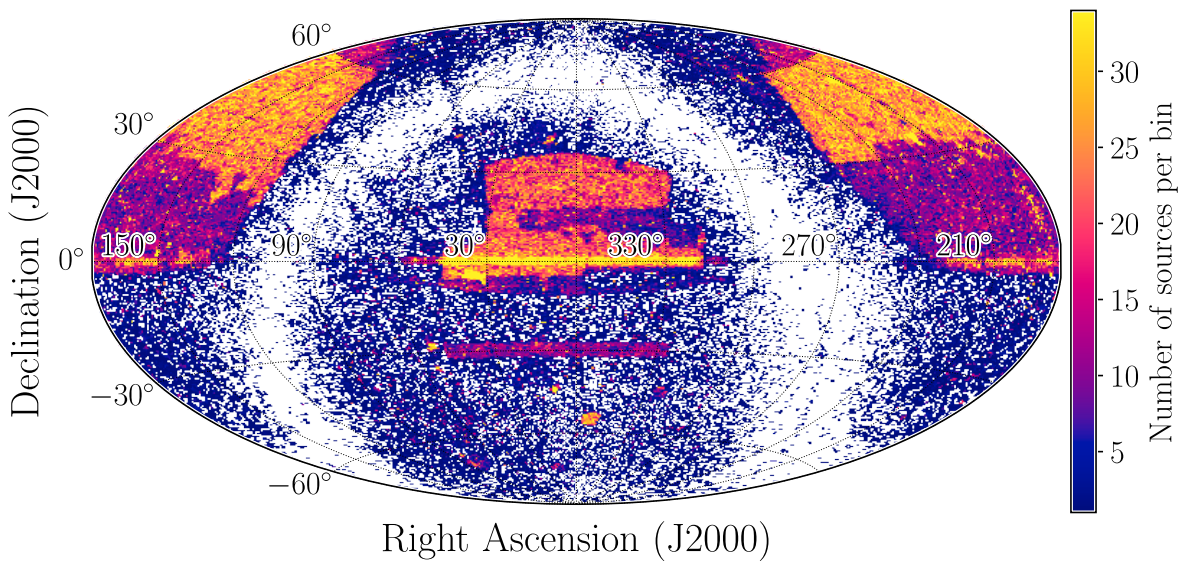


Figure 1.7: Million Quasar Catalog v7.4d source density in a Hammer-Aitoff projection (Snyder, 1987; Snyder, 1997) of the sky. Each coloured rectangle shows the number of [AGN](#) in that particular region of the sky as catalogued by the [MQC](#) following the code in the colorbar. Each overdensity, with respect to its surroundings, represents a different source catalogue or listing from which [AGN](#) have been drawn. More noticeable are, for instance, the areas covered by the [SDSS](#) observations.

Survey ([COSMOS](#); Scoville et al., 2007) field, which has been extensively observed in several wavelengths.

1.1.2 Redshift determination

In order to determine a precise distribution of [AGN](#) across cosmic time, unambiguous redshift measurements are needed (e.g. Huterer et al., 2006; Tanaka et al., 2018; van den Busch et al., 2020; Naidoo et al., 2023). Spectroscopic redshifts, being the most precise measurements, can be determined for a large range of objects, from supernovae (e.g. Frederiksen et al., 2014; Baltay et al., 2021), to galaxies (e.g. Le Fèvre et al., 2015; Galametz et al., 2013), and [AGN](#) (e.g. Rajagopal et al., 2021). Spectroscopic redshifts can be obtained by cross-correlation or fitting of the observed data and set of templates (Tonry and Davis, 1979; Schuecker, 1993; Glazebrook et al., 1998; Aihara et al., 2011; Machado et al., 2013) or by the direct detection and matching of powerful spectral features (Kurtz and Mink, 1998; Stoughton et al., 2002; Garilli et al., 2010). However, their determination can take long and high-quality observations, which are not always available for all sources, rendering them not suited for large-sky catalogues (see, for instance, Silva et al., 2011; Pacifici et al., 2023).

Photometric redshifts are an option which comes from the use of photometry measurements and not explicit spectral features of an object (Salvato et al., 2019; Brescia et al., 2021; Newman and Gruen, 2022). In general, they use observations that take less integration time

than a comparable spectroscopic measurement and, thus, are used for large surveys that need measurements for large numbers of objects (e.g. Hoyle et al., 2018; Tanaka et al., 2018). They are also an option for faint sources.

Photometric redshift methods can deliver a probability for their redshift estimations in the form of a [probability density function \(PDF or \$p\(z\)\$ \)](#). These functions can deliver a measure of the uncertainties that photometric redshifts might have. In general terms, photometric redshifts can be obtained using two different methods: template-based techniques and empirical relations.

Template-based methods come from the fitting of multi-wavelength photometry of a source to a model template (Baum, 1957; Baum, 1962; Loh and Spillar, 1986; Bolzonella et al., 2000; Newman and Gruen, 2022; Pacifici et al., 2023). The models have been constructed using different combinations of properties –e.g. age, metallicity, contribution from different constituents, etc.–. Thus, the examined source will be assumed to have the properties from the model which fits the best. However, and depending upon the number and quality of the photometry measurements (e.g. low spectral resolution), these properties can have, sometimes, large uncertainties. Even though this method can use less precise values to determine a redshift, it can take a significative amount of time since it needs to contrast the measured [SED](#) to the full set of model templates and, when the number of available measurements is low, the quality of the estimation is largely degraded (e.g. Norris et al., 2019).

Using this method, redshift estimations can be obtained from, for instance, galaxies (e.g. Hernán-Caballero et al., 2021), and [AGN](#) (e.g. Ananna et al., 2017; Brescia et al., 2019). As expected, the quality of photometric redshift estimates is highly correlated with the quality of the photometry data used for their determination (Newman et al., 2015; Newman and Gruen, 2022). Some example tools that use template-based methods to retrieve photometric redshifts are [Easy and Accurate \$z_{\text{phot}}\$ from Yale \(EAZY; Brammer et al., 2008\)](#), [Bayesian Photometric Redshifts \(BPZ; Benítez, 2000\)](#), and [Photometric Analysis for Redshift Estimate \(Le PHARE; Arnouts et al., 1999; Ilbert et al., 2006\)](#).

For the case of empirical relations, the retrieval of photometric redshifts relies on the use of statistics and large sets of observables (e.g. fluxes and their uncertainties) to determine redshifts and correlations between them which can be used with future observations. Most of these empirical redshift determination methods are related to the use of [machine learning \(ML; Samuel, 1959\)](#). These techniques will be further described in this work.

Finally, redshift values can also be determined approximately. Using differences among magnitudes –i.e. colours– it is possible to establish the redshift range in which a source is located.

CHAPTER 1. INTRODUCTION

This technique –called drop-out (Steidel et al., 1996a; Steidel et al., 1996b)– is, by no means, precise, but can lead to further investigation of sources that are at relevant redshifts ranges for the researcher (with, for instance, the previously described photometric redshift methods). In this way, drop-outs are employed as a mean to generate candidates for pertinent redshift values. Given that it requires no more calculations than the comparison of some series of colours, it is highly efficient at generating rough redshifts of large samples. It has been, mainly, used to generate and study high-redshift sources or candidates that, otherwise, would not have enough information to produce a precise redshift value (e.g. Bouwens et al., 2020; Carvajal et al., 2020; Merlin et al., 2021; Uzgil et al., 2021; Champagne et al., 2023; Atek et al., 2023).

Since its first uses, this technique has allowed the detection of high-redshift galaxies (Steidel and Hamilton, 1992; Steidel et al., 1996a) through the detection of sharp break in flux between broadband filters that sample the vicinities of the Lyman Break (at a rest-frame wavelength of 912 Å). The location of such break is a function of redshift allowing, thus, to obtain a crude estimate of the redshift for the studied objects.

All the techniques and methods listed and described in this section highlight the ever-increasing number of different procedures for the detection, selection, and characterisation of extra-galactic sources. From their intrinsically different nature, all of them have their own advantages and pitfalls which need to be accounted for when compiling properties from a large sample of sources.

1.2 Challenges in the analysis of astronomical data

The progress of technology and methods used in astrophysics has been one of the main drivers for the advancement in our knowledge and understanding of the processes taking place in the Universe. But this undeniable improvement has brought some drawbacks that pose serious challenges that might hinder our ability of retrieving useful results from astronomical data. Most of these problems are rooted in the very large number of new and different observational efforts carried out throughout the years. This abundance of measurements can impact the processes that lead to new calculations and results since more resources and steps are needed to treat a large number of measurements consistently.

As more sources are needed to better constrain the properties of astronomical sources, new data sets have been compiled and published. Nowadays, multi-wavelength data are available for large fractions of the sky (e.g Gaia Collaboration et al., 2016; Chambers et al., 2016; Lacy et al.,

2020; Kollmeier et al., 2017; Wright et al., 2010; Skrutskie et al., 2006; Abbott et al., 2018). But this profusion of observations has come with new challenges with the most relevant being the volume of data. Lately, analysing all observations, one by one with traditional methods, has become unfeasible in terms of the time needed to fulfil the task (see, for instance, Brescia et al., 2021). This issue will become greater as future surveys and telescopes are put into service, with relevant examples being the [SKA](#) and the [Legacy Survey of Space and Time \(LSST\)](#) ([LSST Science Collaboration et al., 2009](#); [Ivezic et al., 2019](#)).

Furthermore, over the last couple of decades, the observational capabilities of single instruments have been improved largely. It has become possible to retrieve measurements of very large areas of the sky without important variations in the observational properties (noise, calibration, etc.). The improvement in the overall properties of observations has made possible the production of surveys than can cover relevant fractions of the sky. Some examples include the [FIRST](#) survey, the [Two Micron All Sky Survey \(2MASS\)](#) ([Cutri et al., 2003a](#); [Cutri et al., 2003b](#); [Skrutskie et al., 2006](#); [Wright et al., 2010](#); hereafter [2M](#)), [VLASS](#), the [Panoramic Survey Telescope and Rapid Response System \(Pan-STARRS\)](#) ([Chambers et al., 2016](#)), the [Galaxy Evolution Explorer \(GALEX\)](#) ([Morrissey et al., 2007](#)), and [AllWISE](#) ([Cutri et al., 2013](#); hereafter [AW](#)). In the near future, they will be complemented by the [LSST](#) in the [Vera C. Rubin Observatory](#), [SKA](#), [ngVLA](#), and [Euclid](#) (e.g. [Euclid Collaboration et al., 2022](#)), among others.

While being able to obtain information from more sources and regions of the sky is, by itself, a very relevant improvement, such number of new measurements to analyse have brought some issues related to the treatment of very large datasets (for a review focused on the challenges of future radio surveys, see [Norris, 2017](#)). Some of these obstacles are described in the following sub-sections.

1.2.1 Computational costs

Using very large surveys and catalogues for any sort of calculation involves, accordingly, very high computational costs. Recent observational catalogues might have up to billions of entries with several attributes each and large-area images can cover thousands of square degrees with very high angular resolution, reaching total sizes of tens of TB of data and tens of PB for future surveys ([Mickaelian, 2020](#); [Zhang and Zhao, 2015](#)). Additionally, survey instruments will have data transfer rates well above the normal capabilities of a medium-sized server, reaching up to several TB/day rates ([Enke et al., 2012](#)). Dealing with such large datasets requires large

CHAPTER 1. INTRODUCTION

amount of resources that are not completely available to everyone (Garofalo et al., 2017).

Additionally, most of the methods traditionally used for the detection, classification, and extraction of properties for astrophysical sources have not been developed, or updated, to be used with very large catalogues. For this reason, using them in the most recent catalogues and surveys can take restrictive running times that not even the most powerful computing facilities can deal with given their memory or [central processing unit \(CPU\)](#) usage (Mathews et al., 2023). Even if current methods are optimised for their use in large computational facilities, running times would still be prohibitively long. For instance, state-of-the-art [SED](#) methods can take between 50 to 100 [CPU](#) hours for the analysis of a single galaxy (Leja et al., 2019; Tacchella et al., 2022).

A further factor to consider is that of the energy expense of running such methods for long times in powerful machines. Excessive power consumption can impact negatively, first, in the economical costs of running calculations and, second, in the emission of greenhouse effect gases derived from the energy needed for computation. As a way to put these costs into number, it is possible to take the example of the [LSST](#), which is expected to produce photometry for $\sim 10^{10}$ galaxies (Ivezić et al., 2019). Using traditional methods, analysing such number of sources would produce an estimate of 10^8 kg of CO₂, comparable to 200 days of continuous operation of a wide-body aircraft (Mathews et al., 2023). Effective reduction of CO₂ emissions from energy consumption can help alleviating the impact from the climate change (IPCC, 2022). While complete net-zero systems are expected to solve this issue, short-term reduction in the use of energy spending are needed to help limit global warming.

With a focus on ease of use and code readability, Python has become a standard language in most of recent astrophysical packages (Astropy Collaboration et al., 2022). Conversely, code written in Python tends to be one of the least efficient in its ecological impact (Portegies Zwart, 2020). Thus, and taking into account that the popularity of Python is not expected to decrease for the moment, it is needed to use techniques and code that can obtain results in shorter times than those available to date.

1.2.2 Missing measurements

As with any sort of physical measurement, a fraction of observations might have issues that can render them unusable for any meaningful calculation (Rubin, 1976; Josse and Reiter, 2018). These problems include malfunction of detectors or incorrect cleaning of the data,

among others. If different measurements (i.e. in different points in time) are to be combined, some sources might have been observed in one instance but not in the remaining ones. This might affect the study of time series or multi-wavelength, multi-instrument observations as this effect might increase the level of uncertainties. Furthermore, some analysis methods require all measurements to be available and, thus, the lack of one of them can render the full set of quantities from a source useless (Little and Rubin, 2014) or with very relevant uncertainties and biases.

1.2.3 Data heterogeneity

Another source of criticism for the use of [ML](#) methods is that the use of multi-wavelength observations of large areas of the sky can give rise to heterogeneity issues. Over time, many surveys and instruments gather data from many different areas in the sky and with very different sensitivities and observational properties. This makes applying [ML](#) techniques, and most of astronomical studies in general, a difficult task. [ML](#) modelling assumes, in general, that the data for all elements in the data set come from the same sources and have the same properties (Witten et al., 2011; Brescia et al., 2021; Surana et al., 2020) and thus steps have to be taken in order to obtain such properties when measurements of different quality are used.

One way to overcome this obstacle is generating observations of very large areas in the sky which can be analysed and compared with different data sets, thus covering a larger fraction of the available parameter space. As mentioned previously, in the following years, new facilities will be built and put into service delivering observations with similar qualities for large areas of the sky. This will allow the study of much more objects and sources in a statistical way without facing the downsides of inhomogeneous data.

1.2.4 Multi-wavelength counterpart identification

In the case of observations with different filters or different instruments, a new problem might arise. It involves the correct identification of the sources observed in each of the filters. Given that the emission in different wavelengths and different moments in time might come from separate components and processes in the studied objects, each observed instance can present a structure that does not match the others. For this reason, finding and matching counterparts for detected sources can be difficult. This problem is enhanced when observations in several bands and different instruments need to be combined as different [point-spread function \(PSF\)](#) have to

CHAPTER 1. INTRODUCTION

be involved in calculations.

While optical and [IR](#) observations have reached sub-arcsecond positional accuracy (e.g. Wright et al., 2010; Chambers et al., 2016), deep radio surveys have only recently obtained such resolutions (e.g. Sweijen et al., 2022; Ye et al., 2023). Thus, most of radio identifications lack accurate positional measurements needed for precise counterpart identification and to reduce uncertainties in the use of [SED](#) modelling.

There are a few approaches to find and link multi-wavelength, multi-instrument counterparts of sources. One of the simplest way to find such sources is through direct cross match between catalogues. A search radius is defined and centred in the position of the source for which counterparts are needed. Then, all sources in the target catalogue located inside the circle of the previously defined radius are considered candidate counterparts. Depending on the conditions of the problem and the used catalogues, one of these candidates can be selected as the proper counterpart (e.g. the closest source either in angular or geometrical distance). Examples of the use of direct cross match of catalogues are Barbieri and Bertola (1972), Agüeros et al. (2005), Bianchi et al. (2007), Drake et al. (2014), Norris et al. (2021), and Storey-Fisher et al. (2023).

When postional errors are large or [PSF](#) or synthesised beams are large enough to have several sources from the other catalogue inside it, direct cross matching cannot be used. A more advanced approach is that of [maximum likelihood ratio](#) ([MLR](#); Richter, 1975; de Ruiter et al., 1977; Prestage and Peacock, 1983; Wolstencroft et al., 1986; Sutherland and Saunders, 1992). As defined by Sutherland and Saunders (1992), it looks for the sources that optimise the ratio of the likelihoods of being a genuine counterpart over that of being a background candidate. These likelihoods depend on the density of sources in both catalogues, their magnitude distributions, and their positional errors (Brusa et al., 2007). One advantage of this technique is that it can output the degree of reliability of each counterpart allowing the researcher to select, if needed, the most secure sources. Some examples of the application of the [MLR](#) method include Brusa et al. ([XMM-COSMOS](#); 2007), Abdo et al. ([Fermi](#); 2010), Xue et al. ([Chandra Deep Field-South](#); 2011), LaMassa et al. ([Stripe 82X](#); 2016), Marchesi et al. ([Chandra COSMOS](#); 2016), Ananna et al. ([Stripe 82X](#); 2017), Auge et al. (2023), Hardcastle et al. ([LoTSS](#); 2023), and Whittam et al. ([MIGHTEE-COSMOS](#); 2024).

A third method is the Bayesian approach. Contrary to the previous techniques, it does not rely on the specific distribution of sources in the studied catalogues, using Bayesian priors to derive the most likely counterparts of the base catalogue. In this way, it does not suffer from being applied to small areas (Salvato et al., 2018; NWAY). This method was first introduced by

Budavári and Szalay (2008) and it can be applied to the search for counterparts in simultaneous catalogues.

Additionally, **ML**-based methods can be used to derive the most likely counterpart of sources in catalogues. By using photometric information (or other properties) from sources detected in other wavelengths, it is possible to train a model and extract the probability of that source to have a counterpart in a new catalogue. One early example of such technique is the work by Rohde et al. (2005) and Rohde et al. (2006) where the authors used support vector machine (SVM; Vapnik, 1995; Cortes and Vapnik, 1995)s, together with model calibration (see Sect. 3.3) in order to obtain a counterpart probability. More recently, Liu et al. (2019) used Gaussian process (GP; Rasmussen and Williams, 2005) modelling to quantify the confidence of associations of Atacama large millimeter/submillimeter array (ALMA) detections in the COSMOS fields. Furthermore, Schneider et al. (2022) used SVMs to extract stellar counterparts of sources in the eROSITA Final Equatorial Depth Survey (eFEDS; Brunner et al., 2022).

1.3 Machine-assisted pattern detection

Taking into account all the issues that the analysis of large datasets might pose, new tools have been developed as a way to tackle them. For astrophysics, in particular, the existence of these major AGN detection, radio measurement, and redshift determination methods raises the need of new techniques which might be able to obtain these properties for large amounts of astrophysical sources with enough precision within a shorter amount of time.

Given that this is a problem suffered by several scientific and, even, non-scientific disciplines (e.g. business-related applications; Costa-Climent et al., 2023), large efforts have been put in order to solve it and many techniques have been developed to deal with the ever-increasing data volumes. New statistical and computer methods can analyse thousands or millions of elements and find relevant trends among their properties (Garofalo et al., 2017) within reasonable time frames. One branch of these techniques is able to, using previously-fed data, predict, with relevant confidence, the behaviour new data will have –i.e. the values of their properties–. This is what has been called **ML**.

In Astronomy, **ML** has been used in a wide range of subjects, such as redshift determination (e.g. Nakoneczny et al., 2021; Wenzl et al., 2021), morphological classification (e.g. Ma et al., 2019; Lukic et al., 2019; Mostert et al., 2021; Vardoulaki et al., 2021; Burhanudin et al., 2021), emission prediction (e.g. Dobbels and Baes, 2021), anomaly detection (e.g. Baron and

CHAPTER 1. INTRODUCTION

Poznanski, 2017; Giles and Walkowicz, 2019; Lochner and Bassett, 2021; Storey-Fisher et al., 2021; Wagstaff et al., 2022), image reconstruction (e.g. Guglielmetti et al., 2022; Adam et al., 2023; Wilber et al., 2023), observations planning (e.g. Garcia-Piquer et al., 2017; Jia et al., 2023; Sravan et al., 2023), and more (Ball and Brunner, 2010; Baron, 2019; Sen et al., 2022; Huertas-Company and Lanusse, 2023).

With **ML**, it is possible to use previously available measurements and extract useful trends and correlations that can suggest the behaviour of properties from future observations or simulations. **ML** models are, in general, only fed with measurements and not with physical assumptions (Desai and Strachan, 2021) and they do not need to check the consistency of the predictions or results they provide. This can bring, as a consequence, that running times for this kind of algorithms might be less than typical physically-based codes (e.g. Buchner, 2019; Mathews et al., 2023). One way to incorporate physical knowledge or assumptions into **ML** methods is through what has been called physics-informed **ML** (Miller et al., 2020; Karniadakis et al., 2021). Under this paradigm, algorithms can be modified to incorporate physical rules as priors or general conditions that analysed observables must follow. For example, loss or target functions can be adjusted to reproduce border conditions or other physical principles.

1.3.1 Types of machine-assisted analyses

Concentrating our review on the application of **ML**, two main branches exist for the application of such techniques. The first of them, called supervised learning, deals with the idea that, for each set of measurements, there is a response value that, via modelling, we can predict with some degree of confidence (James et al., 2023). This definition implies that it is possible to determine, for a studied sample, values that could, otherwise, be measured. On the other side, unsupervised learning refers to the analysis of data that does not have an associated quantity. One of the most popular applications of unsupervised learning is clustering of elements (e.g. Garcia-Dias et al., 2018; Reis et al., 2021; Mohale and Lochner, 2023). Modelling data would imply separating them by how similar are their properties (or a combination of them).

Then, in the case of supervised learning, further divisions are possible. If the predicted variable (target) is a discrete quantity, this prediction is called a classification (e.g Saz Parkinson et al., 2016; Baron and Poznanski, 2017; Ma et al., 2019; Lukic et al., 2019; Giles and Walkowicz, 2019). Opposite to that, if the predicted target is continuous, the process is called regression (e.g. Vanzella et al., 2004; Nakoneczny et al., 2021).

1.3.2 Ensemble learning

By design, each [ML](#) algorithm has been developed and tuned to work better with certain data conditions, that is, balance of target categories, ranges of base features, sparsity of values, etc. One technique used to combine the properties of algorithms and improve the results of a prediction is that of ensemble learning. It involves the joint use of individual results from [ML](#) models, that have been trained to solve the same problem, into one larger model or rule that can deliver a final prediction (Schapire, 1990; Breiman, 1996; Freund and Schapire, 1996). It has been shown that the combination of several models, and their predictions, can improve the overall prediction results (Opitz and Maclin, 1999).

In order to combine several prediction into a final result, several options are available. The most used, and one of the earliest, ways to merge all individual predictions consists of averaging each predicted value into the final prediction (e.g. Sollich and Krogh, 1995). Such average can be obtained for either different models or several instances of the same model, as in the case of [random forests \(RFs; Breiman, 2001\)](#). This option is useful for both regression and classification tasks (using its output scores). For the specific case of classification, a voting system can be implemented, where the majority of decisions of the base individual predictors is taken as the final predicted class. This method has been proven to work efficiently (Schapire et al., 1998) with a reduction in the test errors.

The predicting power of different algorithms can be combined with the use of meta-learners (Vanschoren, 2019). Meta-learners use the properties or predictions from other algorithms (base learners) as additional information during their training stages. A simple implementation of this procedure (and a third method to combine individual predictions) is called Generalised Stacking (Wolpert, 1992) which can be interpreted as the addition of priors to the model training stage. In this way, two levels of predictors are used. The first level includes all the individual models that are trained on the training set. The second level corresponds to a single model which is trained only on the outputs of the first-level models. Generalised stacking has been applied in several astrophysical problems. That is the case of Zitlau et al. (2016), Carvajal et al. (2021), Cunha and Humphrey (2022), Moya and López-Sastre (2022), Zammit and Adami (2023), Euclid Collaboration et al. (2023a), and Euclid Collaboration et al. (2023b).

CHAPTER 1. INTRODUCTION

1.3.3 Model explainability and feature importance

Despite the large number of applications it might have, **ML** has received important criticism related to the lack of interpretability –or explainability, as it is also called in **ML** jargon– of the their derived models, trends, and correlations (e.g. Linardatos et al., 2021; Gao and Guan, 2023). Some of the most complex **ML** models, after taking a series of measurements and properties as input, deliver a prediction of a different property (or a set of them). But they cannot provide coefficients or an analytical expression, that might allow to find an equation for future predictions (Goebel et al., 2018). An important counter-example of this fact is the use of Symbolic Regression (Gerwin, 1974; Langley, 1977; Langley, 1979; Langley et al., 1981; Langley and Zytkow, 1990), which has been developed to extract explicit analytic expressions from the analysed data. Some examples of the use of symbolic regression in astrophysics are Cranmer et al. (2020), Villaescusa-Navarro et al. (2021), and Cranmer (2023). The lack of explainability implies that, for most **ML** models, it is not a simple task to determine which properties, and to what extent, help predict and interpret another attribute (e.g. Roscher et al., 2020a). This fact hinders our capability to understand the results in physical terms and extrapolate **ML** results into further ranges of properties.

Besides the development of symbolic regression, recent work has been done to overcome the low levels of explainability in **ML** models (Främling, 2023). The most widely used assessment is done with feature importance (Casalicchio et al., 2019; Roscher et al., 2020b), both global and local (Saarela and Jauhainen, 2021). Feature importance analysis helps to know the relative weights that the measured properties have in the decision-making process (D’Isanto et al., 2018; Främling, 2023). In this way, physical insight might be gained about the correlations or triggers between different properties (observed or derived) of the objects of study.

Global feature importances

Overall, mean or global feature importances can, usually, be retrieved from models that are based on **decision trees (DTs)** (e.g. random forests and boosting models, Breiman, 2001; Breiman, 2003). For each feature, the decrease in impurity (a term frequently used in the literature related to **ML**) of the dataset is calculated for all the nodes of the tree in which that feature is used. Features with the highest impurity decrease will be more important for the model (Louppe et al., 2013). For some models that are not based on **DT**, feature importances can be obtained from the coefficients that the training process delivers for each feature. These

coefficients are related to the level to which each quantity is scaled to obtain a final prediction (as in the coefficients from a polynomial regression). Insight into the decision-making of the pipeline can only rely on the specific weights of the original set of features (see Sect. 3.4). An additional example method of the retrieval of global feature importances is that of the creation and training of simple, linear surrogate models, which are completely explainable for the studied sample (e.g. Saarela and Jauhainen, 2021).

Local feature importances

As opposed to the global (or mean) assessment of feature importances derived from the decrease in impurity, local (i.e. source by source) information on the performance of such features can be obtained from, for instance, Shapley values. This is a method from coalitional game theory that tells us how to fairly distribute the dividends (the prediction in our case) among the features (Shapley, 1953). The previous statement means that the relative influence of each property from the dataset can be derived for individual predictions in the decision made by the model (which is not the same as obtaining causal correlations between features and the target; Ma and Tourani, 2020). Game theory based analyses, such as the Shapley and SHapley Additive exPlanations (SHAP) values, have also been used to understand the importance of features in astrophysics (e.g. Machado Poletti Valle et al., 2021; Carvajal et al., 2021; Dey et al., 2022; Anbagane et al., 2022; Alegre et al., 2022; Carvajal et al., 2023a; Pearl et al., 2023).

A different approach to local feature importances is that of Local Interpretable Model-agnostic Explanations (LIME; Tulio Ribeiro et al., 2016). LIME can be used to explain individual predictions regardless of the type of model used. It is based on the idea that a fully explainable model can be created to mimic the result of a specific prediction. Then, this prediction can be perturbed by the removal of each of the involved features. The analysis of this perturbation will return the feature importance reported by LIME. In astrophysics, LIME has been used by, for instance, Ulmer-Moll et al. (2019) and Pasquato et al. (2023).

1.4 This thesis

As mentioned earlier in this text, most multi-wavelength measurements from extra-galactic sources convey information from AGN and their host galaxies. Thus, separating both components becomes a complex process given that different wavelengths will carry different fractions

CHAPTER 1. INTRODUCTION

of information from each component of the observed sources.

Then, and as also presented in Sect. 1.1, one relevant exception to this behaviour are radio measurements. Given that radio light can escape the galaxy without major obscuration or absorption, this emission has been, historically, better suited for obtaining direct information from the central regions of bright AGN.

However, until recently, major radio observatories and surveys lacked the capabilities to resolve, meaningfully, the emission from distant (and, sometimes, faint) AGN. Only with the advent of recent facilities, we have the capabilities to better establish the radio nature of high-redshift sources. To add more complications, these new exquisite measurements are as sensitive as to capture emission from faint SF episodes as it happens with other wavelengths.

Consequently, we face a complex issue if we want to extract information from AGN (and in particular, high-redshift AGN). We are able to observe them directly in radio wavelengths but, so far, it is difficult to determine the exact origin of radio emission. On the other hand, the lack of strong interaction from the AGN radio emission with their host galaxies makes it difficult to establish strong correlations or trends between their intensities and other galactic measurements (mostly, in other wavelengths).

Attending, then, to the difficulties in relating radio emission from AGN with measurements of these sources in additional wavelengths, the main goal of this thesis is to explore and understand possible indicators of the radio emission in AGN from multi-wavelength, multi-instrument, measurements. Thus, we want to develop a process that, in particular, can take information from IR-detected sources (for which there is all-sky coverage with good sensitivity levels) and deliver an indication of whether these sources can correspond to AGN and, more specifically, to radio-detectable AGN or not.

Given the importance of the detection of AGN in early epochs of the Universe, we also aim to use the aforementioned machinery to derive estimates of photometric redshifts for the sources labelled as prospective radio-detectable AGN. In that way, the focus of our search can be put in the selection of sources as close as possible to the EoR. Or at least, in redshift ranges suitable for specific studies.

Having outlined the major issues that exist with the use of new astronomical datasets and surveys (cf. Sect. 1.2), the use of machine-assisted techniques (and in particular, ML, which aims at the use of available datasets to find relevant trends among their properties to estimate the behaviour of new, unseen data; Samuel, 1959) becomes more relevant than ever before. The possibility of analysing very large datasets with reduced computational costs (in time and energy

consumption, Sect. 1.2.1), and with minimal homogenisation procedures applied to them, is one of the main drivers behind the development of this work.

In Fig. 1.8, we present a flowchart of the prediction pipeline we propose for the generation of radio-detectable AGN candidates. We aim to start with a set of IR-detected sources with ancillary multi-band data that can be fed into the a first step that classifies between AGN and SFGs (i.e. not hosting an AGN). Given that we are interested in AGN, we use the predicted AGN and feed them into the second step, which classifies AGN according to their radio detectability. After this step, we select the predicted AGN that have a high likelihood of being radio-detectable. A final step uses the predicted radio-detectable AGN and estimates a redshift value for them. Consequently, the prediction pipeline delivers a set of candidate radio-detectable AGN with an redshift estimate.

Taking into consideration the structure of the pipeline, the ML models in each step will be trained with a different sample of sources. The first step, classification between AGN and SFGs will be trained with all available sources that have been labelled previously as either AGN or SFGs. The second step, classification of radio detection in AGN, will be modelled only with confirmed AGN (with or without radio detections). Finally, the third step of the pipeline, which estimates photometric redshifts, will be trained with radio-detected AGN. Our focus on radio-detectable AGN is the basis for the omission of the remaining sources in the data sets.

Following the production of candidates for radio-detectable AGN, together with their redshift values, we aim to understand the predictions and how they relate to physical properties of the analysed sources. For this goal, we want to apply feature importance analyses to the prediction processes. These techniques can help understanding the inner correlations and trends that allow the creation of several selection rules and prediction schemes for the creation of predicted sources and some of their properties.

Once the mechanisms leading to the prediction of radio-detectable AGN, and their redshift values, have been understood, we want to apply such indicators and the candidates derived from their use to the analysis and possible solution of different problems related to the observation, classification, and distribution of radio-detected AGN. The application of ML techniques can help creating large collections of candidate radio-AGN that might not have been available previously. The use of such sources might, then, contribute to the improvement of the answers for the questions previously mentioned.

Part of this thesis is based on the work and analyses presented by Carvajal et al. (2021) and Carvajal et al. (2023a). In the following chapters, we present the data sets (as well as the

CHAPTER 1. INTRODUCTION

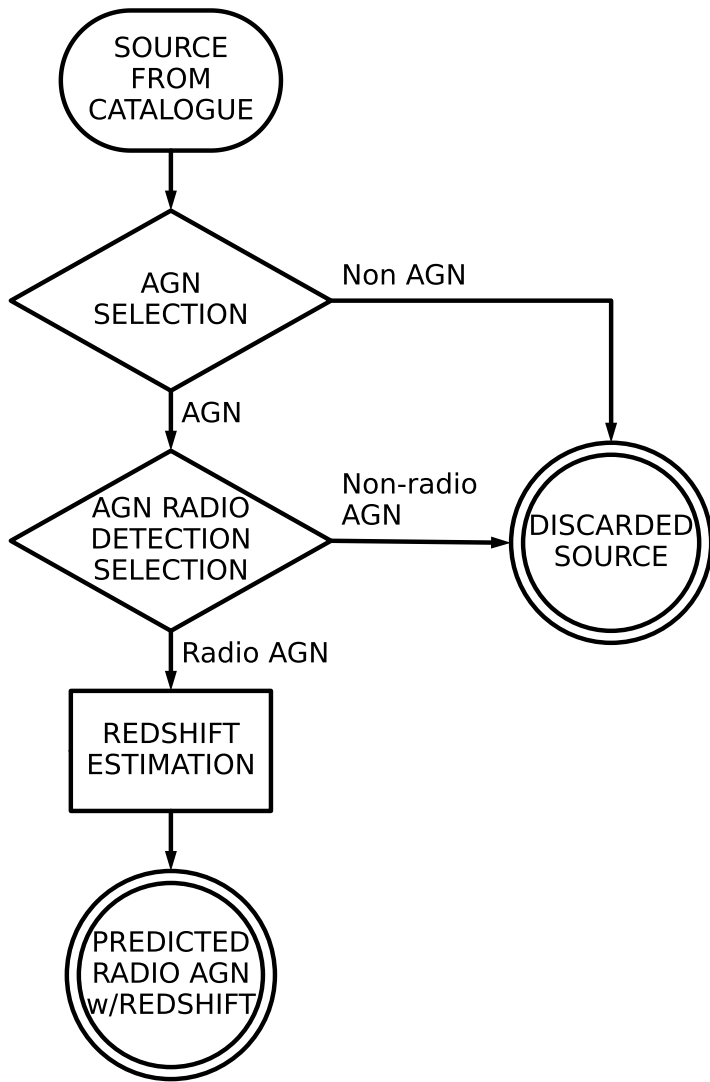


Figure 1.8: Flowchart representing the proposed prediction pipeline used to predict the presence of radio-detected **AGN** and their redshift values from **IR**-detected sources.

treatment applied to them) used for the generation of the models (Chapter 2), the result of the selection of models and their training (Chapter 3), and the analyses of the use of the prediction pipeline on the selected data sets (Chapter 4). Furthermore, Chapter 5 describes the analysis of the predictions and the models themselves using different approaches. Finally, Chapters 6 and 7 introduce extensions of the use of the results from the prediction pipeline in different contexts as well as future developments to be applied to the prediction pipeline and its individual steps. This thesis concludes with a summary, where final remarks and findings are outlined.

Datasets for training and testing

In order to train all models efficiently and test them without fears of obtaining biased metrics, good quality data are needed. This requirement can be translated into selecting a field with coverage in several bands and by diverse instruments. Such variety can help the training of the models to cover a broad fraction of the parameter space.

Furthermore, these measurements need to be spread over a sufficiently large area as a way to avoid any biases from using sources that might be connected in some manner (e.g. cosmic variance; Driver and Robotham, 2010). Additionally, in order to validate the predictions from the models, the selected field needs to have an adequate number of sources with validated classifications.

As an extension of the previous requirement, it is desirable that the surveys that cover the selected area also have a much larger footprint. In this way, it will be possible to apply the trained models to different areas of the sky as an further test to our techniques. Thus, all-sky measurements will be prefered over compact (but maybe deeper) surveys.

Finally, and given that one of the goals is predicting radio detectability of sources, the chosen area must have sufficiently deep and homogeneous radio coverage. If a shallow radio survey is used, the trained model will have access to only a small fraction of possible detections of RGs, which might bias the predictions and their assessment.

2.1 HETDEX Spring field

As training field we selected the area of the Hobby-Eberly Telescope Dark Energy Experiment (HETDEX; Hill et al., 2008) Spring field that is covered by the first data release of the LoTSS. The LoTSS - data release 1 (LoTSS-DR1; Shimwell et al., 2019) survey covers 424 deg^2 in the HETDEX Spring field (hereafter, HETDEX field, see Fig. 2.1) with Low Frequency Array (LOFAR; van Haarlem et al., 2013) 150 MHz observations that have a median sensitivity of $71 \mu\text{Jy}/\text{beam}$. The deep radio observations in this field can help the training stages to retrieve

CHAPTER 2. DATASETS FOR TRAINING AND TESTING

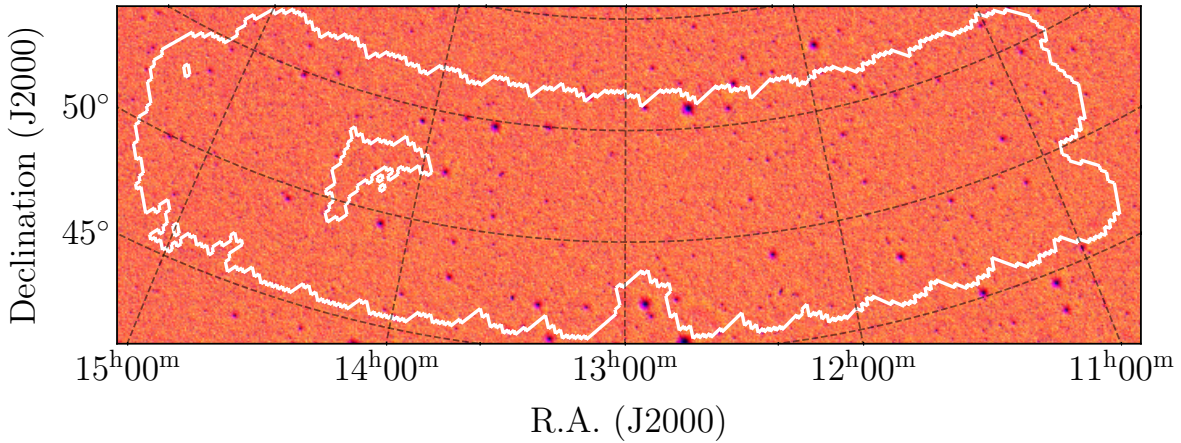


Figure 2.1: Footprint of the area used in the [HETDEX](#) field for this work. In the background, W1 image from the [unWISE](#) coadds (Lang, 2014; Meisner et al., 2022). The white contours limit the area of the [HETDEX LoTSS-DR1](#) field, covering 424 deg².

information from a large fraction of sources in the area. The [HETDEX](#) field has, as well, multi-wavelength homogeneous coverage as described in Sect. 2.3.

2.2 Stripe 82 field

In order to test the performance of the models when applied to different areas of the sky, and with different coverages from radio surveys, we have selected the [SDSS Stripe 82](#) ([S82](#); Annis et al., 2014; Jiang et al., 2014) field. For the [S82](#) field, we collected data from the same surveys as with the [HETDEX](#) field (see the following section) but with one important caveat: no [LoTSS-DR1](#) data is available in the field and, thus, we gathered the radio information from the [VLA SDSS Stripe 82 Survey](#) ([VLAS82](#); Hodge et al., 2011). [VLAS82](#) covers an area of 92 deg² with a median rms noise of 52 μJy/beam at 1.4 GHz. We have selected the [S82](#) field (and, in particular, the area covered by [VLAS82](#), see Fig. 2.2) from the fact that it presents deep radio observations but taken with a different instrument than [LOFAR](#). This difference allows us to test the suitability of our models and procedures in conditions that are not exactly the same as those from the training.

One expected caveat is that, given the shallower nature of the radio observations in [S82](#), the model might predict the radio detection of a source but it might be fainter than the limit from [S82](#). Assuming a synchrotron radio slope of $\alpha = -0.7$ (e.g. Sabater et al., 2019), the 5σ detection limit of [LoTSS](#) (355 μJy/beam) at the frequency of [VLAS82](#) would be ≈ 72 μJy/beam, which is below the 5σ detection limit of [VLAS82](#), 260 μJy/beam. This difference will be taken into account when comparing metrics between fields.

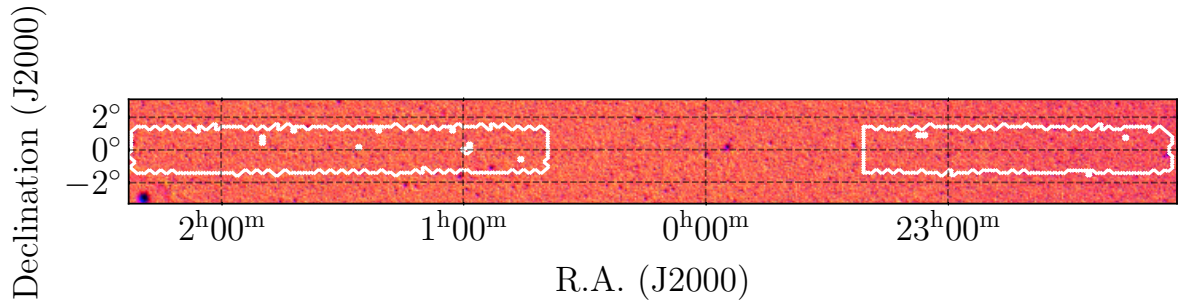


Figure 2.2: Footprint of the area used in the [VLAS82](#) field for this work. In the background, W1 image from the unWISE coadds (Lang, 2014; Meisner et al., 2022). The white contours limit the area of the [VLAS82](#) field, which covers an area of 92 deg^2 split in two sections.

2.3 Photometry measurements

The base survey from which all the studied sources have been drawn is the [CatWISE2020](#) (Marocco et al., 2021; hereafter [CW](#)). It lists NIR-detected elements selected from [WISE](#) and Near-Earth Object [WISE](#) (NEOWISE; Mainzer et al., 2011; Mainzer et al., 2014) over the entire sky at $3.4 \mu\text{m}$, $4 \mu\text{m}$ and $6 \mu\text{m}$ (W1 and W2 bands, respectively). This catalogue includes sources detected at 5σ in either of the used bands (i.e. $\text{W1} \sim 17.43$ and $\text{W2} \sim 16.47 \text{ mag}_{\text{Vega}}$ respectively). The [HETDEX](#) field contains 15 136 878 sources listed in [CW](#). Conversely, in the [S82](#) field, there are 3 590 306 of them.

Multi-wavelength counterparts for [CW](#) sources were found on other catalogues applying a $1.\prime 1$ search radius criteria. These catalogues include Pan-STARRS Data Release 1 (Chambers et al., 2016; Flewelling et al., 2020; hereafter [PS1](#)), [2M](#), and [AW](#)¹. The adopted search radius corresponds to the distance that has been used by Wright et al. (2010) to match radio sources to [PS1](#) and [WISE](#) observations and is the smallest PSF size of the bands included in [PS1](#) (Chambers et al., 2016). Furthermore, the source density of the radio ([LOFAR](#), [Very Large Array \(VLA\)](#)) and [2M](#) catalogues imply a low statistical ($< 1\%$) spurious counterpart association, this is not the case for [PS1](#), where the source density is higher. For these reasons, and to maintain a statistically low spurious association between [CW](#) and [PS1](#), we limited our search radius to $1.\prime 1$. A list of used bands and their origin instruments and surveys is shown in Table 2.1.

For the purposes of this work, observations in [LoTSS-DR1](#) and [VLAS82](#) are only used to determine whether a source is radio detected, or not. In particular, no check has been performed on whether a selected source is extended or not in any of the radio surveys. A single Boolean feature is created from the radio measurements (see Sect. 2.5) and no further analyses were

¹For the purposes of the analyses, and except when clearly stated otherwise, all photometric measurements were converted to AB magnitudes.

CHAPTER 2. DATASETS FOR TRAINING AND TESTING

Table 2.1: Bands available for model training in our dataset

Survey	Band (Column name)
Pan-STARRS (PS1)	g (<code>gmag</code>), r (<code>rmag</code>), i (<code>imag</code>), z (<code>zmag</code>), y (<code>ymag</code>)
2MASS (2M)	J (<code>Jmag</code>), H (<code>Hmag</code>), Ks (<code>Kmag</code>)
CatWISE2020 (CW)	W1 (<code>W1mproPM</code>), W2 (<code>W2mproPM</code>)
AllWISE (AW)	W3 (<code>W3mag</code>), W4 (<code>W4mag</code>)

^a In parentheses are shown the names of the columns or features in our dataset that represent each band.

performed regarding the detection levels that might be found in any of the fields.

Additionally, we have discarded the measurement errors of all bands. Traditionally, [ML](#) algorithms cannot incorporate uncertainties in a straightforward way during training (e.g. Jiang et al., 2021; Michelucci and Venturini, 2023) and, thus, we opted to avoid attempting to use them for training. One significant counter-example corresponds to [GPs](#), where measurement uncertainties are needed by the algorithm to generate predictions. Additionally, the astronomical community has attempted to modify existing techniques to include uncertainties in their [ML](#) studies. Some examples include the works by Ball et al. (2008), Reis et al. (2019), and Shy et al. (2022). Furthermore, Euclid Collaboration et al. (2023b) have shown that, in specific cases, the inclusion of measurement errors does not add new information to the training of the models and can be even detrimental to the prediction metrics. The degradation of the model by including uncertainties can likely be related to the fact that, by virtue of the large number of sources included in the training stages, the uncertainties are already encoded in the dataset in the form of scatter. Thus, including explicit uncertainties might dilute the information from the photometric measurements.

The number of valid measurements in Fig. 2.3 for each field and band can be used to determine the relative difference of density of sources between both fields. This density can be obtained by dividing the number of valid measurements over the effective area of each field (Sects. 2.1 and 2.2). Table 2.2 shows these densities.

2.4 Missing data treatment

In general, [ML](#) methods (and their underlying statistical methods, as introduced in Sect. 1.2.2) cannot work with catalogues that have empty entries (Allison, 2001; Josse et al., 2019). Several techniques have been devised to handle datasets that lack some of their

Table 2.2: Density of detected sources (in units of sources per square degree) per band and field.

HETDEX Field							
Band	Density (deg ⁻²)	Band	Density (deg ⁻²)	Band	Density (deg ⁻²)	Band	Density (deg ⁻²)
g	6380.66	z	10 331.93	H	1335.55	W2	35700.18
r	9304.58	y	6735.97	Ks	1335.55	W3	14045.08
i	11 242.35	J	1335.55	W1	35 700.18	W4	14044.78

S82 Field							
Band	Density (deg ⁻²)	Band	Density (deg ⁻²)	Band	Density (deg ⁻²)	Band	Density (deg ⁻²)
g	8249.04	z	13 214.70	H	2330.92	W2	39025.05
r	12 962.35	y	9226.45	Ks	2330.92	W3	15393.12
i	14 507.01	J	2330.92	W1	39 025.01	W4	15472.75

entries. The simplest of them is listwise deletion, which drops all observations that miss, at least, one measurement (Pepinsky, 2018). This process is inefficient as it reduces the size of the parameter space from which the models can obtain information for its training. A second method is imputation. Imputation is the process of replacing non-available measurements with substitute values. In general, there is enough information in the remaining entries to derive a meaningful substitute value (Kalton and Kasprzyk, 1982). In this way, typical quantities used for replacement are the mean of the remaining entries or a function of the other measurements of the same entry.

Depending on the origin of the substitute value, different categories of imputation exist. Using the definitions from Kalton and Kasprzyk (1982) and Chattopadhyay (2017), it is possible to separate it in multiple and single imputation. In turn, single imputation can be divided into mean, random, regression, hot deck, and cold deck imputation. Single imputation replaces each missing entry with a single value. Opposite to it, multiple imputation, and as initially proposed by Rubin (1987), creates a set of possible values (usually, based upon statisticall arguments) which are included as new instances of the measured object.

Focusing on single imputation, mean imputation replaces all missing measurements with the mean value of the available values. Random imputation uses any value from the existent measurements in the data set to replace the missing entry. Regression imputation uses the full set of available data to derive a possible value for the missing entry. Hot and cold deck imputations replace the missing value with other instances of the data set (or additional data sets in cold deck imputation) that have the same values for the remaining measurements.

CHAPTER 2. DATASETS FOR TRAINING AND TESTING

Given its simplicity, we have used an ad-hoc variation of single imputation to replace missing values and magnitudes fainter than 5σ limits with meaningful quantities that represent the lack of a measurement. We have opted for the inclusion of the same 5σ limiting magnitudes as the value to impute with. This method of imputation, with some variations, has been successfully applied and tested, recently, by Arsioli and Dedin (2020), Carvajal et al. (2021), Curran (2022), and Curran et al. (2022).

In this way, observations from 12 non-radio bands were gathered (as listed in Table 2.1). The magnitude density distribution for the sample from the **HETDEX** and **S82** fields, without any imputation, is shown in Fig. 2.3. After imputation, the distribution of magnitudes changes, as shown in Fig. 2.4. Each panel of the figure shows the number of sources which have a measurement above its 5σ limit in such band. Additionally, a representation of the observational 5σ limits of the bands and surveys used in this work is presented in Fig. 2.5. It is worth noting the depth difference between **VLAS82** and **LoTSS** is ~ 1.5 mag for a typical synchrotron emitting source ($F_\nu \propto \nu^\alpha$ with $\alpha = -0.7$), allowing the latter survey reach fainter sources (see Sect. 2.2). Following the same argument of measurement errors, upper limit values have been removed and a missing value is assumed instead.

2.5 Additional features

As mentioned in the previous sections, each magnitude corresponds to one feature that will be used in the training stages. In order to give the models more information to improve their training, we have generated more quantities as described below.

First, **AGN** labels and redshift information were obtained by cross-matching (with a $1''1$ search radius) the catalogue with the version v7.4d of the **MQC** (Flesch, 2021), which lists information from more than 1 500 000 objects that have been classified as optical **QSO**, **AGN**, or Blazars. Sources listed in the **MQC** may have additional counterpart information, including radio or X-ray associations. For the purposes of this work, only sources with secure spectroscopic redshifts were used. The matching yielded 50 538 spectroscopically confirmed **AGN** in **HETDEX** and 17 743 confirmed **AGN** in **S82**. A depiction of the source density in the **MQC** v7.4d has been presented in Fig. 1.7.

Similarly, the sources in our parent catalogue (i.e. **CW**) were cross-matched with the **SDSS** Data Release 16 (SDSS-DR16; Ahumada et al., 2020). This cross-match was done solely to determine which sources have been spectroscopically classified as **SFGs** (`spClass == GALAXY`)

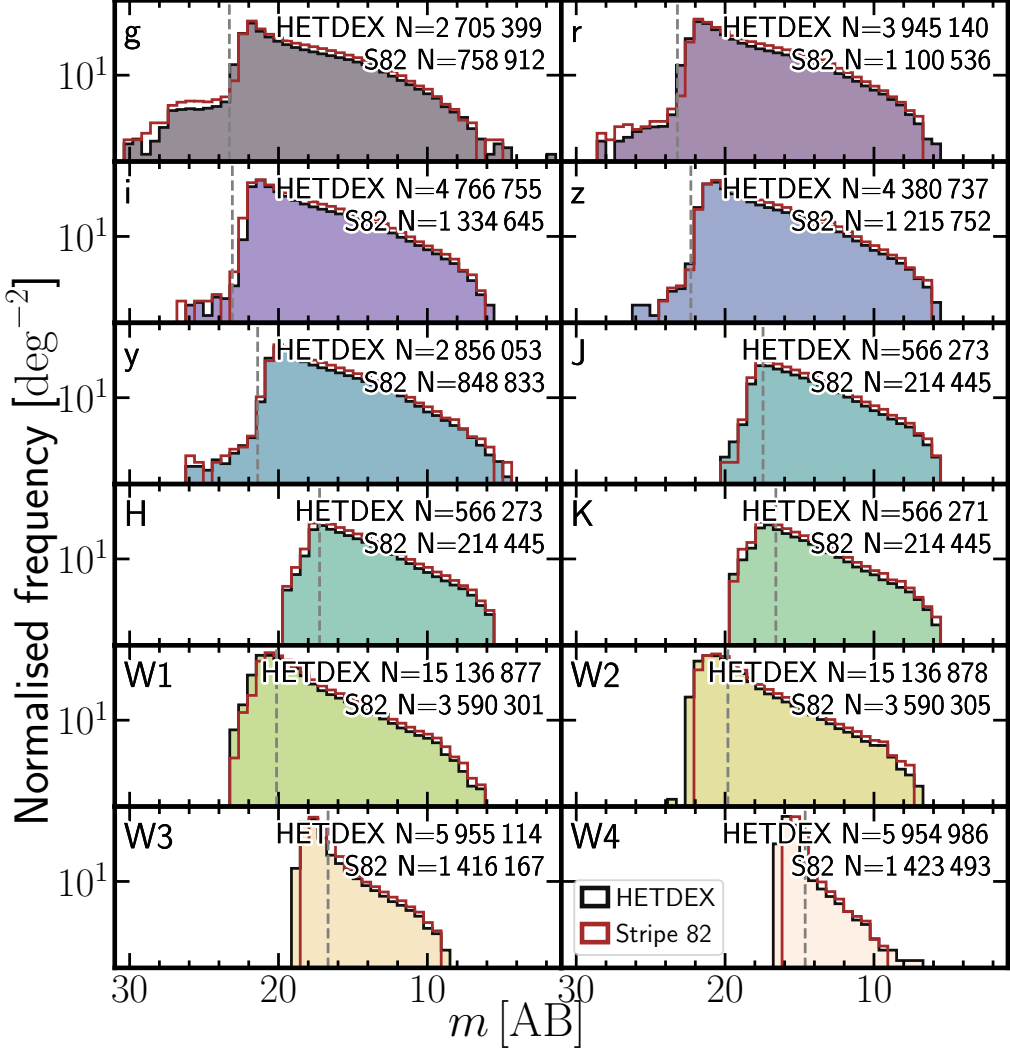


Figure 2.3: Histograms of base collected, non-imputed, non-radio bands for [HETDEX](#) (clean, background histograms) and [S82](#) (empty, brown histograms) fields. Each panel shows the distribution of measured magnitudes of detected sources divided by the total area of the field. Dashed, vertical lines represent the 5σ magnitude limit for each band. The number in the upper right corner of each panel shows the number of measured magnitudes included in their corresponding histogram.

and no magnitude measurements were extracted from it. For most of these [SFGs](#), [SDSS-DR16](#) lists a spectroscopic redshift value (for which no check on the quality of the measurement was made), which will be used in some stages of this work. In the [HETDEX](#) field, [SDSS-DR16](#) provides 68 196 spectroscopically confirmed galaxies. In the [S82](#) field, [SDSS-DR16](#) identifies 4085 galaxies spectroscopically. Given that [MQC](#) has access to more [AGN](#) detection methods than [SDSS](#), when sources were identified as both [SFGs](#) (in [SDSS-DR16](#)) and [AGN](#) (in the [MQC](#)), a final label of [AGN](#) was given. A description of the number of elements in each field and the multi-wavelength counterparts found for them is presented in Table 2.3.

Then, colours from measured and imputed magnitudes were added as features. We created 66 of them, which correspond to all the available combinations of two magnitudes between the 12 selected bands, symbolised by the expression $\binom{12}{2}$. These colours are labelled in the form X_Y

CHAPTER 2. DATASETS FOR TRAINING AND TESTING

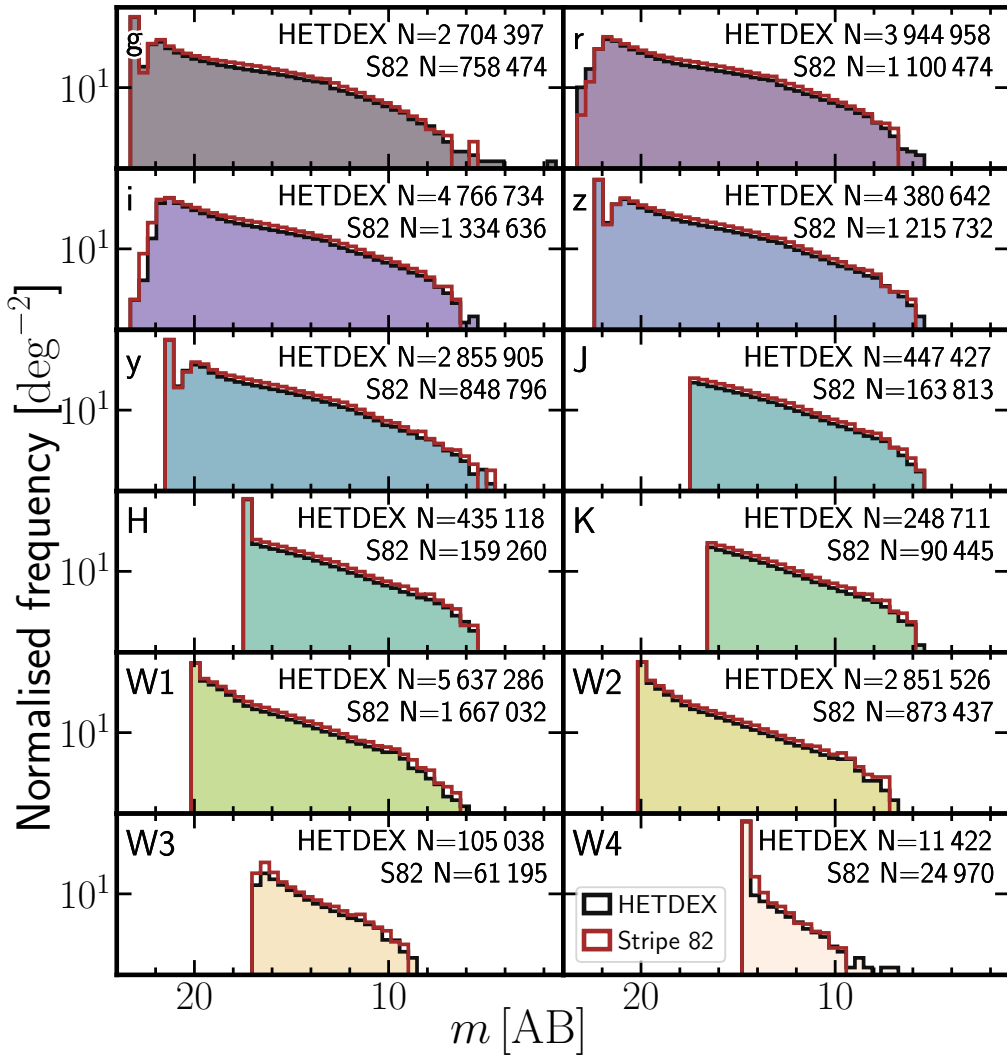


Figure 2.4: Histograms of base collected non-radio bands for **HETDEX** (clean, background histograms) and **S82** (empty, brown histograms) fields. Description as in Fig. 2.3. The number in the upper right corner of each panel shows the number of sources with magnitudes originally measured above the 5σ limit included in their corresponding histogram for each field.

where X and Y are the respective magnitudes. Depending on the stage of the training process, the number of used colour might be reduced.

An additional feature shows the number of non-radio bands in which a source has valid (i.e. non imputed) measurements. We have called it `band_num` and it has been produced counting the number of valid values that each source showed before imputation. The values of this feature can range from 2 (source only detected in **CW**) up to 12 (source detected in every band of all selected surveys). This feature could be, very loosely, assimilated to the total flux a source can display. A higher `band_num` will imply that such source can be detected in more bands, implying that it has a higher flux (regardless of redshift). The use of features with counting or aggregation of elements in the studied dataset is well established in **ML** as has been presented by, for example, Zheng and Casari (2018), Duboue (2020), Sánchez-Sáez et al. (2021), and Euclid Collaboration

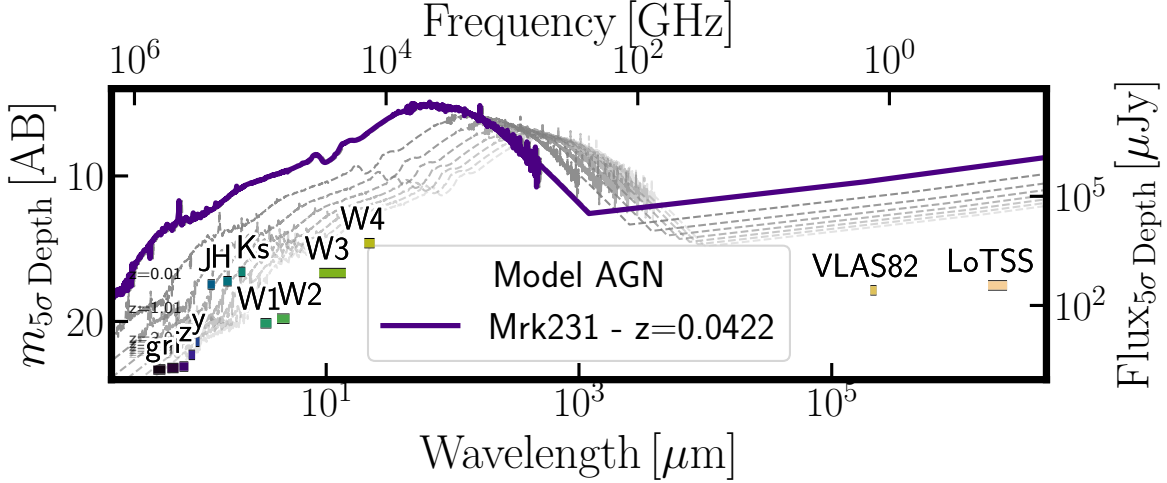


Figure 2.5: Flux and magnitude depths (5σ) from the surveys and bands used in this work. Limiting magnitudes and fluxes were obtained from the description of the surveys, as referenced in Sect. 2.3. In purple, rest-frame SED from Mrk231 ($z = 0.0422$, Brown et al., 2019) is displayed as an example AGN. Redshifted (from $z = 0.001$ to $z = 7$) versions of this SED are shown in dashed grey lines.

Table 2.3: Composition of initial catalogue and number of cross matches with additional surveys and catalogues.

Survey	HETDEX	Stripe82
CatWISE2020	15 136 878	3 590 306
AllWISE	5 955 123	1 424 576
Pan-STARRS	4 837 580	1 346 915
2MASS	566 273	214 445
LoTSS	187 573	...
VLAS82	...	8747
MQC (AGN)	50 538	17 743
SDSS (Galaxy)	68 196	4085

et al. (2023b).

In order to test whether or not a source has been detected in any of the selected radio surveys we have used in Sect. 2.3, we created a feature, called `radio_detect`, which shows a Boolean flag. Its value is `True` (1) if we have a valid entry (i.e. a detection) in its corresponding radio catalogue. As such, this flag can only tell if a source can be detected with radio observations similar to the deepest survey from our set and cannot give information of the existence, or not, of radio emission in general.

Lastly, we created an additional boolean feature, called `class`, which shows whether a source has been cross-matched with an element of the `MQC` or with a galaxy in `SDSS-DR16`. A value of zero (0) means that the source has been found in the `SDSS-DR16` galaxy sample, a value of one (1) implies that the source has been identified by the `MQC`. Sources that have not

CHAPTER 2. DATASETS FOR TRAINING AND TESTING

Table 2.4: Names of columns or features used in the code and what they represent.

Photometry measurements (magnitudes and fluxes)					
Code name	Feature	Code name	Feature	Code name	Feature
gmag	g (PS1)	ymag	y (PS1)	W1mpoPM	W1 (CW)
rmag	r (PS1)	Jmag	J (2M)	W1mpoPM	W2 (CW)
imag	i (PS1)	Hmag	H (2M)	W3mag	W3 (AW)
zmag	z (PS1)	Kmag	Ks (2M)	W4mag	W4 (AW)
Colours					
66 colours from all combinations of non-radio magnitudes. (A sub-sample of them is shown.)					
Code name	Feature	Code name	Feature	Code name	Feature
g_r	g - r (PS1)	W2_W3	W2 (CW) - W3 (AW)
g_i	g - i (PS1)	W2_W4	W2 (CW) - W4 (AW)
g_z	g - z (PS1)	W3_W4	W3 - W4 (AW)
Categorical flags					
Code name	Feature	Code name	Feature	Code name	Feature
band_num	Number of bands with measurements				
Boolean flags					
Code name	Feature	Code name	Feature	Code name	Feature
class	AGN or SFG	radio_detect			Detection in, at least, one radio band.
Redshift					
Code name	Feature	Code name	Feature	Code name	Feature
Z	Spectroscopic redshift				
Outputs of base models					
Code name	Feature	Code name	Feature	Code name	Feature
XGBoost	XGBoost	ET	Extra Trees		Gradient Boosting
CatBoost	CatBoost	GBC	Gradient Boosting	GBR	Regressor
RF	Random Forest		Classifier		

been included neither as [AGN](#) nor as [SFGs](#) (i.e. unknown sources) have not given any value for `class`. It is worth mentioning that a value of `0` in this flag does not mean directly that a source is not an [AGN](#). It only implies that the studied source has not been listed in the [MQC](#) as a confirmed [AGN](#). A list of the features created for this work and their representation in the code and in some of the figures is presented in Table 2.4.

2.6 Data re-scaling and normalisation

Attending to the intrinsic differences between [ML](#) algorithms, not all of them have the same performance when being trained with features that have absolute values spanning a wide range of values (i.e. several orders of magnitude). In particular, linear modelling of data might overrepresent features with larger absolute values when measuring distances between data point. For this reason, it is customary to re-scale the available values to either be contained within the range [0, 1] or to have similar distributions (e.g. Toth et al., [1993](#); Sola and Sevilla, [1997](#)). We applied a version of the latter transformation to our features (not the targets) as to have a mean value of $\mu = 0$ and a standard deviation of $\sigma = 1$ for each feature (i.e. standardisation). Additionally, these new values were power-transformed to resemble a Gaussian distribution. This transformation helps the models avoid using the distribution of values as additional information for the training (Kamiran and Calders, [2012](#)). For this work, a Yeo-Johnson transformation (Yeo and Johnson, [2000](#)) was applied. A representation of the steps performed for the pre-processing of the data (both in [HETDEX](#) and [S82](#)), and also described in Sects. [2.3](#), [2.4](#), and [2.5](#), is presented in Fig. [2.6](#).

2.7 Data splitting

Given that we need to be able to compare the results from the training and the application of the [ML](#) models with values obtained independently (i.e. ground truth), we divided our dataset into labelled and unlabelled sources. Labelled sources are all elements of our catalogue that have been classified as either [AGN](#) or [SFGs](#). Unlabelled sources are those which lack such classification and that will only be subject to the prediction of our models, not taking part in any training step. Labelled data will be used for training procedures and to, properly, assess the performance of the models.

Before any calculation or transformation is applied to the data from the [HETDEX](#) field, we split the labelled dataset into training, validation, calibration, and testing subsets. The early creation of these subsets helps avoid information leakage from the test subset into the models. Initially, a 20 % of the dataset has been reserved as testing data. Of the remaining elements, an 80 % of them have been used for training, and the rest of the data has been divided equally between calibration and validation subsets (i.e. a 10 % each). In the case of data from [S82](#), the only separation is done between labelled and unlabelled sources. Given that sources from [S82](#)

CHAPTER 2. DATASETS FOR TRAINING AND TESTING

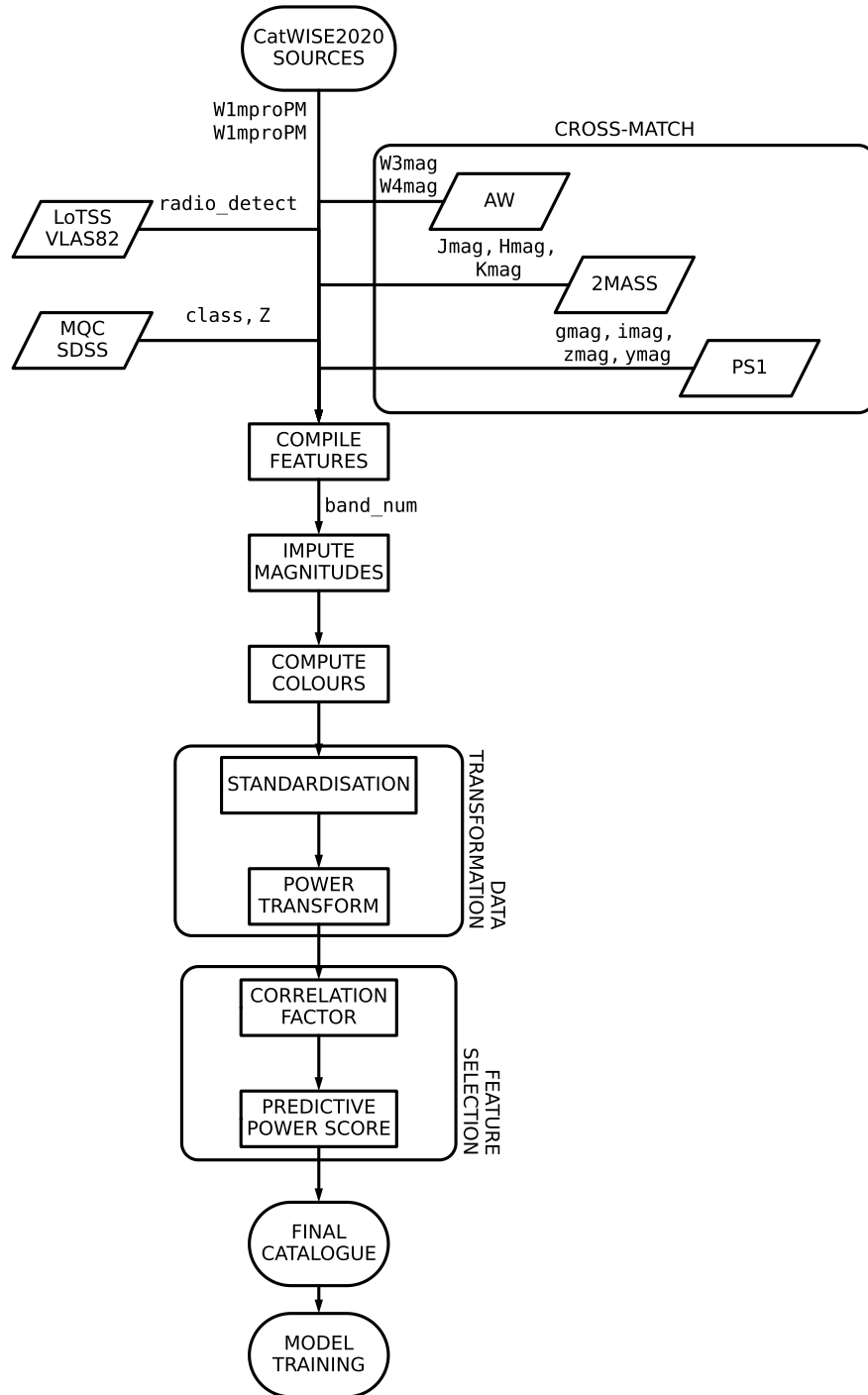


Figure 2.6: Flowchart with steps for data pre-processing. Labels in arrows state the features produced from each step or data catalogue.

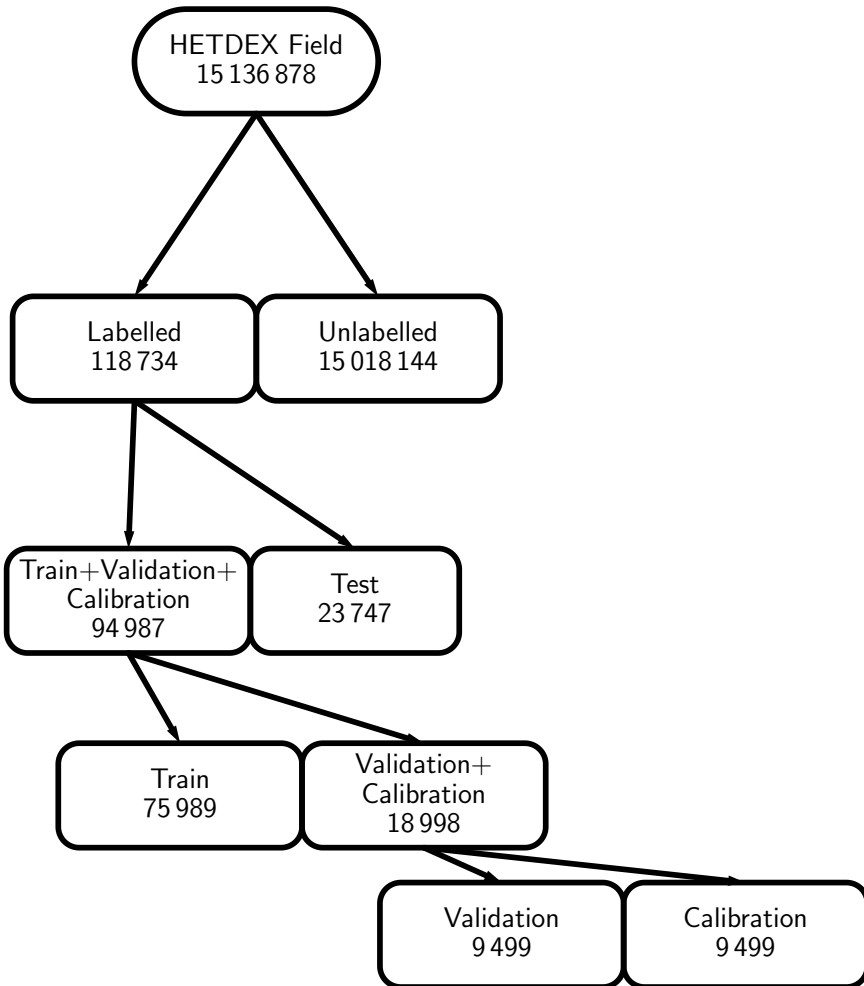


Figure 2.7: Composition of data from [HETDEX](#) used for the different steps of this work.

do not take part into the training of the models, they only need to be isolated from the elements in [HETDEX](#). The splitting process and the number of elements for each subset are shown in Figs. 2.7 and 2.8.

Depending on the model, the needed sources are selected from each of the subsets that have been already created. The training set will be used to select algorithms for each step and to optimise their hyper-parameters. The inclusion of the validation subset helps in the parameter optimisation of the models. The probability calibration of the trained model is performed over the calibration subset and, finally, the completed models are tested on the test subset and the labelled sources in [S82](#). The use of these subsets will be expanded further in the text.

It is worth noting that the fraction of labelled sources, both in the [HETDEX](#) and [S82](#) fields, is very low when compared to the total size of the datasets (0.8 % for [HETDEX](#) and 0.6 % for [S82](#)). These fractions confirm that the problems exhibited in Chapter 1.2 are ubiquitous and more analysis tools are needed to understand the nature of sources detected in existing

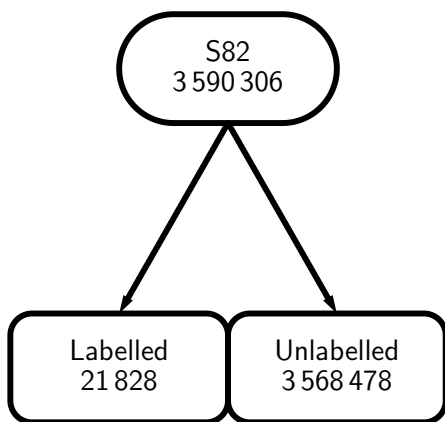


Figure 2.8: Composition of data from [S82](#) used for the different steps of this work.

catalogues.

Training of models

In this chapter, we present the results of the creation of the prediction pipeline and the models that make part of it. This procedure includes, for each step (as shown in Fig. 3.1, which is a more detailed version of Fig. 1.8), the selection of features, and the optimisation of algorithms and hyperparameters.

3.1 Prediction metrics

Several methods exist to assess the results from machine-assisted methods. Most of them have been designed for supervised tasks. In general, predictions are compared with the original (or true) quantities and a new quantity, a metric, is derived to determine how good the prediction is (i.e. how close to the true values or classes). A set of metrics will be used to understand the reliability of the results and put them in context with results in the literature. Since our work includes the use of classification and regression models, we briefly discuss the appropriate metrics in the following sections.

3.1.1 Classification metrics

The main tool to assess the performance of classification methods is the confusion matrix (also known as contingency or error matrix; Mead and Meyer, 1977; Hoffer and Fleming, 1978; Card, 1982; Congalton et al., 1983). It is a two-dimension (predicted vs. true) matrix where the number of true and predicted classes are compared and results stored in cells with the rate of **true positives (TPs)**, **true negatives (TNs)**, **false positives (FPs)**, and **false negatives (FNs)**. An example diagram showing the elements of a confusion matrix is shown in Table 3.2. An ideal classifier would be represented by a diagonal matrix with no incorrectly predicted elements. As mentioned earlier in Sect. 1.4, we seek to maximise the number of positive-class sources that are recovered as such. Using the elements of the confusion matrix, this aim can be translated into the maximisation of TPs and, consequently, the minimisation of FNs.

CHAPTER 3. TRAINING OF MODELS

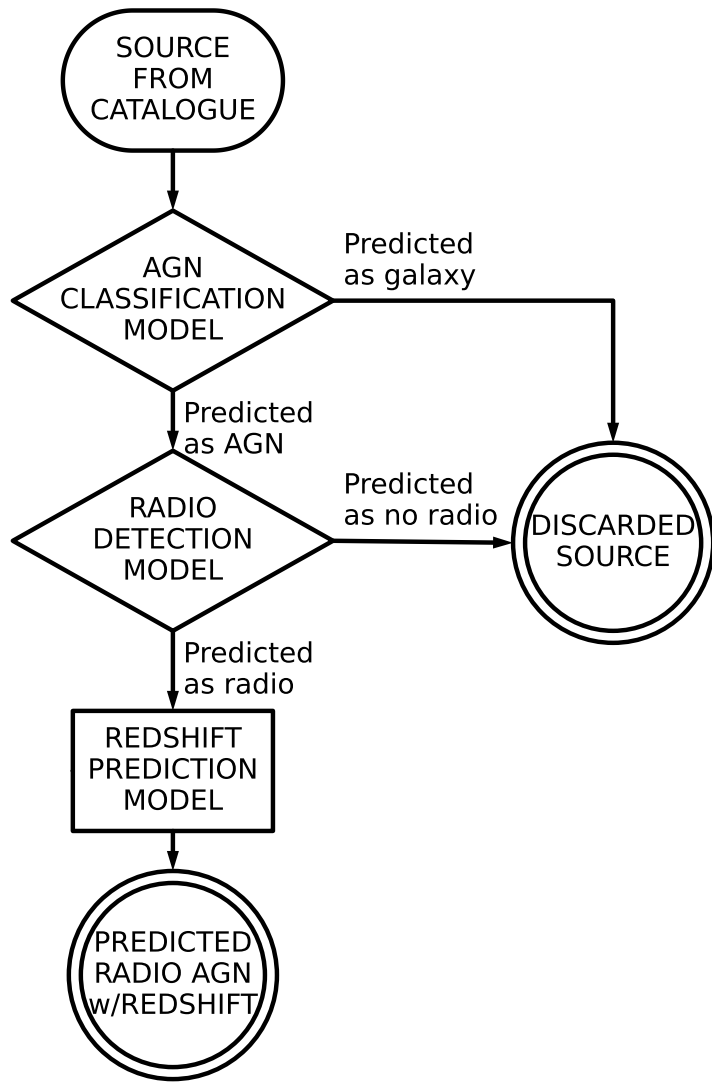


Figure 3.1: Flowchart representing the proposed prediction pipeline, with its ML-based models, used to predict the presence of radio-detected AGN and their redshift values from IR-detected sources.

From the elements of the confusion matrix, we can obtain additional metrics, such as the F_1 and F_β scores (Dice, 1945; Sørenson, 1948; van Rijsbergen, 1979), and the Matthews correlation coefficient (MCC; Yule, 1912; Cramér, 1946; Matthews, 1975) which are better suited for unbalanced data (i.e. when the fraction of elements of one class is much higher than that of the other) as they take into account the behaviour and correlations among all elements of the confusion matrix. As such, the F_1 coefficient is defined as:

$$F_1 = \frac{2TP}{2TP + FN + FP} . \quad (3.1)$$

F_1 values can go from 0 (no prediction of positive instances) to 1 (perfect prediction of elements

		True Classes	
		SFG	AGN
	SFG	True Negative (TN)	False Positive (FP)
	AGN	False Negative (FN)	True Positive (TP)
Predicted Classes			

Figure 3.2: Diagram of confusion matrix for the classification of sources between AGN and SFGs.

with positive labels). This definition assigns equal weight (importance) to both the number of FNs and FPs. An extension to the F1 score, which adds a non-negative parameter, β , to increase the importance given to each one of them is the F-Score (F_β), defined as:

$$F_\beta = \frac{(1 + \beta^2) \times TP}{(1 + \beta^2) \times TP + \beta^2 \times FN + FP}. \quad (3.2)$$

Using $\beta > 1$, more relevance is given to the optimisation of FNs. When $0 \leq \beta < 1$, the optimisation of FPs is more relevant. If $\beta = 1$, the initial definition of F1 is recovered. As with F1, F_β values can be in the range [0, 1]. Given that we seek to minimise the number of FNs detection, we adopt a conservative value of $\beta = 1.1$, giving more significance to their reduction without removing the aim for FPs. Also, this value is still close enough to $\beta = 1$, which will allow us to compare our scores to those produced in previous works.

MCC is defined as:

$$MCC = \frac{TP \times TN - FP \times FN}{\sqrt{(TP + FP)(TP + FN)(TN + FP)(TN + FN)}}, \quad (3.3)$$

which includes also the information about the TN elements. MCC can range from -1 (total disagreement between true and predicted values) to +1 (perfect prediction) with 0 representing a prediction analogous to a random guess.

CHAPTER 3. TRAINING OF MODELS

The Recall (also called Completeness, Sensitivity, or True Positive Rate –TPR–; Yerushalmi, 1947) corresponds to the rate of relevant, or correct, elements that have been recovered by a process. Using the elements from the confusion matrix, it can be defined as:

$$\text{Recall} = \text{TPR} = \frac{\text{TP}}{\text{TP} + \text{FN}}. \quad (3.4)$$

The true positive rate (TPR) can go from 0 to 1, with a value of 1 meaning that the model can recover all the true instances.

The last metric used is Precision (also known as Purity), which can be defined as the ratio between the number of correctly classified elements and the number of sources in the positive class (AGN or radio detectable, depending on the step of the pipeline):

$$\text{Precision} = \frac{\text{TP}}{\text{TP} + \text{FP}}. \quad (3.5)$$

Precision can range from 0 to 1, where higher values show that more real positive instances of the studied set were retrieved as such by the model.

In order to establish a baseline from which the aforementioned metrics can be assessed, it is possible to obtain them in the case of a random, or no-skill prediction. Following, for instance, the derivations and notation from Poisot (2023), a no-skill confusion matrix has the form:

$$\begin{pmatrix} (1-p)^2 & p(1-p) \\ (1-p)p & p^2 \end{pmatrix} \quad (3.6)$$

where p corresponds to the ratio between the elements of the positive class and the total number of elements involved in the prediction. From Eq. 3.6, no-skill versions of classification metrics (Eqs. 3.2–3.5) are then:

$$F_\beta^{\text{no-skill}} = p, \quad (3.7)$$

$$\text{MCC}^{\text{no-skill}} = 0, \quad (3.8)$$

$$\text{Recall}^{\text{no-skill}} = p, \quad (3.9)$$

$$\text{Precision}^{\text{no-skill}} = p. \quad (3.10)$$

It is expected, then, that the metrics from our prediction pipeline improve upon the no-skill values.

3.1.2 Regression metrics

Usually, regression tasks are assessed with the use of metrics such as [mean squared error \(MSE\)](#), [root mean square error \(RMSE\)](#), and [mean absolute error \(MAE\)](#). These measure the deviation of the predicted value from the original quantity. If the original value is called y_{True} and its predicted version is $y_{\text{Predicted}}$, these three regression metrics can be defined as follows.

The [MSE](#) is

$$\text{MSE}(y) = \frac{1}{d} \sum_i^d (y_{\text{True}} - y_{\text{Predicted}})^2 , \quad (3.11)$$

with d being the number of elements in the studied sample (i.e. its size). A direct modification of [MSE](#) appears when calculating its square root. Then, the root mean squared error is

$$\text{RMSE}(y) = \sqrt{\frac{1}{d} \sum_i^d (y_{\text{True}} - y_{\text{Predicted}})^2} . \quad (3.12)$$

A third way to quantify the deviation of the predictions from the true values is through the [MAE](#):

$$\text{MAE}(y) = \frac{1}{d} \sum_i^d |y_{\text{True}} - y_{\text{Predicted}}| , \quad (3.13)$$

While [MSE](#) and [RMSE](#) are sensitive to large deviations in the predictions, the [MAE](#) has a linear behaviour with respect to the fluctuations in predicted quantities.

For the case of redshift value determination, the previous metrics are not fully able to assimilate its logarithmic behaviour. Thus, further modifications are needed in order to use suitable metrics. Namely, a factor must be included to take into account the fact that differences between low redshift values should be penalized more strongly than those at higher redshifts. It is possible to start with the difference between true (z_{True}) and predicted ($z_{\text{Predicted}}$) redshift values,

$$\Delta z = z_{\text{True}} - z_{\text{Predicted}} , \quad (3.14)$$

and its normalised difference,

$$\Delta z^N = \frac{z_{\text{True}} - z_{\text{Predicted}}}{1 + z_{\text{True}}} . \quad (3.15)$$

CHAPTER 3. TRAINING OF MODELS

If the comparison is made over a larger sample of elements, the bias of the redshift is used (Dahlen et al., 2013), with the median of the quantities instead of its mean to avoid the strong influence of extreme values:

$$\Delta z_{\text{Total}} = \text{median}(z_{\text{True}} - z_{\text{Predicted}}) = \text{median}(\Delta z), \quad (3.16)$$

$$\Delta z_{\text{Total}}^N = \text{median}\left(\frac{z_{\text{True}} - z_{\text{Predicted}}}{1 + z_{\text{True}}}\right) = \text{median}(\Delta z^N). \quad (3.17)$$

Using the previous definitions, four additional metrics can be calculated. These are the **MAD** and the **normalised median absolute deviation (NMAD, σ_{NMAD})**; Hoaglin et al., 1983; Ilbert et al., 2009), which are less sensitive to outliers. Also, the standard deviation of the predictions, σ_z , and its normalised version, σ_z^N are typically used. They are defined as:

$$\sigma_{\text{MAD}} = 1.48 \times \text{median}(|\Delta z|), \quad (3.18)$$

$$\sigma_{\text{NMAD}} = 1.48 \times \text{median}(|\Delta z^N|), \quad (3.19)$$

$$\sigma_z = \sqrt{\frac{1}{d} \sum_i^d (\Delta z)^2}, \quad (3.20)$$

$$\sigma_z^N = \sqrt{\frac{1}{d} \sum_i^d (\Delta z^N)^2}. \quad (3.21)$$

Additionally, the outlier fraction (η , as used in Dahlen et al., 2013; Lima et al., 2022) is considered, which is defined as the fraction sources with a predicted redshift difference ($|\Delta z^N|$, Eq. 3.15) larger than a previously set value. Taking the results from Ilbert et al. (2009) and Hildebrandt et al. (2010), we have selected this threshold to be 0.15, leaving the definition of the outlier fraction as:

$$\eta = \frac{\#(|\Delta z^N| > 0.15)}{d}. \quad (3.22)$$

where $\#$ symbolises the number of sources fulfilling the described relation, and d corresponds to the size of the selected sample.

Most metrics presented in this section have been specially devised or adapted for the study of redshift values and their particular properties. Their use in **ML** algorithms can be, then,

considered a rudimental application of physics-informed ML (cf. Sect. 1.3).

3.2 Classification thresholds

Metrics presented in Sect. 3.1.1 work with a prediction of the status (class) of an element. However, most classifiers deliver a score rather than a definite class prediction. Scores, in the range $[0, 1]$ need to be translated into positive or negative classes. A threshold is defined to separate both states. By default, these models set a threshold at 0.5 in score (which we will call a naive threshold) but, in principle and given the characteristics of the problem, a different optimal threshold might be needed.

In our case, we want to optimise (increase) the number of recovered elements in each model (i.e. AGN or radio-detectable sources). This maximisation corresponds to obtaining thresholds that optimise the recall (Eq. 3.4). This can be done by decreasing the threshold by which a source is classified as a positive instances. Setting this threshold to its minimum, 0.0, would increase the recall. But every source would be predicted to be an AGN or detected on the radio regardless of their properties, defeating the purpose of the prediction pipeline. Thus, a different approach must be taken.

An optimised threshold can be obtained through the use of the statistical tool called precision-recall (PR) curve. Thresholds derived from the PR curves will be labelled as PR. PR curves can help to understand the behaviour of a classifier as a function of its threshold. In well-behaved models, both quantities, precision (Eq. 3.5) and recall, show an inverse correlation, and both depend on the selected threshold. Thus, they can be used to retrieve the score value for which both quantities are balanced. This optimisation is done by finding the threshold that maximises the F_β score (Eq. 3.2). This operation can be performed over the union of training and validation sets, which have been used to create and train each model.

3.3 Classification calibration

Classifiers deliver scores in the range $[0, 1]$, which could be, roughly, associated to the probability of a studied source being part of the relevant class (in our work, AGN or radio detectable). The classifier uses a threshold above which, any predicted element would be considered a positive instance.

With the exception of few algorithms (including the family of logistic regressions), scores

CHAPTER 3. TRAINING OF MODELS

from classifiers cannot be directly used as probabilities (Caruana and Niculescu-Mizil, 2006). As a consequence of this inability, such values cannot be compared from one type of model to some other and can not be combined to obtain a joint score. Therefore, in order to retrieve joint scores and treat them as probabilities, scores (and, by extension, the classifiers) need to be calibrated. This calibration means that, when taking all predictions with a probability P of being of a class C ($P(C)$), a fraction P of them really belong to that class (e.g. Lichtenstein et al., 1982; Silva Filho et al., 2023).

Calibration of these scores can be done by applying a transformation to their values. For our work, we will apply a Beta transformation. Beta transformation functions have the general form

$$\mu_{beta}(s; a, b, c) = \frac{1}{1 + \frac{1}{\left(e^c \frac{s^a}{(1-s)^b} \right)}}, \quad (3.23)$$

with s being the score from the classifier and a, b, c , free parameters to be optimised. It allows one to re-distribute the scores of a classifier allowing them to get closer to the definition of probability (Kull et al., 2017a; Kull et al., 2017b). Calibration steps in our workflow have been applied using the Python package `betacal`. In the case of the radio detection model, the new scores have a wider range than the original, uncalibrated scores.

Calibration (or reliability) plots (Niculescu-Mizil and Caruana, 2005) show how well calibrated the predicted scores of a classifier are by displaying the fraction of sources that are part of a given class as a function of the predicted probability. A perfectly calibrated classifier would have all its prediction lying in the $x = y$ line. The magnitude of the deviations from that line give information of the miscalibration a model has (see, for instance, Bröcker and Smith, 2007; Van Calster et al., 2019).

3.3.1 Calibration metrics

One of the most used analytical metrics to assess calibration of a model is the [Brier score](#) ([BS](#); Brier, 1950). It measures the mean square difference between the predicted probability of an element and its true class. If the total number of elements in the studied sample is d , the [BS](#) can be written (for binary classification problems, as the ones studied in this work) as:

$$\text{BS} = \frac{1}{d} \sum_i^d (\mathbb{C} - \text{class})^2, \quad (3.24)$$

where \mathbb{C} is the predicted class and class the true class of each of the elements in the sample (0 or 1). The BS can range between 0 and 1 with 0 representing a model that is completely reliable in its predictions. Additionally, the BS can be used to compare the reliability (or calibration) between a model and a reference using the [Brier skill score \(BS; Glahn and Jorgensen, 1970\)](#):

$$\text{BSS} = 1 - \frac{\text{BS}}{\text{BS}_{\text{ref}}}. \quad (3.25)$$

In our case, BS_{ref} corresponds to the value calculated from the uncalibrated model. The BSS can take values between -1 and 1 . The closer the BSS gets to 1 , the more reliable the analysed model is. These values include the case where $\text{BSS} \approx 0$, in which both models perform similarly in terms of calibration.

For our pipeline, after a model has been fully trained, a calibrated version of their scores will be obtained. With both of them, the BSS will be calculated and, if it is not considerably lower than 0 , that calibrated transformation will be used as the final scores from the prediction.

3.4 Feature selection

[ML](#) algorithms, as most data analysis tools, require execution times which increase with the size of the datasets. In order to reduce training times without losing relevant information for the model, the most important features were selected at each step through a process called feature selection (e.g. Blum and Langley, 1997; Kohavi, Ron and John, 1997; Guyon and Elisseeff, 2003). Feature selection can also help avoiding the inclusion of data that might add noise to the model predictions.

For each model, the process of feature selection begins with 79 base features (Table 2.4) and three targets (`class`, `LOFAR_detect`, and `Z`). Feature selection is run, independently, for each trained model (i.e. [AGN-SFG](#) classification, radio detection, and redshift predictions), delivering three different sets of features. To avoid redundancy, the process starts discarding features that have a high correlation with another property of the dataset. For discarding features, we calculated Pearson's correlation matrix (built with the Pearson's correlation factors, ρ , between features; Bravais, 1844; Galton, 1886; Pearson and Galton, 1895) for the full train+validation dataset only and selected the pairs of features that showed a correlation factor

CHAPTER 3. TRAINING OF MODELS

higher than $\rho = 0.75$, in absolute values. A value of $\rho = 0.75$ is a compromise between very stringent thresholds (e.g. $\rho = 0.5$) and more relaxed values (e.g. $\rho \approx 0.9$) (for an explanation on how to consider different correlation values, see, for instance Ratner, 2009). From each pair, we discarded the feature with the lowest [relative standard deviation \(RSD; Johnson and Leone, 1964\)](#), which is defined as the ratio between the standard deviation of a set and its mean value. A feature which covers a small portion of its probable values (i.e. low coverage of parameter space, and lower [RSD](#)) will give less information to a model than one with largely spread values. Thus, its elimination might not have a large impact the final model.

For the [AGN-SFG](#) classifier, feature selection was applied in the train+validation subset with 85 488 confirmed elements (galaxies from [SDSS-DR16](#) and [AGN](#) from [MQC](#), i.e. `class == 0` or `class == 1`). After the selection procedure described in Sect. 3.4, 18 features were selected for training: `band_num`, `W4mag`, `g_r`, `r_i`, `r_J`, `i_z`, `i_y`, `z_y`, `z_W2`, `y_J`, `y_W1`, `y_W2`, `J_H`, `H_K`, `H_W3`, `W1_W2`, `W1_W3`, and `W3_W4`. The target feature is `class`. In the case of the radio detection classifier, feature selection was applied to the train+validation subset, with 36 387 confirmed [AGN](#). The target feature is `LOFAR_detect` and the base of 17 selected features are: `band_num`, `W4mag`, `g_r`, `g_i`, `r_i`, `r_z`, `i_z`, `z_y`, `z_W1`, `y_J`, `y_W1`, `J_H`, `H_K`, `K_W3`, `K_W4`, `W1_W2`, and `W2_W3`.

Finally, feature selection (cf. Sect. 3.4) was applied to the train+validation subset for the photometric redshift regressor, with 4612 sources, leading to the selection of 17 features. The target feature is `Z` and the selected base features are `band_num`, `W4mag`, `g_r`, `g_W3`, `r_i`, `r_z`, `i_z`, `i_y`, `z_y`, `y_J`, `y_W1`, `J_H`, `H_K`, `K_W3`, `K_W4`, `W1_W2`, and `W2_W3`.

It is important to highlight that, for all three models, a similar number of features was selected. Additionally, the base of adopted features contains quantities that are analogous among them. This fact might suggest that our full dataset might be reduced to a minimum number of features which carry the same information as the full sample of 77 quantities, independent of the studied target.

3.5 Model stacking

Base and meta learners (cf. Sect. 1.3.2) have been selected based upon the metrics described in Sect. 3.1. We have trained five algorithms with the training subset and calculated the metrics for all of them using a 10-fold [cross-validation \(CV\)](#) approach (e.g. Stone, 1974; Allen, 1974) over the same training subset. For each metric, the learners have been given a rank

(from 1 to 5, with 1 being the best possible value) and a mean value has been obtained from them. Out of the analysed algorithms, the one with the best overall performance (i.e. best mean rank) is selected to be the meta learner while the remaining four are used as base learners.

For the **AGN-SFG** classification and radio detection problems, we tested five classification algorithms: **RF**, gradient boosting classifier (**GBC**; Friedman, 2001), **Extra Trees** (**ET**; Geurts et al., 2006), extreme gradient boosting (**XGBoost**, v1.5.1; Chen and Guestrin, 2016), and **Category Boosting** (**CatBoost**, v1.0.5; Prokhorenkova et al., 2018; Dorogush et al., 2018). For the redshift prediction problem, we tested five regressors as well: **RF**, **ET**, **XGBoost**, **CatBoost**, and **gradient boosting regressor** (**GBR**; Friedman, 2001). We have used the Python implementations of these algorithms and, in particular for **RF**, **ET**, **GBC**, and **GBR**, the versions offered by the package **scikit-learn**¹ (v0.23.2; Pedregosa et al., 2011). These algorithms were selected given that they offer tools to interpret the global and local influence of the input features in the training and predictions (cf. Sect. 1.3.3).

All the algorithms selected for this work fall into the broad family of tree-based models. Additionally, forest models (**RF** and **ET**) rely on a collection of decision trees to, after applying a majority vote, predict either a class or a continuum value. Each of these decision trees uses a different, randomly-selected subset of features to make a decision on the training set (Breiman, 2001). Opposite to forests, gradient boosting models (**GBC**, **GBR**, **XGBoost**, and **CatBoost**) apply decision trees sequentially to improve the quality of the previous predictions (Friedman, 2001; Friedman, 2002).

3.6 Model training

The procedure described in Sect. 3.5 includes an initial fit of the selected algorithms to the training data (including the selected features) to optimise their parameters. The stacking step includes a new optimisation of the parameters of the meta-learner using 10-fold **CV** on the training data with the addition of the output from the base learners, which are treated as regular features (see last section of Table 2.4). Then, following Michailidis (2017), the hyper-parameters of the stacked models are optimised over the training subset (a brief description of this step is presented in Sect. 3.6.1).

The final step involves a last parameter fitting instance but using, this time, the combined train+validation subset, which includes the output of the base algorithms, to ensure wider

¹<https://scikit-learn.org>

CHAPTER 3. TRAINING OF MODELS

Table 3.1: Best performing models for the [AGN-SFG](#) classification

Model	F_β ($\times 100$)	MCC ($\times 100$)	Precision ($\times 100$)	Recall ($\times 100$)	Rank
CatBoost	95.70 ± 0.28	92.46 ± 0.48	95.45 ± 0.32	95.91 ± 0.37	1.00
XGBoost	95.67 ± 0.27	92.40 ± 0.48	95.41 ± 0.39	95.88 ± 0.34	2.00
RF	95.52 ± 0.36	92.14 ± 0.63	95.28 ± 0.46	95.71 ± 0.40	3.00
ET	95.40 ± 0.40	91.94 ± 0.69	95.13 ± 0.43	95.63 ± 0.47	4.00
GBC	95.26 ± 0.31	91.66 ± 0.54	94.82 ± 0.41	95.63 ± 0.35	5.00

^a Metrics obtained using the default probability threshold of 0.5.

^b Algorithms are sorted by decreasing recall values.

^c For display purposes, all metrics have been multiplied by 100.

^d Uncertainties show standard deviation of metrics obtained across all 10 training folds (cf. Sect. 3.5)

Table 3.2: Best performing models the radio detection classification

Model	F_β ($\times 100$)	MCC ($\times 100$)	Precision ($\times 100$)	Recall ($\times 100$)	Rank
XGBoost	29.98 ± 2.29	29.81 ± 2.17	56.74 ± 2.93	21.61 ± 2.00	2.75
CatBoost	29.57 ± 1.62	30.56 ± 1.71	60.10 ± 2.85	20.85 ± 1.36	2.25
GBC	29.60 ± 1.66	31.31 ± 1.93	62.55 ± 3.95	20.66 ± 1.40	1.75
RF	29.16 ± 2.47	30.26 ± 2.65	60.03 ± 3.73	20.48 ± 1.96	3.75
ET	28.40 ± 1.27	29.73 ± 1.47	60.06 ± 2.85	19.80 ± 1.05	4.50

^a Values and uncertainties as in Table 3.1.

coverage of the parameter space and better-performing models. Consequently, only the testing set is available for assessing the quality of the predictions made by the models.

The results of model testing for the [AGN-SFG](#) classification are reported in Table 3.1. The [CatBoost](#) algorithm provides the best metric values (highest mean rank) and is therefore selected as the meta-model. [XGBoost](#), [RF](#), [ET](#), and [GBC](#) were used as base learners.

Training of the radio detection model was applied only to sources confirmed to be [AGN](#) (`class == 1`). The performance of the tested algorithms is shown in Table 3.2. In this case, [GBC](#) shows the highest mean rank. For this reason, we used it as the meta-learner and [XGBoost](#), [CatBoost](#), [RF](#), and [ET](#) were selected as base-learners.

The redshift value prediction model was applied to sources confirmed to be radio-detected [AGN](#) (i.e. `class == 1` and `radio_detect == 1`). The tested algorithms performed as shown in Table 3.3. Based on their mean rank values, [RF](#), [CatBoost](#), [XGBoost](#), and [GBR](#) were selected as base learners and [ET](#) was used as meta-learner.

It is worth noting that, while the use of the mean rank is helpful to select a meta learner, the proper differences in metric values between models are small. These similarities might imply that most algorithms (at least classifiers) can extract the same level of information from

Table 3.3: Results of initial fit for redshift value prediction

Model	σ_{MAD} ($\times 100$)	σ_{NMAD} ($\times 100$)	σ_z ($\times 100$)	σ_z^N ($\times 100$)	η ($\times 100$)	Rank
RF	17.88 ± 1.41	7.95 ± 0.50	42.02 ± 5.28	19.38 ± 2.44	19.51 ± 1.98	2.0
ET	18.53 ± 1.03	8.42 ± 0.43	41.12 ± 4.16	18.65 ± 2.26	19.24 ± 1.16	1.8
CatBoost	21.71 ± 1.38	10.08 ± 0.47	40.35 ± 3.03	18.52 ± 1.39	21.93 ± 1.55	2.2
XGBoost	22.89 ± 1.05	10.84 ± 0.78	43.14 ± 3.99	19.62 ± 1.78	24.15 ± 1.84	4.0
GBR	27.73 ± 1.57	12.72 ± 0.74	44.82 ± 3.80	20.41 ± 1.67	28.67 ± 2.25	5.0

^a Algorithms sorted by increasing σ_{MAD} values.^b Uncertainties as in Table 3.1.

the data. For this reason, the use of ensemble learning is justified to help the algorithms extract even more information than that they can retrieve on their own.

3.6.1 Hyperparameters optimisation

After the selection of the meta learners of each prediction stage of our pipeline, the predicted values (scores for classifiers and redshift for the regressor) are incorporated to the feature set as new quantities to learn from. Thus, and as shown in Table 2.4, four new feature are added per training instance.

In Table 3.4, we present the optimised hyper-parameters from our meta-learners. For all three instances of modelling (**AGN-SFG**, radio detection, and redshift), hyper-parameters were optimised using the `SkoptSearch` algorithm embedded in the package `tune-sklearn`² (v0.4.1; Head et al., 2021), which implements a Bayesian search in the hyper-parameter space.

3.6.2 Calibration of models

In Fig. 3.3, we present the reliability curves for the uncalibrated classifiers (see Sect. 3.3). It can be seen that the scores for the **AGN-SFG** classifier can be found clustered in a small range around 0.5. This behaviour might indicate some issue with the predictions. But, as presented in Table 3.1, all models used in the training show very high (i.e. satisfactory) metric values. This apparent contradiction might be explained by two factors. First, the sample used for training is highly unbalanced, with most of the sources being labelled as galaxies. Thus, there might be a fraction of elements of both classes that share a significant region of the parameter space. When **ML** algorithms try to classify elements under these two circumstances, they tend to deliver

²<https://github.com/ray-project/tune-sklearn>

CHAPTER 3. TRAINING OF MODELS

Table 3.4: Hyper-parameters values for meta-learners in modified pipeline after tuning.

AGN-SFG model (CatBoost)			
Parameter	Value	Parameter	Value
<code>learning_rate</code>	0.0075	<code>random_strength</code>	0.1
<code>depth</code>	6	<code>l2_leaf_reg</code>	10
Radio detection model (GradientBoosting)			
Parameter	Value	Parameter	Value
<code>n_estimators</code>	187	<code>min_samples_leaf</code>	2
<code>learning_rate</code>	0.0560	<code>max_depth</code>	9
<code>subsample</code>	0.3387	<code>max_features</code>	0.5248
<code>min_samples_split</code>	5		
Redshift prediction model (ET)			
Parameter	Value	Parameter	Value
<code>n_estimators</code>	100	<code>criterion</code>	<code>mae</code>
<code>max_depth</code>	None	<code>min_samples_split</code>	2
<code>max_features</code>	auto	<code>min_samples_leaf</code>	1
<code>bootstrap</code>	<code>False</code>		

^a This table shows the parameters which were subject to tuning.

^b Remaining hyper-parameters used their default values as defined by their developers.

predictions with very low certainties (see, for instance, Vuttipittayamongkol et al., 2021; Santos et al., 2022). This issue can be solved, among other techniques, with the use of probability calibration, which has been implemented in our pipeline.

The previously presented problem does not seem the exist, in the same fashion, in the classification of radio-detectable AGN. There, the distribution of prediction scores ranges from 0.0 up to ~ 0.8 . In this case, and given the conditions of the problem of finding indicators of the detection of radio sources from optical and infrared measurements, the source of a lack of scores close to 1.0 can be related to the impossibility of the models of finding stronger connections between all measurements rather than, for example, problems with the balance of datasets.

In Fig. 3.4, we present the reliability curves for the calibrated versions of the classifiers. For the AGN-SFG classifier, the improvement is remarkable. Now, predicted probabilities are distributed in the range [0, 1] and they follow closely the line of perfect calibration. In the case of the radio detectability prediction, the improvement is milder, with the new probabilities getting closer to the line of perfect probability calibration. Nevertheless, the new probabilities maintain the same distribution as the original scores (between 0.0 and ~ 0.8). This result implies that probability calibration cannot be used to solve issues with the extraction of information from the available features.

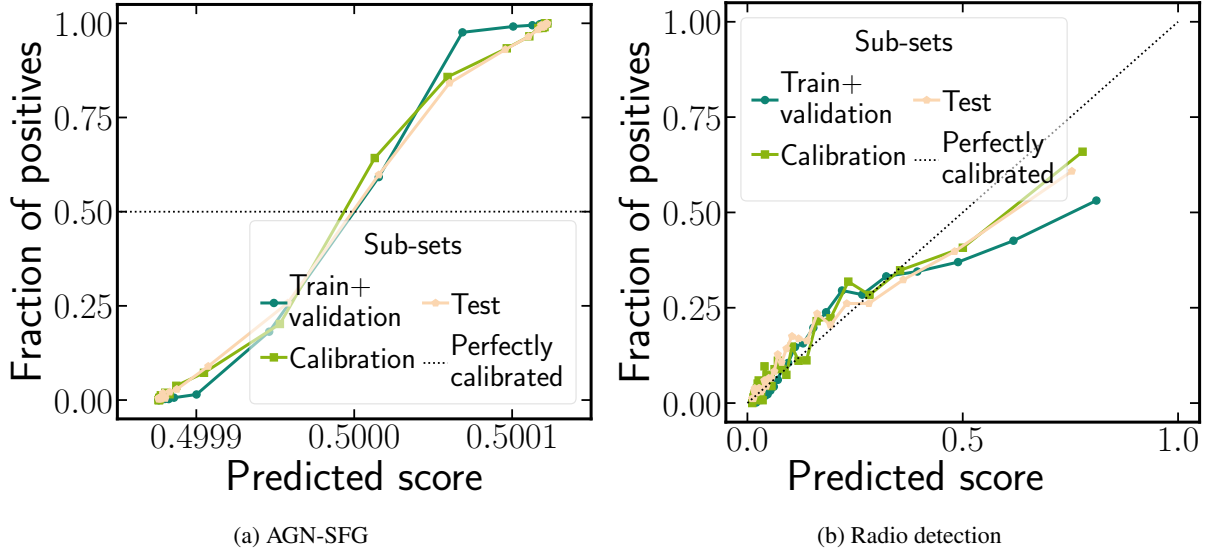


Figure 3.3: Reliability curves for uncalibrated classifiers. Each line represents the calibration curve for each subset in [HETDEX](#) field. Data has been binned and each bin (represented by the points) has the same number of elements per curve. Dashed line represents a perfectly calibrated model. (a) [AGN-SFG](#) classification model. (b) Radio detection model.

From a numerical point of view, when obtaining the [BSS](#) values for both classification, the [AGN-SFG](#) classifier has a score of $BSS = -0.002$, demonstrating that no major changes were applied to the intrinsic distribution of scores. For the radio detection classifier, the score is $BSS = -0.434$. Even though the [BSS](#) value is slightly negative for the [AGN-SFG](#) classifier, we keep it since its range of values now can be compared and combined with additional probabilities. In the case of the radio detection classifier, the [BSS](#) shows a degradation of the calibration, but we will keep the calibrated model given that it provides, overall, better values for the remaining metrics. Additionally, and as mentioned previously, the use of calibrated probabilities allows one to combine them through consecutive models, which is our goal with the prediction of radio-detectable [AGN](#).

3.6.3 Threshold selection

[PR](#) curves (see Sect. 3.2) for all subsets used in our classification models are shown in Fig. 3.5. In the case of [AGN-SFG](#) classification, it can be seen (Fig. 3.5a) that the [PR](#) curve does not present any abnormality (i.e. the curves are smooth and can reach close to the upper-right side of the plot). From the optimisation of the F_β score, the optimal threshold for the calibrated meta model is 0.348 95. This value was used for the [AGN-SFG](#) model throughout this work. It might also be seen that the behaviour of the [PR](#) curve is consistent among subsets, an indication that the model has been properly trained and, probably, very low levels of over-fitting are present.

On the other side, the [PR](#) curves for the calibrated radio-detectability meta model

CHAPTER 3. TRAINING OF MODELS

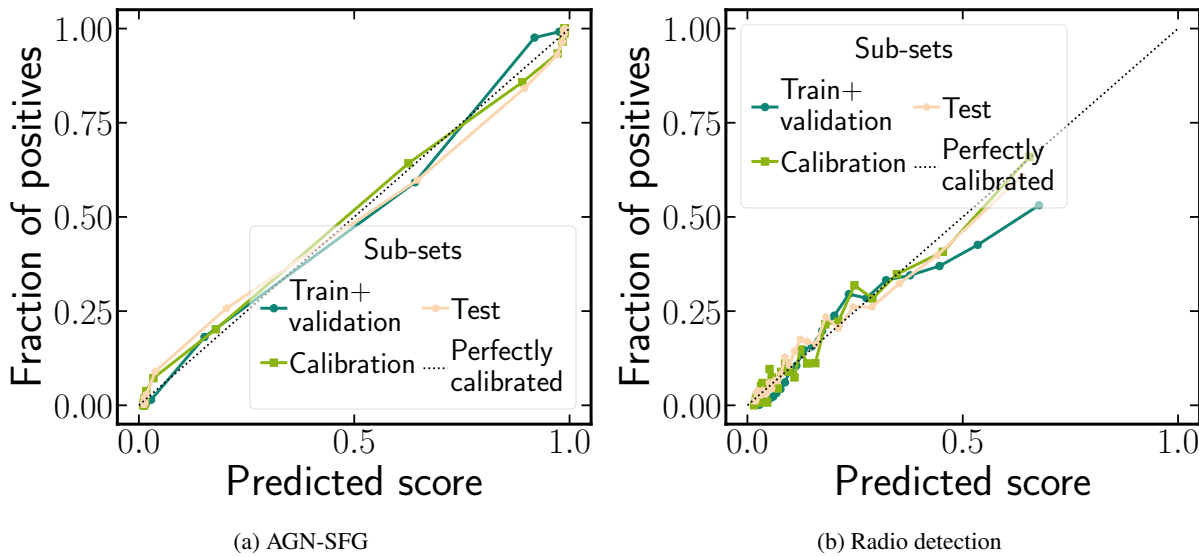


Figure 3.4: Reliability curves for calibrated classifiers. (a) AGN-SFG classification model. (b) Radio detection model. Details as in Fig. 3.3.

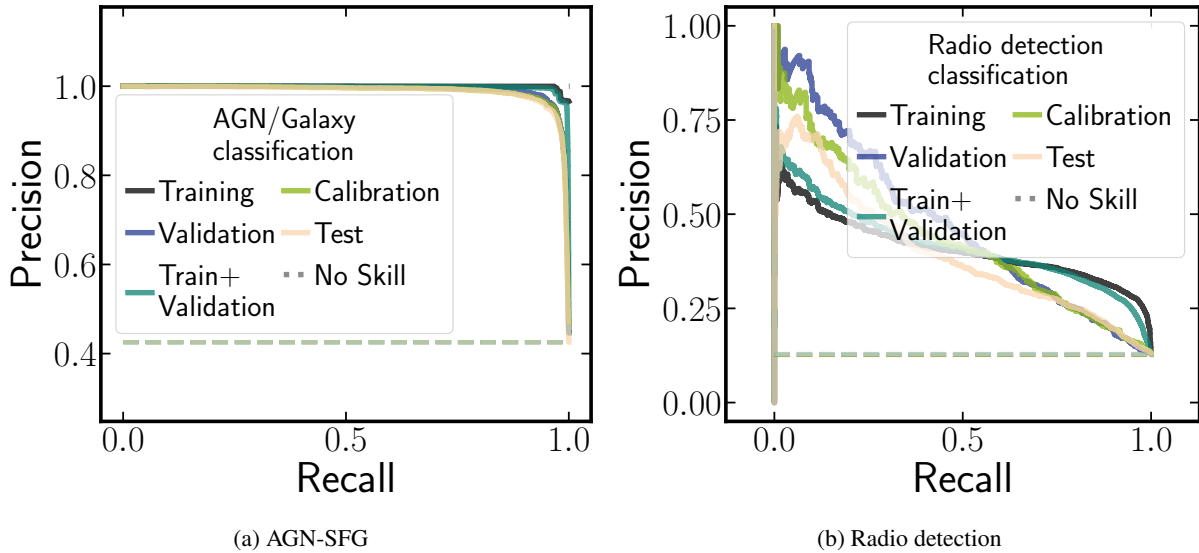


Figure 3.5: Precision-Recall curves for the (a) AGN-SFG and (b) radio detection classification models.

(Fig. 3.5b) present a different behaviour, with noticeable variation among subsets. Such behaviour might be the expression of a lack of enough retrieval of information from the training set, making the model unsuited for a successful application in a different dataset. Additionally, each curve shows high levels of irregularities, highlighting the possibility that the model is very sensitive to, even small, changes of threshold. As mentioned in Sect. 3.2, PR curves underline the relation between precision and recall in a model. Figure 3.5b hints a highly extreme relation between both metrics, where no similar combination of values can be found. Finally, from the maximisation of the F_β score, the optimal threshold for this model is found to be 0.204 60.

Prediction of radio-AGN candidates

After training the models, tuning their hyperparameters, and calibrating their scores, we were able to use them for predicting values in data sets which have not been used in the previous stages. In our case, this is the testing subset, which is different in its size for each [ML](#) problem (classification or regression), and the labelled sources from the [S82](#) field.

4.1 AGN-SFG classification

The results of the application of the stacked and calibrated model for the testing subset and the labelled sources in [S82](#) are presented in the two first blocks of Table 4.1 ([HETDEX](#)-test and [S82](#)-label). The metrics are shown for the use of two different thresholds, the naive value of 0.5 and the [PR](#)-derived value of 0.348 95. The confusion matrix of the predictions (calculated on the testing dataset) is shown in Fig. 4.1.

Overall, the model is able to separate [AGN](#) from [SFGs](#) with a very high (recall $\gtrsim 94\%$) success rate, regardless of the selected threshold. It is possible to see that the [MCC](#) scores for the two analysed subsets are in similar levels. That can be taken as an indication of a good training process, in which no substantial over-fitting can be detected, in line with the results presented in Sect. 3.6.3 for the [PR](#) analysis. In general, values using the naive threshold are, when considering the uncertainty values, compatible with those obtained with the [PR](#) threshold. Since in both cases, the scores are fairly high, it is possible that the model is, already, extracting most of the information from the dataset and, regardless of the treatment applied to the scores, predictions will mostly be correct.

One important caveat to the good results presented in Table 4.1 is that of the relatively low [MCC](#) values obtained for the [S82](#) field. Considering that, among the metrics used in this work, is the only one that incorporates the number of [TNs](#) (cf. Sect. 3.1.1), the [MCC](#) reflects the imbalance between classes in a dataset. As discussed in Sect. 2.5, the [HETDEX](#) and [S82](#) fields have different fraction of sources ([AGN](#) and [SFGs](#)) among them and, thus, different values of [MCC](#) are expected.

CHAPTER 4. PREDICTION OF RADIO-AGN CANDIDATES

Table 4.1: Resulting metrics of [AGN-SFG](#) classification model for the test subset and the labelled sources in [S82](#) using two different threshold values. [HETDEX](#) and [S82](#) pipeline results are described in Sect. 4.4.

Subset	Threshold	F_β ($\times 100$)	MCC ($\times 100$)	Precision ($\times 100$)	Recall ($\times 100$)
HETDEX-test	Naive	95.37 ± 0.36	91.81 ± 0.67	97.47 ± 0.69	95.89 ± 2.27
	PR	95.42 ± 0.38	91.85 ± 0.70	94.49 ± 0.65	96.21 ± 0.43
S82-label	Naive	94.15 ± 0.44	70.54 ± 2.02	95.16 ± 0.41	93.33 ± 0.66
	PR	94.37 ± 0.36	70.67 ± 1.72	94.81 ± 0.40	94.01 ± 0.59
HETDEX-pipe	Naive	95.37 ± 0.36	91.81 ± 0.67	97.47 ± 0.69	95.89 ± 2.27
	PR	95.42 ± 0.38	91.85 ± 0.70	94.49 ± 0.65	96.21 ± 0.43
S82-pipe	Naive	94.15 ± 0.44	70.54 ± 2.02	95.16 ± 0.41	93.33 ± 0.66
	PR	94.37 ± 0.36	70.67 ± 1.72	94.81 ± 0.40	94.01 ± 0.59

^a All metrics have been multiplied by 100.

^b Uncertainties show standard deviation of metrics obtained across all 10 training folds (cf. Sect. 3.5)

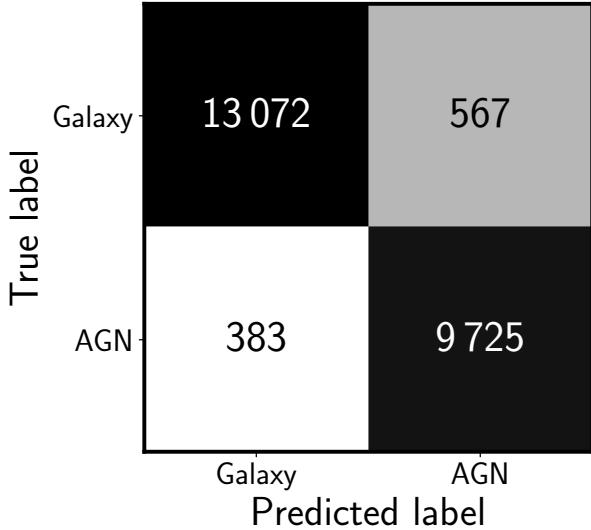


Figure 4.1: Confusion matrix from the results of application of [AGN-SFG](#) classification model to the [HETDEX](#) test subset. Rows represent the separation of sources according to their true (or original) classification. Columns divide the sample in their predicted classes. A description of confusion matrices, in general, is offered in Sect. 3.1.1 and, specifically, in Fig. 3.2.

A closer inspection to the confusion matrix in Fig. 4.1 shows that close to a 4 % of the [AGN](#) from the [MQC](#) were discarded by our model. And less than 6 % of the predicted [AGN](#) are not labelled as such by the [MQC](#). Additionally, it is possible to see the level of imbalance present in this dataset, where almost 60 % of the sources are, originally, labelled as [SFGs](#). Despite this disparity, our model achieves high-quality metric values in both [HETDEX](#) and [S82](#) fields, which creates a well-predicted dataset to be fed into the following step of the prediction pipeline.

Table 4.2: Resulting metrics of the radio detection model on the test subset and the labelled sources in S82 using two different threshold values. HETDEX and S82 pipeline results shown as part of the discussion in Sect. 4.4

Subset	Threshold	F_β ($\times 100$)	MCC ($\times 100$)	Precision ($\times 100$)	Recall ($\times 100$)
HETDEX-test	Naive	24.87 ± 2.94	27.36 ± 3.46	60.61 ± 8.18	16.72 ± 2.31
	PR	42.88 ± 2.93	32.47 ± 3.49	35.28 ± 2.74	52.16 ± 3.59
S82-label	Naive	27.15 ± 2.28	23.36 ± 2.27	25.72 ± 1.91	28.47 ± 3.24
	PR	21.62 ± 1.20	19.37 ± 1.64	12.29 ± 0.73	58.16 ± 3.06
HETDEX-pipe	Naive	24.37 ± 3.53	26.93 ± 4.18	59.36 ± 7.17	16.38 ± 2.63
	PR	41.57 ± 4.16	31.67 ± 4.81	34.65 ± 3.24	49.80 ± 5.85
S82-pipe	Naive	26.52 ± 5.44	23.29 ± 5.73	25.71 ± 5.89	27.72 ± 5.21
	PR	20.19 ± 2.84	18.40 ± 4.07	11.45 ± 1.58	54.78 ± 8.44

^a Values and uncertainties as in Table 4.1.

4.2 Radio detection classification

The application of the stacked model for the prediction of the radio detection of the training, testing, and validation subset is summarised in the two first blocks of Table 4.2 (labelled as HETDEX-test and S82-label). Contrary to the results from the previous step of the prediction pipeline, the metrics for the radio detection prediction are somewhat lower. This difference might be a demonstration that the model is not able to extract an amount of information that is enough to discriminate between both classes.

Another difference with the results from the AGN-AGN classifier is that there is a noticeable disparity between the metrics obtained from the use of the naive threshold and those from the application of the PR-based threshold. Even when factoring the uncertainties in, metrics in both cases remain incompatible. This difference emphasises the importance of the use of the PR curve for the extraction of optimised classification thresholds, even though it is, also, an expression of the instability of such curve for this classifier (which, as shown in Sect. 3.6.3, is very sensitive to changes in threshold).

Similarly, the confusion matrix derived from the prediction results over the test sample is shown in Fig. 4.2. From it, the reasons for the low metrics can be seen more patently, with rather high values for FN and FP sources. Again, such values might find their roots in the possible inability of this model to extract all the available information to make a higher quality decision about the radio detectability of AGN.

CHAPTER 4. PREDICTION OF RADIO-AGN CANDIDATES

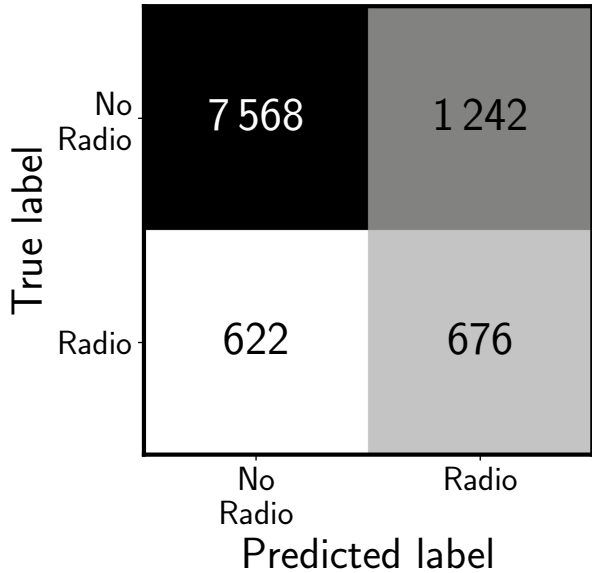


Figure 4.2: Confusion matrix from the results of application of radio-detection classification model for AGN to the HETDEX test subset. Description as in Fig. 4.1.

4.3 Redshift prediction

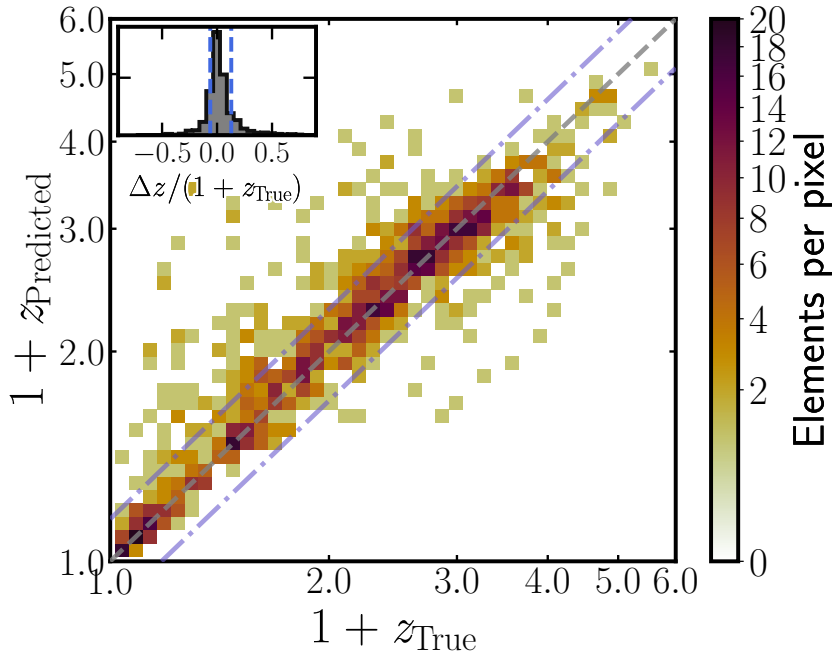
In the case of redshift values prediction, the application of the stacked model over the testing subset and the labelled sources in the [S82](#) field is summarised in the two first rows of Table 4.3 (named as [HETDEX-test](#) and [S82-label](#)).

These results show some degree of over-fitting, since the testing scores are a factor of two worse than those from the training and test subsets. This happens for all used metrics. One reason for these differences might be due to the design of our prediction pipeline itself. As each step has been trained in a smaller dataset (and with sources that have to fulfill even more conditions than in the previous model), the possibilities that the redshift prediction model to extract information that can be successfully applied into independent datasets are inferior. Consequently, its application in the [S82](#) field might (and does, as shown in Table 4.3) provide lower-quality results.

Likewise, the comparison between the original redshift values and those derived from the prediction results in the test subset is shown in Fig. 4.3. Apart from the good quality of predictions (as shown by the large fraction of sources located inside the outlier region), an interesting effect can be noted. For sources with $z_{\text{True}} \lesssim 1.0$, predicted values tend to be overestimated while, for z_{True} values above that limit, predictions do not show a preferred direction. These differences might hint issues with the prediction of radio-[AGN](#) redshifts at that range. Further in this text, more analyses will be presented in this topic.

Table 4.3: Redshift prediction metrics for the test subset from **HETDEX** and **S82** labelled sources as discussed in Sect. 4.4

Subset	σ_{MAD} ($\times 100$)	σ_{NMAD} ($\times 100$)	σ_z ($\times 100$)	σ_z^N ($\times 100$)	η ($\times 100$)
HETDEX-test	16.54 ± 2.55	7.27 ± 0.99	41.14 ± 9.97	20.56 ± 5.98	19.03 ± 3.35
S82-label	18.66 ± 2.26	9.28 ± 1.37	51.08 ± 11.62	24.69 ± 4.36	24.29 ± 4.68
HETDEX-pipe-Naive	8.11 ± 3.95	5.42 ± 2.19	32.00 ± 12.27	20.97 ± 9.69	19.01 ± 8.22
HETDEX-pipe-PR	15.86 ± 1.77	7.17 ± 0.81	37.80 ± 3.06	22.93 ± 2.73	18.91 ± 1.59
S82-pipe-Naive	15.17 ± 2.70	9.14 ± 1.23	43.05 ± 7.20	24.32 ± 5.00	24.09 ± 4.52
S82-pipe-PR	20.71 ± 1.23	9.84 ± 0.56	45.14 ± 4.42	26.14 ± 3.77	25.18 ± 2.26

^a Values and uncertainties as in Table 4.1.Figure 4.3: Density plot of comparison between original and predicted redshifts from the results of application of redshift prediction model to testing subset. Each point is colour-coded following the colorbar. Grey, dashed line shows $x = y$ relation and purple, dot-dashed lines show the limits where outliers are defined (cf. Eqn. 3.22). Inset shows the distribution of Δz^N values from the points shown in main plot, with a $\langle \Delta z^N \rangle = 0.0442$.

4.4 Prediction from pipeline

The sequential combination of the models described in Sect. 3.6 defines the pipeline for the prediction of radio-detectable **AGN** and their redshift. As separate tasks, the pipeline was applied to the labelled sources in the **HETDEX** testing subset, to the labelled sources in **S82**, and to all unlabelled sources across both fields. In addition to that, **S82** provides a fully independent test of the pipeline as no data in this field was used for training the different models.

Metrics can be presented for each of the step in their sequential application. That implies obtaining, first, metrics for the selection between **AGN** and **SFGs**. Then, metrics for the application of the radio detection model to sources predicted to be **AGN** (independent of their

true class). And finally, metrics from the prediction of redshift values for predicted **AGN** that were also predicted to have radio detections. Such metrics are presented in Tables 4.1, 4.2, and 4.3 for the rows labelled as ‘pipe’. In these cases, results are mixed when comparing them with the individual metrics (i.e. with labels ‘test’ or ‘label’). It is important to note that, for the **AGN-SFG** classification, both analysed datasets are the same since this is the first step of the pipeline.

The metrics for the pipeline application of the radio-detection classification for the predicted **AGN** shows, when inspecting the mean values, a decrease (improvement) in all the metrics. But when considering the uncertainties, both values, from the individual application of the model and as part of the pipeline, are compatible. These results imply that no discernible change is found when using the pipeline. One possible explanation for this robustness in the metrics might be related to the good performance of the first step of the pipeline (**AGN-SFG** classification). As most of the sources used in the second step of the pipeline have been correctly classified in the previous stage, no considerable change in the parameter space has been applied and the radio detection classifier would deliver results of the same quality.

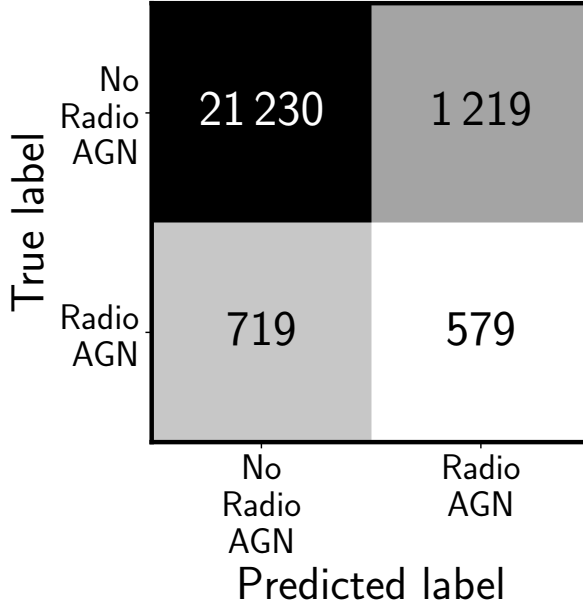
In the case of the redshift prediction, the use of the uncertainties lead to full compatibility between the metrics in the individual models (‘test’ or ‘label’) and those that are part of the pipeline (‘pipe-**PR**’) and the large uncertainties are to be blamed for these results. Attending to the low (when compared to the **AGN-SFG** model) metrics of the radio detection model, it is expected that results have large uncertainties given the, apparent, inability of the model to extract fully meaningful data for the classification and application to different datasets from the training subset. Regardless of their compatibility, if uncertainties are omitted and only the mean metrics are considered, different evolutions are seen in each metric and subset. For the sources in the **HETDEX** field, all metrics improve when using the structure of the pipeline, except the value of σ_z^N . When analysing the source in the **S82** field, all metrics worsen except the value of σ_z . As defined in Sect. 3.1.2, both σ_z and σ_z^N have a structure that is similar to obtaining mean values of a sample. Opposite to that, σ_{MAD} and σ_{NMAD} use the median values of the sample. Thus, the latter metrics are less affected by outliers, which might be the reason behind their distinct behaviour.

This degradation might be, then, understood by the fact that the pipeline is composed of three sequential models. Each additional step is fed with sources classified by the previous algorithm. And some of these sources might not be similar, in terms of features, to those used for training, thus adding noise to the output of such model.

Table 4.4: Results of application of radio **AGN** prediction pipeline to the labelled sources in the **HETDEX** and **S82** fields

Subset	Threshold	F_β ($\times 100$)	MCC ($\times 100$)	Precision ($\times 100$)	Recall ($\times 100$)
HETDEX-test	Naive	20.68 ± 3.17	24.93 ± 3.72	52.34 ± 6.56	13.79 ± 2.27
	PR	37.99 ± 2.59	33.66 ± 2.79	32.20 ± 2.72	44.61 ± 2.46
S82-label	Naive	24.08 ± 3.44	21.43 ± 3.53	25.44 ± 3.64	23.07 ± 3.72
	PR	19.42 ± 2.31	17.23 ± 3.08	11.33 ± 1.32	47.36 ± 6.22

^a Values and uncertainties as in Table 4.1.

Figure 4.4: Combined confusion matrix from the full radio-**AGN** detectability prediction computed using the testing subset from **HETDEX**. Description as in Fig. 4.1.

Additionally, both classification steps can be combined into one single stage (i.e. classification of radio-**AGN**), and metrics can be obtained accordingly. Their joint metrics are shown in Table 4.4 for the **HETDEX** test sample and the labelled sources in **S82**. Here, the differences between naive and **PR**-based results are varied, depending on the analysed score. Taking into account that our classifiers have been optimised for the recall values, it is expected that this value presents the best evolution when applying the **PR**-based thresholds, even at the expense of the remaining metrics. In this way, an improvement of 25 % to 30 % can be verified for the recall.

Figures 4.4 and 4.5 show the confusion matrices for the joint application of the radio-**AGN** prediction over the **HETDEX** and **S82** fields, respectively. The most relevant trait of both matrices is the very high imbalance between the two analysed classes (radio-**AGN** and non-radio-**AGN**). Taking into account the areas of both fields (Sects. 2.1 and 2.2), the density of both true and predicted radio-**AGN** is larger in the **S82** field.

On the other side, Figs. 4.6 and 4.7 show the contrast between the true and predicted

CHAPTER 4. PREDICTION OF RADIO-AGN CANDIDATES

		Predicted label	
		No Radio AGN	Radio AGN
True label	No Radio AGN	17 992	3 021
	Radio AGN	429	386

Figure 4.5: Combined confusion matrix from the full radio-AGN detectability prediction computed using the labelled sources from the S82 field. Description as in Fig. 4.1.

redshifts for the sources predicted to be radio-AGN in the HETDEX and S82 fields. As with the results of the individual application of the model (Fig. 4.3), there are two distinct behaviours in the studied sample at both sides of the $z_{\text{True}} \sim 1.0$ value. The sources with $z_{\text{True}} \lesssim 1.0$ will have their predicted redshift values equal or higher than the true value. Above that value, predictions can go in both directions, with a hint of general underprediction for both fields.

The application of the prediction pipeline to the unlabelled sources from the HETDEX field led to 9 974 990 predicted AGN, from which 68 252 were predicted to be radio detectable. The pipeline predicts, as well, 2 073 997 AGN in the unlabelled data from S82, being 22 445 of them candidates to be detected in the radio (to the detection level of LoTSS-DR1). The pipeline outputs for a small sample of the predicted radio AGN are presented in Tables B.4 and B.5 for HETDEX and S82 respectively, while the full tables are available, from Carvajal et al. (2023b), at <https://zenodo.org/doi/10.5281/zenodo.10220008>.

As a different graphical method to compare the predictions from our pipeline and those compiled previously in the literature, the normalised distribution of the predicted redshifts for radio-AGN in HETDEX and S82 is presented in Fig. 4.8. These histograms allow one to assess even predictions for sources that do not have a previous true value, as the analysis is focused on the distributions rather than the individual values.

Even though ML models do not explicitly aim to reproduce the distribution of training targets when predicting in a dataset, they can reproduce biases and hidden correlations ingrained

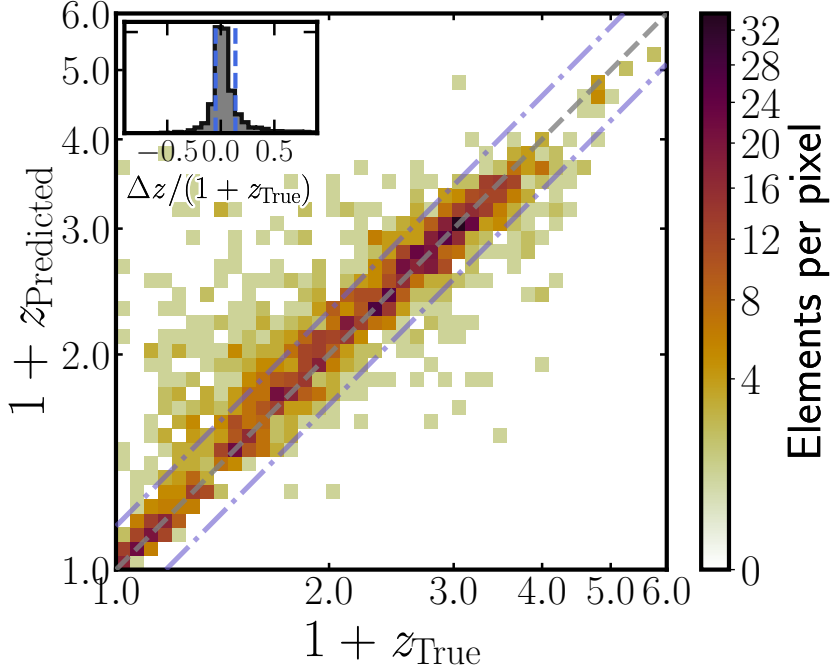


Figure 4.6: Density plot of comparison between original and predicted redshifts from the results of application of redshift prediction model to sources predicted to be radio-detectable AGN in the testing subset. Details as in Fig. 4.3.

in the original data (e.g. Du et al., 2021). While data preprocessing (cf. Sect. 2.6) aims to solve these issues (Kamiran and Calders, 2012), it is still possible to see, in Fig. 4.8, that the predicted redshifts, in both **HETDEX** and **S82** fields, have very similar distributions.

A different, and diverging, approach to explain the distributions in Fig. 4.8 assumes that the similarity between predicted redshifts is an indicator that the application of the model, in two separate fields, does not affect the quality of the predictions. The model has already obtain all the necessary connections between the measurements in the training sample and it has become robust to changes in the features. In this way, rather than a disadvantage, their resemblance can be taken as a good symptom of solid models.

4.5 No-skill classification

As presented in Sect. 3.1.1, Eqs. 3.7 to 3.10 show the base results for a classification with no skill. Table 4.5 presents the scores generated by using this procedure in sources of the **HETDEX** and **S82** fields. These values are the base from which any improvement, from a random selection, can be assessed.

Subsets and prediction modes displayed in Table 4.5 are the same as those exhibited in Tables 4.1, 4.2, and 4.4. For instance, in the test **HETDEX** sub-sample, $\sim 43\%$ of sources are

CHAPTER 4. PREDICTION OF RADIO-AGN CANDIDATES

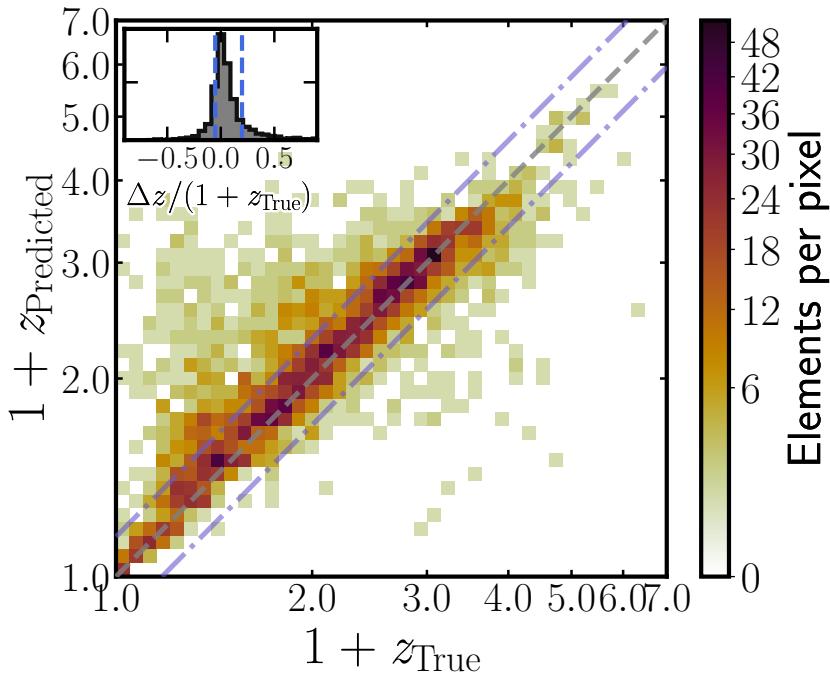


Figure 4.7: Density plot of comparison between original and predicted redshifts from the results of application of redshift prediction model to sources predicted to be radio-detectable **AGN** among labelled sources in the **S82** field. Details as in Fig. 4.3.

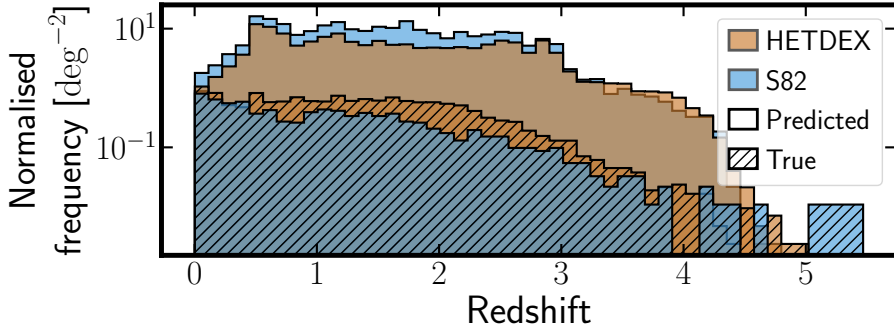


Figure 4.8: Redshift density distribution of the predicted radio-**AGN** within the unlabelled sources (clean histograms) in **HETDEX** (ochre histograms) and **S82** (blue histograms) and true redshifts from labelled radio-**AGN** (dashed histograms).

labelled as **AGN**. From all **AGN**, $\sim 13\%$ of them have radio detections. These percentages can be summarised stating that $\sim 6\%$ of all sources in the test sub-sample are radio-detected **AGN**.

Contrasting the results of Table 4.5 with those presented in Tables 4.1, 4.2, and 4.4 can give some insight into the level at which the trained models have learned the correlations and links between the used features. It is possible to see that all models present a very high improvement upon a random selection. With the exception of the **AGN-SFG** classification in the **S82** field, all instances show improvements of $\gtrsim 40\%$ in the recall values. Such relevant changes can hint that all models are, indeed, learning effectively about their tasks and the data underlying the classifications.

The case of the **AGN-SFG** classification in the **S82** field presents an interesting view on the

Table 4.5: Results of no-skill selection of sources in different stages of pipeline to the labelled sources in the [HETDEX](#) test subset and [S82](#) fields

Subset	Prediction	F_β ($\times 100$)	MCC ($\times 100$)	Precision ($\times 100$)	Recall ($\times 100$)
HETDEX	AGN-SFG	42.57	0.00	42.57	42.57
	Radio-detection (label)	12.84	0.00	12.84	12.84
	Radio AGN	5.47	0.00	5.47	5.47
S82	AGN-SFG	81.29	0.00	81.29	81.29
	Radio-detection (label)	4.59	0.00	4.59	4.59
	Radio AGN	3.73	0.00	3.73	3.73

^a All metrics have been multiplied by 100.

quality of the models. Even though [S82](#) has a better base upon which improve for a classification between [AGN](#) and [SFGs](#), the trained model does not take the metrics further than that in the [HETDEX](#) field. This behaviour might indicate that the model has already extracted all needed information and there is no room for over-fitting or other training issues.

This page intentionally left blank.

Analysis of prediction method and results

5.1 Comparison with previous works

In this section, we provide a few examples of related published works as well as plausible explanations for observed discrepancies with our results when these are present. This comparison attempts to be representative of the literature on the subject but does not intend to be complete in any way.

5.1.1 AGN detection prediction

In order to understand the significance of our results and ways for future improvement, we separate the comparison with previous works in two parts. First, we present previously published results from traditional methodologies. In second place, we offer a comparison with [ML](#) methods.

As presented in Sect. 1.1.1, traditional [AGN](#) selection methods are based on the comparison of the measured [SED](#) photometry to a template library (Walcher et al., 2011). A recent example of its application is presented by Thorne et al. (2022b), where best-fit classifications were calculated for more than 700 000 galaxies in the [D10](#) field of the Deep Extragalactic VIable Legacy Survey ([DEVILS](#); Davies et al., 2018a) and the [Galaxy and Mass Assembly](#) ([GAMA](#); Driver et al., 2011; Liske et al., 2015) fields. The 91 % recovery rate of [AGN](#), selected through various means (X-ray measurements, narrow and broad emission lines, and [MIR](#) colours), is very much in line with our findings in [S82](#), where our rate (recall) reaches 89 %, setting a baseline from which our results can be properly assessed.

Traditional methods also encompass the colour-based selection of [AGN](#). While less precise, they provide access to a much larger base of candidates with a very low computational cost. We implemented some of the most common colour criteria on the data from [S82](#). Of particular interest is the predicting power of the [MIR](#) colour selection due to its potential to detect hidden or heavily obscured [AGN](#) activity.

CHAPTER 5. ANALYSIS OF PREDICTION METHOD AND RESULTS

Based on *WISE* data, Stern et al. (2012: hereafter S12) proposed a threshold at $W1 - W2 \geq 0.8$ to separate **AGN** from non-AGN using data from **AGN** in the **COSMOS** field. A more stringent criterion was developed by Mateos et al. (2012: hereafter M12), the **AGN** wedge, which can be defined by the sources located inside the region defined by the relations $W1 - W2 < 0.315 \times (W2 - W3) + 0.791$, $W1 - W2 > 0.315 \times (W2 - W3) - 0.222$, and $W1 - W2 > -3.172 \times (W2 - W3) + 7.624$. In order to define this wedge, they used data from X-ray selected **AGN** over an area of 44.43 deg^2 in the northern sky. Mingo et al. (2016: hereafter M16) cross-correlated data from *WISE* observations with X-ray and radio surveys creating a sample of **SFGs** and **AGN** in the northern sky. They developed individual relations to separate classes of **SFGs** and **AGN** in the $W1 - W2$, $W2 - W3$ space and, for **AGN** the criterion, the relation is $W1 - W2 \geq 0.5$ and $W2 - W3 < 4.4$. More recently, Blecha et al. (2018: hereafter B18) analysed the quality of **MIR** colour selection methods for the identification of obscured **AGN** involved in mergers. Using hydrodynamic simulations for the evolution of **AGN** in galaxy mergers, they developed a selection criterion from *WISE* colours which is shown to be able to separate, with high reliability, starburst galaxies from **AGN**. The expressions have the form $W1 - W2 > 0.5$, $W2 - W3 > 2.2$, and $W1 - W2 > 2 \times (W2 - W3) - 8.9$.

The results from the application of these criteria to our samples in the testing subset and in the labelled sources of **S82** field are summarised in Table 5.1 and a graphical representation of the boundaries they create in their respective parameter spaces is presented in Fig. 5.1. Table 5.1 shows that previous colour-colour criteria have been designed and calibrated to have very high precision values. Thus, most of the sources deemed to be **AGN** by them are, indeed, of such class. Despite being tuned to maximise their recall (and F_β to a lesser extent), our classifier still shows precision values compatible with those of such criteria. This result underlines the power of **ML** methods. They can be on a par with traditional colour-colour criteria and excel in additional metrics.

Figure 5.1 is constructed as a confusion matrix, plotting in each quadrant the whole *WISE* population in the background and in colour contours the corresponding fraction of the testing set (**TP**, **TN**, **FP**, and **FN**, see Fig. 4.1 and Sect. 3.1.1). As expected, our pipeline is able to separate with high confidence sources which are closer to the **AGN** or the **SFG** locus (**TP** and **TN**) while sources in the **FN** and **FP** quadrant show a different situation. **AGN** predicted to be **SFGs** (**FN**, 1.6 % of sources for **HETDEX**, and 4.9 % for **S82**) are located in the **SFG** region of the colour-colour diagram. On the opposite corner of the plot, **SFGs** predicted to be **AGN** (**FP**, 2.4 % of sources for **HETDEX**, and 4.2 % for **S82**) cover the areas of **AGN** and **SFGs** uniformly.

Table 5.1: Results of application of several **AGN** detection criteria to our testing subset and the labelled sources from the **S82** field. Last row includes results from the first step of our prediction pipeline as presented in Table 4.1.

Method	HETDEX test set			
	F_β ($\times 100$)	MCC ($\times 100$)	Precision ($\times 100$)	Recall ($\times 100$)
S12	86.10	78.78	93.98	80.51
M12	51.80	49.71	98.87	37.18
M16	67.21	61.30	97.48	53.48
B18	82.14	75.76	97.54	72.66
Our pipeline	95.42	91.85	94.49	96.21
Method	S82 (labelled)			
	F_β ($\times 100$)	MCC ($\times 100$)	Precision ($\times 100$)	Recall ($\times 100$)
S12	83.59	45.47	93.93	76.62
M12	46.80	28.22	99.59	32.54
M16	64.69	37.76	98.80	50.32
B18	79.71	51.07	98.72	68.77
Our pipeline	94.37	70.67	94.81	94.01

^a Naming codes for the used methods are described in the main text (cf. Sect. 5.1.1)

^b All metrics have been multiplied by 100.

FN sources might be sources that are identified as **AGN** by means not included in our feature set (e.g. X-ray, radio emission). Sources in **FP** quadrant, alternatively, might be **SFGs** with extreme properties, similar to **AGN**.

For the case of **ML**-based models for **AGN-SFG** classification, several analyses have been published in recent years. An example of their application is provided in Clarke et al. (2020) where a **RF** model for the classification of stars, **SFGs** and **AGN** was trained using photometric data from more than 3 000 000 sources in the **SDSS** (DR15; Aguado et al., 2019) and **WISE** with associated spectroscopic observations. Close to 400 000 sources have a **QSO** spectroscopic label and, from the application of their model to a validation subset, they obtain a recall of 0.929 and **F1**-score of 0.943 for the **QSO** classification. These scores are of the same order as those obtained when applying our **AGN-SFG** model to the testing set (see Table 4.1). Thus, and despite using an order of magnitude fewer sources for the full training and validation process, our model can achieve equivalently good scores. Such difference in the number of training source can underline the fact that our models are able to extract, effectively, information for the connection between features and targets.

Expanding on the results from Clarke et al. (2020), Cunha and Humphrey (2022) built

CHAPTER 5. ANALYSIS OF PREDICTION METHOD AND RESULTS

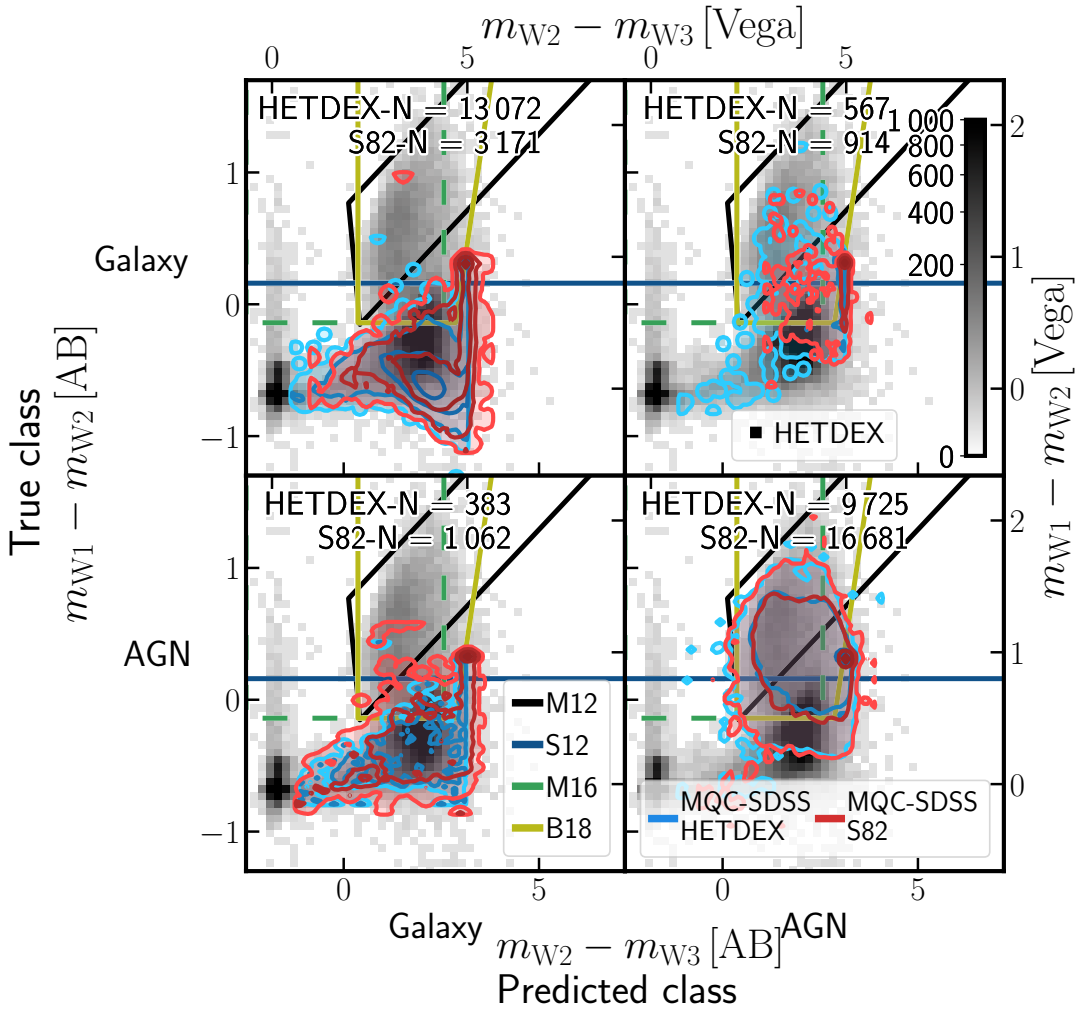


Figure 5.1: $W_1 - W_2$, $W_2 - W_3$ colour-colour diagrams for sources in the testing subset, from [HETDEX](#), and labelled sources from [S82](#) given their position in the [AGN-SFG](#) confusion matrix (see, for [HETDEX](#), Fig. 4.4 and, for [S82](#), Fig. 4.5). In the background, density plot of all [CW](#)-detected sources in the full [HETDEX](#) field sample is displayed. Colour of each square represents the number of sources in that position of parameter space, with darker squares having more sources (as defined in the colorbar of the upper-right panel). Contours represent distribution of sources for each of the aforementioned subsets at 1, 2, 3 and 4 σ levels (shades of blue, for testing set and shades of red for labelled [S82](#) sources). Coloured, solid lines display limits from the criteria for the detection of [AGN](#) described in Sect. 5.1.1.

an [ML](#) pipeline, [SHEEP](#), for the classification of sources into stars, [SFGs](#) and [QSO](#). In contrast to Clarke et al. (2020) or the pipeline described in this thesis, the first step in their analysis is the redshift prediction, which is used as part of the training features by the subsequent classifiers. They extracted [WISE](#) and [SDSS Data Release 15](#) (SDSS-DR15; Aguado et al., 2019) photometric data for almost 3 500 000 sources classified as stars, [SFGs](#) or [QSO](#). The application of their pipeline to sources predicted to be [QSO](#) led to a recall of 0.960 and an [F1](#) score of 0.967. The improved scores in their pipeline might be a consequence not only of the slightly larger pool of sources, but also the inclusion of the coordinates of the sources (right ascension, declination) and the predicted redshift values as features in the training that might hint hidden correlations between sources that are, for instance, located in similar regions of the sky (i.e. with comparable

line-of-sight properties).

A test with a larger number of **ML** methods was performed by Poliszczuk et al. (2021). For training, they used optical and infrared data from close to 1500 sources (**SFGs** and **AGN**) located at the AKARI **North Ecliptic Pole (NEP)** Wide-field (Lee et al., 2009; Kim et al., 2012) covering a 5.4 deg^2 area. They tested **linear regression (LR)**, **SVM**, **RF**, **ET**, and **XGBoost** including the possibility of generalised stacking. In general, they obtained results with **F1**-scores between $0.60 - 0.70$ and recall values in the range of $50\% - 80\%$. These values, lower than the works described here, can be fully understood given the small size of the training sample and the studied area. A larger photometric sample covers a wider range of the parameter space which significantly helps the metrics of any given model.

5.1.2 Radio detection prediction

We have not found in the literature any work attempting the prediction of **AGN** radio detection at any level and therefore this is, to the best of our knowledge, the first attempt at doing so. In the literature we do find several correlations between the **AGN** radio emission (flux) and that at other wavelengths (e.g. with **IR** emission, Helou et al., 1985; Condon, 1992) and substantial effort has been done towards classifying radio galaxies based upon their morphology (e.g. Aniyam and Thorat, 2017; Wu et al., 2019; **Fanaroff-Riley class I (FRI)**, **Fanaroff-Riley class II (FRII)**, bent jets, etc.) and its connection to environment (Miley and De Breuck, 2008; Magliocchetti, 2022). None of these extensive works has directly focused on the a priori presence or absence of radio emission above a certain threshold. Therefore, the results presented here are the first attempt at such an effort.

The $\sim 2x$ success rate of the pipeline to identify radio emission in **AGN** ($\sim 44.61\%$ recall and $\sim 32.20\%$ precision; see Table 4.4) with the respect to a 'no-skill' or random ($\lesssim 30\%$) selection, provides the opportunity to understand what the model has learned from the data and, therefore, gain some insight into the nature or triggering mechanisms of the radio emission.

5.1.3 Redshift prediction

We compare our results to that of Ananna et al. (2017: hereafter Stripe 82X) where the authors analysed multi-wavelength data from more than 6100 X-ray detected **AGN** from the 31.3 deg^2 of the Stripe 82X survey. They obtained photometric redshifts for almost 6000 of these sources using the template-based fitting code LePhare (Arnouts et al., 1999; Ilbert et al., 2006).

CHAPTER 5. ANALYSIS OF PREDICTION METHOD AND RESULTS

Their results present a normalised median absolute deviation of $\sigma_{\text{NMAD}} = 0.062$ and an outlier fraction of $\eta = 13.69 \%$, values which are similar to our results in [HETDEX](#) and [S82](#) except for a better outlier fraction (as shown in Table 4.3, we obtain $\eta_{\text{S82}} = 25.18 \%$, $\sigma_{\text{NMAD}}^{\text{HETDEX}} = 0.071$, and $\eta^{\text{HETDEX}} = 18.9 \%$). Such results reinforce the use of [ML](#) methods, and in particular our pipeline, for the estimation of photometric redshifts of radio-detectable [AGN](#).

On the [ML](#) side, we compare our results to those produced by Carvajal et al. (2021) in [S82](#), with $\sigma_{\text{NMAD}} = 0.1197$ and $\eta = 29.72 \%$, and find that our redshift prediction model improves by at least 25 % for any given metric. The source of improvement is probably many-fold. First, it might be related to the different sets of features used (colours vs ratios) and second, the more specific population of radio-[AGN](#) used to train our models. Carvajal et al. (2021) used a limited set of colours to train their model, while we have allowed the use of all available combinations of magnitudes (Sect. 2.5). Additionally, their redshift model was trained on all available [AGN](#) in [HETDEX](#), while we have trained (and tested) it only with radio-detected [AGN](#). Using a more constrained sample reduces the likelihood of handling sources that are too different in the parameter space.

Another example of the use of [ML](#) for [AGN](#) redshift prediction has been presented by Luken et al. (2019). They studied the use of the [k-nearest neighbours \(KNN; Cover and Hart, 1967\)](#) algorithm, a non-parametric supervised learning approach, to derive redshift values for radio-detectable sources. They combined 1.4 GHz radio measurements, infrared, and optical photometry in the [European Large Area ISO Survey-South 1 \(ELAIS-S1; Oliver et al., 2000\)](#) and [extended Chandra Deep Field South \(eCDFS; Lehmer et al., 2005\)](#) fields, matching their sensitivities and depths to the expected values in the [Evolutionary Map of the Universe \(EMU; Norris et al., 2011\)](#) field. From the different experiments they run, their resulting [NMAD](#) values are in the range $\sigma_{\text{NMAD}} = 0.05$ to 0.06 , and their outlier fraction can be found between $\eta = 7.35 \%$ and $\eta = 13.88 \%$. As an extension to the previous results, Luken et al. (2022) analysed multi-wavelength data from radio-detected sources the [eCDFS](#) and the [ELAIS-S1](#) fields. Using [KNN](#) and [RF](#) methods to predict the redshifts of more than 1300 [RGs](#), they have developed regression methods that show [NMAD](#) values between $\sigma_{\text{NMAD}} = 0.03$ and $\sigma_{\text{NMAD}} = 0.06$, $\sigma_z = 0.10$ to 0.19 , and outlier fractions of $\eta = 6.36 \%$ and $\eta = 12.75 \%$. Their results are, in general, one order of magnitude better than our metrics for the redshift prediction. One of the reasons for the dissimilarity might be based upon the different set of measurements used by Luken et al. (2022). In particular, they have used measurements from *Spitzer* rather than from WISE, having access to different regions of the [SEDs](#) of [RGs](#).

In addition to the previous work, Norris et al. (2019) compared a number of methodologies, mostly related with **ML** but also LePhare, for predicting redshift values for radio sources. They have used more than 45 photometric measurements (including 1.4 GHz fluxes) from different surveys in the **COSMOS** field. From several settings of features, sensitivities, and parameters, they retrieved redshift predictions with **NMAD** values between $\sigma_{\text{NMAD}} = 0.054$ and $\sigma_{\text{NMAD}} = 0.48$ and outlier fractions that range between $\eta = 7\%$ and $\eta = 80\%$. The broad span of obtained values might be due to the combinations of properties for each individual training set (including the use of radio or X-ray measurements, the selection depth, and others) and to the size of these sets, which was small for **ML** purposes (less than 400 sources). The slightly better results can be understood given the heavily populated photometric data available in **COSMOS**.

Specifically related to the **HETDEX** field, it is possible to compare our results to those from Duncan et al. (2019). They used a hybrid photometric redshift approach combining traditional template fitting redshift determination (Brammer et al., 2008; Salvato et al., 2018; Salvato et al., 2011; Brown et al., 2014) and **ML**-based methods. In particular, they implemented a **GP** algorithm (GPz; Almosallam et al., 2016b; Almosallam et al., 2016a), which is able to model both the intrinsic noise and the uncertainties of the training features. Their redshift prediction analysis of **AGN** with a spectroscopic redshift detected in the **LoTSS-DR1** (6.811 sources) found a **NMAD** value of $\sigma_{\text{NMAD}} = 0.102$ and an outlier fraction of $\eta = 26.6\%$. The differences between these results and those obtained from the application of our models (individually and as part of the prediction pipeline) might be due to the differences in the creation of the training sets. Duncan et al. (2019) used information from all available sources in the **HETDEX** field for training the redshift **GP** whilst our redshift model has been only trained on radio-detected **AGN**, giving it the opportunity to focus its parameter exploration only on these sources.

Finally, Cunha and Humphrey (2022) also produced photometric redshift predictions for almost 3 500 000 sources (stars, **SFGs**, and **QSO**) as part of their pipeline (see Sect. 5.1.1). They combined three algorithms for their predictions: **XGBoost**, **CatBoost**, and **Light Gradient Boosting Machine** (**LightBGM**; Ke et al., 2017). This procedure leads to $\sigma_{\text{NMAD}} = 0.018$ and $\eta = 2\%$. As with previous examples, the differences with our results can be a consequence of the number of training samples. Also, in the case of Cunha and Humphrey (2022), they applied an additional post-processing step to the redshift predictions attempting to predict and understand the appearance of catastrophic outliers.

5.2 Influence of data imputation

One effect which might influence the training of the models and, consequently, the prediction for new sources is related to the imputation of missing values (cf. Sect. 2.4 and the work by Curran, 2022; Curran et al., 2022). In Fig. 5.2, we have plotted the distributions of predicted scores (for classification models) and predicted redshift values as a function of the number of measured bands (`band_num`) for each step of the pipeline as applied to sources predicted to be of each class in the test subset.

The top panel of Fig. 5.2 shows the influence of the degree of imputation in the classification between **AGN** and **SFGs**. For most of the bins, probabilities for predicted **SFGs** are distributed close to 0.0, without any noticeable trend, implying a low impact of the imputation and robustness of the predictions. In the case of predicted **AGN**, the combination of low number of sources in some bins and high degree of imputation (`band_num < 5`) lead to low mean probabilities. Only from analysing the plot, it is possible to state that studied sources might have between 5 and 9 proper measurements (i.e. 3 to 7 missing entries) and, still, have reliable **AGN** predictions.

The case of radio detection classification is somewhat different. Given the number and distribution of sources per bin, it is not possible to extract any strong trend for the probabilities of radio-predicted sources. The absence of evolution with the number of observed bands is stronger for sources predicted to be devoid of radio detection. This lack of strong probabilities, combined with the previous analyses of the radio detection model, can be translated into the low metrics found for this classifier.

Finally, a stronger effect can be seen with the evolution of predicted redshift values for radio-detectable **AGN**. Despite the lower number of available sources, it is possible to recognise that sources with higher number of available measurements are predicted to have lower redshift values. Sources that are closer to us have, then, higher chances to be detected in a large number of bands. Thus, it is expected that our model predicts lower redshift values for the sources with the largest number of measurements in the field. Apart from being a data-based correlation, the behaviour seen between the number of measurements and the predicted redshift has its foundations in the physical connection between distance from a source and measured fluxes.

One interesting feature of all panels in Fig. 5.2 is the lack of sources with `band_num = 11`. This effect might be caused by the inclusion of measurements from **2M**. As seen in Fig. 2.3, all three **2M** bands have the highest (and almost the same) number of missing measurements. Thus, it is possible to infer that the inclusion of a measurement in one of the **2M** bands will imply the

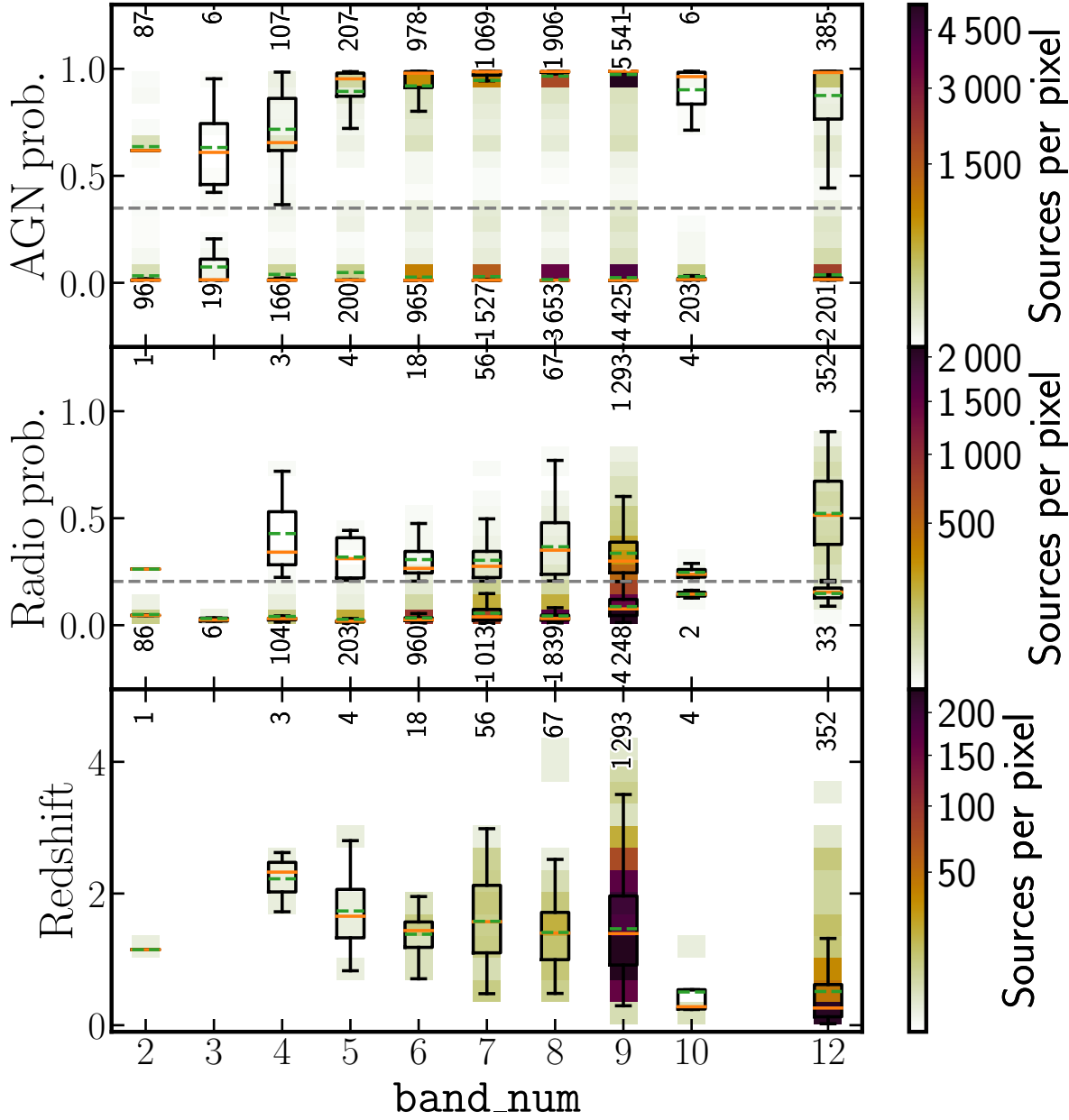


Figure 5.2: Evolution of predicted probabilities (top: probability to be **AGN**, middle: probability of **AGN** to be radio-detected) and redshift values for radio-detectable **AGN** (bottom panel) as function of number of observed bands for sources in test set. In top panel, sources have been divided between those predicted to be **AGN** and **SFGs**. In middle panel, sources are divided between predicted **AGN** that are predicted to be radio-detected and those predicted to not have radio detection. Background density plots (following colour coding in colorbars) show location of predicted values. Overlaid boxplots display main statistics for each number of measured bands. Black rectangles encompass sources in second and third quartiles. Vertical lines show place of sources from first and fourth quartiles. Orange lines represent median value of sample and dashed, green lines indicate their mean values. Dashed, grey lines show PR thresholds for **AGN-SFG** and radio detection classifications. Close to each boxplot, written values correspond to number of sources considered to create each set of statistics.

CHAPTER 5. ANALYSIS OF PREDICTION METHOD AND RESULTS

addition, almost always, of the two remaining bands.

In consequence, Fig. 5.2 allows us to understand the influence of imputation over the predictions. The most highly affected quantity is the redshift, where large fractions of measured magnitudes are needed to obtain scores that are in line with previous results (cf. Sect. 5.1.3). The AGN-SFG and radio detection classifications show a mild influence of imputation in their results.

5.3 Global feature importances

Following the description of Sect. 1.3.3, all algorithms selected in this work (RF, CatBoost, XGBoost, ET, GBR, and GBC) belong to the DT class. Thus, it is a simple task to obtain their global feature importances. Table 5.2 presents the ranked combined importances from the observables selected in each of the three sequential models that compose the pipeline. They have been combined using the importances from the meta-learner (as shown in Table 5.3) and that of base-learners. The derived importances will be dependent on the dataset used, including any imputation for the missing data, and the details of the models, that is, algorithms used and stacking procedure. We first notice in Table 5.2 that the order of the features is different for all three models. This difference reinforces the need, as stated in Chapter 4, of developing separate models for each of the prediction stages of this work that would evaluate the best feature weights for the related classification or regression task.

For the AGN-SFG classification model, it is very interesting to note that the most important feature for the predicted probability of a source to be an AGN is the WISE colour W1 - W2 (as well as W1 - W3). This colour is indeed one of the axes of the widely used WISE colour-colour selection, with the second axis being the W2 - W3 colour (cf. Sect 5.1.1). The WISE W3 photometry is though significantly less sensitive than W1, W2 or PS1 (see Fig. 2.5) and a significant number of sources will be represented as upper limits in such plot (see Table 2.3).

One of the main potential uses of the pipeline is its capability to identify radio-detectable AGN. The global features analysis for the radio detection model shows a high dependence on the near- and mid-IR magnitudes and colours, especially those coming from WISE. As a useful outcome similar to the AGN-SFG classification, we can use the most relevant features to build diagnostic diagrams for the pre-selection of these sources and get insight into the origin of the radio emission. This is the case for the W4 histogram, shown in Fig. 5.3, where sources predicted to be radio-emitting AGN extend to brighter measured W4 magnitudes. This added

Table 5.2: Relative importances (rescaled to add to 100) for observed features from the three models combined between meta and base models.

AGN-SFG (meta-model: CatBoost)					
Feature	Importance	Feature	Importance	Feature	Importance
W1_W2	68.945	H_K	1.715	z_W2	1.026
W1_W3	4.753	y_W1	1.659	z_y	0.722
g_r	4.040	y_W2	1.513	W3_W4	0.669
r_J	4.006	i_y	1.441	W4mag	0.558
r_i	3.780	i_z	1.366	H_W3	0.408
band_num	1.842	y_J	1.187	J_H	0.371
Radio detection (meta-model: GBC)					
Feature	Importance	Feature	Importance	Feature	Importance
W2_W3	9.609	y_W1	7.150	W4mag	4.759
y_J	8.102	g_r	7.123	K_W4	2.280
W1_W2	8.010	z_W1	7.076	J_H	1.283
g_i	7.446	r_z	6.981	H_K	1.030
K_W3	7.357	i_z	6.867	band_num	1.018
z_y	7.321	r_i	6.588		
Redshift prediction (meta-model: ET)					
Feature	Importance	Feature	Importance	Feature	Importance
y_W1	35.572	y_J	3.018	i_z	1.215
W1_W2	13.526	r_z	3.000	J_H	1.162
W2_W3	12.608	r_i	2.896	g_W3	1.000
band_number	6.358	z_y	2.827	K_W3	0.925
H_K	4.984	W4mag	2.784	K_W4	0.762
g_r	4.954	i_y	2.408		

^a Relative feature importance values are specific to each model training and cannot be compared, numerically, to the values obtained in a different model. A meaningful comparison can be done by contrasting the order in which features are sorted.

MIR flux might be simply due to an increased SFRs in these sources. In fact the 24 μm flux is often used, together with that of H α as a proxy for SFR (Kennicutt et al., 2009). The radio detection for these sources might have a strong component linked to the ongoing SF, especially for the sources with real or predicted redshift below $z \sim 1.5$.

Finally, the redshift prediction model shows that the final estimate is mostly driven by the results of the base learners, accounting for $\sim 82\%$ of the predicting power. The overall combined importance of features shows also in this case a strong dependence on several NIR colours of which y - W1 and W1 - W2 are the most relevant ones (these colours have also been highlighted in previous ML redshift determinations, such as Kunsági-Máté et al., 2022). The model still relies, to a lesser extent, on a broad range of optical features needed to trace the broad

CHAPTER 5. ANALYSIS OF PREDICTION METHOD AND RESULTS

Table 5.3: Relative feature importances (rescaled to add to 100) for base algorithms in each prediction step.

AGN-SFG model (CatBoost)			
Feature	Importance	Feature	Importance
gbc	49.709	xgboost	14.046
et	19.403	rf	8.981
Remaining feature importances:			7.861
Radio detection model (GBC)			
Feature	Importance	Feature	Importance
rf	12.024	catboost	7.137
et	7.154	xgboost	6.604
Remaining importances:			67.081
Redshift prediction model (ET)			
Feature	Importance	Feature	Importance
xgboost	25.138	catboost	21.072
gbr	21.864	rf	13.709
Remaining importances:			18.217

^a Relative feature importance values are specific to each model training and cannot be compared, numerically, to the values obtained in a different model. A meaningful comparison can be done by contrasting the order in which features are sorted.

range of redshift possibilities ($z \in [0, 6]$, the base of our training sample).

5.4 Local feature importances

The combination of Shapley values with several other model explanation methods was used by Lundberg and Lee (2017) to create the **SHAP** values, which are a more computationally efficient way to calculate Shapley values for **ML**. In this work, **SHAP** values were calculated using the python package **SHAP**¹ and, in particular, its module for tree-based predictors (Lundberg et al., 2020). To speed calculations up, the package **FastTreeSHAP**² (v0.1.2; Yang, 2021) was also used, which allows the user to run multi-thread computations.

One graphical way to display these **SHAP** values is through the so-called decision plots. They can show how individual predictions are driven by the inclusion of each feature. Besides determining the most relevant properties that help the model make a decision, it is possible to detect sources that follow different prediction paths which could be, eventually and upon further examination, labelled as outliers. An example of this decision plot, linked to the

¹<https://github.com/slundberg/shap>

²<https://github.com/linkedin/fasttreeshap>

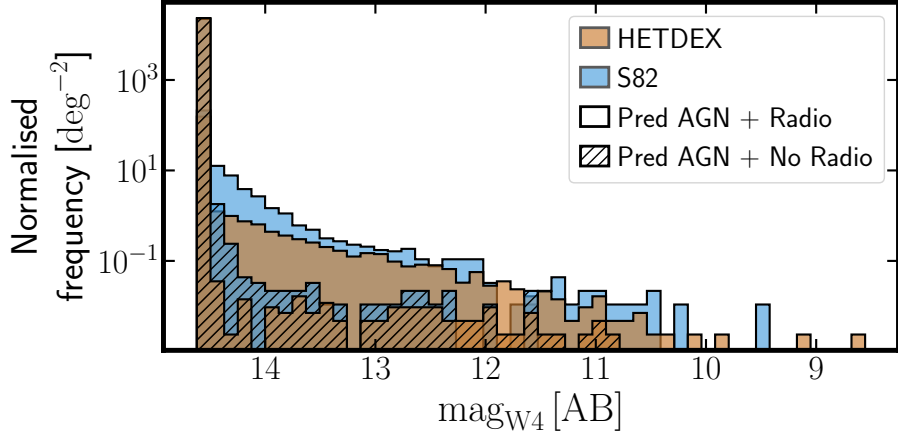


Figure 5.3: W4 magnitudes density distribution of the newly predicted radio-[AGN](#) (clean histograms) in [HETDEX](#) (ochre histograms) and [S82](#) (blue histograms) and W4 magnitudes from predicted [AGN](#) that are predicted to not have radio detection (dashed histograms).

[AGN-SFG](#) classification, is shown in Fig. 5.4 for a subsample of the high-redshift ($z \geq 4.0$) spectroscopically classified [AGN](#) in the [HETDEX](#) field (121 sources, regardless of them being part of any subset involved in the training or validation of the models). The different features used by the meta-learner are stacked on the vertical axis with increasing weight and these final weight are summarised in Table 5.4. Similarly, [SHAP](#) decision plots for the radio-detection and redshift prediction are presented in Figs. 5.5 and 5.6, respectively. A thin trace of predictions (i.e. the set of lines as evolving through features) is a sign that the displayed sources have very similar values of the features involved (e.g. bottom features in Fig. 5.4). Once the lines flare out, the model shows that the studied sources occupy a wider region on the parameter space for these features and it is easier to differentiate them for classification (or regression) purposes.

As it can be seen, for the three models, base learners are amongst the features with the highest influence. This result raises the question of what drives these individual base predictions. Figs. 5.7, 5.8, and 5.9 show [SHAP](#) decision plots for all base learners used in this work. Additionally, and to be able to compare these results with the features importances from Sect. 5.3, we constructed Table 5.5, which displays the combined [SHAP](#) values of base and meta learners but, in this case, for the same 121 high-redshift confirmed [AGN](#) (with 29 of them detected by [LoTSS](#)). Table 5.5 shows, as Table 5.2, that the colour W1 - W2 is the most important discriminator between [AGN](#) and [SFGs](#) for this specific set of sources. The importance of the rest of the features is mixed: similar colours are located on the top spots (e.g. g - r, W1 - W3 or r - i). When comparing these results with those obtained with global feature importances (Sect. 5.3), it is possible to see that both methods present W1 - W2 as the most relevant feature. But, the values of the importances vary by a factor of two. This difference might point to the

CHAPTER 5. ANALYSIS OF PREDICTION METHOD AND RESULTS

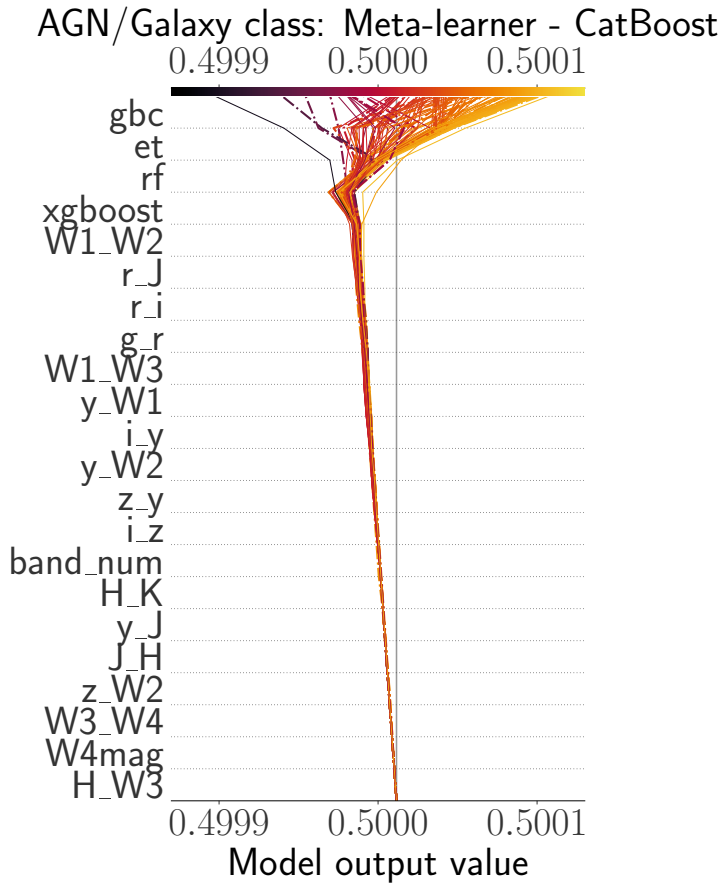


Figure 5.4: Decision plot from SHAP values for AGN-SFG classification from the 121 high redshift ($z \geq 4$) spectroscopically confirmed AGN in HETDEX. Horizontal axis represents the model’s output with a starting value for each source centred on the selected naive threshold for classification. Vertical axis shows features used in the model sorted, from top to bottom, by decreasing mean absolute SHAP value. Each prediction is represented by a coloured line corresponding to its final predicted value as shown by the colorbar at the top. Moving from the bottom of the plot to the top, SHAP values for each feature are added to the previous value in order to highlight how each feature contributes to the overall prediction. Predictions for sources detected by LOFAR are highlighted with a dotted, dashed line.

fact that analysing only high-redshift sources can be harder for the model as it needs a higher input from the remaining features. One additional attribute of the meta AGN-SFG is the range in which the predictions are located. This issue is reflected in the narrow decision margin for the non-calibrated stacked model (see model output values –x-axis– close to ~ 0.5 in Fig. 5.6 and Sect. 3.6.2).

For the radio classification step of the pipeline, we find that features linked to those 121 high- z AGN perform at the same level as for the overall population (as shown by the global feature importances). As introduced in Sect. 4.2, radio-detection model shows difficulties when producing a classification based on the provided dataset. The improved metrics with respect to those obtained from the no-skill selection do indicate that the model has learned some connections between the data and the radio emission. Feature importance has changed when compared to the overall population. If the radio emission observed from these sources were

Table 5.4: **SHAP** values (rescaled to add to 100) for base algorithms in each prediction step for observed features using 121 spectroscopically confirmed **AGN** at high redshift values ($z > 4$).

AGN-SFG model (CatBoost)			
Feature	SHAP value	Feature	SHAP value
gbc	36.250	rf	21.835
et	30.034	xgboost	7.198
Remaining SHAP values:			4.683
Radio detection model (GBC)			
Feature	SHAP value	Feature	SHAP value
rf	11.423	catboost	5.696
xgboost	7.741	et	5.115
Remaining SHAP values:			70.025
Redshift prediction model (ET)			
Feature	SHAP value	Feature	SHAP value
xgboost	41.191	gbr	13.106
catboost	20.297	rf	11.648
Remaining SHAP values:			13.758

^a **SHAP** values are specific to each model training and cannot be compared, numerically, to the values obtained in a different model and with different data. A meaningful comparison can be done by contrasting the order in which features are sorted.

exclusively due to **SF**, this connection would imply **SFR** of several hundred $M_{\odot} \text{ yr}^{-1}$. This explanation can not be completely ruled out from the model side but some contribution of radio emission from the **AGN** is expected.

For the redshift prediction model, Fig. 5.6 shows that, apart from the base models, W1 - W2 and g - r, are the most relevant, individual features. When combinining results from each base model, and as given by Table 5.5, g - r keeps its position as the most influential feature, followed, closely, by y - W1 and W2 - W3.

Analysing the decision plots from each individual base model can give additional insight into the behaviour of single sources and how they relate with the rest of the selected sample (in this case, sources with $z \geq 4.0$). Base **AGN-SFG** classifiers (in Fig. 5.7) show a plethora of different behaviours. Initially, and in contrast with the decision plot from the meta learner, deviations from the bulk of the predictions start much lower in the list of features. This difference might imply that individual models need to rely on more observations than the meta model, which has that information encoded in each of the features from the base classifiers. Additionally, it is possible to see that some predictions change drastically when arriving to the last feature (in this case, W1 - W2). Such changes highlight the importance of W1 - W2 as a decisive feature.

CHAPTER 5. ANALYSIS OF PREDICTION METHOD AND RESULTS

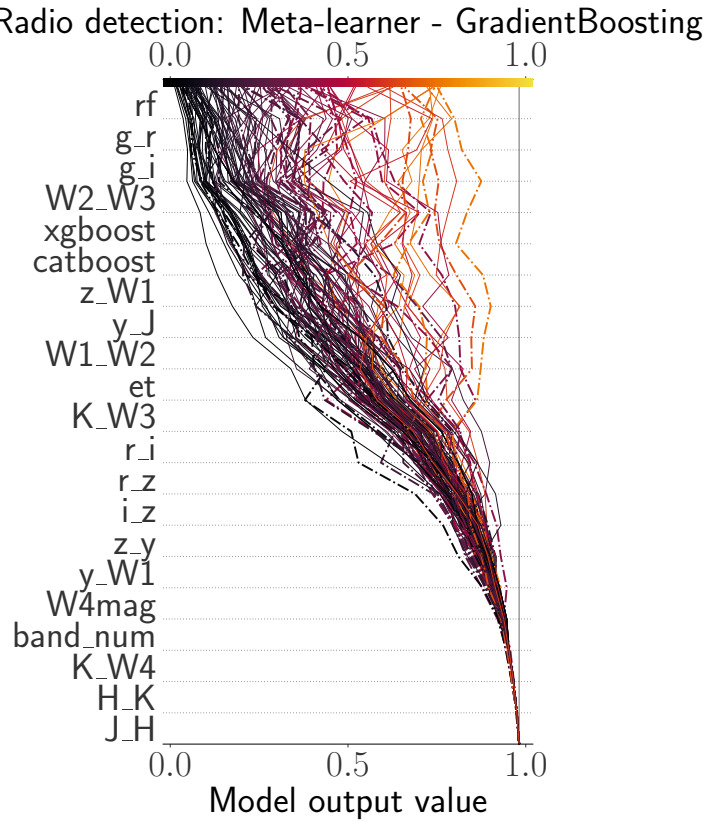


Figure 5.5: Decision plot from the SHAP values for all features from the radio detection model in the 121 high redshift ($z \geq 4$) spectroscopically confirmed AGN from HETDEX. Description as in Fig. 5.4.

Similarly, Fig. 5.8 shows the decision plots for the individual radio detection base learners. In this case, most predictions arrive in the leftmost zone of the final scores, showing that base models struggle with deciding when a source could be detected in the radio.

For the redshift predictions in Fig. 5.9, most sources follow a similar prediction path. As the analysed sources have, originally, high redshift values, their predicted values tend to be in the same range. Such behaviour is an indication of the good predicting power of all base regressors.

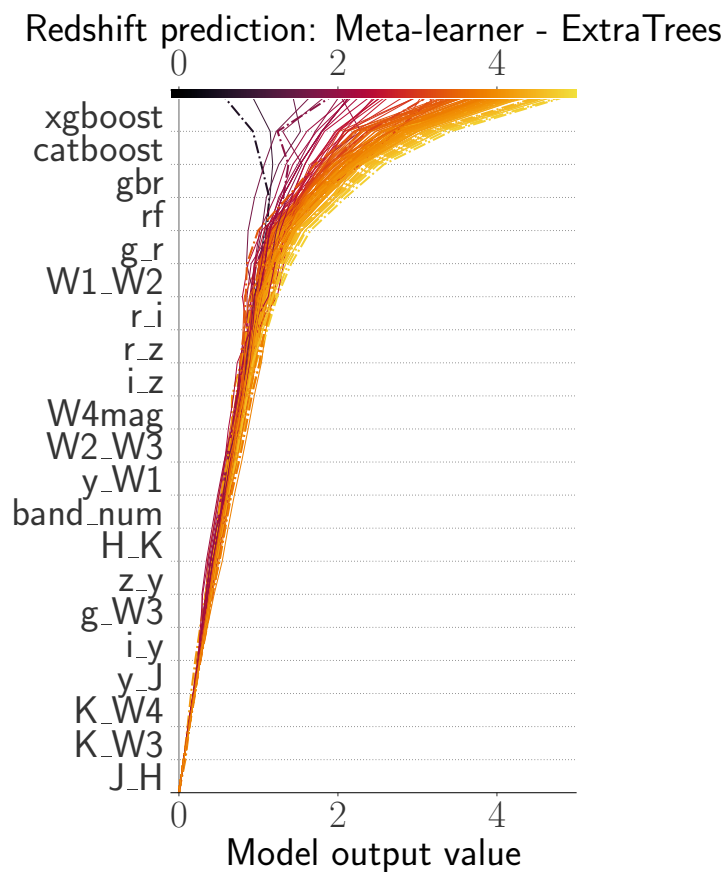


Figure 5.6: Decision plot from the SHAP values for all features from the redshift prediction model in the 121 high redshift ($z \geq 4$) spectroscopically confirmed AGN from HETDEX. Description as in Fig. 5.4.

CHAPTER 5. ANALYSIS OF PREDICTION METHOD AND RESULTS

Table 5.5: Combined and normalised (rescaled to add to 100) mean absolute SHAP values for observed features from the three models using 121 spectroscopically confirmed AGN at high redshift values ($z \geq 4$).

AGN-SFG model					
Feature	SHAP value	Feature	SHAP value	Feature	SHAP value
W1_W2	32.458	i_y	5.086	z_y	1.591
g_r	11.583	y_W1	4.639	H_W3	1.048
W1_W3	8.816	band_num	4.050	W4mag	0.514
r_i	7.457	y_W2	3.228	H_K	0.466
i_z	6.741	z_W2	2.348	W3_W4	0.466
r_J	6.613	y_J	1.718	J_H	0.178
Radio detection model					
Feature	SHAP value	Feature	SHAP value	Feature	SHAP value
g_i	14.120	z_W1	6.751	W4mag	2.691
W2_W3	13.201	r_i	5.577	band_num	2.661
g_r	12.955	r_z	5.161	K_W4	0.939
y_J	8.224	i_z	4.512	H_K	0.719
K_W3	7.441	z_y	4.121	J_H	0.190
W1_W2	6.874	y_W1	3.864		
Redshift prediction model					
Feature	SHAP value	Feature	SHAP value	Feature	SHAP value
g_r	32.594	z_y	3.557	W4mag	1.639
y_W1	20.770	y_J	3.010	g_W3	1.479
W2_W3	12.462	band_num	2.595	K_W3	0.853
W1_W2	5.692	i_y	2.381	K_W4	0.451
r_i	4.381	H_K	2.230	J_H	0.146
r_z	3.755	i_z	2.005		

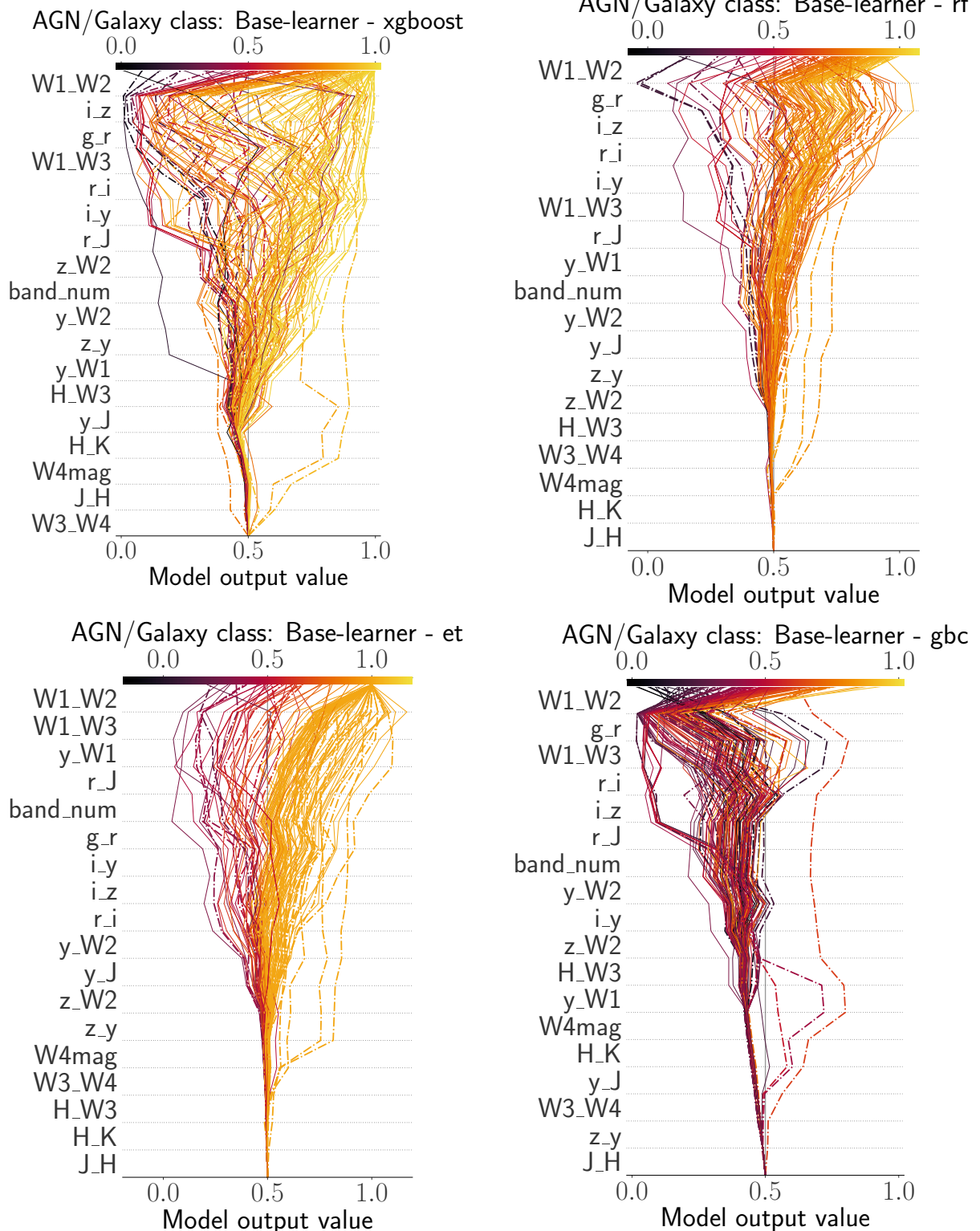


Figure 5.7: SHAP decision plots for base AGN-SFG algorithms. Details as described in Figs. 5.4. Starting point of predictions is the naive classification threshold. From left to right and from top to bottom, each panel shows the results from XGBoost, RF, ET, and GBC.

DRAFT - March 15, 2024 - DRAFT

CHAPTER 5. ANALYSIS OF PREDICTION METHOD AND RESULTS

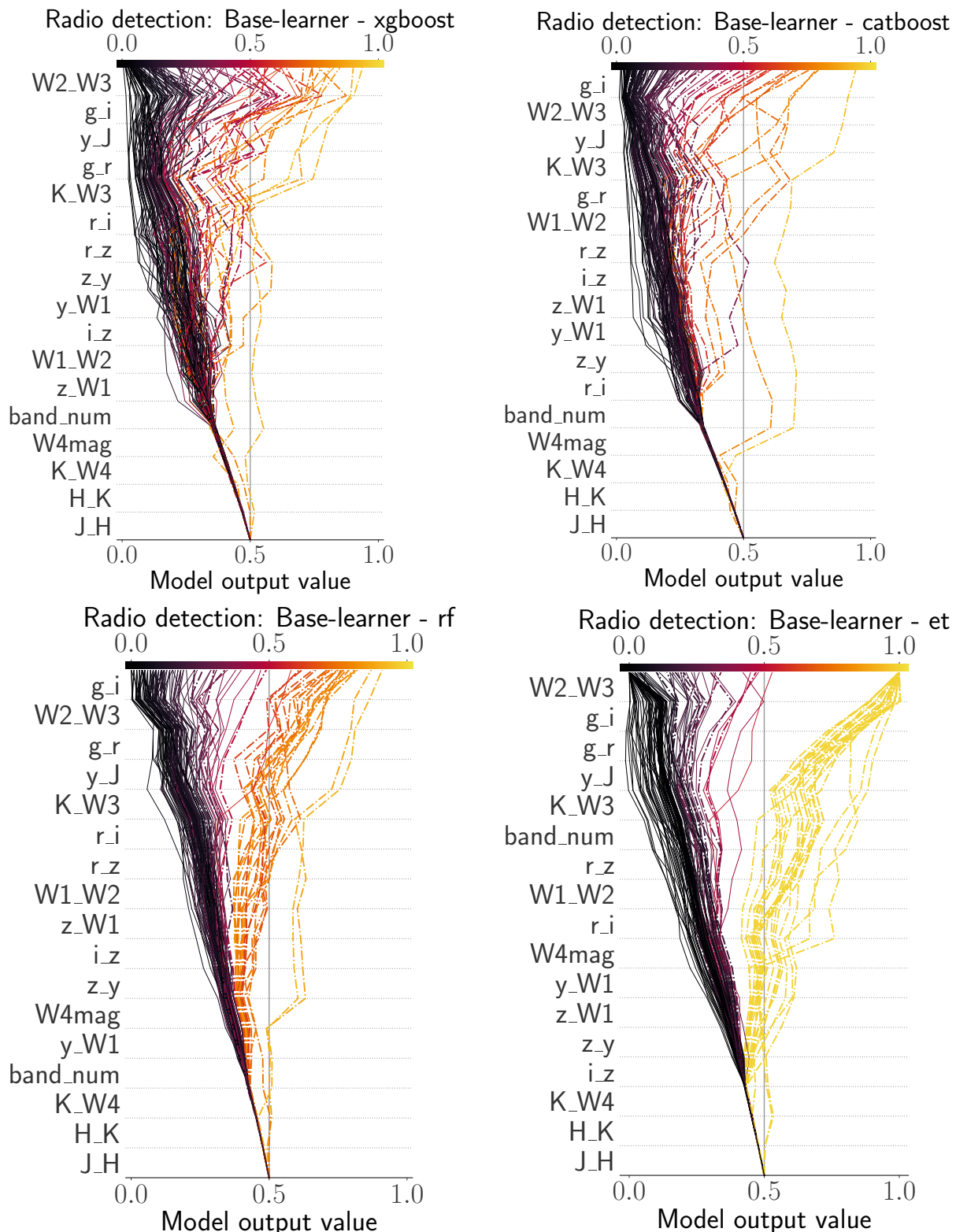


Figure 5.8: SHAP decision plots from base radio algorithms. Details as Figs. 5.4 and 5.7. Each panel with results for [XGBoost](#), [CatBoost](#), [RF](#), and [ET](#).

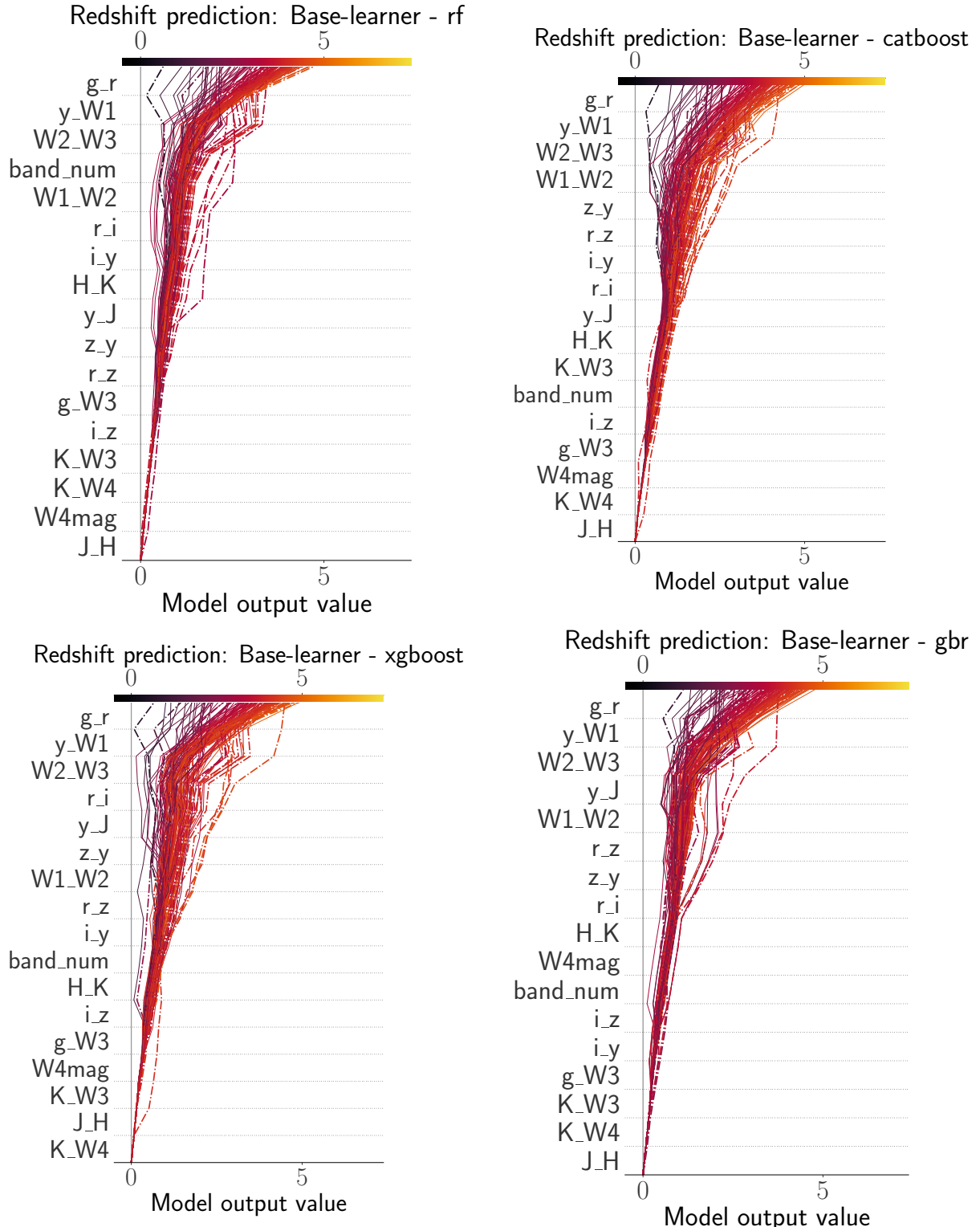


Figure 5.9: **SHAP** decision plots from base redshift algorithms. Details as in Fig 5.4. Each panel shows results for **ET**, **CatBoost**, **XGBoost**, and **GBR**.

DRAFT - March 15, 2024 - DRAFT

This page intentionally left blank.

Machine-assisted learning from models

The use of [ML](#) methods can be extended beyond the predictions that specific models were trained to perform. Given that [ML](#) models need to extract correlations and connections between the features they have had access to, they can deliver additional information about the behaviour of the properties of the studied sources (not only those used for training, but also the test or prediction sets). Thanks to its sequential, and fairly independent stages, our prediction pipeline, as presented in this thesis, can be used to extract information for a number of different aspects of the analysis of radio-detectable [AGN](#) (together with their redshift values).

In this chapter, we present, with different levels of detail, three examples in which the prediction pipeline can be used to extend the knowledge about our object of study, radio-detectable [AGN](#). In first instance, an example of the extraction of information from the learning process the models use to derive a new, and simple, [AGN](#) selection criterion. Then, an example of the use of how the outputs from the prediction pipeline can be directly applied to extract further knowledge from the distribution of radio-detectable [AGN](#) in different epochs. And finally, we present the concept of the use of the results of the prediction pipeline for a different goal from its initial purpose, that is, the assessment of multi-wavelength counterparts of radio detections.

6.1 Colour-colour AGN selection criterion

In the introduction of [AGN](#) selection methods in Sect. 1.1.1, it was shown that a combination of photometric colours can be used to determine selection criteria for different subsets of [AGN](#). Each one of these criteria is able to retrieve information on specific properties (e.g. redshift) or processes from [AGN](#) and their hosts. Additionally, it is possible to extract details from the evolutionary state of some sources by observing their position in the colour-colour, or colour-magnitude diagrams.

From the feature importances in Table 5.5 and the values presented in Fig. 2.3, we infer that

CHAPTER 6. MACHINE-ASSISTED LEARNING

using optical colours could in principle create novel selection criteria with metrics equivalent to those shown in Table 5.1 but for a much larger number of sources (100 000 sources for colour plots using W3 vs 4 700 000 sources for colours based in r, i or z magnitudes, see Fig. 2.3 and Table 2.2). We tested this hypothesis and derived a selection criterion in the g - r vs W1 - W2 colour-colour parameter space as shown in Fig. 6.1 using the labelled sources in the test subset of the [HETDEX](#) field. These colours correspond to the features with the highest [SHAP](#) values in the [AGN-SFG](#) classification model (Table 5.5), thus, they have the highest potential to carry enough information to separate both populations. The results of the application of this criterion to the testing data and to the labelled sources in S82 are presented in the last row of Table 5.1. Their limits are defined by the following expressions:

$$g - r > -0.76, \quad (6.1)$$

$$g - r < 1.8, \quad (6.2)$$

$$W1 - W2 > 0.227 \times (g - r) + 0.43, \quad (6.3)$$

where W1, W2, g, and r are Vega magnitudes. Our colour criteria provides better and more homogeneous scores across the different metrics with purity (precision) and completeness (recall) above 87 %. Avoiding the use of the longer [WISE](#) wavelength (W3 and W4), the criteria can be applied to a much larger dataset (as seen in the number of missing values in Figs. 2.3 and 2.4). These boundaries were drawn to contain, at least, 86 % and, and most 99 % of the [AGN](#) (as presented by their distribution contours). Even though each colour has been used for [AGN](#) diagnostics separately (e.g. Obrić et al., 2006; Assef et al., 2013; Yan et al., 2013; Secrest et al., 2015; Gatica et al., 2024), prior to the development of our pipeline, the combination of (W1, W2) and (g, r) colours has not been extensively used for the separation between [AGN](#) and [SFGs](#).

One fairly recent example of the the use of such combination of colours was presented by Zeraatgari et al. (2024). They analysed the application of [ML](#) classification for the separation of stars, [AGN](#), and galaxies using [SDSS Data Release 17 \(SDSS-DR17\)](#); Abdurro'uf et al., 2022) and [WISE](#) measurements of close to 1 500 000 sources. As part of their preparatory analysis, a (W1, W2) (g, r) colour-colour diagram (among others) was used to asses the usefulness of separate features to divide sources in classes. Besides their presentation, the (W1, W2) (g, r) colour-colour was not studied further.

Table 6.1 displays metrics for our new criterion in comparison with previous W1 - W2 vs

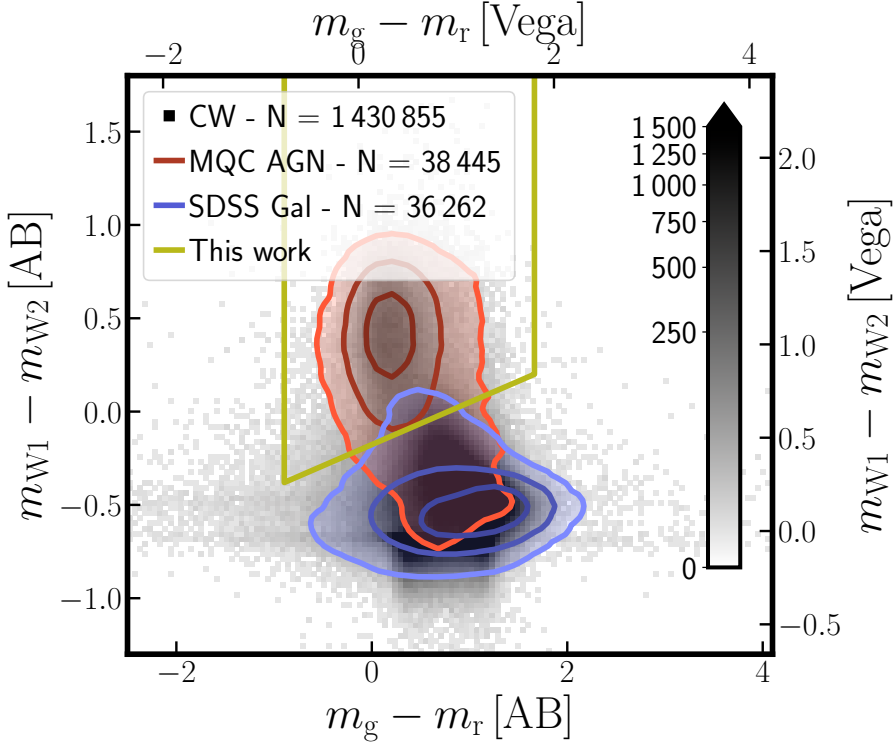


Figure 6.1: **AGN** classification colour-colour plot in the **HETDEX** field using **CW** (W1, W2) and **PS1** (g, r) passbands. Grey-scale density plot include all **CW** detected and non-imputed sources. Red contours highlight the density distribution of the **AGN** in the **MQC** and blue contours show the density distribution for the **SFGs** from **SDSS-DR16**. Contours are located at 1, 2 and 3σ levels. Ochre line limits the selection criterion determined from the application of our prediction pipeline (Eqs. 6.1, 6.2, and 6.3).

W2 - W3 **AGN** colour-colour selection criteria (as presented in Sect. 5.1.1 and Table 5.1). Our classification method can recover, in the **HETDEX** field, 15 % and 59 % more **AGN** than said formulae. In the **S82** field, these differences range between 17 % and 61 %. Such differences highlight the fact that most of the information that separates **AGN** from **SFGs** is traced by the selected features (mostly colours). Also, the increase in the recovery rate underlines the importance of using photometric information from the combination of several bands for such task, as opposed to traditional, two colour-colour criteria.

Depending on the degree of available information, the step of the pipeline and the research goals, other combination of colours and features could be used to create more selection criteria for **AGN**, radio-detected sources, and sources at specific redshift ranges. The use of such methods can be seen as an alternative to the recurrent use of the full set of **ML** models in our pipeline. Additionally, the creation of these colour-based criteria can be thought as a direct application of the knowledge gathered by the models, rather than a blind application of the latter, as the researcher can select the features that are more accessible given the conditions of the observed region.

CHAPTER 6. MACHINE-ASSISTED LEARNING

Table 6.1: Results of application of several colour-colour AGN diagnostics criteria to our testing subset and the labelled sources from the S82 field. Same as Table 5.1 but including colour-colour criteria from this work.

Method	HETDEX test set			
	F_β (×100)	MCC (×100)	Precision (×100)	Recall (×100)
S12	86.10	78.78	93.98	80.51
M12	51.80	49.71	98.87	37.18
M16	67.21	61.30	97.48	53.48
B18	82.14	75.76	97.54	72.66
Eqs. 6.1; 6.2; 6.3	92.71	87.64	94.00	91.67

Method	S82 (labelled)			
	F_β (×100)	MCC (×100)	Precision (×100)	Recall (×100)
S12	83.59	45.47	93.93	76.62
M12	46.80	28.22	99.59	32.54
M16	64.69	37.76	98.80	50.32
B18	79.71	51.07	98.72	68.77
Eqs. 6.1; 6.2; 6.3	90.63	58.53	94.15	87.91

^a Naming codes for the used methods are described in the main text (cf. Sect. 5.1.1)

^b Last row of each sub-table corresponds to the colour-colour criterion derived in this work.

^c All metrics have been multiplied by 100.

Nevertheless, and understanding that the application of our newly derived colour-colour diagnostics criterion (or any other colour-colour criterion), we advocate for the use of the full prediction pipeline for the selection of (IR-detected) radio-AGN. Tables 5.1 and 6.1 show that the analysis of a full set of multi-wavelength information, in the form of our prediction pipeline, can deliver, overall, better results than those given by traditional colour-colour criteria.

6.2 Radio luminosity function

A full study of the evolution of the distribution of sources in a region of the sky can be done with the use of LFs (cf. Sect. 1.1), which, using the definition from Salpeter (1955), correspond to the density of sources of a defined class in a range of luminosities (or, equivalently, magnitudes). As the performance and inner works of our prediction pipeline have already been assessed (cf. Chapters 3, 4, and 5), we can apply small variations to it as a way to emphasise the goals of this section. For this reason, we decided to run the full training sequence one more time, where two relevant changes have been introduced. The first change is related to the cross-match of the radio information for the training set. Instead of using a 1'1 search radius to

find radio detections around the **CW**-selected sources (see Sect. 2.3), we adopted a 6'' circle, which corresponds to the spatial resolution of **LoTSS-DR1**. With this change, we ensure the selection of radio detections for a larger fraction of sources. This modification is done at the expense of possible misidentifications of radio counterparts. The second change is the inclusion of a complete new branch of predictions. Taking the description of the pipeline of Figs. 1.8 and 3.1, new models have been added to analyse the sources that have been predicted as **SFGs** (i.e. not as **AGN**) by the first model. Thus, these sources will be subject to a prediction of their radio detectability and, those predicted as being radio detectable, will have their photometric redshift values estimated. The inclusion of a new branch is related to the need to compare the radio luminosity distributions between **AGN** and regular **SFGs** (see Chapter 1). A detailed description of the modified datasets and the models produced with them can be found in Appendix B.

In order to study the distribution of luminosities of **AGN** as derived from our prediction pipeline, and as part of the efforts to study the behaviour in areas that will be subject to future radio surveys, we have selected, as test field, the area of the **EMU-PS**, which is part of the **EMU** survey, a precursor of **SKA**. The **EMU-PS** catalogue¹ has radio information, at 944 MHz from 178 921 compact sources in an area of 270 deg² in the southern sky with a depth of 25 μ Jy/beam to 30 μ Jy/beam rms and a spatial resolution of 18'' (see Fig. 6.2 for a footprint of the area of **EMU-PS**). If we assume a synchrotron radio slope of $\alpha = -0.7$ (e.g. Sabater et al., 2019), the 5σ detection limit of **LoTSS** (355 μ Jy/beam) at the frequency of **EMU-PS** would be $\approx 95 \mu\text{Jy}/\text{beam}$, which is below the 5σ detection limit of **EMU-PS**, 125 $\mu\text{Jy}/\text{beam}$. Thus, and assuming ideal conditions, if **LoTSS** had observed the **EMU-PS** area, some of its fainter detections might have not been caught by the **EMU-PS** catalogue.

For the purposes of this exercise, and as presented in Sect. 2.3, we have collected measurements in the **EMU-PS** area to apply the prediction pipeline. Thus, we have started with the selection of **CW**-detected sources in the selected area, finding 10 355 457 detections and successive cross-matches were performed using a search radius of 1''.1. One exception to this distance was used for the cross-match with the **EMU-PS** catalogue itself, where a 10'' radius was used instead, which is the maximum search radius used by Norris et al. (2021) to find **CW** counterparts for their radio detections. The reason for this change is twofold: a larger distance is similar to the size of the restoring beam (18'') and the need for testing the effectiveness of the use of our models for the assessment of radio counterparts. As aforementioned, an additional branch of two models has been included in the prediction pipeline. One that can predict the

¹EMU-PS data can be obtained from <https://doi.org/10.25919/exq5-t894>

CHAPTER 6. MACHINE-ASSISTED LEARNING

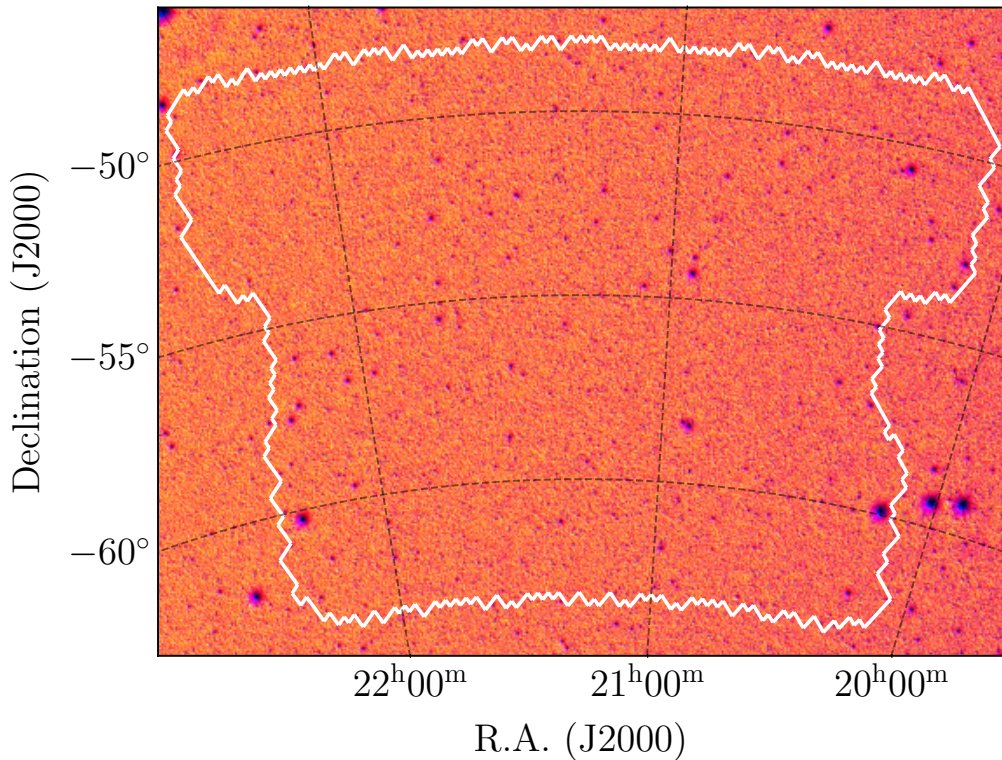


Figure 6.2: Footprint of the area of the [EMU-PS](#) field. In the background, W1 image from the [unWISE](#) coadds (Lang, 2014; Meisner et al., 2022). The white contours limit the area of the [EMU-PS](#) field, which covers 270 deg^2 .

radio detectability of [SFGs](#) (i.e. not [AGN](#)) and a second model that can predict photometric redshift values for radio-detected [SFGs](#).

Given that [PS1](#) does not cover the [EMU-PS](#) area, a different survey was selected to obtain optical measurements of the studied sources. Hence, we have retrieved them from the [DES Data Release 2 \(DES-DR2\)](#) (Abbott et al., 2021). We have used the same search radius, $1.^{\circ}1$, to obtain the counterparts for the [CW](#)-detected sources.

In contrast to the identification of sources in [HETDEX](#) and [S82](#) fields and due to their different positions in the sky, the [EMU-PS](#) catalogue was cross-matched with alternative catalogues for the association of known [AGN](#) and [SFGs](#). In the case of [AGN](#), a more recent version of [MQC](#) (v8; Flesch, 2023) was used² as well as [QSO](#) identifications from the spectroscopic sample of [DES-DR2](#) (Yang and Shen, 2023) and the [Gaia-unWISE Spectroscopic Quasar catalog](#) (Quaia G20.5; Storey-Fisher et al., 2023), which is based upon observations from [Gaia](#) data release 3 (DR3) extragalactic content (Gaia Collaboration et al., 2023a) and the [unWISE](#) reprocessing (Lang, 2014; Meisner et al., 2019) of the [WISE](#) data. For the [SFGs](#) present in the [EMU-PS](#) field, and from the lack of [SDSS](#) measurements, we have included the identifications from the

²For this exercise, all sources identified as [AGN](#) by [MQC](#) were selected, not only those with a redshift measurement, as done in the main model training.

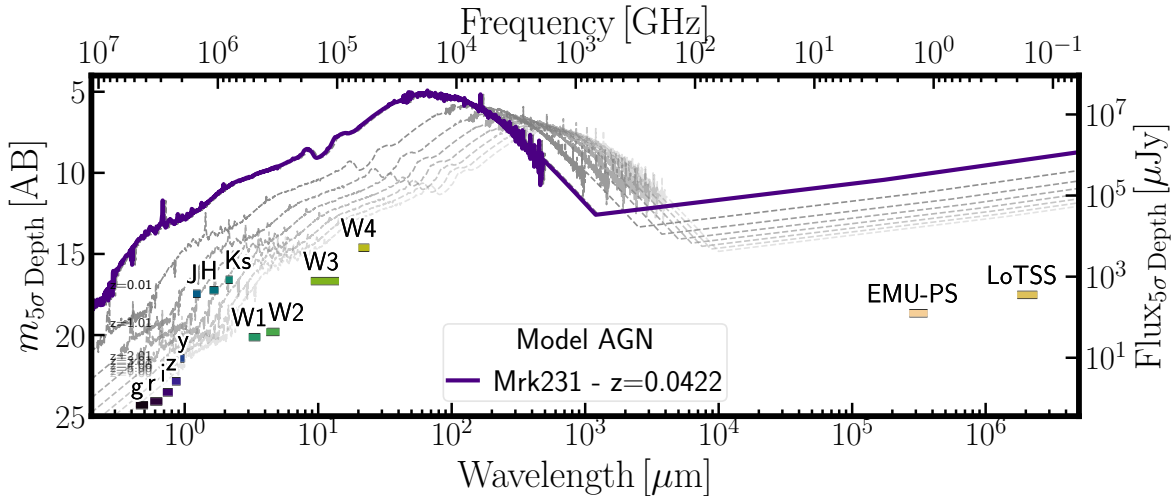


Figure 6.3: Flux and magnitude depths (5σ) from the surveys and bands covering the [EMU-PS](#) area. Limiting magnitudes and fluxes were obtained from the description of the surveys, as referenced in the main text. In purple, rest-frame [SED](#) from Mrk231 ($z = 0.0422$, Brown et al., 2019) is displayed as an example [AGN](#). Redshifted (from $z = 0.001$ to $z = 7$) versions of this [SED](#) are shown in dashed grey lines.

spectroscopic catalogue in the final [VEXAS Data Release 2](#) (VEXAS-DR2; Khamtsov et al., 2021). In this way, the [EMU-PS](#) area harbours 12 692 known [AGN](#) and 1806 known [SFGs](#), from which 2375 and 870, respectively, have a counterpart in the [EMU-PS](#) catalogue. As in the [S2](#) field, the ratio of the number of [AGN](#) and [SFGs](#) in the [EMU-PS](#) field is the opposite to what can be found in the [HETDEX](#) field. Having a larger number of [AGN](#) than of [SFGs](#) can reflect the efforts made in each field to catalogue each class of sources and not the underlying density of sources of the region.

In order to retrieve a large sample of redshift measurements, we included those provided by [MQC v8](#), [Quaia G20.5](#), and spectroscopic redshifts from the [Dark Energy Spectroscopic Instrument \(DESI\)](#) imaging surveys (Dey et al., 2019; Zou et al., 2019), which are contained in the full [EMU-PS](#) catalogue. A summary of the number of sources and counterparts found in all different catalogues and surveys can be seen in Table 6.2.

The application of the modified prediction pipeline to the more than 10 300 000 [IR](#)-detected sources in the [EMU-PS](#) area creates 89 040 candidates to be radio-detectable [AGN](#) and 116 400 to be radio-detectable [SFGs](#). Out of them, 36 466 have a radio counterpart in the [EMU-PS](#) catalogue (15 123 predicted [AGN](#) and 21 343 predicted [SFGs](#)), that is, a measured radio flux. These numbers imply a 637 % and 1182 % increment of sources for radio-detected [AGN](#) and radio-detected [SFGs](#) respectively. The distribution of predicted photometric redshifts of both samples is depicted in Fig 6.4.

It can be seen in Fig 6.4 that the distribution of radio-detectable [SFGs](#) is concentrated

CHAPTER 6. MACHINE-ASSISTED LEARNING

Table 6.2: Composition of initial catalogue and number of cross matches with additional surveys and catalogues in the area of the [EMU-PS](#)

Survey	EMU-PS area
CatWISE2020	10 355 457
DES-DR2	7 091 485
AllWISE	4 066 594
2MASS	932 926
EMU-PS (10 '')	170 702
MQC v8 (AGN)	614
Quaia G20.5 (AGN)	12 491
DES-DR2 (AGN)	46
Total AGN	12 692
VEXAS Spec V2 (SFGs)	1806

between redshift 0 to 1.2. This behaviour corresponds to the original distribution of [SFGs](#) used for training in the [HETDEX](#) field and thus, to the parameter space coverage of such sources. As expected, the model trained with them can only associate new sources to the values in that region of the space of parameters. For the same reason, the distribution of predicted redshifts for radio-detectable [AGN](#) spans a larger range, similar to the values of the training in the [HETDEX](#) field.

From the point of view of the sources detected in the [EMU-PS](#) catalogue that are counterpart of a [CW](#) source (170 702, as indicated in Table 6.2), it is possible to analyse of the application of the pipeline. From the 170 702 [CW-EMU](#) sources, 34 332 have been predicted to be [AGN](#) and 136 368, to be [SFGs](#). From them, 15 123 elements have been predicted to be radio-[AGN](#) and 21 343, to be radio-[SFGs](#). Thus, close to 80 % of [EMU-PS](#) sources have been predicted to not have radio detections.

Radio luminosities can be obtained from the use of radio fluxes and redshift values of the sources. Fluxes are obtained from the [EMU-PS](#) catalogue, which lists them in its column `flux_int`. A distribution of these values is presented in Fig 6.5. Using Eq. A.4, they can be transformed into luminosities, at 944 MHz, with the predicted photometric redshift and, either assuming a radio spectral index of $\alpha = -0.7$ (see, for instance, Simpson et al., 2012; Magliocchetti et al., 2014; Šlaus et al., 2020; Mandal et al., 2021; van der Vlugt et al., 2022; Lyu et al., 2022) or using, in the case of [EMU-PS](#), the α values provided by the catalogue itself, in the column `spectral_index`. These spectral indices have been calculated from the use of the Taylor terms at the peak pixel of each fitted component (Norris et al., 2021). In order to obtain

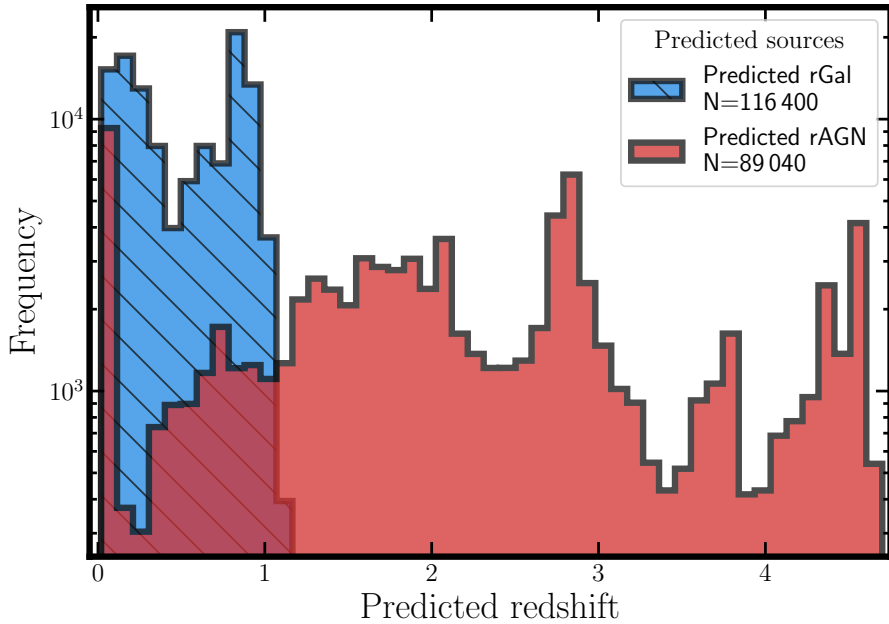


Figure 6.4: Distribution of predicted photometric redshift values for, in hatched blue, predicted radio-detectable SFGs and, in red, predicted radio-detectable AGN in the area of the EMU-PS catalogue.

the luminosity distances for the sources, we have adopted a flat Λ cold dark matter (Λ CDM) cosmology, with $\Omega_m = 0.31$, $\Omega_\Lambda = 0.69$, and $H_0 = 67.7 \text{ km s}^{-1} \text{ Mpc}^{-1}$, as presented by the Planck Collaboration et al. (2020).

Most of works on radio luminosity functions (RLFs) have used luminosity values at 1.4 GHz (e.g. Mauch and Sadler, 2007; Simpson et al., 2012; McAlpine et al., 2013; Šlaus et al., 2020). In order to have the opportunity to compare our results with previous literature, we will convert our EMU luminosities to be at that frequency. Using Eq. A.5, we can obtain luminosities at 1.4 GHz from our values at 944 MHz. The distribution of such luminosities, as a function of predicted photometric redshift, is presented for both samples, predicted AGN and SFGs, in Fig. 6.6.

Taking into consideration the intrinsic uncertainties of the original pipeline and the changes introduced to the models in the extended prediction pipeline, the luminosity distributions of Fig. 6.6 appear to be relatively homogeneous. Two potential issues can be, nevertheless, identified. First, a fraction of luminosities are located below the 5σ detection limit of EMU-PS. The presence of these populations (both SFGs and AGN) can be explained by two interrelated factors. One of them is that the detection limit presented in Fig. 6.6 has been calculated with the mean detection depth of the survey ($25 \mu\text{Jy}/\text{beam}$) and the other issue is that the detection limit used the fixed spectral index $\alpha = -0.7$, while the detected sources have been analysed with their own spectral indices.

CHAPTER 6. MACHINE-ASSISTED LEARNING

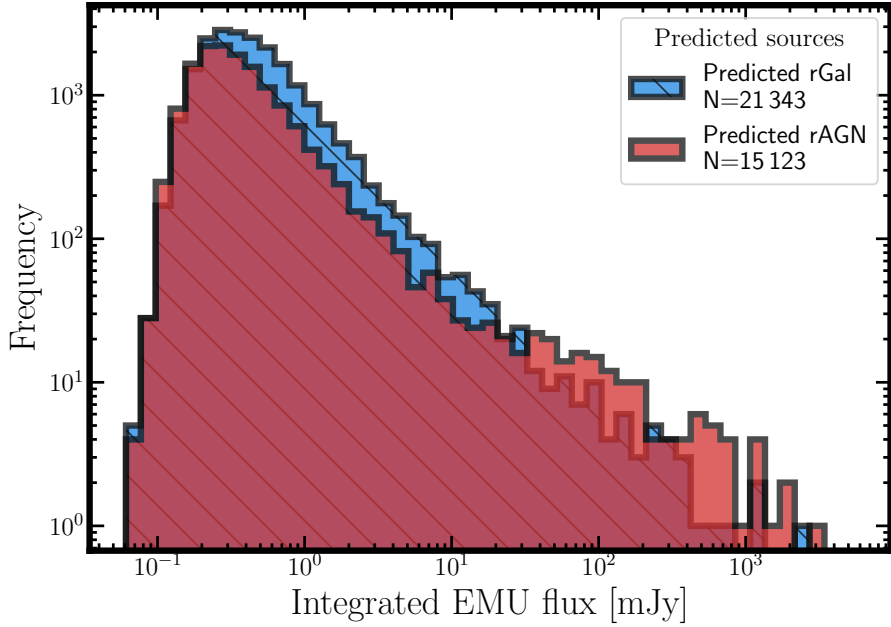


Figure 6.5: Distribution of EMU integrated fluxes (at 944 MHz) for, in hatched blue, predicted radio-detectable SFGs and, in red, predicted radio-detectable AGN in the area of the EMU-PS catalogue.

Recalling the overview given in Sect. 1.1.1, an additional issue is related to sources with radio luminosities that are low enough to have a high probability of being originated, mostly, from star formation episodes but are labelled as AGN. As a way to reduce this potential problem, we decided to use the thresholds of Eq. 1.2 and its description in our EMU-PS sample to alleviate the existence of too-bright radio SFGs. Thus, all predicted radio SFGs that presented a 1.4 GHz luminosity above the mentioned limit were re-labelled as predicted AGN and the corresponding branch of the prediction pipeline is applied to them. That is, a new photometric redshift value is predicted for all of them. The modified distributions of luminosities and redshifts of the re-labelled AGN and SFGs sets are presented in Fig. 6.7 with 23 741 and 12 532 predicted and EMU-PS-detected radio-AGN and radio-SFGs respectively.

It is possible to see, in Fig. 6.7, that the locus, in the (z, L) plane, of predicted radio-detectable SFGs is much smaller than previously (see Fig. 6.6). The new distribution is consistent with the expectation that, in general, radio emission from AGN is stronger than that of SF episodes. After the re-labelling, 12 561 sources are classified as predicted radio SFGs, and 23 712, as predicted AGN.

In order to obtain RLFs for our predicted radio-detected AGN, and from the description in Sect. 1.1.1, we implemented a version of the determination method presented by Page and Carrera (2000), which is called a binned estimator. This method, that is described in detail in Appendix A, is constructed in order to obtain an average of the LF over L and z bins (Alqasim

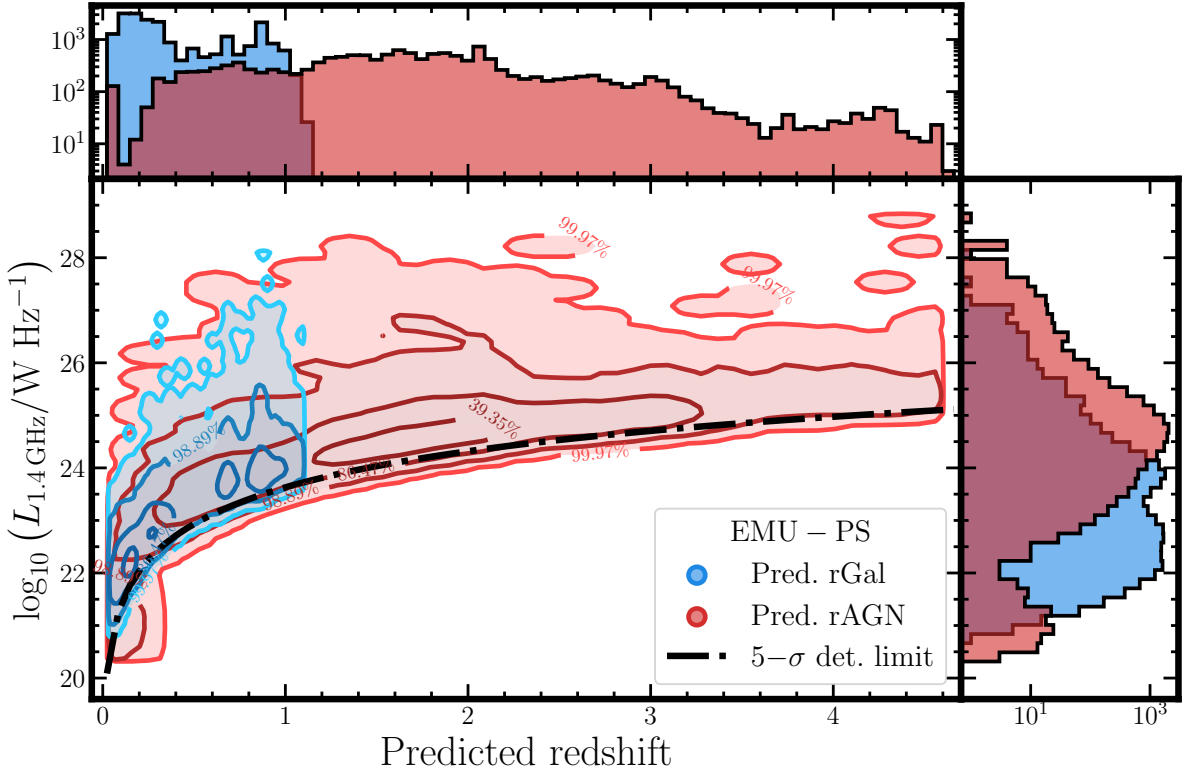


Figure 6.6: Distribution of predicted 1.4 GHz luminosities vs predicted photometric redshifts for radio-detectable AGN (in red) and radio-detectable SFGs (blue) in the area of the EMU-PS catalogue. In the top panel, the histograms of the predicted redshifts for both populations are presented. In the right-hand side of the figure, the distributions of predicted 1.4 GHz luminosities are displayed following the color code of the legend. In the central panel, two contour plots represent the joint distribution of 1.4 GHz luminosities and predicted photometric redshifts of both predicted radio-detectable AGN and radio-detectable SFGs. Contours represent the 1, 2, 3 and 4σ two-dimensional levels of the distribution (39.35 %, 86.47 %, 98.89 % and 99.97 %, respectively, of the corresponding sample). Black, dashed line represents the luminosity of a source at five times the noise level of the EMU-PS survey (25 mJy). That is to say, it represents the detection limit of the EMU-PS catalogue.

and Page, 2023).

Taking advantage of the use of ML predictions, it is possible to obtain a correction, as a function of redshift and radio luminosity, for both completeness (recall) and purity (precision) of the radio-AGN and radio-SFGs in our selected sample that can be added to the selection function, $\mathcal{P}(z, L)$. In order to obtain these values, we took all known radio-detected sources (i.e. AGN and SFGs) in the HETDEX field as well as their predicted class, redshift values, and estimated 1.4 GHz luminosities (assuming a spectral index $\alpha = -0.7$; Sabater et al., 2019). For each element in the $(z_{\text{Predicted}}, \log_{10}(L_{1.4\text{GHz}}))$ plane, all the sources located within a dimensionless distance of 1 are selected (i.e. their nearest neighbours). For these subsets of known radio sources, the class recall (cf. Eq. 3.4) and precision (cf. Eq. 3.5) are calculated independently. Their distributions of values are presented in Figs. 6.8 and 6.9 as a function of redshift and radio luminosity.

Then, each of the predicted sources from the EMU-PS catalogue is placed in the same plane

CHAPTER 6. MACHINE-ASSISTED LEARNING

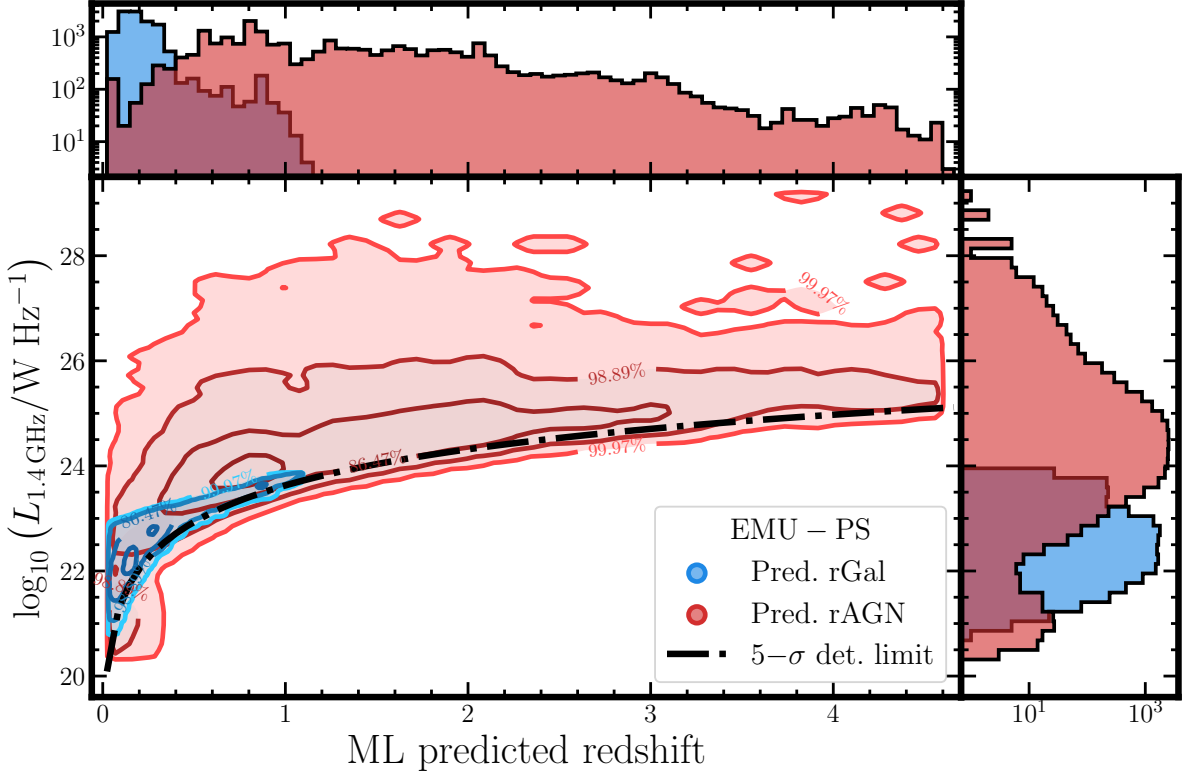


Figure 6.7: Distribution of predicted 1.4 GHz luminosities vs predicted photometric redshifts for radio-detectable [AGN](#) (in red) and radio-detectable [SFGs](#) (blue) in the area of the [EMU-PS](#) catalogue. [SFGs](#) with high 1.4 GHz luminosities have been re-labelled as [AGN](#), following the prescriptions by [Magliocchetti et al. \(2014\)](#) and [Magliocchetti \(2022\)](#). Description as in Fig. 6.6.

of their corresponding class among the [HETDEX](#) sources. The ten closest [HETDEX](#) sources, with a Euclidean distance, are selected and their recall, or precision, values are averaged with the inverse of their distance to the [EMU-PS](#) source as weights. This averaged value is assigned to the predicted source as their estimated recall or precision. The distributions of such values are presented in Figs. 6.10 and 6.11. This method for the calculation of [LF](#) correction factors takes, one step further, what has been usually the procedure of binning the (z, L) plane into regions that contain a reasonable amount of sources for the calculation of, for instance, recall values (e.g. [Richards et al., 2006](#); [Cameron and Driver, 2007](#); [Šlaus et al., 2020](#); [van der Vlugt et al., 2022](#)). In our case, and making use of the large number of [AGN](#) and [SFGs](#) produced by our pipeline, we can obtain an estimate of recall and precision for each individual source rather than for groups of sources.

Having obtained the completeness and purity values for the predicted sources among the [EMU-PS](#) sources, it is possible to generate an initial definition for the selection function. In first place, and from the definitions in Sect. 3.1.1, the recall indicates the fraction of sources that a prediction is missing given that they are present. Conversely, the purity is related to, given the

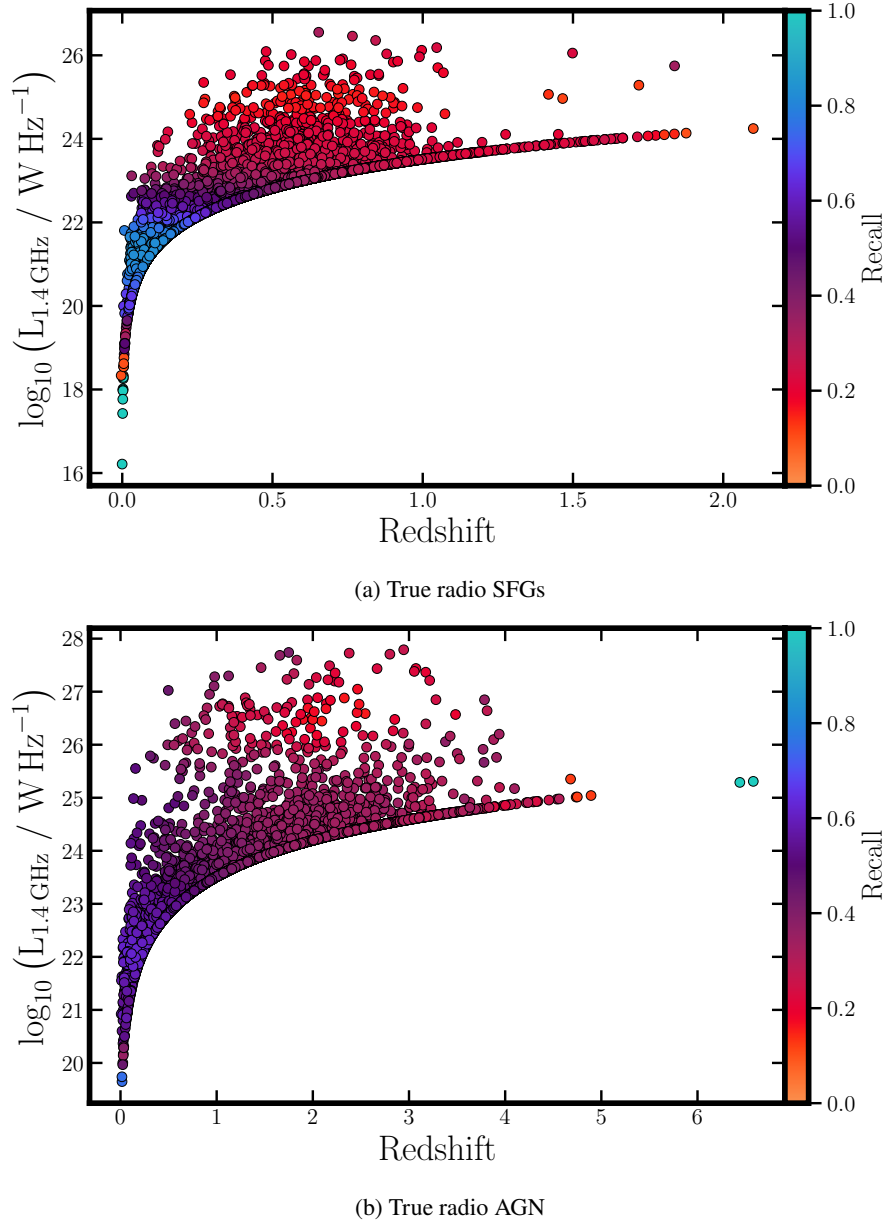


Figure 6.8: True 1.4 GHz luminosity vs redshift for (a) radio SFGs and (b) radio AGN in the HETDEX catalogue. Sources are coloured according to their estimated recall values and following each individual colourbar.

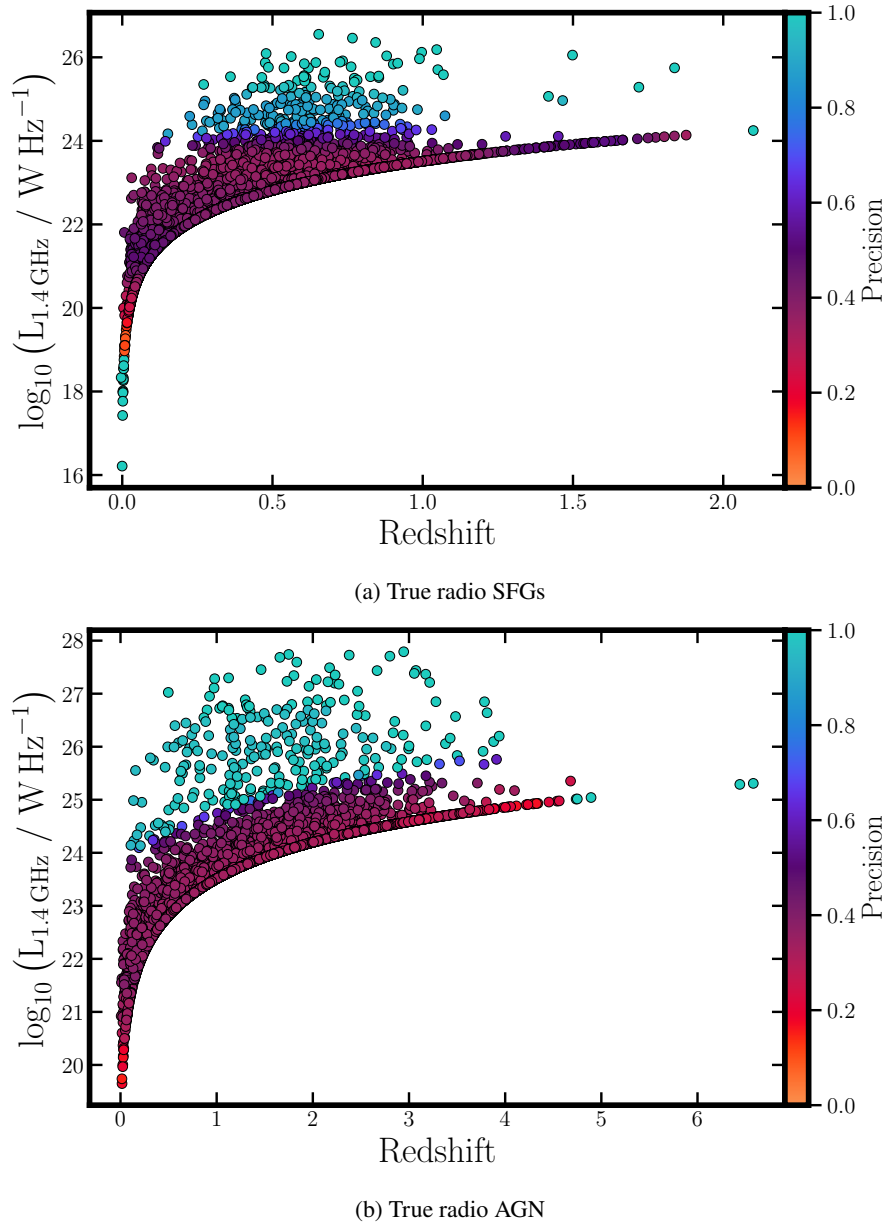


Figure 6.9: True 1.4 GHz luminosity vs redshift for (a) radio SFGs and (b) radio AGN in the HETDEX catalogue. Colour coding as in Fig. 6.8.

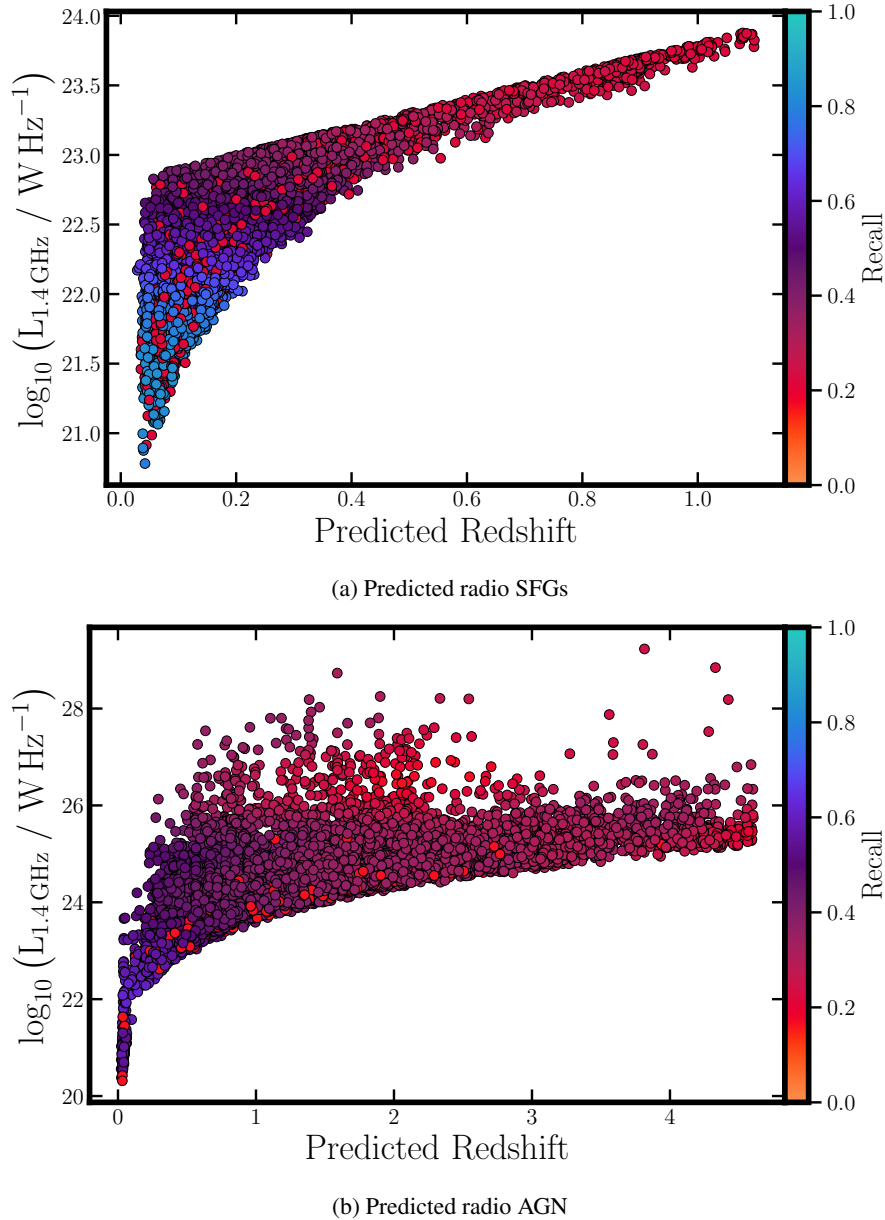


Figure 6.10: Predicted 1.4 GHz luminosity vs predicted redshift for predicted (a) radio SFGs and (b) radio AGN in the EMU-PS catalogue. Sources are coloured according to their estimated recall values and following each individual colourbar.

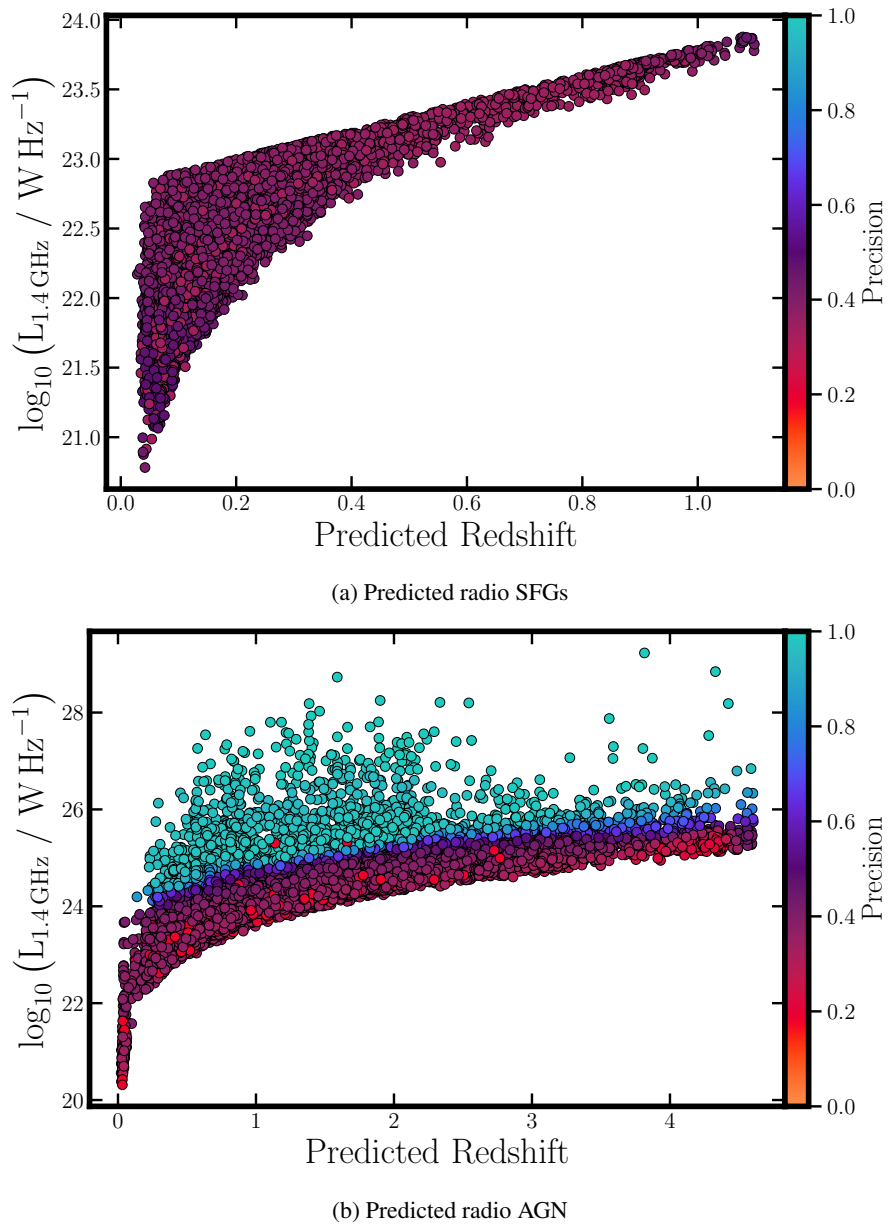


Figure 6.11: Predicted 1.4 GHz luminosity vs predicted redshift for predicted (a) radio SFGs and (b) radio AGN in the EMU-PS catalogue. Sources are coloured according to their estimated precision values and following each individual colourbar.

predicted elements, how many of them are not part of the desired class. Any correction based on those quantities will use the completeness as a reducing factor and the purity as an increasing quantity. In this way, the selection function, $\mathcal{P}(z_i, L_i)$, can be written as:

$$\mathcal{P}(z_i, L_i) = \frac{\text{Recall}_{\text{ML}}(z_i, L_i)}{\text{Precision}_{\text{ML}}(z_i, L_i)}, \quad (6.4)$$

with the **ML**-based recall and precision ranging between 0 and 1. Then, the selection function values can be any non-negative real quantity. It can be seen, then, as the recall decreases, the selection function follows the same behaviour, while an decrease of the precision will imply an increment of the selection function values. Additional factors might be included in the definition of the selection function. Some of them involve a correction for the resolution bias (e.g. Prandoni et al., 2001; Prandoni et al., 2018; Mandal et al., 2021) and a correction for the Eddington bias (Eddington, 1913; Eddington, 1940). For our project, and since it is more a proof of concept rather than a full analysis, only a **ML**-based correction (i.e. precision and recall) will be applied to the studied sources.

Taking into account the distribution of predicted redshifts from our set of predicted radio-detected **AGN** and the search for a distribution of sources that has a smooth number evolution across redshifts and radio luminosities (as done, for example, with radio-detected **SFGs** by van der Vlugt et al., 2022), 12 redshift bins were created: (0.01, 0.08], (0.08, 0.25], (0.25, 0.35], (0.35, 0.5], (0.5, 0.7], (0.7, 1.0], (1.0, 1.3], (1.3, 1.6], (1.6, 2.0], (2.0, 2.5], (2.5, 3.2], and (3.2, 4.8]. Radio-**AGN** are spread in all redshift bins while, in the case of radio-detected **SFGs**, the first seven redshift bins contain sources of this type (i.e. up to $z = 1.30$). The number of sources in each redshift bin is shown in Table 6.3.

We will obtain **LF** values from the use of binned estimations in each predicted redshift range with a chosen bin of size $\Delta \log_{10} L = 0.3$ following, for instance, Ross et al. (2013), Kondapally et al. (2022), Yuan et al. (2022), and Alqasim and Page (2023). Luminosity bins are defined starting from the faintest source available in the subset. Binned **LFs**, for each redshift interval, are then displayed in Fig. 6.12. Before establishing any comparison with previously derived **RLFs**, it is important to note that the values derived by us should be considered as a lower limit for a full **RLF**. The sources considered for this work are selected, as described earlier in the text, by their detection in the **CW** catalogue. That means that all our predicted sources need to be **IR**-detected. This construction does not include sources (either **AGN** or **SFGs**) that can be detected in radio bands (in particular, in **EMU-PS**) but do not present **IR** detections. Out

CHAPTER 6. MACHINE-ASSISTED LEARNING

Table 6.3: Number of predicted radio-detectable sources (**AGN** and **SFGs**) in the **EMU-PS** area by predicted redshift bin. For radio-**AGN** and radio-**SFGs**, first column shows the absolute number of predicted sources, while the second column presents the count weighted by selection function values (which are used for the calculation of the **RLFs** as presented in Eq. 6.4).

z bin	Radio AGN		Radio SFGs	
	Absolute count	Weighted count	Absolute count	Weighted count
$0.01 < z \leq 0.08$	157	146.41	1007	993.42
$0.08 < z \leq 0.25$	138	121.15	7541	7419.56
$0.25 < z \leq 0.35$	392	456.23	2692	3012.58
$0.35 < z \leq 0.50$	893	1095.80	564	775.12
$0.50 < z \leq 0.70$	3044	3820.24	313	470.11
$0.70 < z \leq 1.00$	5460	7522.44	384	606.24
$1.00 < z \leq 1.30$	2447	3815.81	31	58.41
$1.30 < z \leq 1.60$	2641	4383.97
$1.60 < z \leq 2.00$	3443	5832.04
$2.00 < z \leq 2.50$	2529	4153.77
$2.50 < z \leq 3.20$	1839	2732.65
$3.20 < z \leq 4.80$	758	1150.97
Total	23 741	35 231.48	12 532	13 335.45

of the 178 921 detections in the **EMU-PS** catalogue, 8219 do not have a counterpart in **CW** (i.e. close to a 5 % of them). For this reason, our **RLF** should be called, more precisely, **IR**-detected **RLF**. Nevertheless, we will keep the usual **RLF** nomenclature for the sake of simplicity and easiness of comparison with previous works.

Figure 6.12 depicts the values of the binned **RLF** calculated for predicted radio-**AGN**, radio-**SFGs**, and the total radio-predicted population in the **EMU-PS** field with **EMU** 944 MHz detections. Along these values, **RLFs** from previous works (**AGN**, **SFGs**, and total values; Mauch and Sadler, 2007; M07; **AGN**; Pracy et al., 2016; P16; **SFGs**; van der Vlugt et al., 2022; VdV22) have been included. Mauch and Sadler (2007) computed local **RLFs** using 7824 radio sources from the 1.4 GHz **NRAO VLA Sky Survey** (NVSS; Condon et al., 1998), covering an area of 7076 deg^2 in a redshift range $0.003 < z < 0.3$ (with a median redshift $z \approx 0.043$), which have been classified into **AGN** and **SFGs**. Pracy et al. (2016) have compiled a sample of 5026 $0.005 < z < 0.75$ optically detected and confirmed **AGN** in a $\sim 900 \text{ deg}^2$ area in the **FIRST** survey. Also, van der Vlugt et al. (2022) have constructed 1.4 GHz **RLFs** for 1290 **SFGs** in the **COSMOS-XS** survey (van der Vlugt et al., 2021) with redshifts in the range $0.1 < z < 4.6$.

Considering the redshift ranges in which the **RLFs** have been calculated for the previous works, they have only been included in the bins of Fig. 6.12 that match their distribution with ours. An exception has been made for the **RLF** from Pracy et al. (2016), which has been added

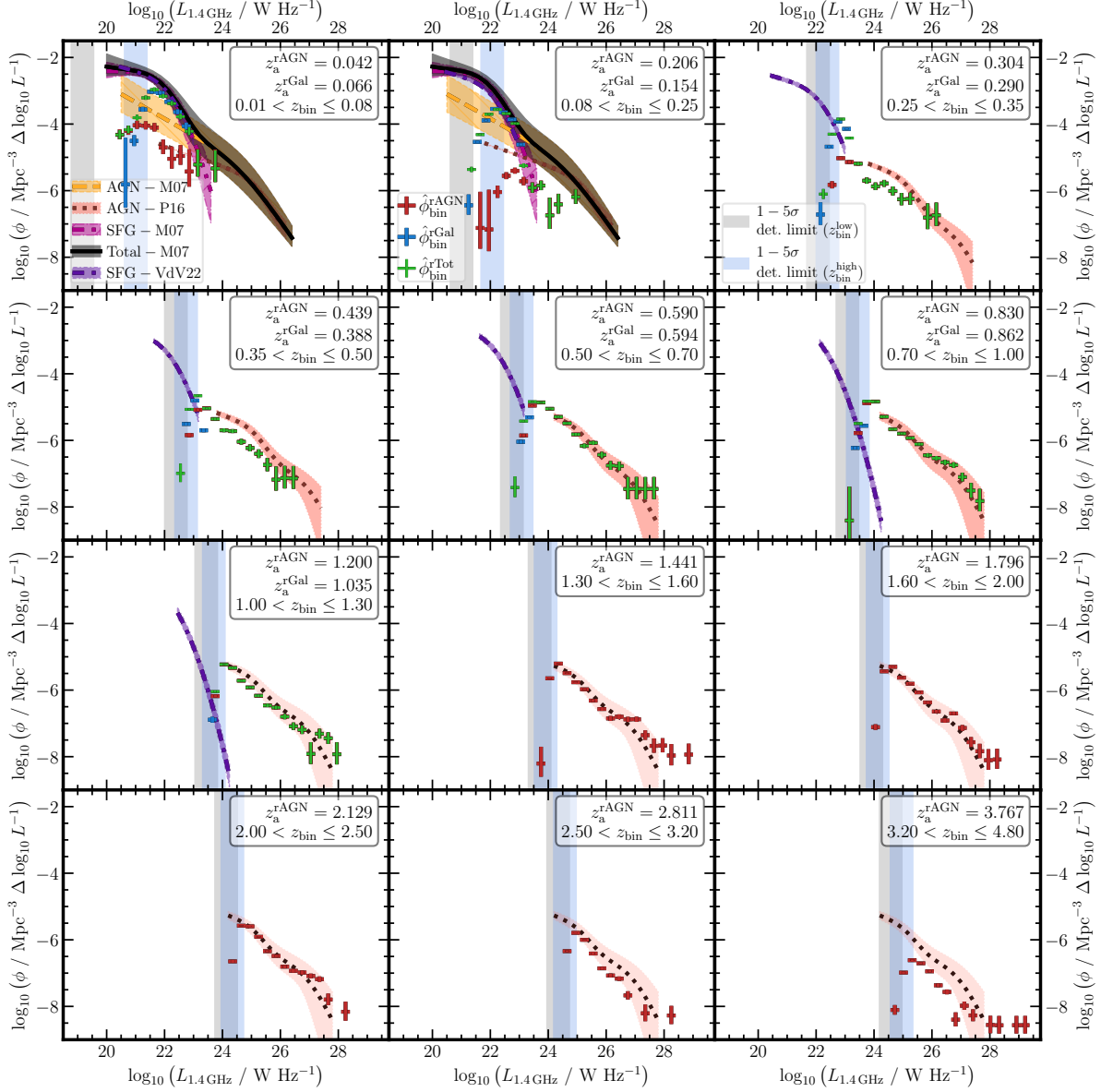


Figure 6.12: RLF (at 1.4 GHz) in EMU-PS binned by predicted z values. In red, values for predicted radio AGN; in blue, predicted radio SFGs, and in green, full predicted sample with 1σ uncertainty error bars included. Horizontal uncertainties correspond to $\Delta \log L = 0.3$. Vertical uncertainties have been obtained following Clopper and Pearson (1934) and Gehrels (1986) with the inclusion of the cosmic variance following the recipes by Trenti and Stiavelli (2008). Solid lines and shadowed regions show previous RLF determinations with 1σ uncertainties (AGN, SFGs, and total values; Mauch and Sadler, 2007; M07; AGN; Pracy et al., 2016; P16; SFGs; van der Vlugt et al., 2022; VdV22). Grey and blue regions show 1 to 5σ detection levels from EMU-PS measurements calculated using the lower (grey) and upper (blue) limits of each redshift bin. Upper-right corner of each panel shows median z of radio-AGN and radio-SFG, and z bin.

DRAFT - March 15, 2024 - DRAFT

CHAPTER 6. MACHINE-ASSISTED LEARNING

to redshift intervals with $z > 0.7$ solely for comparison and visual guidance purposes. It is worth mentioning that, given the different origins of the data and their treatment, it is expected that the **RLFs** from previous works show different behaviours.

Figure 6.12 shows that the very last luminosity bin, for higher luminosities at every redshift range, the **RLF** presents a noticeable rise. This effect has been discussed in previous works. For instance, Miyaji et al. (2001), Cara and Lister (2008), Croom et al. (2009), Palanque-Delabrouille et al. (2016), and Yuan and Wang (2013) have noted that the method by Page and Carrera (2000: binned **LF**), might cause pronounced biases near the flux cutoff of the analysed sample. The choice of the specific point in the $\log(L)$ bin can seriously impact in the final estimated value. Additionally, by assuming a uniform distribution in every luminosity bin, this method is unable to correct for the incompleteness in each individual sub-range. This last issue can be of the utmost relevance in the brightest end of the **LF**, where the number of sources decreases significantly. Thus, no meaningful conclusions should be extracted from the last luminosity bins.

All redshift intervals show, for the faintest luminosities, a clear decrease in the values of the **RLFs**. Such drop is due to the lower number of sources available to the calculations. As the grey and blue vertical shaded regions show, these luminosities correspond to the **EMU-PS** flux detection limits and, not all anticipated sources are detected. Thus, the number of sources is below the expectation. As we have not corrected our measurements for the completeness of the measurements in the **EMU-PS** survey, it is expected to see such behaviour in the faint end of the **RLFs**. For the case of **LoTSS-DR1**, Fig. 14 from Shimwell et al. (2019) presents the radio-detection completeness values for the **LOFAR** observations in the **HETDEX** field, with a 90 % completeness at 0.45 mJy. Such values have not been included in our selection function as only **ML**-based corrections have been considered.

In the closest redshift bin ($0.01 < z_{\text{Predicted}} < 0.08$), and besides the low-luminosity drop mentioned earlier, our binned **RLFs** follow one of the curves from previous works. Nevertheless, some issues are apparent. In first place, the **AGN LF** has a sharp jump at $\log(L_{1.4 \text{ GHz}}/\text{W Hz}^{-1}) \approx 21.5$. This jump implies that the density of local, low-luminosity radio-detectable **AGN** has an abrupt change. Such change is not seen in previous works, raising the question of its origin. Figures 6.6 and 6.7 show a clear overdensity of **AGN** in the first redshift bin which, according to typical radio-**AGN** redshift distributions (e.g. Simpson et al., 2012; Pracy et al., 2016; Šlaus et al., 2020; Ceraj et al., 2020; Bonato et al., 2021) should not be present.

One possible explanation for such overdensity is related to the (probably low) predicting power of our pipeline at low redshift values. One piece of evidence towards this hypothesis

can be seen in Fig. 6.4. The redshift bin with the largest number of predicted radio-**AGN** is the lowest one. The number of sources it has is compatible with the bins for predicted radio-**SFGs**. Thus, there is a strong likelihood of that a fraction of these low-redshift predicted radio-**AGN** are, radio-**SFGs** instead. As a way to test this possibility, Fig. 6.13 shows the two-dimensional distributions of the output probabilities from each step of the prediction pipeline as a function of the predicted redshift of all sources used in the calculation of the **RLFs**.

As expected, the second and fourth panels of Fig. 6.13 show a large number of predicted radio-**AGN** at low predicted redshift values. Prominently, a large fraction of them have low probabilities (i.e. $P(\text{AGN}) \lesssim 0.7$) whereas, for the rest of the redshifts, their distribution is more homogeneous. From the point of view of the pipeline, if a source is predicted to be an **AGN**, but with a low certainty, it will probably will be predicted to have very low redshift. Conversely, and as also shown by the last panel in Fig. 6.13, the prediction of the radio detectability of such sources is not as strongly affected by this effect as the **AGN** classification.

The distribution of predicted probabilities shows that low-redshift radio-detectable **AGN**, in general, have not been classified as certainly as expected. And thus, the inclusion of such sources in the calculation of the **RLF** cannot be used to extract conclusions. For this reason, only the higher redshift bins will be considered for analysis.

From the second redshift bin in Fig. 6.12 onwards, **RLFs** do not show unexpected features. Nevertheless, one appealing detail is noticeable in the redshift bin $0.08 < z \leq 0.25$, where radio-**AGN** do not follow the distributions from previous works. From a numerical perspective, such difference arrives from the corrections (selection function) applied to the number of sources in the bin, which cannot enhance their distribution as to match previously obtained studies. That level of corrections is, most likely, due to the fact that sources in the LoTSS-DR1 area that are predicted to be in that redshift bin exhibit high metric values. Bearing in mind that our selection function only includes corrections from the application of **ML** models, and not from the observational properties of the studied surveys, there is no prior expectation for the values of the **RLF**. Thus, such issue with radio-**AGN** in the $0.08 < z \leq 0.25$ can be seen in the opposite view, where the unexpected result is that, based upon **ML** corrections, our **RLFs** can match previous results.

Another point to underline from our **AGN RLFs** can be found in the bins between $z = 0.25$ and $z = 2.5$, at luminosities in the region of 24.5 dex to 26.5 dex, depending on the redshift value. In these ranges, the **AGN LF** has a weak bump of less than 0.3 dex in **LF** units. All these features, when including uncertainties, are still present. One possible explanation for

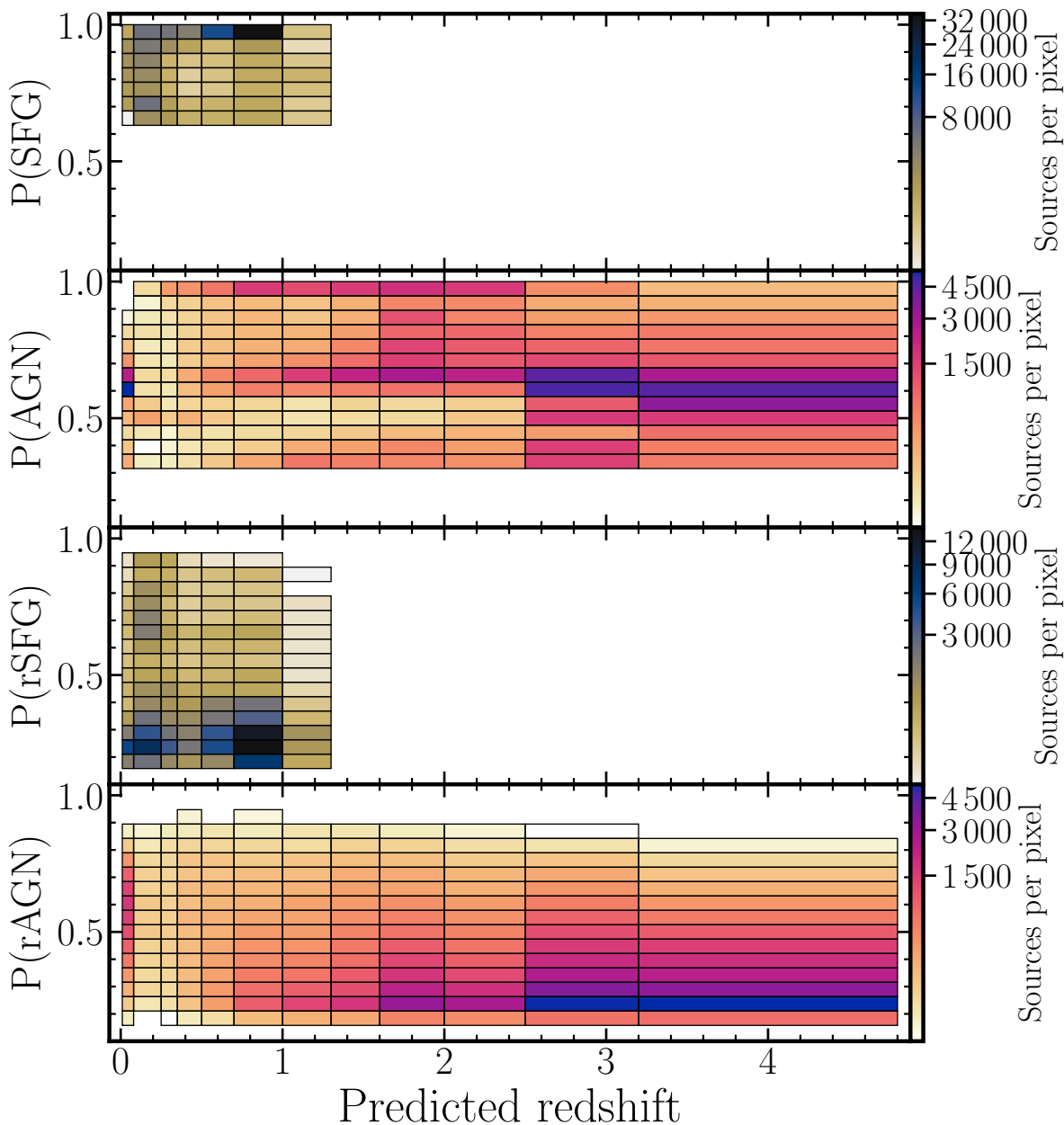


Figure 6.13: Two-dimensional histograms for the distribution of predicted probabilities (of each step in our modified prediction pipeline) as a function of predicted redshift for sources predicted to be radio-detected **AGN** and radio-detected **SFGs** and included in the calculation of the **RLF**. The darker the colour of the bin, the highest the number of sources with that combination of probability and predicted redshift, following the coding of the colorbars. From top to bottom, first panel shows the probabilities of a source to be **SFG**. Second panel presents the probability of a source to be an **AGN**. In the third panel, the probabilities of **SFGs** to be radio detected are included. Last panel shows the probability that a source predicted to be **AGN** can be detected in the radio. Bins in redshift correspond to the values defined in Table 6.3.

this elevation that our sample is influenced by the existence of an additional high-luminosity sub-population that has a stronger presence at high redshift values. Previous **RLF** studies can give some hints on the existence of such population. The first of them is from Pracy et al. (2016), who separated the study of radio **AGN** into **LERGs** and **HERGs**. Their Fig. 10 shows the **RLFs** for **LERGs** and **HERGs** at $z < 0.75$. For their $z > 0.5$ bin, both fitted and observed **LFs** cross at around $\log(L_{1.4\text{GHz}}/\text{W Hz}^{-1}) \sim 25.5$, being consistent with the presence of the bump in the corresponding bin of our sample. From a more analytical point of view, Willott et al. (2001) analysed radio sources at redshifts $glsz \lesssim 4$ and fitted a number of models to their density distributions. They assumed a two-population sample, with low-luminosity sources (**FRIIs** and low-excitation **FRIIs**) and high-luminosity subset (mostly, **FRII QSOs** with strong emission lines). In all the realisations of their models at $z > 0.5$, the total **RLFs** show a break that starts at $\log(L_{151\text{MHz}}/\text{W Hz}^{-1}) \sim 26.1$ (which, using $\alpha = -0.7$, corresponds to $\log(L_{1.4\text{GHz}}/\text{W Hz}^{-1}) \sim 26.5$). Again, their results match with the bumps found in our **AGN RLFs**.

Similar results are shown by Best and Heckman (2012), Best et al. (2014), Ceraj et al. (2018), Williams et al. (2018), Butler et al. (2019), and Kondapally et al. (2022), who separated their **AGN** population into two subsets and by Smolčić et al. (2017), Slob et al. (2022), and Šlaus et al. (2023) who analysed their full **AGN** dataset.

A different point of attention regarding the analysis of **RLFs** is that of their evolution (or lack thereof) as a function of redshift. One option for the display of our **RLF** as a function of redshift is through Fig. 6.14. In this way, rather and focusing on the individual obtained values for the **RLFs**, the emphasis is on their overall variation in time.

Figure 6.14a shows the evolution of the radio-**SFGs** while Fig. 6.14b does it for sources predicted to be radio-**AGN**. For the radio-**SFGs**, and given their narrow distribution, a qualitative analysis on their **RLF** evolution is possible in the range $22.5 \lesssim \log(L_{1.4\text{GHz}}/\text{W Hz}^{-1}) \lesssim 23.5$. In the case of radio-**AGN**, Fig. 6.14b can be analysed in the range $24 \lesssim \log(L_{1.4\text{GHz}}/\text{W Hz}^{-1}) \lesssim 28$. For both **RLFs**, a smooth evolution in redshift can be identified. Although further investigation is necessary for the correct quantification of such variations, it is possible to estimate that our **RLFs** decrease with redshift as much as ~ 1.5 dex in the range $0.5 \lesssim z \lesssim 4$.

In order to extract more information from our **RLFs**, a modification can be implemented in the previous calculations. If all the sources that are predicted to be radio detectable but do not have a counterpart in the **EMU-PS** catalogue are assumed to have a low flux (below the detection limit of **EMU-PS**), then the number of available sources for the determination of the

CHAPTER 6. MACHINE-ASSISTED LEARNING

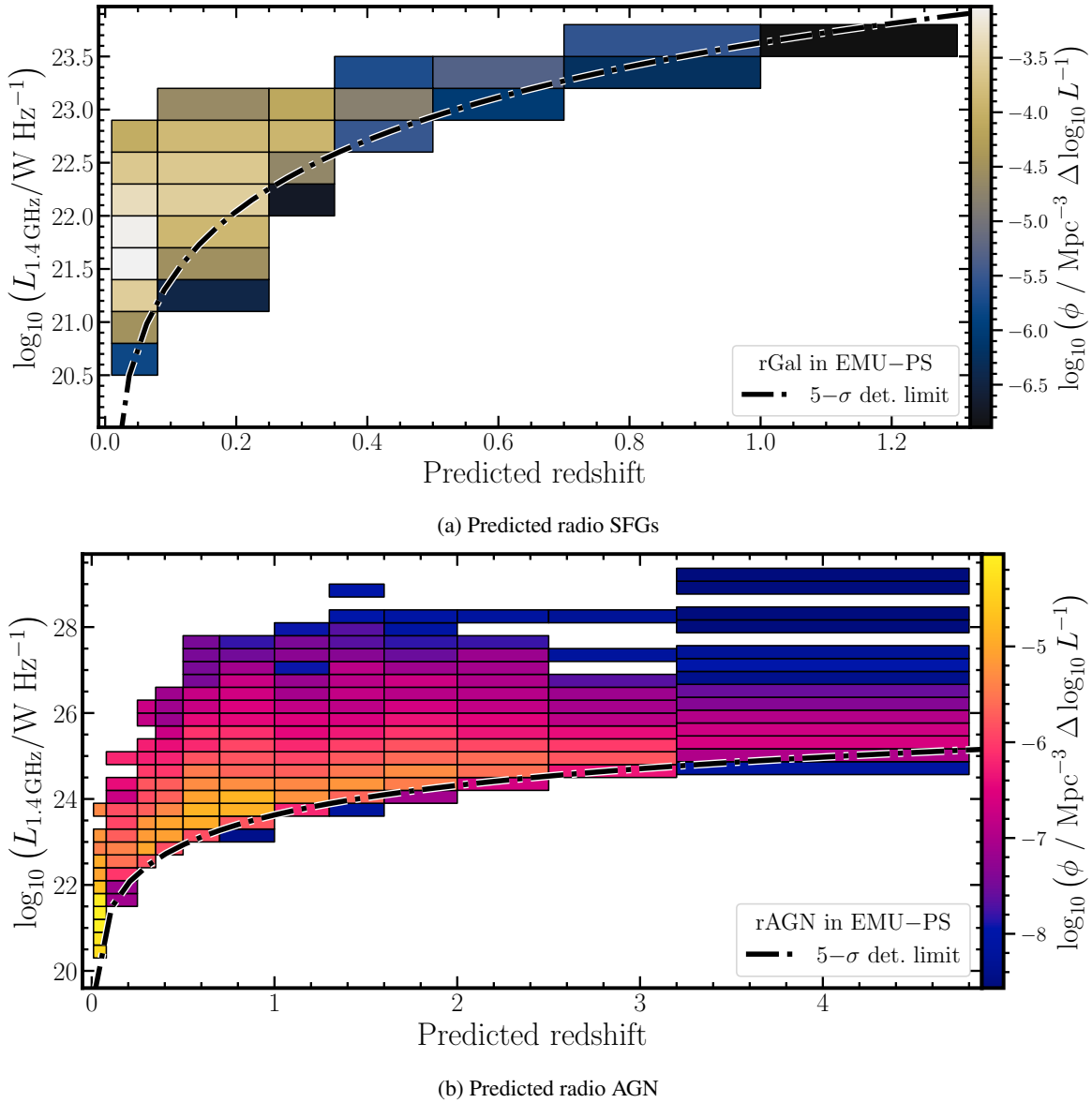


Figure 6.14: Predicted 1.4 GHz luminosity vs predicted redshift for predicted (a) radio SFGs and (b) radio AGN in the EMU-PS catalogue. Luminosity and redshift bins as in Fig. 6.12. Sources are coloured according to their estimated precision values and following each individual colourbar. Dot-dashed black line represents 5σ detection limit in EMU-PS.

RLF can clearly increase. As mentioned previously in this section, and using a spectral index value of $\alpha = -0.7$ for flux conversion, the detection limit of LoTSS-DR1 is lower than that of EMU-PS. Thus, it is possible to assign (as an imputed value) an EMU flux for these sources without an entry in the EMU-PS catalogue. From the lack of knowledge of the behaviour of the missing fluxes, we have assumed a Uniform, $F \sim U(5\sigma_{\text{LoTSS-DR1}}^{944 \text{ MHz}}, 5\sigma_{\text{EMU-PS}})$, distribution to allocate the imputed values. In this way, and after the application of the prediction correction of Eq. 1.2, our analysis now has 97 658 and 107 589 predicted and EMU-PS-measured radio-AGN and radio-SFGs, respectively. Their distribution in the $(z, L_{1.4 \text{ GHz}})$ plane is shown in Fig. 6.15. As expected, a large number of sources are concentrated below and around the detection limit

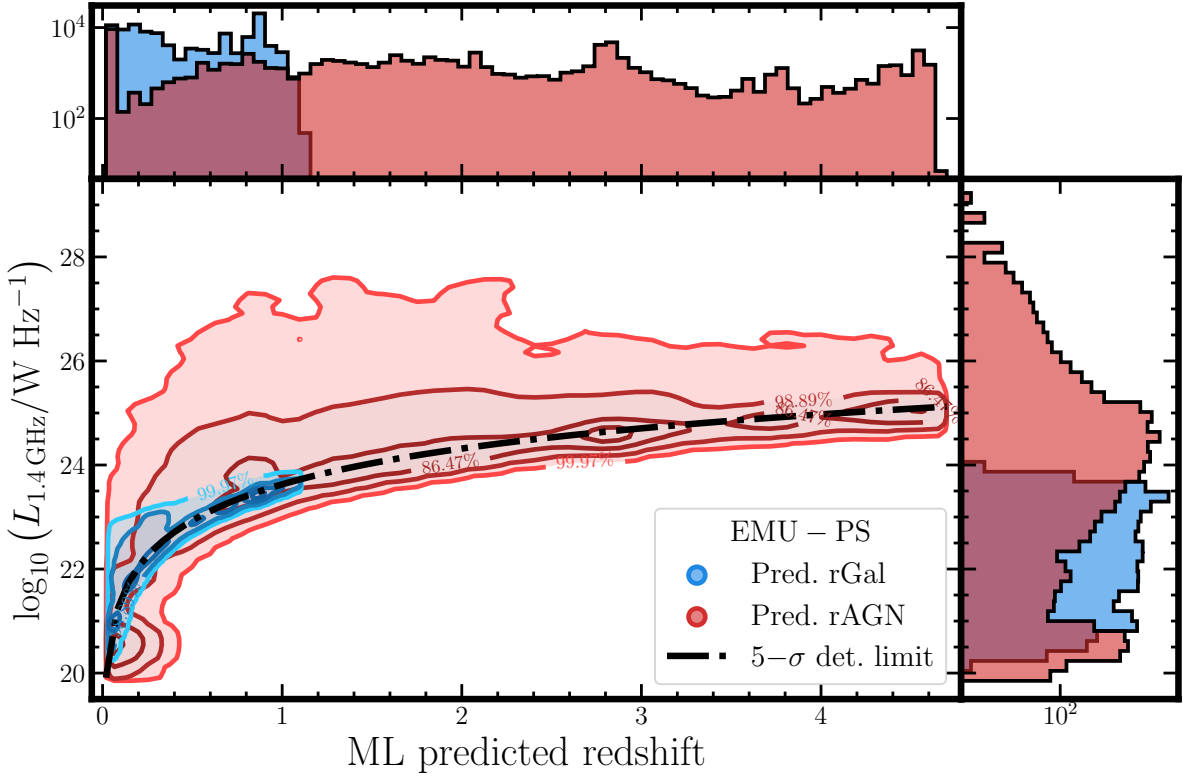


Figure 6.15: Distribution of predicted 1.4 GHz luminosities vs predicted photometric redshifts for radio-detectable AGN (in red) and radio-detectable SFGs (blue) in the area of the EMU-PS catalogue. SFGs with high 1.4 GHz luminosities have been re-labelled as AGN, following the prescriptions by Magliocchetti et al. (2014) and Magliocchetti (2022). Fluxes have been imputed for sources predicted to be radio detectable but without an entry in the EMU-PS catalogue. Description as in Fig. 6.6.

for EMU-PS.

Assuming a flux for the predicted sources missing in the EMU-PS catalogue can be considered as an additional correction applied to our predictions. Without it, the mere verification of a detection in EMU-PS could have been associated to a correction by purity, where the total number of elements is reduced by their detectability. This detection validation affects, mostly, the faint end of the RLF, decreasing the number of low-luminosity sources. The flux imputation allows one to discard such pseudo-correction and only focus on the selection function based upon values from LoTSS-DR1.

With the new extended available radio measurements, it is possible to construct updated RLFs following the steps described earlier in this text. Using the same bin widths and corrections, their values and shapes are presented in Fig. 6.16 as well as in Fig 6.17 for a condensed view. The new imputed fluxes affect mostly the faintest luminosity bins in each redshift range with minor changes at higher values (due to the re-arrangement of the luminosity bins). Upon inspection of Fig. 6.16, it is possible to see that fainter luminosity bins now follow closer previous RLFs than those shown in Fig. 6.12. This effect is more pronounced, in low-redshift bins, for SFG RLFs

CHAPTER 6. MACHINE-ASSISTED LEARNING

than for those from **AGN**.

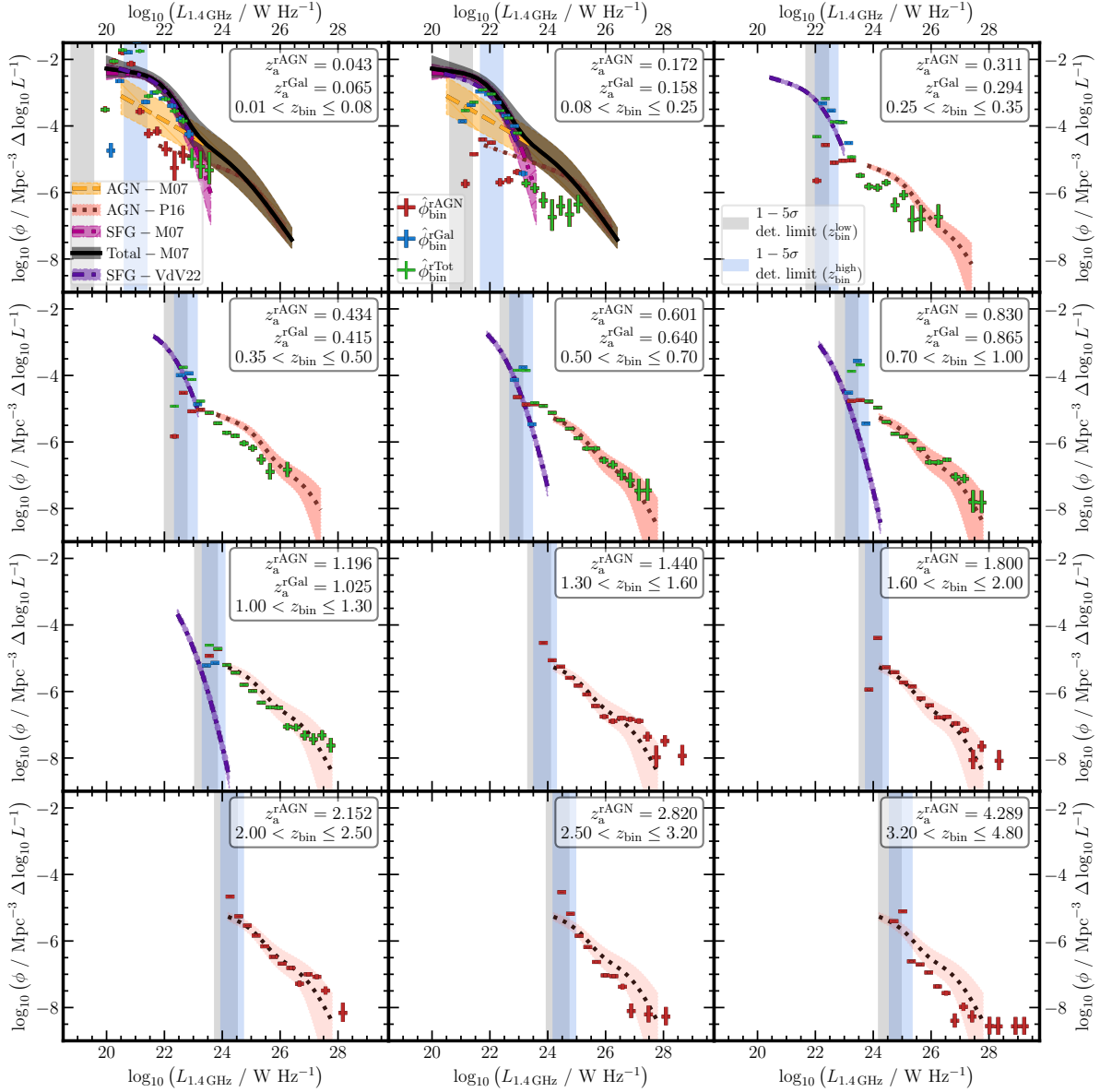


Figure 6.16: RLF (at 1.4 GHz) in **EMU-PS** binned by predicted z values using all sources predicted to be radio-**AGN** and radio-**SFGs** with assumed fluxes when missing. Figure description as in Fig. 6.12.

Most of the features present in Fig. 6.12 are still visible in Fig. 6.16. For instance, the very high number of predicted radio-**AGN** in the first redshift bin, the distance between our **AGN-RLF** and previous works in the second redshift bin ($0.08 < z \leq 0.25$), and the upturn of the values in the brightest luminosity bins for almost all redshift ranges. Differences between both figures start with the sizes of error bars. The larger number of sources available for lower luminosities make the uncertainties, from both the number of elements and cosmic variance, smaller.

Another difference can be seen in the $0.25 < z \leq 0.35$ redshift bin. The previous version

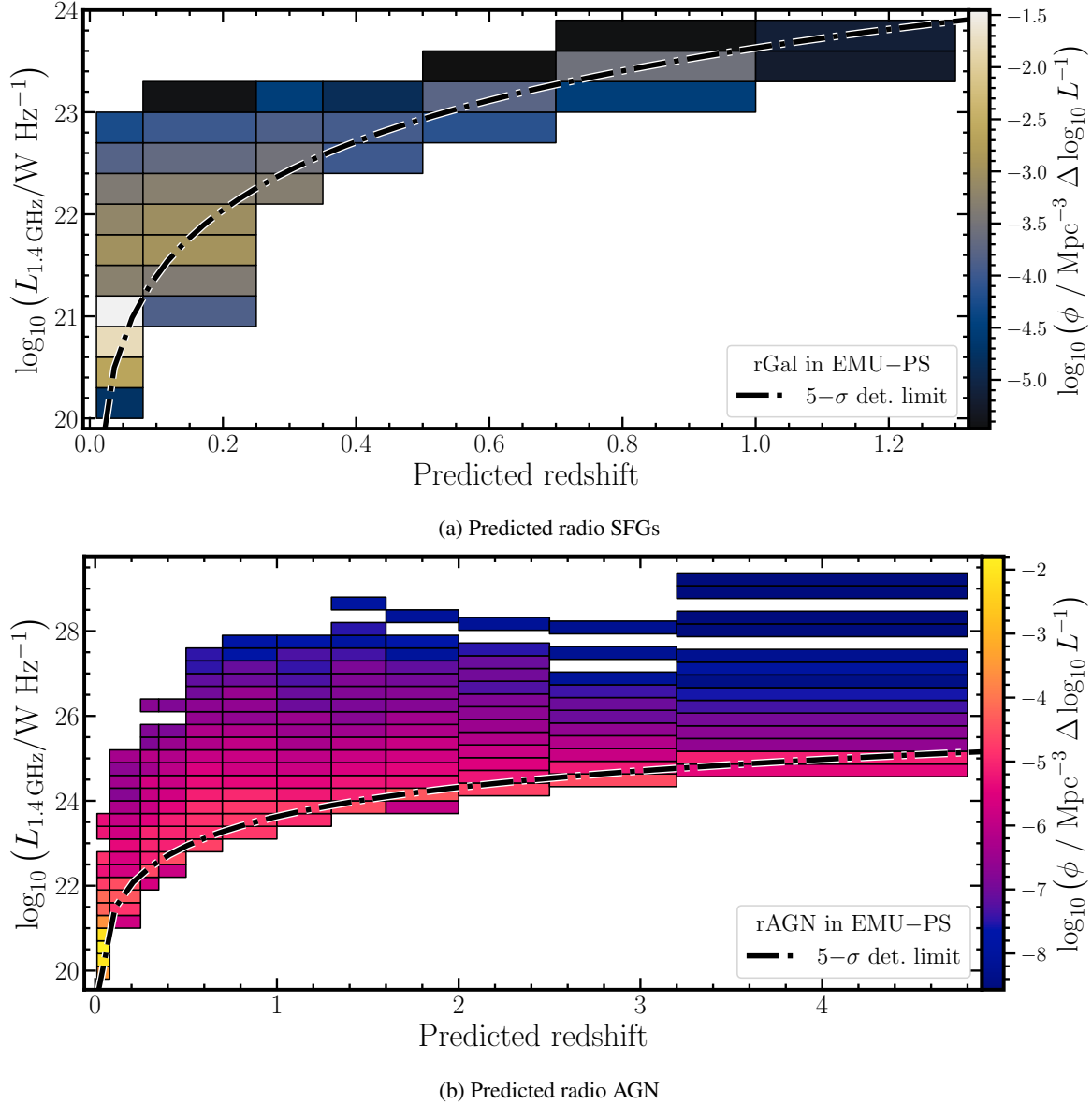


Figure 6.17: Predicted 1.4 GHz luminosity vs predicted redshift for predicted (a) radio SFGs and (b) radio AGN in the EMU-PS catalogue with imputed fluxes. Luminosity and redshift bins as in Fig. 6.12. Sources are coloured according to their estimated precision values and following each individual colourbar. Dot-dashed black line represents 5σ detection limit in EMU-PS.

of the AGN RLF showed a hint for the bump is present in other redshift ranges. However, the bin in Fig. 6.16 does not show such bump as clearly as previously. Thus, we cannot extract conclusions on this regard for it. Consequently, we can now claim that the bump in the AGN RLF is present in the range $0.35 < z \leq 2.5$.

With the corrected RLFs, it is possible to comment on their very good agreement with RLFs from previous works. After taking into account that the redshift values used for our estimates and for the plotting of previous RLFs are slightly different, our estimates are (for non-local sources) are fully compatible with those early RLFs for both radio-AGN and radio-SFGs.

From Fig. 6.17, it is possible to study the evolution of our RLF estimates as a function of

CHAPTER 6. MACHINE-ASSISTED LEARNING

redshift. For both **AGN** and **SFGs**, the change is smooth for similar luminosity ranges. In the case of radio-**AGN**, and if only the bins at $z > 0.35$ are selected, a detailed view of the evolution can be seen in Fig. 6.18.

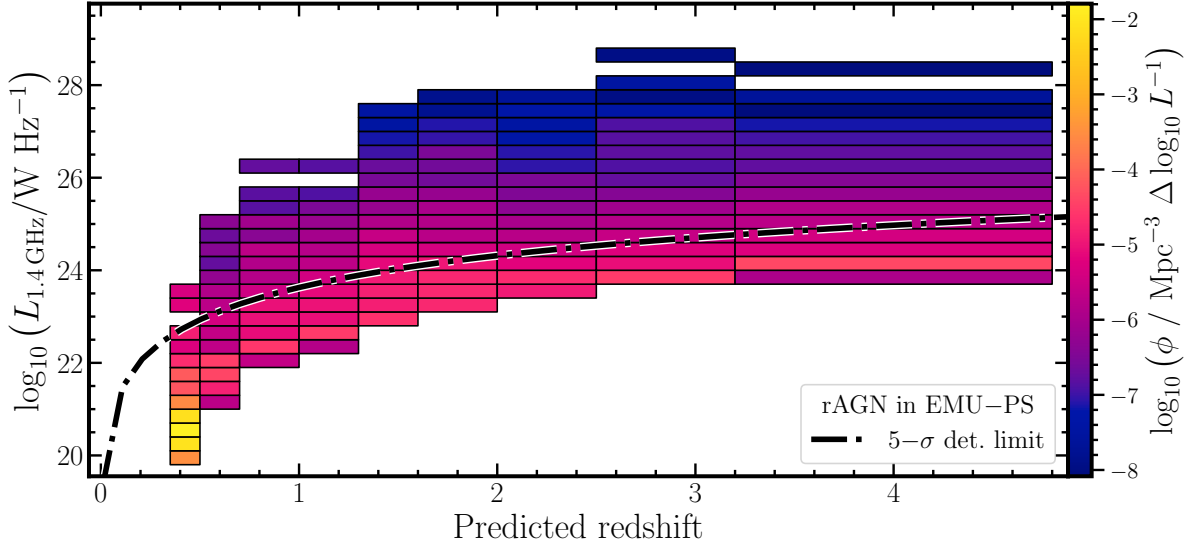


Figure 6.18: Predicted 1.4 GHz luminosity vs predicted redshift for predicted radio **AGN** in the **EMU-PS** catalogue with imputed fluxes at $z > 0.35$. Details as in Fig. 6.17.

Now, and as before, focusing in the range $24 \lesssim \log(L_{1.4 \text{ GHz}}/\text{W Hz}^{-1}) \lesssim 28$, the horizontal change is still close to 1 dex between $z \sim 0.5$ and $z \sim 4$. But now, it is possible to see that, in the region of $0.5 \lesssim z \lesssim 2$, there is a peak in the values of the **RLF**. This peak is, for instance, consistent with what Pracy et al. (2016) has found for their **AGN** sample.

All these estimates for the **RLFs** can be contrasted, additionally, with values obtained from simulations. In particular, for radio-**AGN**, our results can be compared with those from Amarantidis et al. (2019), who compiled number density estimates from several cosmological simulations. For their intermediate-redshift range ($0.8 < z < 1.0$), their simulation-based estimated are compatible with our corresponding bin ($0.7 < z \leq 1.0$). This compatibility takes into consideration that our estimates are based on **IR** detections while those from Amarantidis et al. (2019) consider the full radio population derived from the simulations.

In consequence, it is possible to utilise the results from our prediction pipeline and, only applying **ML**-based corrections, obtain **RLF** estimates that are highly compatible with the current calculations from very diverse methods and surveys.

6.3 Radio counterpart assessment

One of the main issues of multi-wavelength studies of astrophysical sources is the identification of counterparts in observations from different instruments and bands (cf. Sect. 1.2.4). Accurate positioning of sources is crucial to allow further studies (e.g. spectroscopic targeting).

In particular, the radio astronomical community has forecast that the use of **ML** will be instrumental to find radio counterparts of large catalogues (Lazio et al., 2014). Nevertheless, and as stated in Sect. 5.1.2, the number of works using **ML** for predicting the radio detectability of sources (problem comparable to finding radio counterparts) is, to date, very low.

The lack of such studies prompts us to investigate the potential use of **ML** techniques to quantify the probability of a detection to have a counterpart in a different photometric catalogue. In order to assess the idea, we will utilise the radio-detection classification model described in Sect. 6.2 and Appendix B (which is a modification of the model presented in Chapters 4 and 6). Following the discussion of Rohde et al. (2006), we can make direct use of the output probabilities given by the models since they have been calibrated and their distribution is well behaved.

The pipeline described in Sect. 6.2 and Appendix B was applied to the **IR**-detected sources in the **EMU-PS** area. In order to test the radio counterparts, we selected the sources, regardless of their initial classification, that were predicted to be radio-detectable **AGN**. In particular, we focused on the sources that presented high probabilities to be of such class (i.e. probability of being **AGN** higher than $P(\text{C}) = 0.7$ and probability to have radio detection higher than $P(\text{C}) = 0.8$). Then, we plotted these predicted radio-detectable sources on top of the map of **EMU-PS** together with all other **IR**-detections in the surrounding region. Some sources from this selection are shown in Figs. 6.19 to 6.22a.

It is worth noting that in each image, all **IR**-detected sources have been plotted, regardless of their initial or predicted class. The inclusion of the full sample implies that the radio prediction model was applied to all candidates and thus, more uncertainties have been included in the results from its application. These uncertainties do not hinder the analysis regarding radio counterparts.

A first example is shown in Fig. 6.19. It presents a radio-detected **AGN** (ID 00017656) that has been predicted to have be in the same category (i.e. radio-detectable **AGN**, an accurate prediction). The star in the middle of the field shows that the source has been detected in the **EMU-PS** data, as put in evidence by the bright region in the background image. There are two additional **CW**-detected sources within one synthesised beam of distance from the selected target.

CHAPTER 6. MACHINE-ASSISTED LEARNING

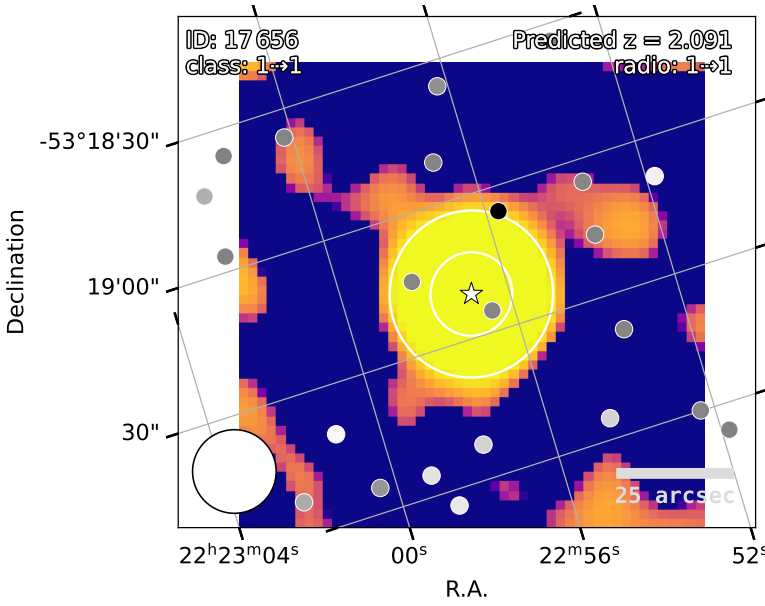


Figure 6.19: Postage stamp of [CW](#)-detected source ID [00017656](#) in the [EMU-PS](#) area (located in the centre of the image). All small circles show the position of a [CW](#) detection in the displayed region without a radio counterpart, while all stars are [CW](#) detections with a confirmed radio detection. Face colours of stars and small circles correlate with the predicted probability of such [CW](#) detections to have a radio detection associated to them, where a brighter hue represents a higher probability. For displaying purposes, all emission below a 1σ detection limit has been set to zero (0). Concentric white circles in the centre of the image limit two regions with a radius of 1 and 2 [full width at half maximum \(FWHM\)](#) centred in the selected source. White circle in bottom right corner represents the [EMU-PS](#) synthesised beam size and gray horizontal lines in the bottom right corner denote a 25'' scale. In the top left corner of figure, the identification number of source is written, as well as its confirmed and predicted AGN (i.e. class) states, where 0 represents a [SFGs](#), 1 represents an [AGN](#), and -1, a source without prior identification. In the top right corner of the figure, the predicted redshift of the source is included, as well as its confirmed and predicted radio detection (i.e. radio_detect) status, with 0 representing a source without radio detection (confirmed or predicted) and 1 stands for radio detection.

They present a darker face colour, indicating that their probability of having a radio counterpart is lower than that of [00017656](#). Thus, the use of the pipeline with the selected source shows that it can be inferred that the large radio source in the background (and only associated by means of distance) can be the counterpart of [00017656](#) with a high likelihood. What Fig. 6.19 presents, then, is the expected output of our prediction pipeline, that is, a radio-[AGN](#) predicted to be such.

The same behaviour can be seen in Figs. 6.20a, 6.20b, 6.20c, 6.20d, and 6.21a. In particular, Figs. 6.20a and 6.20b show two confirmed radio-detected [AGN](#) that have been correctly predicted surrounded by several [CW](#) sources with lower probability of having radio counterparts. Interestingly, the radio source in Fig. 6.20b resembles the emission of a central source with two lobular arms, as radio [AGN](#) with a bent jet. Then, Figs. 6.20c, 6.20d, and 6.21a depict [EMU-PS](#) confirmed detections that do not have an associated [AGN](#) or [SFGs](#) confirmation. Nevertheless, they have been predicted as [AGN](#) with high confidence. As previously, these predictions have the highest likelihood of being detected in the radio in their surroundings (within two [FWHM](#) from their position). It is important to note that the emission depicted in Fig. 6.20d might not appear, in terms of shape, to that of an [AGN](#) or a similar source. Even

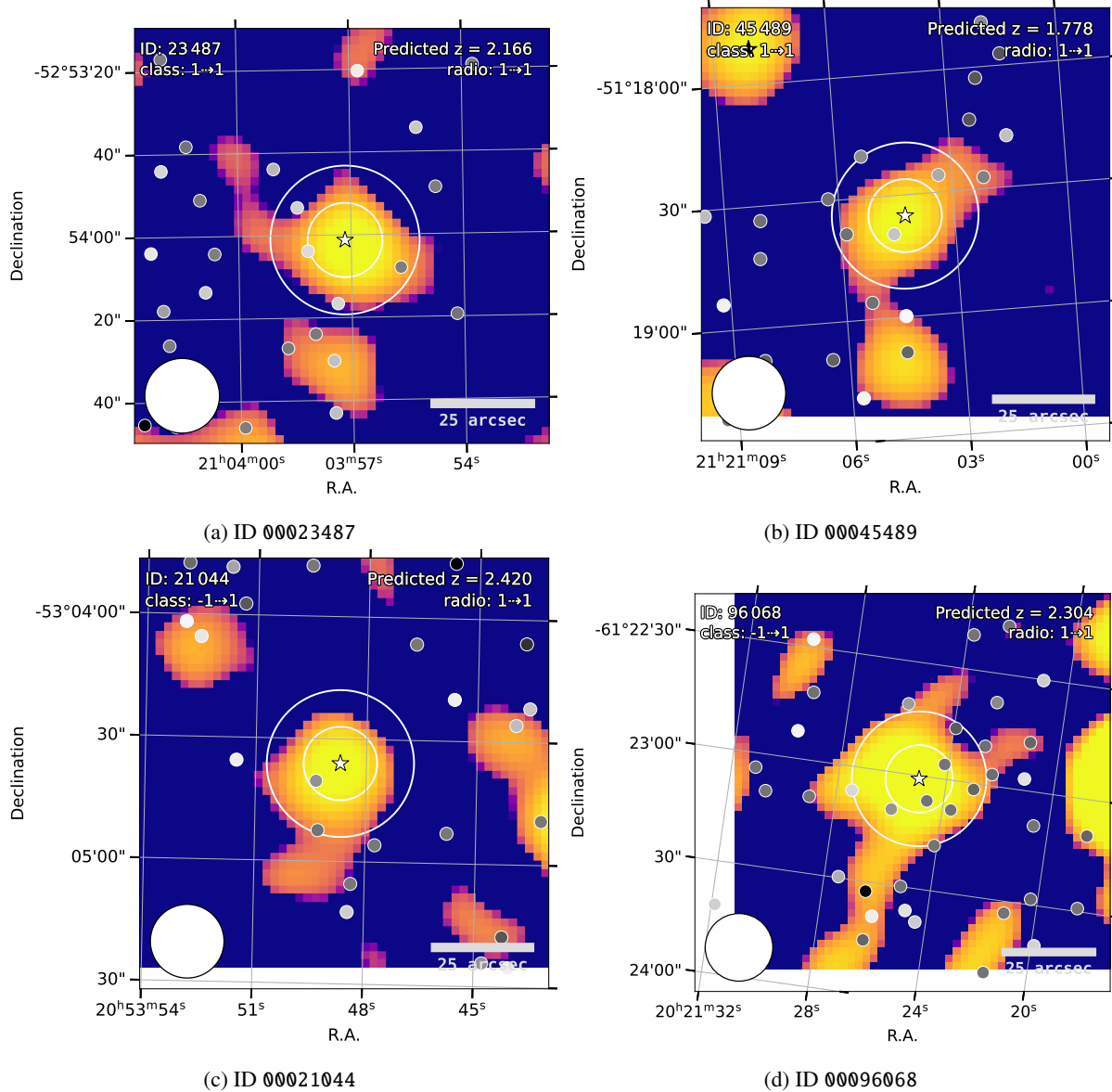


Figure 6.20: Postage stamp of CW-detected sources IDs 00023487, 00045489, 00021044, and 00096068 in the EMU-PS area. Description and details as in Fig. 6.19.

CHAPTER 6. MACHINE-ASSISTED LEARNING

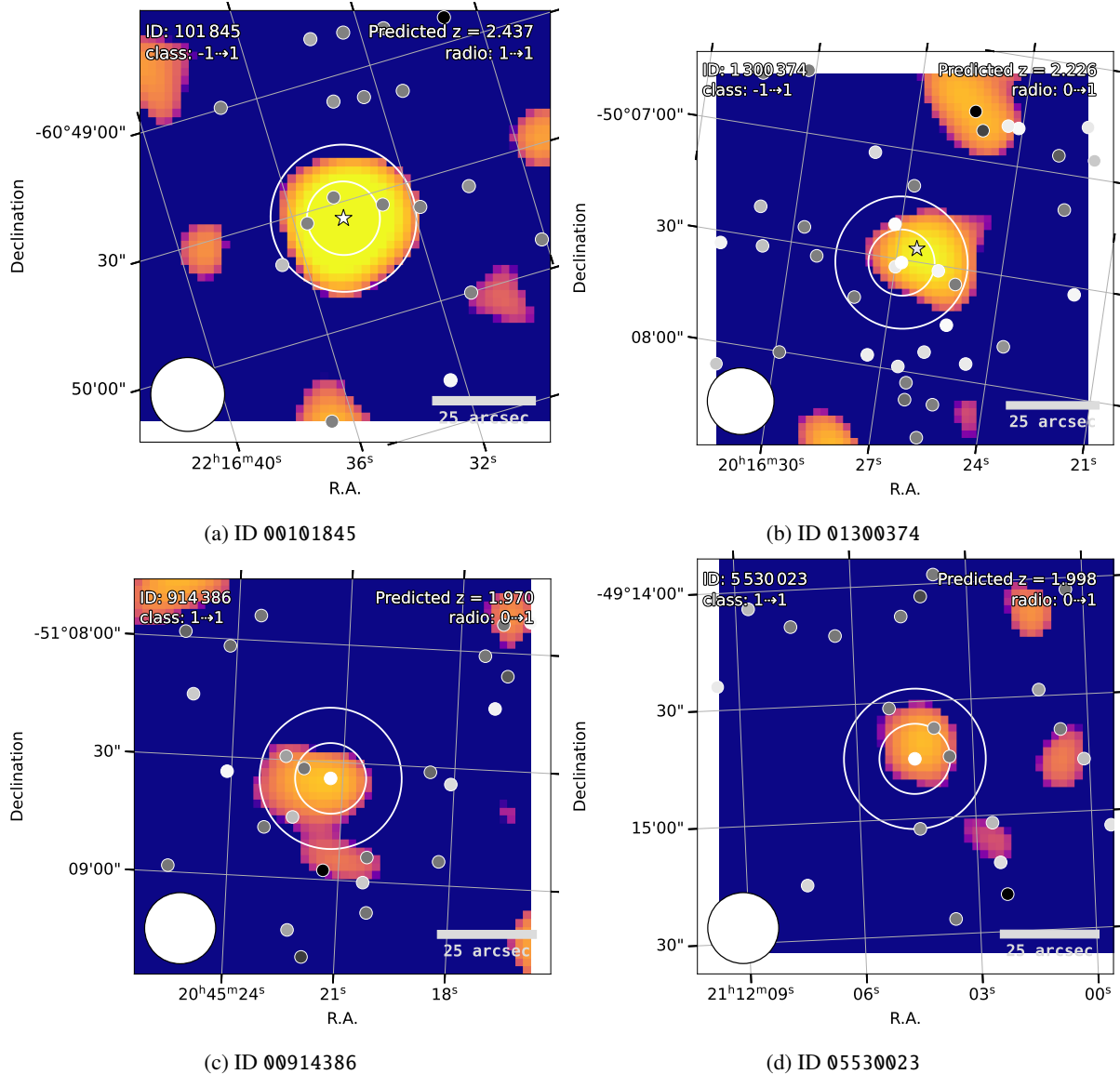


Figure 6.21: Postage stamp of CW-detected sources IDs 00101845, 01300374, 00914386, and 05530023 in the EMU-PS area. Description and details as in Fig. 6.19.

though the radio prediction and the cross-match are in agreement, further studies are needed to confirm the nature of such source.

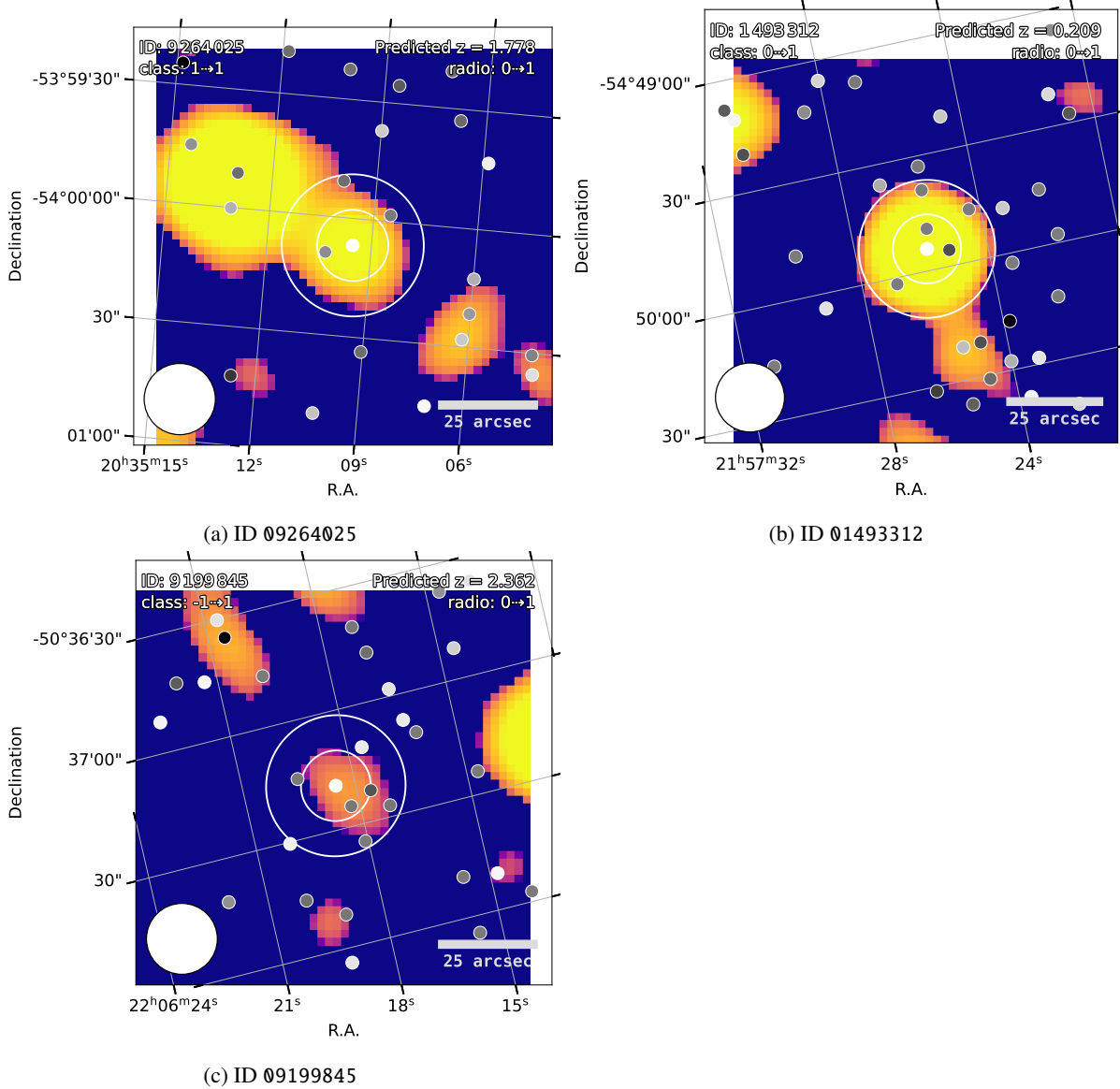


Figure 6.22: Postage stamp of CW-detected sources IDs 09264025, 01493312, and 09199845 in the EMU-PS area. Description and details as in Fig. 6.19.

A different scenario is shown in Figs. 6.21b, 6.21c, 6.21d, 6.22a, 6.22b, and 6.22c, where all CW-detected sources could not be associated (with a direct cross-match) to a source in the EMU-PS catalogue. It is important to note that all emission shown in the postage stamps is above a 1σ limit, while the detections listed in the EMU-PS catalogue are above the 5σ limit (Norris et al., 2021). Thus, it is possible that the catalogue misses faint sources that are picked and predicted by our pipeline.

Figure 6.21b presents an example worth noting. Source ID 01300374, which does not present any prior classification, shows the highest probability of radio detection in its

CHAPTER 6. MACHINE-ASSISTED LEARNING

surroundings, but there is an additional source that has been labelled as the counterpart to the background radio source. This source, shown as a star with a darker face colour, has obtained a lower probability to be detected in the radio bands. Therefore, our detection pipeline has contested the radio counterpart assignation by distance. Additional measurements are needed to determine the most likely counterpart.

Sources ID 00914386 and ID 05530023, depicted in Figs. 6.21c and 6.21d, have been originally labelled as an **AGN** without any radio detection. Our pipeline has assigned to them a high probability to have a radio counterpart over their neighbouring sources. At the same time, their background images show a bright source in the same position. Thus, we have predicted that these source can have a radio counterpart (which might have been previously catalogued should **EMU-PS** have used a lower detection threshold). A similar situation can be seen in Fig. 6.22a with source ID 09264025. Its main difference is that it is located in what might be a more radio-populated region that could present some overlapping sources.

Finally, two sources without an original **AGN** label are presented. Source ID 01493312 (Fig. 6.22b), with a prior label as **SFG**, is located in a very **IR**-crowded region and it has been given, by our prediction pipeline, the highest radio-detection likelihood over their neighbours. In the background **EMU-PS** image, it is possible to see bright radio emission from a point-like source that has a bright appendix. Thus, we have been able to predict the existence of radio emission that was missed by the **EMU-PS** catalogue. Our last example source is ID 09199845 in Fig. 6.22c. Without any prior label (in either `class` or `radio_detect`), it has been predicted to be a radio-detectable **AGN** among all its neighbouring detections. The **EMU-PS** image shows a relatively bright source that might be associated to our prediction.

All these examples show that our prediction pipeline can be used, without any further modification, to understand the location and distribution of radio counterparts of **IR**-detected sources. By virtue of its training with very deep radio observations (i.e. with **LoTSS-DR1**), our pipeline can also help finding sources that might have been overlooked or discarded by other radio surveys and catalogues, as was the case with the **EMU-PS** catalogue.

Future developments

The results presented in this thesis allow us to look for further developments. We list here some steps that can be taken in order to expand our knowledge on either the prediction pipeline or the results obtained from its use.

7.1 Extensive feature importance analysis

Expanding on the analysis of Chapter 5, the behaviour of the model, when applied to different data sets, can be studied extensively.

Each of the models in our prediction pipeline can be studied extensively in order to understand the influence of each of the features that go into their training and optimisation. Beyond the analyses presented in Chapter 5, subsets of sources can be selected and the distributions of their properties can be studied and put in context together with the output values given by the prediction pipeline.

7.2 Evolutionary Map of the Universe

Starting with Sects. 6.2 and 6.3, which show possible applications of the prediction pipeline on data from the EMU-PS, more studies can be performed on the areas covered by EMU. The full products from the EMU survey can be subject to our prediction pipeline and as a way to obtain a large number of radio-AGN candidates. The main barrier to achieve such goal is related to the existence of coverage from deep and homogeneous optical surveys. Our training data incorporates measurements from PS1, which is not fully available in the southern hemisphere. For the EMU-PS data, measurements from the

7.3 Square Kilometre Array

Ultimately, our prediction pipeline can be applied to the full area covered by the future [SKA](#) in order to accelerate the detection of [AGN](#).

Summary

This is the summary of the text we have produced.

With the ultimate intention of better understanding the triggering of radio emission in **AGN**, in this paper, we have shown that it is possible to build a pipeline to detect **AGN**, determine their detectability in radio, within a given flux limit, and predict their redshift value.

Most importantly, we have described a series of methodologies to understand the driving properties of the different decisions, in particular for the radio detection which is, to our best knowledge, the first attempt at doing so.

We have trained the models using multi-wavelength photometry from almost 120 000 spectroscopically identified infrared-detected sources in the **HETDEX** field and created stacked models with them.

These models were applied, sequentially, to 15 018 144 infrared detections in the **HETDEX** Spring field, arriving to the creation of 68 252 radio **AGN** candidates with their corresponding predicted redshift values. Additionally, we applied the models to 3 568 478 infrared detections in the **S82** field, obtaining 22 445 new radio **AGN** candidates with their predicted redshift values.

We have, then, applied a number of analyses on the models to understand the influence of the observed properties over the predictions and their confidence levels. In particular, the use of **SHAP** values gives the opportunity to extract the influence that the feature set has for each individual prediction.

From the application of the prediction pipeline on labelled and unlabelled sources and the analysis of the predictions and the models themselves, the following conclusions can be drawn.

- Generalised stacking is a useful procedure which collects results from individual **ML** algorithms into a single model that can outperform each of the individual models, while preventing the inclusion of biases from individual algorithms. Proper selection of models and input features, together with detailed probability and threshold calibration maximises the metrics of the final model.
- Classification between **AGN** and **SFGs** derived from our model is in line with previous works. Our pipeline is able to retrieve a high fraction of previously-classified **AGN** from

CHAPTER 7. FUTURE DEVELOPMENTS

HETDEX (recall = 0.9621, precision = 0.9449) and from the **S82** field (recall = 0.9401, precision = 0.9481).

- Radio detection classification for predicted **AGN** has proven to be highly demanding in terms of data needed for creating the models. Thanks to the use of the techniques shown in this article (i.e. feature creation and selection, generalised stacking, probability calibration, and threshold optimisation), we are able to retrieve previously-known radio-detectable **AGN** in the **HETDEX** field (recall = 0.5216, precision = 0.3528) and in the **S82** field (recall = 0.5816, precision = 0.1229). These rates improve significantly upon a purely random selection(4 times better for the **HETDEX** field and 13 times better for **S82**), showing the power of **ML** methods for obtaining new **RG** candidates.
- The prediction of redshift values for sources classified to be radio-detectable **AGN** can deliver results that are in line with works that use either traditional or **ML** methods.
- Our models (classification and regression) can be applied to areas of the sky which have different radio coverage from that used for training without a strong degradation of the prediction results. This feature can lead to the use of our pipeline over very distinct datasets (in radio and multi-wavelength coverage) expecting to recover the sources predicted to be radio-detectable **AGN** with a high probability.
- **ML** models cannot be only used for a direct prediction of a value (or a set of values). They can also be subject to analyses that allow to extract additional results. We took advantage of this fact by using global and local feature importances to derive novel colour-colour **AGN** selection methods.

With the next generation of observatories already producing source catalogues with an order of magnitude better sensitivity over large areas of the sky than previously, such as the **Rapid ASKAP Continuum Survey (RACS; McConnell et al., 2020)**, **EMU**, and **MIGHTEE**, the need to understand the fraction of those radio detections related to **AGN** and determine counterparts across wavelengths is more necessary than ever. Although we developed the pipeline as a tool to better understand the aforementioned issues, we foresee additional possibilities in which the pipeline can be of great use. The first of this possibilities involves the use of the pipeline to assist with the selection of radio-detectable **AGN** within any set of observations. This application might turn particularly valuable in recent surveys carried out with **MeerKAT** or the future **SKA**.

where the population at the faintest sources will be dominated by **SFGs**. This change needs to use the corresponding data in the training set.

Future developments of the pipeline will concentrate on minimising the existent biases in the training sample as well as in increasing the coverage of the parameter space. We also plan to generalise the pipeline to make it useful for non-radio or galaxy-related research communities. These developments include, for instance, the capability to carry the full analysis for the galactic and stellar populations (i.e. models to determine if a **SFG** can be detected in the radio and to predict redshift values for **SFGs** and non-radio **AGN**).

In order to increase the parameter space of our training sets, we plan to include information from radio surveys with different characteristics. Namely, shallower, but with larger area, and less extended but with deeper multi-wavelength data. Similarly, the inclusion of **FIR**, X-ray, and multi-survey radio measurements makes part of our efforts to improve detections, not only in radio, but in additional wavelengths.

This page intentionally left blank.

Data and software acknowledgements

This work made use of data products from the Wide-field Infrared Survey Explorer, which is a joint project of the University of California, Los Angeles, and the Jet Propulsion Laboratory/California Institute of Technology, funded by the National Aeronautics and Space Administration.

LOFAR data products were provided by the LOFAR Surveys Key Science project (LSKSP¹) and were derived from observations with the International LOFAR Telescope (ILT). LOFAR (van Haarlem et al., 2013) is the Low Frequency Array designed and constructed by ASTRON. It has observing, data processing, and data storage facilities in several countries, which are owned by various parties (each with their own funding sources), and which are collectively operated by the ILT foundation under a joint scientific policy. The efforts of the LSKSP have benefited from funding from the European Research Council, NOVA, NWO, CNRS-INSU, the SURF Co-operative, the UK Science and Technology Funding Council and the Jülich Supercomputing Centre.

The Pan-STARRS1 Surveys (PS1) and the PS1 public science archive have been made possible through contributions by the Institute for Astronomy, the University of Hawaii, the Pan-STARRS Project Office, the Max-Planck Society and its participating institutes, the Max Planck Institute for Astronomy, Heidelberg and the Max Planck Institute for Extraterrestrial Physics, Garching, The Johns Hopkins University, Durham University, the University of Edinburgh, the Queen's University Belfast, the Harvard-Smithsonian Center for Astrophysics, the Las Cumbres Observatory Global Telescope Network Incorporated, the National Central University of Taiwan, the Space Telescope Science Institute, the National Aeronautics and Space Administration under Grant No. NNX08AR22G issued through the Planetary Science Division of the NASA Science Mission Directorate, the National Science Foundation Grant No. AST-1238877, the University of Maryland, Eötvös Loránd University (ELTE), the Los Alamos National Laboratory, and the Gordon and Betty Moore Foundation.

This thesis makes use of data products from the Two Micron All Sky Survey, which is a joint project of the University of Massachusetts and the Infrared Processing and Ana-

¹<https://lofar-surveys.org/>

lysis Center/California Institute of Technology, funded by the National Aeronautics and Space Administration and the National Science Foundation.

This work made use of public data from the Sloan Digital Sky Survey, Data Release 16. Funding for the Sloan Digital Sky Survey IV has been provided by the Alfred P. Sloan Foundation, the U.S. Department of Energy Office of Science, and the Participating Institutions. SDSS-IV acknowledges support and resources from the Center for High Performance Computing at the University of Utah. The SDSS website is www.sdss.org. SDSS-IV is managed by the Astrophysical Research Consortium for the Participating Institutions of the SDSS Collaboration including the Brazilian Participation Group, the Carnegie Institution for Science, Carnegie Mellon University, Center for Astrophysics | Harvard & Smithsonian, the Chilean Participation Group, the French Participation Group, Instituto de Astrofísica de Canarias, The Johns Hopkins University, Kavli Institute for the Physics and Mathematics of the Universe (IPMU) / University of Tokyo, the Korean Participation Group, Lawrence Berkeley National Laboratory, Leibniz Institut für Astrophysik Potsdam (AIP), Max-Planck-Institut für Astronomie (MPIA Heidelberg), Max-Planck-Institut für Astrophysik (MPA Garching), Max-Planck-Institut für Extraterrestrische Physik (MPE), National Astronomical Observatories of China, New Mexico State University, New York University, University of Notre Dame, Observatório Nacional / MCTI, The Ohio State University, Pennsylvania State University, Shanghai Astronomical Observatory, United Kingdom Participation Group, Universidad Nacional Autónoma de México, University of Arizona, University of Colorado Boulder, University of Oxford, University of Portsmouth, University of Utah, University of Virginia, University of Washington, University of Wisconsin, Vanderbilt University, and Yale University.

This scientific work uses data obtained from Inyarrimanha Ilgari Bundara / the Murchison Radio-astronomy Observatory. We acknowledge the Wajarri Yamaji People as the Traditional Owners and native title holders of the Observatory site. CSIRO's ASKAP radio telescope is part of the Australia Telescope National Facility (<https://ror.org/05qajvd42>). Operation of ASKAP is funded by the Australian Government with support from the National Collaborative Research Infrastructure Strategy. ASKAP uses the resources of the Pawsey Supercomputing Research Centre. Establishment of ASKAP, Inyarrimanha Ilgari Bundara, the CSIRO Murchison Radio-astronomy Observatory and the Pawsey Supercomputing Research Centre are initiatives of the Australian Government, with support from the Government of Western Australia and the Science and Industry Endowment Fund.

Part of this work is based on data obtained from the ESO Science Archive Facility with

DOI(s): <https://doi.org/10.18727/archive/56>.

This project used public archival data from the Dark Energy Survey (DES). Funding for the DES Projects has been provided by the U.S. Department of Energy, the U.S. National Science Foundation, the Ministry of Science and Education of Spain, the Science and Technology Facilities Council of the United Kingdom, the Higher Education Funding Council for England, the National Center for Supercomputing Applications at the University of Illinois at Urbana-Champaign, the Kavli Institute of Cosmological Physics at the University of Chicago, the Center for Cosmology and Astro-Particle Physics at the Ohio State University, the Mitchell Institute for Fundamental Physics and Astronomy at Texas A&M University, Financiadora de Estudos e Projetos, Fundação Carlos Chagas Filho de Amparo à Pesquisa do Estado do Rio de Janeiro, Conselho Nacional de Desenvolvimento Científico e Tecnológico and the Ministério da Ciência, Tecnologia e Inovação, the Deutsche Forschungsgemeinschaft, and the Collaborating Institutions in the Dark Energy Survey. The Collaborating Institutions are Argonne National Laboratory, the University of California at Santa Cruz, the University of Cambridge, Centro de Investigaciones Energéticas, Medioambientales y Tecnológicas-Madrid, the University of Chicago, University College London, the DES-Brazil Consortium, the University of Edinburgh, the Eidgenössische Technische Hochschule (ETH) Zürich, Fermi National Accelerator Laboratory, the University of Illinois at Urbana-Champaign, the Institut de Ciències de l'Espai (IEEC/CSIC), the Institut de Física d'Altes Energies, Lawrence Berkeley National Laboratory, the Ludwig-Maximilians Universität München and the associated Excellence Cluster Universe, the University of Michigan, the National Optical Astronomy Observatory, the University of Nottingham, The Ohio State University, the OzDES Membership Consortium, the University of Pennsylvania, the University of Portsmouth, SLAC National Accelerator Laboratory, Stanford University, the University of Sussex, and Texas A&M University. Based in part on observations at Cerro Tololo Inter-American Observatory, National Optical Astronomy Observatory, which is operated by the Association of Universities for Research in Astronomy (AURA) under a cooperative agreement with the National Science Foundation.

This work has made use of data from the European Space Agency (ESA) mission *Gaia* (<https://www.cosmos.esa.int/gaia>), processed by the *Gaia* Data Processing and Analysis Consortium (DPAC, <https://www.cosmos.esa.int/web/gaia/dpac/consortium>). Funding for the DPAC has been provided by national institutions, in particular the institutions participating in the *Gaia* Multilateral Agreement.

The Legacy Surveys imaging of the DESI footprint is supported by the Director, Office

of Science, Office of High Energy Physics of the U.S. Department of Energy under Contract No. DE-AC02-05CH1123, by the National Energy Research Scientific Computing Center, a DOE Office of Science User Facility under the same contract; and by the U.S. National Science Foundation, Division of Astronomical Sciences under Contract No. AST-0950945 to NOAO.

This project makes use of the MaNGA-Pipe3D dataproducts. We thank the IA-UNAM MaNGA team for creating this catalogue, and the Conacyt Project CB-285080 for supporting them.

This research has made use of NASA’s Astrophysics Data System, TOPCAT² (Taylor, 2005), JupyterLab³ (Kluyver et al., 2016), ‘Aladin sky atlas’ (v11.0.24; Bonnarel et al., 2000) developed at CDS, Strasbourg Observatory, France, and the VizieR catalogue access tool, CDS, Strasbourg, France (DOI : 10.26093/cds/vizier). The original description of the VizieR service was published in Ochsenbein et al. (2000). This research has also made use of hips2fits,⁴ a service provided by CDS.

This research has made use of the Spanish Virtual Observatory (<https://svo.ca.b.inta-csic.es>; Rodrigo and Solano, 2020; Rodrigo et al., 2012) project funded by MCIN/AEI/10.13039/501100011033/ through grant PID2020-112949GB-I00

This work made extensive use of the Python packages PyCaret⁵ (v2.3.10; Ali, 2020), scikit-learn (v0.23.2; Pedregosa et al., 2011), pandas⁶ (v1.4.2; McKinney, 2010), Astropy⁷, a community-developed core Python package for Astronomy (v5.0; Astropy Collaboration et al., 2013; Astropy Collaboration et al., 2018; Astropy Collaboration et al., 2022), Matplotlib (v3.5.1; Hunter, 2007), betacal⁸ (v1.1.0), CMasher⁹ (v1.6.3; van der Velden, 2020), faiss¹⁰ (v1.7.2; Johnson et al., 2019), skyproj¹¹ (v1.1.0), and mocpy¹² (v0.13.1; Baumann et al., 2023).

²<http://www.star.bris.ac.uk/~mbt/topcat/>

³<https://jupyter.org>

⁴<https://alasky.cds.unistra.fr/hips-image-services/hips2fits>

⁵<https://pycaret.org>

⁶<https://pandas.pydata.org>

⁷<https://www.astropy.org>

⁸<https://betacal.github.io>

⁹<https://github.com/1313e/CMasher>

¹⁰<https://faiss.ai>

¹¹<https://github.com/LSSTDESC/skyproj>

¹²<https://github.com/cds-astro/mocpy/>

References

- Abbott, T. M. C., Abdalla, F. B., et al. (Dec. 2018). ‘The Dark Energy Survey: Data Release 1’. In: ApJS 239.2, 18, p. 18. doi: [10.3847/1538-4365/aae9f0](https://doi.org/10.3847/1538-4365/aae9f0).
- Abbott, T. M. C., Adamów, M., et al. (Aug. 2021). ‘The Dark Energy Survey Data Release 2’. In: ApJS 255.2, 20, p. 20. doi: [10.3847/1538-4365/ac00b3](https://doi.org/10.3847/1538-4365/ac00b3).
- Abdo, A. A., Ackermann, M., et al. (May 2010). ‘The First Catalog of Active Galactic Nuclei Detected by the Fermi Large Area Telescope’. In: ApJ 715.1, pp. 429–457. doi: [10.1088/0004-637X/715/1/429](https://doi.org/10.1088/0004-637X/715/1/429).
- Abdurro’uf, Accetta, K., et al. (Apr. 2022). ‘The Seventeenth Data Release of the Sloan Digital Sky Surveys: Complete Release of MaNGA, MaStar, and APOGEE-2 Data’. In: ApJS 259.2, 35, p. 35. doi: [10.3847/1538-4365/ac4414](https://doi.org/10.3847/1538-4365/ac4414).
- Abramson, I. S. (1982). ‘On Bandwidth Variation in Kernel Estimates-A Square Root Law’. In: *The Annals of Statistics* 10.4, pp. 1217–1223. issn: 00905364. url: <http://www.jstor.org/stable/2240724> (visited on 20/01/2024).
- Adam, A., Perreault-Levasseur, L., et al. (July 2023). ‘Pixelated Reconstruction of Foreground Density and Background Surface Brightness in Gravitational Lensing Systems Using Recurrent Inference Machines’. In: ApJ 951.1, 6, p. 6. doi: [10.3847/1538-4357/accf84](https://doi.org/10.3847/1538-4357/accf84).
- Aguado, D. S., Ahumada, R., et al. (Feb. 2019). ‘The Fifteenth Data Release of the Sloan Digital Sky Surveys: First Release of MaNGA-derived Quantities, Data Visualization Tools, and Stellar Library’. In: ApJS 240.2, 23, p. 23. doi: [10.3847/1538-4365/aaf651](https://doi.org/10.3847/1538-4365/aaf651).
- Agüeros, M. A., Ivezić, Ž., et al. (Sept. 2005). ‘The Ultraviolet, Optical, and Infrared Properties of Sloan Digital Sky Survey Sources Detected by GALEX’. In: AJ 130.3, pp. 1022–1036. doi: [10.1086/432160](https://doi.org/10.1086/432160).
- Ahumada, R., Prieto, C. A., et al. (July 2020). ‘The 16th Data Release of the Sloan Digital Sky Surveys: First Release from the APOGEE-2 Southern Survey and Full Release of eBOSS Spectra’. In: ApJS 249.1, 3, p. 3. doi: [10.3847/1538-4365/ab929e](https://doi.org/10.3847/1538-4365/ab929e).
- Aihara, H., Allende Prieto, C., et al. (Apr. 2011). ‘The Eighth Data Release of the Sloan Digital Sky Survey: First Data from SDSS-III’. In: ApJS 193.2, 29, p. 29. doi: [10.1088/0067-0049/193/2/29](https://doi.org/10.1088/0067-0049/193/2/29).
- Alegre, L., Sabater, J., et al. (Nov. 2022). ‘A machine-learning classifier for LOFAR radio galaxy cross-matching techniques’. In: MNRAS 516.4, pp. 4716–4738. doi: [10.1093/mnras/stac1888](https://doi.org/10.1093/mnras/stac1888).
- Ali, M. (Apr. 2020). *PyCaret: An open source, low-code machine learning library in Python*. PyCaret version 2.3. URL: <https://www.pycaret.org>.
- Allen, D. M. (1974). ‘The Relationship Between Variable Selection and Data Agumentation and a Method for Prediction’. In: *Technometrics* 16.1, pp. 125–127. doi: [10.1080/00401706.1974.10489157](https://doi.org/10.1080/00401706.1974.10489157).
- Allison, P. (2001). *Missing Data*. Quantitative Applications in the Social Sciences. SAGE Publications. ISBN: 9781452207902.

REFERENCES

- Almosallam, I. A., Jarvis, M. J., and Roberts, S. J. (Oct. 2016a). ‘GPZ: non-stationary sparse Gaussian processes for heteroscedastic uncertainty estimation in photometric redshifts’. In: MNRAS 462.1, pp. 726–739. doi: [10.1093/mnras/stw1618](https://doi.org/10.1093/mnras/stw1618).
- Almosallam, I. A., Lindsay, S. N., et al. (Jan. 2016b). ‘A sparse Gaussian process framework for photometric redshift estimation’. In: MNRAS 455.3, pp. 2387–2401. doi: [10.1093/mnras/stv2425](https://doi.org/10.1093/mnras/stv2425).
- Alqasim, A. and Page, M. J. (Apr. 2023). ‘A new method to determine X-ray luminosity functions of AGN and their evolution with redshift’. In: MNRAS 520.3, pp. 3827–3846. doi: [10.1093/mnras/stad007](https://doi.org/10.1093/mnras/stad007).
- Amarantidis, S., Afonso, J., et al. (May 2019). ‘The first supermassive black holes: indications from models for future observations’. In: MNRAS 485.2, pp. 2694–2709. doi: [10.1093/mnras/stz551](https://doi.org/10.1093/mnras/stz551).
- An, T., Zhang, Y., and Frey, S. (Sept. 2020). ‘A method for checking high-redshift identification of radio AGNs’. In: MNRAS 497.2, pp. 2260–2264. doi: [10.1093/mnras/staa2132](https://doi.org/10.1093/mnras/staa2132).
- Ananna, T. T., Salvato, M., et al. (Nov. 2017). ‘AGN Populations in Large-volume X-Ray Surveys: Photometric Redshifts and Population Types Found in the Stripe 82X Survey’. In: ApJ 850.1, 66, p. 66. doi: [10.3847/1538-4357/aa937d](https://doi.org/10.3847/1538-4357/aa937d).
- Anbajagane, D., Evrard, A. E., and Farahi, A. (Jan. 2022). ‘Baryonic imprints on DM haloes: population statistics from dwarf galaxies to galaxy clusters’. In: MNRAS 509.3, pp. 3441–3461. doi: [10.1093/mnras/stab3177](https://doi.org/10.1093/mnras/stab3177).
- Andonie, C., Alexander, D. M., et al. (Dec. 2022). ‘A panchromatic view of infrared quasars: excess star formation and radio emission in the most heavily obscured systems’. In: MNRAS 517.2, pp. 2577–2598. doi: [10.1093/mnras/stac2800](https://doi.org/10.1093/mnras/stac2800).
- Aniyan, A. K. and Thorat, K. (June 2017). ‘Classifying Radio Galaxies with the Convolutional Neural Network’. In: ApJS 230.2, 20, p. 20. doi: [10.3847/1538-4365/aa7333](https://doi.org/10.3847/1538-4365/aa7333).
- Annis, J., Soares-Santos, M., et al. (Oct. 2014). ‘The Sloan Digital Sky Survey Coadd: 275 deg² of Deep Sloan Digital Sky Survey Imaging on Stripe 82’. In: ApJ 794.2, 120, p. 120. doi: [10.1088/0004-637X/794/2/120](https://doi.org/10.1088/0004-637X/794/2/120).
- Antonucci, R. (Jan. 1993). ‘Unified models for active galactic nuclei and quasars.’ In: ARA&A 31, pp. 473–521. doi: [10.1146/annurev.aa.31.090193.002353](https://doi.org/10.1146/annurev.aa.31.090193.002353).
- Arévalo, P., Uttley, P., et al. (Sept. 2008). ‘Correlated X-ray/optical variability in the quasar MR2251-178’. In: MNRAS 389.3, pp. 1479–1488. doi: [10.1111/j.1365-2966.2008.13719.x](https://doi.org/10.1111/j.1365-2966.2008.13719.x).
- Arévalo, P., Uttley, P., et al. (Aug. 2009). ‘Correlation and time delays of the X-ray and optical emission of the Seyfert Galaxy NGC 3783’. In: MNRAS 397.4, pp. 2004–2014. doi: [10.1111/j.1365-2966.2009.15110.x](https://doi.org/10.1111/j.1365-2966.2009.15110.x).
- Arnouts, S., Cristiani, S., et al. (Dec. 1999). ‘Measuring and modelling the redshift evolution of clustering: the Hubble Deep Field North’. In: MNRAS 310.2, pp. 540–556. doi: [10.1046/j.1365-8711.1999.02978.x](https://doi.org/10.1046/j.1365-8711.1999.02978.x).
- Arsioli, B. and Dedin, P. (Oct. 2020). ‘Machine learning applied to multifrequency data in astrophysics: blazar classification’. In: MNRAS 498.2, pp. 1750–1764. doi: [10.1093/mnras/staa2449](https://doi.org/10.1093/mnras/staa2449).
- Assef, R. J., Stern, D., et al. (July 2013). ‘Mid-infrared Selection of Active Galactic Nuclei with the Wide-field Infrared Survey Explorer. II. Properties of WISE-selected Active Galactic Nuclei in the NDWFS Boötes Field’. In: ApJ 772.1, 26, p. 26. doi: [10.1088/0004-637X/772/1/26](https://doi.org/10.1088/0004-637X/772/1/26).

- Assef, R. J., Stern, D., et al. (Feb. 2018). ‘The WISE AGN Catalog’. In: ApJS 234.2, 23, p. 23. doi: [10.3847/1538-4365/aaa00a](https://doi.org/10.3847/1538-4365/aaa00a).
- Astropy Collaboration, Price-Whelan, A. M., et al. (Sept. 2018). ‘The Astropy Project: Building an Open-science Project and Status of the v2.0 Core Package’. In: AJ 156.3, 123, p. 123. doi: [10.3847/1538-3881/aabc4f](https://doi.org/10.3847/1538-3881/aabc4f).
- Astropy Collaboration, Price-Whelan, A. M., et al. (Aug. 2022). ‘The Astropy Project: Sustaining and Growing a Community-oriented Open-source Project and the Latest Major Release (v5.0) of the Core Package’. In: ApJ 935.2, 167, p. 167. doi: [10.3847/1538-4357/ac7c74](https://doi.org/10.3847/1538-4357/ac7c74).
- Astropy Collaboration, Robitaille, T. P., et al. (Oct. 2013). ‘Astropy: A community Python package for astronomy’. In: A&A 558, A33, A33. doi: [10.1051/0004-6361/201322068](https://doi.org/10.1051/0004-6361/201322068).
- Atek, H., Chemerynska, I., et al. (Oct. 2023). ‘JWST UNCOVER: discovery of $z > 9$ galaxy candidates behind the lensing cluster Abell 2744’. In: MNRAS 524.4, pp. 5486–5496. doi: [10.1093/mnras/stad1998](https://doi.org/10.1093/mnras/stad1998).
- Auge, C., Sanders, D., et al. (Nov. 2023). ‘The Accretion History of AGN: The Spectral Energy Distributions of X-Ray-luminous Active Galactic Nuclei’. In: ApJ 957.1, 19, p. 19. doi: [10.3847/1538-4357/acf21a](https://doi.org/10.3847/1538-4357/acf21a).
- Avni, Y. and Bahcall, J. N. (Feb. 1980). ‘On the simultaneous analysis of several complete samples. The V/Vmax and Ve/Va variables, with applications to quasars.’ In: ApJ 235, pp. 694–716. doi: [10.1086/157673](https://doi.org/10.1086/157673).
- Bahcall, J. N. and Kozlovsky, B.-Z. (Mar. 1969). ‘Some Models of the Emission-Line Region of 3c 273’. In: ApJ 155, p. 1077. doi: [10.1086/149935](https://doi.org/10.1086/149935).
- Baldwin, J. A., Phillips, M. M., and Terlevich, R. (Feb. 1981). ‘Classification parameters for the emission-line spectra of extragalactic objects.’ In: PASP 93, pp. 5–19. doi: [10.1086/130766](https://doi.org/10.1086/130766).
- Ball, N. M. and Brunner, R. J. (Jan. 2010). ‘Data Mining and Machine Learning in Astronomy’. In: *International Journal of Modern Physics D* 19.7, pp. 1049–1106. doi: [10.1142/S0218271810017160](https://doi.org/10.1142/S0218271810017160).
- Ball, N. M., Brunner, R. J., et al. (Aug. 2008). ‘Robust Machine Learning Applied to Astronomical Data Sets. III. Probabilistic Photometric Redshifts for Galaxies and Quasars in the SDSS and GALEX’. In: ApJ 683.1, pp. 12–21. doi: [10.1086/589646](https://doi.org/10.1086/589646).
- Baltay, C., Grossman, L., et al. (Apr. 2021). ‘Low-redshift Type Ia Supernova from the LSQ/LCO Collaboration’. In: PASP 133.1022, 044002, p. 044002. doi: [10.1088/1538-3873/abd417](https://doi.org/10.1088/1538-3873/abd417).
- Barbieri, C. and Bertola, F. (Jan. 1972). ‘Identification of 5C4 radio sources.’ In: MNRAS 156, pp. 399–409. doi: [10.1093/mnras/156.4.399](https://doi.org/10.1093/mnras/156.4.399).
- Baron, D. (Apr. 2019). ‘Machine Learning in Astronomy: a practical overview’. In: *arXiv e-prints*, arXiv:1904.07248, arXiv:1904.07248.
- Baron, D. and Poznanski, D. (Mar. 2017). ‘The weirdest SDSS galaxies: results from an outlier detection algorithm’. In: MNRAS 465.4, pp. 4530–4555. doi: [10.1093/mnras/stw3021](https://doi.org/10.1093/mnras/stw3021).
- Barrows, R. S., Comerford, J. M., et al. (Dec. 2021). ‘A Catalog of Host Galaxies for WISE-selected AGN: Connecting Host Properties with Nuclear Activity and Identifying Contaminants’. In: ApJ 922.2, 179, p. 179. doi: [10.3847/1538-4357/ac1352](https://doi.org/10.3847/1538-4357/ac1352).
- Baum, W. A. (Feb. 1957). ‘Photoelectric determinations of redshifts beyond 0.2 c.’ In: AJ 62, pp. 6–7. doi: [10.1086/107433](https://doi.org/10.1086/107433).
- (Jan. 1962). ‘Photoelectric Magnitudes and Red-Shifts’. In: *Problems of Extra-Galactic Research*. Ed. by G. C. McVittie. Vol. 15, p. 390.

REFERENCES

- Baumann, M., Marchand, M., et al. (Dec. 2023). *cds-astro/mocpy: Release v0.13.1*. Version v0.13.1. doi: [10.5281/zenodo.10257390](https://doi.org/10.5281/zenodo.10257390).
- Beifiori, A., Courteau, S., et al. (Jan. 2012). ‘On the correlations between galaxy properties and supermassive black hole mass’. In: MNRAS 419.3, pp. 2497–2528. doi: [10.1111/j.1365-2966.2011.19903.x](https://doi.org/10.1111/j.1365-2966.2011.19903.x).
- Benítez, N. (June 2000). ‘Bayesian Photometric Redshift Estimation’. In: ApJ 536.2, pp. 571–583. doi: [10.1086/308947](https://doi.org/10.1086/308947).
- Best, P. N. and Heckman, T. M. (Apr. 2012). ‘On the fundamental dichotomy in the local radio-AGN population: accretion, evolution and host galaxy properties’. In: MNRAS 421.2, pp. 1569–1582. doi: [10.1111/j.1365-2966.2012.20414.x](https://doi.org/10.1111/j.1365-2966.2012.20414.x).
- Best, P. N., Ker, L. M., et al. (Nov. 2014). ‘The cosmic evolution of radio-AGN feedback to $z = 1$ ’. In: MNRAS 445.1, pp. 955–969. doi: [10.1093/mnras/stu1776](https://doi.org/10.1093/mnras/stu1776).
- Best, P. N., Kondapally, R., et al. (Aug. 2023). ‘The LOFAR Two-metre Sky Survey: Deep Fields data release 1. V. Survey description, source classifications, and host galaxy properties’. In: MNRAS 523.2, pp. 1729–1755. doi: [10.1093/mnras/stad1308](https://doi.org/10.1093/mnras/stad1308).
- Bianchi, L., Rodriguez-Merino, L., et al. (Dec. 2007). ‘Statistical Properties of the GALEX-SDSS Matched Source Catalogs, and Classification of the UV Sources’. In: ApJS 173.2, pp. 659–672. doi: [10.1086/516648](https://doi.org/10.1086/516648).
- Bicknell, G. V., Dopita, M. A., and O’Dea, C. P. O. (Aug. 1997). ‘Unification of the Radio and Optical Properties of Gigahertz Peak Spectrum and Compact Steep-Spectrum Radio Sources’. In: ApJ 485.1, pp. 112–124. doi: [10.1086/304400](https://doi.org/10.1086/304400).
- Birchall, K. L., Watson, M. G., and Aird, J. (Feb. 2020). ‘X-ray detected AGN in SDSS dwarf galaxies’. In: MNRAS 492.2, pp. 2268–2284. doi: [10.1093/mnras/staa040](https://doi.org/10.1093/mnras/staa040).
- Blandford, R., Meier, D., and Readhead, A. (Aug. 2019). ‘Relativistic Jets from Active Galactic Nuclei’. In: ARA&A 57, pp. 467–509. doi: [10.1146/annurev-astro-081817-051948](https://doi.org/10.1146/annurev-astro-081817-051948).
- Blecha, L., Snyder, G. F., et al. (Aug. 2018). ‘The power of infrared AGN selection in mergers: a theoretical study’. In: MNRAS 478.3, pp. 3056–3071. doi: [10.1093/mnras/sty1274](https://doi.org/10.1093/mnras/sty1274).
- Blum, A. L. and Langley, P. (1997). ‘Selection of relevant features and examples in machine learning’. In: *Artificial Intelligence* 97.1. Relevance, pp. 245–271. ISSN: 0004-3702. doi: [10.1016/S0004-3702\(97\)00063-5](https://doi.org/10.1016/S0004-3702(97)00063-5).
- Bolzonella, M., Miralles, J. .-, and Pelló, R. (Nov. 2000). ‘Photometric redshifts based on standard SED fitting procedures’. In: A&A 363, pp. 476–492. doi: [10.48550/arXiv.astro-ph/0003380](https://doi.org/10.48550/arXiv.astro-ph/0003380).
- Bonaldi, A., Bonato, M., et al. (Jan. 2019). ‘The Tiered Radio Extragalactic Continuum Simulation (T-RECS)’. In: MNRAS 482.1, pp. 2–19. doi: [10.1093/mnras/sty2603](https://doi.org/10.1093/mnras/sty2603).
- Bonato, M., Prandoni, I., et al. (Jan. 2021). ‘New constraints on the 1.4 GHz source number counts and luminosity functions in the Lockman Hole field’. In: MNRAS 500.1, pp. 22–33. doi: [10.1093/mnras/staa3218](https://doi.org/10.1093/mnras/staa3218).
- Bonnarel, F., Fernique, P., et al. (Apr. 2000). ‘The ALADIN interactive sky atlas. A reference tool for identification of astronomical sources’. In: A&AS 143, pp. 33–40. doi: [10.1051/aas:2000331](https://doi.org/10.1051/aas:2000331).
- Bosman, S. E. I. (Feb. 2022). *All $z > 5.7$ quasars currently known*. Version 1.15. Zenodo. doi: [10.5281/zenodo.6039724](https://doi.org/10.5281/zenodo.6039724).

- Bouwens, R., González-López, J., et al. (Oct. 2020). ‘The ALMA Spectroscopic Survey Large Program: The Infrared Excess of $z = 1.5\text{--}10$ UV-selected Galaxies and the Implied High-redshift Star Formation History’. In: ApJ 902.2, 112, p. 112. doi: [10.3847/1538-4357/abb830](https://doi.org/10.3847/1538-4357/abb830).
- Bowler, R. A. A., Adams, N. J., et al. (Mar. 2021). ‘The rapid transition from star formation to AGN-dominated rest-frame ultraviolet light at $z \approx 4$ ’. In: MNRAS 502.1, pp. 662–677. doi: [10.1093/mnras/stab038](https://doi.org/10.1093/mnras/stab038).
- Bowles, M., Tang, H., et al. (June 2023). ‘Radio galaxy zoo EMU: towards a semantic radio galaxy morphology taxonomy’. In: MNRAS 522.2, pp. 2584–2600. doi: [10.1093/mnras/stad1021](https://doi.org/10.1093/mnras/stad1021).
- Brammer, G. B., van Dokkum, P. G., and Coppi, P. (Oct. 2008). ‘EAZY: A Fast, Public Photometric Redshift Code’. In: ApJ 686.2, pp. 1503–1513. doi: [10.1086/591786](https://doi.org/10.1086/591786).
- Brandt, W. N. and Alexander, D. M. (Jan. 2015). ‘Cosmic X-ray surveys of distant active galaxies. The demographics, physics, and ecology of growing supermassive black holes’. In: A&A Rev. 23, 1, p. 1. doi: [10.1007/s00159-014-0081-z](https://doi.org/10.1007/s00159-014-0081-z).
- Braun, R., Bonaldi, A., et al. (Dec. 2019). ‘Anticipated Performance of the Square Kilometre Array – Phase 1 (SKA1)’. In: *arXiv e-prints*, arXiv:1912.12699, arXiv:1912.12699. doi: [10.48550/arXiv.1912.12699](https://doi.org/10.48550/arXiv.1912.12699).
- Bravais, A. (1844). *Analyse mathématique sur les probabilités des erreurs de situation d'un point*. Impr. Royale Paris.
- Breedt, E., Arévalo, P., et al. (Mar. 2009). ‘Long-term optical and X-ray variability of the Seyfert galaxy Markarian 79’. In: MNRAS 394.1, pp. 427–437. doi: [10.1111/j.1365-2966.2008.14302.x](https://doi.org/10.1111/j.1365-2966.2008.14302.x).
- Breedt, E., McHardy, I. M., et al. (Apr. 2010). ‘Twelve years of X-ray and optical variability in the Seyfert galaxy NGC 4051’. In: MNRAS 403.2, pp. 605–619. doi: [10.1111/j.1365-2966.2009.16146.x](https://doi.org/10.1111/j.1365-2966.2009.16146.x).
- Breiman, L. (Aug. 1996). ‘Bagging predictors’. In: *Machine Learning* 24.2, pp. 123–140. issn: 1573-0565. doi: [10.1007/BF00058655](https://doi.org/10.1007/BF00058655).
- (Oct. 2001). ‘Random Forests’. In: *Machine Learning* 45.1, pp. 5–32. issn: 1573-0565. doi: [10.1023/A:1010933404324](https://doi.org/10.1023/A:1010933404324).
- (2003). ‘Manual on setting up, using, and understanding random forests v4. 0’. In: *Statistics Department University of California Berkeley, CA, USA*.
- Brescia, M., Cavaudi, S., et al. (2021). ‘Photometric Redshifts With Machine Learning, Lights and Shadows on a Complex Data Science Use Case’. In: *Frontiers in Astronomy and Space Sciences* 8, p. 70. issn: 2296-987X. doi: [10.3389/fspas.2021.658229](https://doi.org/10.3389/fspas.2021.658229).
- Brescia, M., Salvato, M., et al. (Oct. 2019). ‘Photometric redshifts for X-ray-selected active galactic nuclei in the eROSITA era’. In: MNRAS 489.1, pp. 663–680. doi: [10.1093/mnras/stz2159](https://doi.org/10.1093/mnras/stz2159).
- Brier, G. W. (1950). ‘Verification of Forecasts Expressed in Terms of Probability’. In: *Monthly Weather Review* 78.1, pp. 1–3. doi: [10.1175/1520-0493\(1950\)078<0001:VOFEIT>2.0.CO;2](https://doi.org/10.1175/1520-0493(1950)078<0001:VOFEIT>2.0.CO;2).
- Bröcker, J. and Smith, L. A. (2007). ‘Increasing the Reliability of Reliability Diagrams’. In: *Weather and Forecasting* 22.3, pp. 651–661. doi: [10.1175/WAF993.1](https://doi.org/10.1175/WAF993.1).
- Brown, M. J. I., Duncan, K. J., et al. (Nov. 2019). ‘The spectral energy distributions of active galactic nuclei’. In: MNRAS 489.3, pp. 3351–3367. doi: [10.1093/mnras/stz2324](https://doi.org/10.1093/mnras/stz2324).
- Brown, M. J. I., Moustakas, J., et al. (June 2014). ‘An Atlas of Galaxy Spectral Energy Distributions from the Ultraviolet to the Mid-infrared’. In: ApJS 212.2, 18, p. 18. doi: [10.1088/0067-0049/212/2/18](https://doi.org/10.1088/0067-0049/212/2/18).

REFERENCES

- Brunner, H., Liu, T., et al. (May 2022). ‘The eROSITA Final Equatorial Depth Survey (eFEDS). X-ray catalogue’. In: A&A 661, A1, A1. doi: [10.1051/0004-6361/202141266](https://doi.org/10.1051/0004-6361/202141266).
- Brusa, M., Zamorani, G., et al. (Sept. 2007). ‘The XMM-Newton Wide-Field Survey in the COSMOS Field. III. Optical Identification and Multiwavelength Properties of a Large Sample of X-Ray-Selected Sources’. In: ApJS 172.1, pp. 353–367. doi: [10.1086/516575](https://doi.org/10.1086/516575).
- Buchner, J. (Oct. 2019). ‘Collaborative Nested Sampling: Big Data versus Complex Physical Models’. In: PASP 131.1004, p. 108005. doi: [10.1088/1538-3873/aae7fc](https://doi.org/10.1088/1538-3873/aae7fc).
- Budavári, T. and Szalay, A. S. (May 2008). ‘Probabilistic Cross-Identification of Astronomical Sources’. In: ApJ 679.1, pp. 301–309. doi: [10.1086/587156](https://doi.org/10.1086/587156).
- Buisson, D. J. K., Lohfink, A. M., et al. (Jan. 2017). ‘Ultraviolet and X-ray variability of active galactic nuclei with Swift’. In: MNRAS 464.3, pp. 3194–3218. doi: [10.1093/mnras/stw2486](https://doi.org/10.1093/mnras/stw2486).
- Burhanudin, U. F., Maund, J. R., et al. (Aug. 2021). ‘Light-curve classification with recurrent neural networks for GOTO: dealing with imbalanced data’. In: MNRAS 505.3, pp. 4345–4361. doi: [10.1093/mnras/stab1545](https://doi.org/10.1093/mnras/stab1545).
- Butler, A., Huynh, M., et al. (May 2019). ‘The XXL Survey. XXXVI. Evolution and black hole feedback of high-excitation and low-excitation radio galaxies in XXL-S’. In: A&A 625, A111, A111. doi: [10.1051/0004-6361/201834581](https://doi.org/10.1051/0004-6361/201834581).
- Cameron, E. and Driver, S. P. (May 2007). ‘The galaxy luminosity-size relation and selection biases in the Hubble Ultra Deep Field’. In: MNRAS 377.2, pp. 523–534. doi: [10.1111/j.1365-2966.2007.11507.x](https://doi.org/10.1111/j.1365-2966.2007.11507.x).
- Camilo, F., Scholz, P., et al. (Apr. 2018). ‘Revival of the Magnetar PSR J1622-4950: Observations with MeerKAT, Parkes, XMM-Newton, Swift, Chandra, and NuSTAR’. In: ApJ 856.2, 180, p. 180. doi: [10.3847/1538-4357/aab35a](https://doi.org/10.3847/1538-4357/aab35a).
- Capetti, A., Brienza, M., et al. (Oct. 2020). ‘The LOFAR view of FR 0 radio galaxies’. In: A&A 642, A107, A107. doi: [10.1051/0004-6361/202038671](https://doi.org/10.1051/0004-6361/202038671).
- Cara, M. and Lister, M. L. (Oct. 2008). ‘Avoiding Spurious Breaks in Binned Luminosity Functions’. In: ApJ 686.1, pp. 148–154. doi: [10.1086/590902](https://doi.org/10.1086/590902).
- Card, D. H. (1982). ‘Using known map category marginal frequencies to improve estimates of thematic map accuracy’. In: *Photogrammetric Engineering and Remote Sensing* 48.3, pp. 431–439.
- Carroll, B. W. and Ostlie, D. A. (2017). *An Introduction to Modern Astrophysics*. 2nd ed. Cambridge University Press. doi: [10.1017/9781108380980](https://doi.org/10.1017/9781108380980).
- Caruana, R. and Niculescu-Mizil, A. (2006). ‘An Empirical Comparison of Supervised Learning Algorithms’. In: *Proceedings of the 23rd International Conference on Machine Learning*. ICML ’06. Pittsburgh, Pennsylvania, USA: Association for Computing Machinery, pp. 161–168. ISBN: 1595933832. doi: [10.1145/1143844.1143865](https://doi.org/10.1145/1143844.1143865).
- Carvajal, R., Bauer, F. E., et al. (Jan. 2020). ‘The ALMA Frontier Fields Survey. V. ALMA Stacking of Lyman-Break Galaxies in Abell 2744, Abell 370, Abell S1063, MACSJ0416.1-2403 and MACSJ1149.5+2223’. In: A&A 633, A160, A160. doi: [10.1051/0004-6361/201936260](https://doi.org/10.1051/0004-6361/201936260).
- Carvajal, R., Matute, I., et al. (Nov. 2023a). ‘Selection of powerful radio galaxies with machine learning’. In: A&A 679, A101, A101. doi: [10.1051/0004-6361/202245770](https://doi.org/10.1051/0004-6361/202245770).

- Carvajal, R., Matute, I., et al. (Oct. 2021). ‘Exploring New Redshift Indicators for Radio-Powerful AGN’. In: *Galaxies* 9.4, p. 86. doi: [10.3390/galaxies9040086](https://doi.org/10.3390/galaxies9040086).
- Carvajal, R., Matute, I., et al. (Dec. 2023b). *Selection of powerful radio galaxies with machine learning*. doi: [10.5281/zenodo.10220009](https://doi.org/10.5281/zenodo.10220009).
- Casalicchio, G., Molnar, C., and Bischl, B. (2019). ‘Visualizing the Feature Importance for Black Box Models’. In: *Machine Learning and Knowledge Discovery in Databases*. Ed. by M. Berlingerio, F. Bonchi, et al. Cham: Springer International Publishing, pp. 655–670. ISBN: 978-3-030-10925-7.
- Ceccarelli, L., Duplancic, F., and Garcia Lambas, D. (Jan. 2022). ‘The impact of void environment on AGN’. In: *MNRAS* 509.2, pp. 1805–1819. doi: [10.1093/mnras/stab2902](https://doi.org/10.1093/mnras/stab2902).
- Ceraj, L., Smolčić, V., et al. (Dec. 2018). ‘The VLA-COSMOS 3 GHz Large Project: Star formation properties and radio luminosity functions of AGN with moderate-to-high radiative luminosities out to $z \sim 6$ ’. In: *A&A* 620, A192, A192. doi: [10.1051/0004-6361/201833935](https://doi.org/10.1051/0004-6361/201833935).
- Ceraj, L., Smolčić, V., et al. (Oct. 2020). ‘The XXL Survey. XLIII. The quasar radio loudness dichotomy exposed via radio luminosity functions obtained by combining results from COSMOS and XXL-S X-ray selected quasars’. In: *A&A* 642, A125, A125. doi: [10.1051/0004-6361/201936776](https://doi.org/10.1051/0004-6361/201936776).
- Chambers, K. C., Magnier, E. A., et al. (Dec. 2016). ‘The Pan-STARRS1 Surveys’. In: *arXiv e-prints*, arXiv:1612.05560.
- Champagne, J. B., Casey, C. M., et al. (Aug. 2023). ‘A Mixture of LBG Overdensities in the Fields of Three $6 < z < 7$ Quasars: Implications for the Robustness of Photometric Selection’. In: *ApJ* 952.2, 99, p. 99. doi: [10.3847/1538-4357/acda8d](https://doi.org/10.3847/1538-4357/acda8d).
- Chattpadhyay, A. K. (2017). ‘Incomplete Data in Astrostatistics’. In: *Wiley StatsRef: Statistics Reference Online*. American Cancer Society, pp. 1–12. ISBN: 9781118445112. doi: [10.1002/9781118445112.stat07942](https://doi.org/10.1002/9781118445112.stat07942).
- Chaves-Montero, J., Bonoli, S., et al. (Dec. 2017). ‘ELDAR, a new method to identify AGN in multi-filter surveys: the ALHAMBRA test case’. In: *MNRAS* 472.2, pp. 2085–2106. doi: [10.1093/mnras/stx2054](https://doi.org/10.1093/mnras/stx2054).
- Chen, C. T. J., Brandt, W. N., et al. (Mar. 2017). ‘Hard X-Ray-selected AGNs in Low-mass Galaxies from the NuSTAR Serendipitous Survey’. In: *ApJ* 837.1, 48, p. 48. doi: [10.3847/1538-4357/aa5d5b](https://doi.org/10.3847/1538-4357/aa5d5b).
- Chen, H., Garrett, M. A., et al. (June 2020). ‘Searching for obscured AGN in $z \sim 2$ submillimetre galaxies’. In: *A&A* 638, A113, A113. doi: [10.1051/0004-6361/201937162](https://doi.org/10.1051/0004-6361/201937162).
- Chen, T. and Guestrin, C. (2016). ‘XGBoost: A Scalable Tree Boosting System’. In: *Proceedings of the 22nd ACM SIGKDD International Conference on Knowledge Discovery and Data Mining*. KDD ’16. San Francisco, California, USA: ACM, pp. 785–794. ISBN: 978-1-4503-4232-2. doi: [10.1145/2939672.2939785](https://doi.org/10.1145/2939672.2939785).
- Ciardi, B. and Ferrara, A. (Feb. 2005). ‘The First Cosmic Structures and Their Effects’. In: *Space Sci. Rev.* 116.3-4, pp. 625–705. doi: [10.1007/s11214-005-3592-0](https://doi.org/10.1007/s11214-005-3592-0).
- Cid Fernandes, R., Stasińska, G., et al. (Apr. 2010). ‘Alternative diagnostic diagrams and the ‘forgotten’ population of weak line galaxies in the SDSS’. In: *MNRAS* 403.2, pp. 1036–1053. doi: [10.1111/j.1365-2966.2009.16185.x](https://doi.org/10.1111/j.1365-2966.2009.16185.x).
- Cid Fernandes, R., Stasińska, G., et al. (May 2011). ‘A comprehensive classification of galaxies in the Sloan Digital Sky Survey: how to tell true from fake AGN?’ In: *MNRAS* 413.3, pp. 1687–1699. doi: [10.1111/j.1365-2966.2011.18244.x](https://doi.org/10.1111/j.1365-2966.2011.18244.x).

REFERENCES

- Clarke, A. O., Scaife, A. M. M., et al. (July 2020). ‘Identifying galaxies, quasars, and stars with machine learning: A new catalogue of classifications for 111 million SDSS sources without spectra’. In: A&A 639, A84, A84. doi: [10.1051/0004-6361/201936770](https://doi.org/10.1051/0004-6361/201936770).
- Clopper, C. J. and Pearson, E. S. (Dec. 1934). ‘The Use of Confidence or Fiducial Limits Illustrated in the Case of the Binomial’. In: *Biometrika* 26.4, pp. 404–413. issn: 0006-3444. doi: [10.1093/biomet/26.4.404](https://doi.org/10.1093/biomet/26.4.404).
- Cochrane, R. K., Kondapally, R., et al. (Aug. 2023). ‘The LOFAR Two-metre Sky Survey: the radio view of the cosmic star formation history’. In: MNRAS 523.4, pp. 6082–6102. doi: [10.1093/mnras/stad1602](https://doi.org/10.1093/mnras/stad1602).
- Coleman, B., Kirkpatrick, A., et al. (Sept. 2022). ‘Accretion history of AGN: Estimating the host galaxy properties in X-ray luminous AGN from $z = 0\text{--}3$ ’. In: MNRAS 515.1, pp. 82–98. doi: [10.1093/mnras/stac1679](https://doi.org/10.1093/mnras/stac1679).
- Condon, J. J. (Jan. 1992). ‘Radio emission from normal galaxies.’ In: ARA&A 30, pp. 575–611. doi: [10.1146/annurev.aa.30.090192.003043](https://doi.org/10.1146/annurev.aa.30.090192.003043).
- Condon, J. J., Cotton, W. D., and Broderick, J. J. (Aug. 2002). ‘Radio Sources and Star Formation in the Local Universe’. In: AJ 124.2, pp. 675–689. doi: [10.1086/341650](https://doi.org/10.1086/341650).
- Condon, J. J., Cotton, W. D., et al. (May 1998). ‘The NRAO VLA Sky Survey’. In: AJ 115.5, pp. 1693–1716. doi: [10.1086/300337](https://doi.org/10.1086/300337).
- Congalton, R. G., Oderwald, R. G., and Mead, R. A. (1983). ‘Assessing Landsat classification accuracy using discrete multivariate analysis statistical techniques’. In: *Photogrammetric engineering and remote sensing* 49.12, pp. 1671–1678.
- Cortes, C. and Vapnik, V. (Sept. 1995). ‘Support-vector networks’. In: *Machine Learning* 20.3, pp. 273–297. issn: 1573-0565. doi: [10.1007/BF00994018](https://doi.org/10.1007/BF00994018).
- Costa-Climent, R., Haftor, D. M., and Staniewski, M. W. (2023). ‘Using machine learning to create and capture value in the business models of small and medium-sized enterprises’. In: *International Journal of Information Management* 73, p. 102637. issn: 0268-4012. doi: [10.1016/j.ijinfomgt.2023.102637](https://doi.org/10.1016/j.ijinfomgt.2023.102637).
- Cover, T. and Hart, P. (1967). ‘Nearest neighbor pattern classification’. In: *IEEE Transactions on Information Theory* 13.1, pp. 21–27. doi: [10.1109/TIT.1967.1053964](https://doi.org/10.1109/TIT.1967.1053964).
- Cramér, H. (1946). *Mathematical methods of statistics*. English. Princeton University Press Princeton, xvi, 575 p.
- Cranmer, M. (May 2023). ‘Interpretable Machine Learning for Science with PySR and SymbolicRegression.jl’. In: *arXiv e-prints*, arXiv:2305.01582, arXiv:2305.01582. doi: [10.48550/arXiv.2305.01582](https://doi.org/10.48550/arXiv.2305.01582).
- Cranmer, M., Sanchez-Gonzalez, A., et al. (June 2020). ‘Discovering Symbolic Models from Deep Learning with Inductive Biases’. In: *arXiv e-prints*, arXiv:2006.11287.
- Croom, S. M., Richards, G. T., et al. (Nov. 2009). ‘The 2dF-SDSS LRG and QSO survey: the QSO luminosity function at $0.4 < z < 2.6$ ’. In: MNRAS 399.4, pp. 1755–1772. doi: [10.1111/j.1365-2966.2009.15398.x](https://doi.org/10.1111/j.1365-2966.2009.15398.x).
- Cunha, P. A. C. and Humphrey, A. (Oct. 2022). ‘Photometric redshift-aided classification using ensemble learning’. In: A&A 666, A87, A87. doi: [10.1051/0004-6361/202243135](https://doi.org/10.1051/0004-6361/202243135).
- Curran, S. J. (May 2022). ‘Quasar photometric redshifts from incomplete data using deep learning’. In: MNRAS 512.2, pp. 2099–2109. doi: [10.1093/mnras/stac660](https://doi.org/10.1093/mnras/stac660).
- Curran, S. J., Moss, J. P., and Perrott, Y. C. (July 2022). ‘Redshifts of radio sources in the Million Quasars Catalogue from machine learning’. In: MNRAS 514.1, pp. 1–19. doi: [10.1093/mnras/stac1333](https://doi.org/10.1093/mnras/stac1333).
- Cutri, R. M., Skrutskie, M. F., et al. (2003a). *2MASS All Sky Catalog of point sources*.

- (June 2003b). ‘VizieR Online Data Catalog: 2MASS All-Sky Catalog of Point Sources (Cutri+ 2003)’. In: *VizieR Online Data Catalog*, II/246, pp. II/246.
- Cutri, R. M., Wright, E. L., et al. (Nov. 2013). *Explanatory Supplement to the AllWISE Data Release Products*.
- D’Isanto, A., Cavaudi, S., et al. (Aug. 2018). ‘Return of the features. Efficient feature selection and interpretation for photometric redshifts’. In: A&A 616, A97, A97. doi: [10.1051/0004-6361/201833103](https://doi.org/10.1051/0004-6361/201833103).
- Dahlen, T., Mobasher, B., et al. (Oct. 2013). ‘A Critical Assessment of Photometric Redshift Methods: A CANDELS Investigation’. In: ApJ 775.2, 93, p. 93. doi: [10.1088/0004-637X/775/2/93](https://doi.org/10.1088/0004-637X/775/2/93).
- Dai, Y. S., Wilkes, B. J., et al. (Aug. 2018). ‘Is there a relationship between AGN and star formation in IR-bright AGNs?’ In: MNRAS 478.3, pp. 4238–4254. doi: [10.1093/mnras/sty1341](https://doi.org/10.1093/mnras/sty1341).
- Davidson, K. and Netzer, H. (Oct. 1979). ‘The emission lines of quasars and similar objects’. In: *Reviews of Modern Physics* 51.4, pp. 715–766. doi: [10.1103/RevModPhys.51.715](https://doi.org/10.1103/RevModPhys.51.715).
- Davies, L. J. M., Robotham, A. S. G., et al. (Oct. 2018a). ‘Deep Extragalactic VIable Legacy Survey (DEVILS): motivation, design, and target catalogue’. In: MNRAS 480.1, pp. 768–799. doi: [10.1093/mnras/sty1553](https://doi.org/10.1093/mnras/sty1553).
- Davies, T. M., Marshall, J. C., and Hazelton, M. L. (2018b). ‘Tutorial on kernel estimation of continuous spatial and spatiotemporal relative risk’. In: *Statistics in Medicine* 37.7, pp. 1191–1221. doi: [10.1002/sim.7577](https://doi.org/10.1002/sim.7577).
- Dayal, P., Volonteri, M., et al. (Jan. 2024). ‘UNCOVERing the contribution of black holes to reionization in the JWST era’. In: *arXiv e-prints*, arXiv:2401.11242, arXiv:2401.11242. doi: [10.48550/arXiv.2401.11242](https://doi.org/10.48550/arXiv.2401.11242).
- de Ruiter, H. R., Willis, A. G., and Arp, H. C. (May 1977). ‘A Westerbork 1415 MHz survey of background radio sources. II. Optical identifications with deep IIIa-J plates.’ In: A&AS 28, pp. 211–293.
- de Veny, J. B., Osborn, W. H., and Janes, K. (Oct. 1971). ‘A Catalogue of Quasars’. In: PASP 83.495, p. 611. doi: [10.1086/129187](https://doi.org/10.1086/129187).
- Deka, P. P., Gupta, N., et al. (Feb. 2024). ‘The MeerKAT Absorption Line Survey (MALS) Data Release. I. Stokes I Image Catalogs at 1–1.4 GHz’. In: ApJS 270.2, 33, p. 33. doi: [10.3847/1538-4365/acf7b9](https://doi.org/10.3847/1538-4365/acf7b9).
- Delhaize, J., Heywood, I., et al. (Mar. 2021). ‘MIGHTEE: are giant radio galaxies more common than we thought?’ In: MNRAS 501.3, pp. 3833–3845. doi: [10.1093/mnras/staa3837](https://doi.org/10.1093/mnras/staa3837).
- Delhaize, J., Smolčić, V., et al. (June 2017). ‘The VLA-COSMOS 3 GHz Large Project: The infrared-radio correlation of star-forming galaxies and AGN to $z \lesssim 6$ ’. In: A&A 602, A4, A4. doi: [10.1051/0004-6361/201629430](https://doi.org/10.1051/0004-6361/201629430).
- Desai, S. and Strachan, A. (June 2021). ‘Parsimonious neural networks learn interpretable physical laws’. In: *Scientific Reports* 11.1, p. 12761. ISSN: 2045-2322. doi: [10.1038/s41598-021-92278-w](https://doi.org/10.1038/s41598-021-92278-w).
- Dey, A., Schlegel, D. J., et al. (May 2019). ‘Overview of the DESI Legacy Imaging Surveys’. In: AJ 157.5, 168, p. 168. doi: [10.3847/1538-3881/ab089d](https://doi.org/10.3847/1538-3881/ab089d).
- Dey, B., Andrews, B. H., et al. (Oct. 2022). ‘Photometric redshifts from SDSS images with an interpretable deep capsule network’. In: MNRAS 515.4, pp. 5285–5305. doi: [10.1093/mnras/stac2105](https://doi.org/10.1093/mnras/stac2105).
- Dice, L. R. (1945). ‘Measures of the Amount of Ecologic Association Between Species’. In: *Ecology* 26.3, pp. 297–302. ISSN: 00129658, 19399170. URL: <http://www.jstor.org/stable/1932409> (visited on 04/10/2022).
- Dobbels, W. and Baes, M. (Nov. 2021). ‘Predicting far-infrared maps of galaxies via machine learning techniques’. In: A&A 655, A34, A34. doi: [10.1051/0004-6361/202142084](https://doi.org/10.1051/0004-6361/202142084).

REFERENCES

- Donley, J. L., Koekemoer, A. M., et al. (Apr. 2012). ‘Identifying Luminous Active Galactic Nuclei in Deep Surveys: Revised IRAC Selection Criteria’. In: ApJ 748.2, 142, p. 142. doi: [10.1088/0004-637X/748/2/142](https://doi.org/10.1088/0004-637X/748/2/142).
- Donley, J. L., Rieke, G. H., et al. (Nov. 2005). ‘Unveiling a Population of AGNs Not Detected in X-Rays’. In: ApJ 634.1, pp. 169–182. doi: [10.1086/491668](https://doi.org/10.1086/491668).
- Dorogush, A. V., Ershov, V., and Gulin, A. (2018). ‘CatBoost: gradient boosting with categorical features support’. In: *CoRR* abs/1810.11363. URL: <http://arxiv.org/abs/1810.11363>.
- Drake, A. J., Graham, M. J., et al. (July 2014). ‘The Catalina Surveys Periodic Variable Star Catalog’. In: ApJS 213.1, 9, p. 9. doi: [10.1088/0067-0049/213/1/9](https://doi.org/10.1088/0067-0049/213/1/9).
- Driver, S. P., Hill, D. T., et al. (May 2011). ‘Galaxy and Mass Assembly (GAMA): survey diagnostics and core data release’. In: MNRAS 413.2, pp. 971–995. doi: [10.1111/j.1365-2966.2010.18188.x](https://doi.org/10.1111/j.1365-2966.2010.18188.x).
- Driver, S. P. and Robotham, A. S. G. (Oct. 2010). ‘Quantifying cosmic variance’. In: MNRAS 407.4, pp. 2131–2140. doi: [10.1111/j.1365-2966.2010.17028.x](https://doi.org/10.1111/j.1365-2966.2010.17028.x).
- Du, M., Yang, F., et al. (2021). ‘Fairness in Deep Learning: A Computational Perspective’. In: *IEEE Intelligent Systems* 36.4, pp. 25–34. doi: [10.1109/MIS.2020.3000681](https://doi.org/10.1109/MIS.2020.3000681).
- Duboue, P. (2020). *The Art of Feature Engineering: Essentials for Machine Learning*. Cambridge University Press. ISBN: 9781108709385.
- Duncan, K. J., Kondapally, R., et al. (Apr. 2021). ‘The LOFAR Two-meter Sky Survey: Deep Fields Data Release 1. IV. Photometric redshifts and stellar masses’. In: A&A 648, A4, A4. doi: [10.1051/0004-6361/202038809](https://doi.org/10.1051/0004-6361/202038809).
- Duncan, K. J., Sabater, J., et al. (Feb. 2019). ‘The LOFAR Two-metre Sky Survey. IV. First Data Release: Photometric redshifts and rest-frame magnitudes’. In: A&A 622, A3, A3. doi: [10.1051/0004-6361/201833562](https://doi.org/10.1051/0004-6361/201833562).
- Eddington, A. S. (Mar. 1913). ‘On a formula for correcting statistics for the effects of a known error of observation’. In: MNRAS 73, pp. 359–360. doi: [10.1093/mnras/73.5.359](https://doi.org/10.1093/mnras/73.5.359).
- (Mar. 1940). ‘The correction of statistics for accidental error’. In: MNRAS 100, p. 354. doi: [10.1093/mnras/100.5.354](https://doi.org/10.1093/mnras/100.5.354).
- Ellis, R. S., Colless, M., et al. (May 1996). ‘Autofib Redshift Survey - I. Evolution of the galaxy luminosity function’. In: MNRAS 280.1, pp. 235–251. doi: [10.1093/mnras/280.1.235](https://doi.org/10.1093/mnras/280.1.235).
- Enke, H., Partl, A., et al. (Nov. 2012). ‘Handling Big Data in Astronomy and Astrophysics: Rich Structured Queries on Replicated Cloud Data with XtreemFS’. In: *Datenbank-Spektrum* 12.3, pp. 173–181. ISSN: 1610-1995. doi: [10.1007/s13222-012-0099-1](https://doi.org/10.1007/s13222-012-0099-1).
- Euclid Collaboration, Bisigello, L., et al. (Apr. 2023a). ‘Euclid preparation - XXIII. Derivation of galaxy physical properties with deep machine learning using mock fluxes and H-band images’. In: MNRAS 520.3, pp. 3529–3548. doi: [10.1093/mnras/stac3810](https://doi.org/10.1093/mnras/stac3810).
- Euclid Collaboration, Humphrey, A., et al. (Mar. 2023b). ‘Euclid preparation. XXII. Selection of quiescent galaxies from mock photometry using machine learning’. In: A&A 671, A99, A99. doi: [10.1051/0004-6361/202244307](https://doi.org/10.1051/0004-6361/202244307).
- Euclid Collaboration, Scaramella, R., et al. (June 2022). ‘Euclid preparation. I. The Euclid Wide Survey’. In: A&A 662, A112, A112. doi: [10.1051/0004-6361/202141938](https://doi.org/10.1051/0004-6361/202141938).

- Falcke, H., Nagar, N. M., et al. (Oct. 2000). ‘Radio Sources in Low-Luminosity Active Galactic Nuclei. II. Very Long Baseline Interferometry Detections of Compact Radio Cores and Jets in a Sample of LINERs’. In: *ApJ* 542.1, pp. 197–200. doi: [10.1086/309543](https://doi.org/10.1086/309543).
- Fan, X., Banados, E., and Simcoe, R. A. (2023). ‘Quasars and the Intergalactic Medium at Cosmic Dawn’. In: *ARA&A* 61. doi: [10.1146/annurev-astro-052920-102455](https://doi.org/10.1146/annurev-astro-052920-102455).
- Faucher-Giguère, C.-A., Lidz, A., et al. (Oct. 2009). ‘A New Calculation of the Ionizing Background Spectrum and the Effects of He II Reionization’. In: *ApJ* 703.2, pp. 1416–1443. doi: [10.1088/0004-637X/703/2/1416](https://doi.org/10.1088/0004-637X/703/2/1416).
- Ferrarese, L. and Merritt, D. (Aug. 2000). ‘A Fundamental Relation between Supermassive Black Holes and Their Host Galaxies’. In: *ApJ* 539.1, pp. L9–L12. doi: [10.1086/312838](https://doi.org/10.1086/312838).
- Flesch, E. W. (Mar. 2015). ‘The Half Million Quasars (HMQ) Catalogue’. In: *PASA* 32, e010, e010. doi: [10.1017/pasa.2015.10](https://doi.org/10.1017/pasa.2015.10).
- (Dec. 2019). ‘The Million Quasars (Milliquas) Catalogue, v6.4’. In: *arXiv e-prints*, arXiv:1912.05614, arXiv:1912.05614. doi: [10.48550/arXiv.1912.05614](https://doi.org/10.48550/arXiv.1912.05614).
 - (May 2021). ‘The Million Quasars (Milliquas) v7.2 Catalogue, now with VLASS associations. The inclusion of SDSS-DR16Q quasars is detailed’. In: *arXiv e-prints*, arXiv:2105.12985, arXiv:2105.12985.
 - (Dec. 2023). ‘The Million Quasars (Milliquas) Catalogue, v8’. In: *The Open Journal of Astrophysics* 6, 49, p. 49. doi: [10.21105/astro.2308.01505](https://doi.org/10.21105/astro.2308.01505).
- Flewelling, H. A., Magnier, E. A., et al. (Nov. 2020). ‘The Pan-STARRS1 Database and Data Products’. In: *ApJS* 251.1, 7, p. 7. doi: [10.3847/1538-4365/abb82d](https://doi.org/10.3847/1538-4365/abb82d).
- Främling, K. (2023). ‘Feature Importance versus Feature Influence and What It Signifies for Explainable AI’. In: *Explainable Artificial Intelligence*. Ed. by L. Longo. Cham: Springer Nature Switzerland, pp. 241–259. ISBN: 978-3-031-44064-9.
- Frederiksen, T. F., Graur, O., et al. (Mar. 2014). ‘Spectroscopic identification of a redshift 1.55 supernova host galaxy from the Subaru Deep Field Supernova Survey’. In: *A&A* 563, A140, A140. doi: [10.1051/0004-6361/201321795](https://doi.org/10.1051/0004-6361/201321795).
- Freund, Y. and Schapire, R. E. (1996). ‘Experiments with a New Boosting Algorithm’. In: *Proceedings of the Thirteenth International Conference on International Conference on Machine Learning*. ICML’96. Bari, Italy: Morgan Kaufmann Publishers Inc., pp. 148–156. ISBN: 1558604197.
- Friedman, J. H. (2001). ‘Greedy function approximation: A gradient boosting machine.’ In: *The Annals of Statistics* 29.5, pp. 1189–1232. doi: [10.1214/aos/1013203451](https://doi.org/10.1214/aos/1013203451).
- (2002). ‘Stochastic gradient boosting’. In: *Computational Statistics & Data Analysis* 38.4. Nonlinear Methods and Data Mining, pp. 367–378. ISSN: 0167-9473. doi: [10.1016/S0167-9473\(01\)00065-2](https://doi.org/10.1016/S0167-9473(01)00065-2).
- Fu, Y., Wu, X.-B., et al. (Oct. 2023). ‘CatNorth: An Improved Gaia DR3 Quasar Candidate Catalog with Pan-STARRS1 and CatWISE’. In: *arXiv e-prints*, arXiv:2310.12704, arXiv:2310.12704. doi: [10.48550/arXiv.2310.12704](https://doi.org/10.48550/arXiv.2310.12704).
- Fukugita, M. and Kawasaki, M. (Aug. 1994). ‘Reionization during Hierarchical Clustering in a Universe Dominated by Cold Dark Matter’. In: *MNRAS* 269, p. 563. doi: [10.1093/mnras/269.3.563](https://doi.org/10.1093/mnras/269.3.563).
- Gaia Collaboration, Bailer-Jones, C. A. L., et al. (June 2023a). ‘Gaia Data Release 3. The extragalactic content’. In: *A&A* 674, A41, A41. doi: [10.1051/0004-6361/202243232](https://doi.org/10.1051/0004-6361/202243232).

REFERENCES

- Gaia Collaboration, Prusti, T., et al. (Nov. 2016). ‘The Gaia mission’. In: A&A 595, A1, A1. doi: [10.1051/0004-6361/201629272](https://doi.org/10.1051/0004-6361/201629272).
- Gaia Collaboration, Vallenari, A., et al. (June 2023b). ‘Gaia Data Release 3. Summary of the content and survey properties’. In: A&A 674, A1, A1. doi: [10.1051/0004-6361/202243940](https://doi.org/10.1051/0004-6361/202243940).
- Galametz, A., Grazian, A., et al. (June 2013). ‘CANDELS Multiwavelength Catalogs: Source Identification and Photometry in the CANDELS UKIDSS Ultra-deep Survey Field’. In: ApJS 206.2, 10, p. 10. doi: [10.1088/0067-0049/206/2/10](https://doi.org/10.1088/0067-0049/206/2/10).
- Galton, F. (1886). ‘Regression Towards Mediocrity in Hereditary Stature.’ In: *The Journal of the Anthropological Institute of Great Britain and Ireland* 15, pp. 246–263. ISSN: 09595295. URL: <http://www.jstor.org/stable/2841583> (visited on 29/02/2024).
- Gao, L. and Guan, L. (Oct. 2023). ‘Interpretability of Machine Learning: Recent Advances and Future Prospects’. In: *IEEE MultiMedia* 30.04, pp. 105–118. ISSN: 1941-0166. doi: [10.1109/MMUL.2023.3272513](https://doi.org/10.1109/MMUL.2023.3272513).
- Garcia-Dias, R., Allende Prieto, C., et al. (May 2018). ‘Machine learning in APOGEE. Unsupervised spectral classification with K-means’. In: A&A 612, A98, A98. doi: [10.1051/0004-6361/201732134](https://doi.org/10.1051/0004-6361/201732134).
- Garcia-Piquer, A., Morales, J. C., et al. (Aug. 2017). ‘Efficient scheduling of astronomical observations. Application to the CARMENES radial-velocity survey’. In: A&A 604, A87, A87. doi: [10.1051/0004-6361/201628577](https://doi.org/10.1051/0004-6361/201628577).
- Garilli, B., Fumana, M., et al. (July 2010). ‘EZ: A Tool For Automatic Redshift Measurement’. In: PASP 122.893, p. 827. doi: [10.1086/654903](https://doi.org/10.1086/654903).
- Garofalo, M., Botta, A., and Ventre, G. (June 2017). ‘Astrophysics and Big Data: Challenges, Methods, and Tools’. In: *Astroinformatics*. Ed. by M. Brescia, S. G. Djorgovski, et al. Vol. 325, pp. 345–348. doi: [10.1017/S1743921316012813](https://doi.org/10.1017/S1743921316012813).
- Gatica, C., Demarco, R., et al. (Jan. 2024). ‘The AGN fraction in high-redshift protocluster candidates selected by Planck and Herschel’. In: MNRAS 527.2, pp. 3006–3017. doi: [10.1093/mnras/stad3404](https://doi.org/10.1093/mnras/stad3404).
- Gebhardt, K., Bender, R., et al. (Aug. 2000). ‘A Relationship between Nuclear Black Hole Mass and Galaxy Velocity Dispersion’. In: ApJ 539.1, pp. L13–L16. doi: [10.1086/312840](https://doi.org/10.1086/312840).
- Gehrels, N. (Apr. 1986). ‘Confidence Limits for Small Numbers of Events in Astrophysical Data’. In: ApJ 303, p. 336. doi: [10.1086/164079](https://doi.org/10.1086/164079).
- Gerwin, D. (1974). ‘Information processing, data inferences, and scientific generalization’. In: *Behavioral Science* 19.5, pp. 314–325. doi: [10.1002/bs.3830190504](https://doi.org/10.1002/bs.3830190504).
- Getachew-Woreta, T., Pović, M., et al. (July 2022). ‘Effect of AGN on the morphological properties of their host galaxies in the local Universe’. In: MNRAS 514.1, pp. 607–620. doi: [10.1093/mnras/stac851](https://doi.org/10.1093/mnras/stac851).
- Geurts, P., Ernst, D., and Wehenkel, L. (Apr. 2006). ‘Extremely randomized trees’. In: *Machine Learning* 63.1, pp. 3–42. ISSN: 1573-0565. doi: [10.1007/s10994-006-6226-1](https://doi.org/10.1007/s10994-006-6226-1).
- Giles, D. and Walkowicz, L. (Mar. 2019). ‘Systematic serendipity: a test of unsupervised machine learning as a method for anomaly detection’. In: MNRAS 484.1, pp. 834–849. doi: [10.1093/mnras/sty3461](https://doi.org/10.1093/mnras/sty3461).
- Giveon, U., Maoz, D., et al. (July 1999). ‘Long-term optical variability properties of the Palomar-Green quasars’. In: MNRAS 306.3, pp. 637–654. doi: [10.1046/j.1365-8711.1999.02556.x](https://doi.org/10.1046/j.1365-8711.1999.02556.x).

- Glahn, H. R. and Jorgensen, D. L. (1970). ‘Climatological Aspects of the Brier p-score’. In: *Monthly Weather Review* 98.2, pp. 136–141. doi: [10.1175/1520-0493\(1970\)098<0136:CAOTBP>2.3.CO;2](https://doi.org/10.1175/1520-0493(1970)098<0136:CAOTBP>2.3.CO;2).
- Glazebrook, K., Offer, A. R., and Deeley, K. (Jan. 1998). ‘Automatic Redshift Determination by Use of Principal Component Analysis. I. Fundamentals’. In: *ApJ* 492.1, pp. 98–109. doi: [10.1086/305039](https://doi.org/10.1086/305039).
- Glikman, E., Langgin, R., et al. (July 2023). ‘A Candidate Dual QSO at Cosmic Noon’. In: *ApJ* 951.1, L18, p. L18. doi: [10.3847/2041-8213/acda2f](https://doi.org/10.3847/2041-8213/acda2f).
- Goebel, R., Chander, A., et al. (2018). ‘Explainable ai: the new 42?’ In: *International cross-domain conference for machine learning and knowledge extraction*. Springer. Springer International Publishing, pp. 295–303. ISBN: 978-3-319-99740-7.
- Gordon, Y. A., Boyce, M. M., et al. (Oct. 2020). ‘A Catalog of Very Large Array Sky Survey Epoch 1 Quick Look Components, Sources, and Host Identifications’. In: *Research Notes of the American Astronomical Society* 4.10, 175, p. 175. doi: [10.3847/2515-5172/abbe23](https://doi.org/10.3847/2515-5172/abbe23).
- Goulding, A. D., Zakamska, N. L., et al. (Mar. 2018). ‘High-redshift Extremely Red Quasars in X-Rays’. In: *ApJ* 856.1, 4, p. 4. doi: [10.3847/1538-4357/aab040](https://doi.org/10.3847/1538-4357/aab040).
- Guglielmetti, F., Arras, P., et al. (Dec. 2022). ‘Bayesian and Machine Learning Methods in the Big Data Era for Astronomical Imaging’. In: *Physical Sciences Forum*. Vol. 5. Physical Sciences Forum, 50, p. 50. doi: [10.3390/psf2022005050](https://doi.org/10.3390/psf2022005050).
- Gültekin, K., Richstone, D. O., et al. (June 2009). ‘The M- σ and M-L Relations in Galactic Bulges, and Determinations of Their Intrinsic Scatter’. In: *ApJ* 698.1, pp. 198–221. doi: [10.1088/0004-637X/698/1/198](https://doi.org/10.1088/0004-637X/698/1/198).
- Gürkan, G., Hardcastle, M. J., et al. (Feb. 2019). ‘LoTSS/HETDEX: Optical quasars. I. Low-frequency radio properties of optically selected quasars’. In: *A&A* 622, A11, A11. doi: [10.1051/0004-6361/201833892](https://doi.org/10.1051/0004-6361/201833892).
- Guyon, I. and Elisseeff, A. (Mar. 2003). ‘An introduction to variable and feature selection’. In: *J. Mach. Learn. Res.* 3.null, pp. 1157–1182. ISSN: 1532-4435.
- Haardt, F. and Madau, P. (Feb. 2012). ‘Radiative Transfer in a Clumpy Universe. IV. New Synthesis Models of the Cosmic UV/X-Ray Background’. In: *ApJ* 746.2, 125, p. 125. doi: [10.1088/0004-637X/746/2/125](https://doi.org/10.1088/0004-637X/746/2/125).
- Habouzit, M., Onoue, M., et al. (Apr. 2022). ‘Co-evolution of massive black holes and their host galaxies at high redshift: discrepancies from six cosmological simulations and the key role of JWST’. In: *MNRAS* 511.3, pp. 3751–3767. doi: [10.1093/mnras/stac225](https://doi.org/10.1093/mnras/stac225).
- Haiman, Z. and Loeb, A. (July 1997). ‘Signatures of Stellar Reionization of the Universe’. In: *ApJ* 483.1, pp. 21–37. doi: [10.1086/304238](https://doi.org/10.1086/304238).
- Hales, C. A., Murphy, T., et al. (Aug. 2012a). *BLOBCAT: Software to Catalog Blobs*. Astrophysics Source Code Library, record ascl:1208.009.
- (Sept. 2012b). ‘BLOBCAT: software to catalogue flood-filled blobs in radio images of total intensity and linear polarization’. In: *MNRAS* 425.2, pp. 979–996. doi: [10.1111/j.1365-2966.2012.21373.x](https://doi.org/10.1111/j.1365-2966.2012.21373.x).
- Hancock, P. J., Murphy, T., et al. (May 2012). ‘Compact continuum source finding for next generation radio surveys’. In: *MNRAS* 422.2, pp. 1812–1824. doi: [10.1111/j.1365-2966.2012.20768.x](https://doi.org/10.1111/j.1365-2966.2012.20768.x).
- Hancock, P. J., Trott, C. M., and Hurley-Walker, N. (Mar. 2018). ‘Source Finding in the Era of the SKA (Precursors): Aegean 2.0’. In: *PASA* 35, e011, e011. doi: [10.1017/pasa.2018.3](https://doi.org/10.1017/pasa.2018.3).

REFERENCES

- Hardcastle, M. J., Horton, M. A., et al. (Oct. 2023). ‘The LOFAR Two-Metre Sky Survey. VI. Optical identifications for the second data release’. In: A&A 678, A151, A151. doi: [10.1051/0004-6361/202347333](https://doi.org/10.1051/0004-6361/202347333).
- Häring, N. and Rix, H.-W. (Apr. 2004). ‘On the Black Hole Mass-Bulge Mass Relation’. In: ApJ 604.2, pp. L89–L92. doi: [10.1086/383567](https://doi.org/10.1086/383567).
- Head, T., Kumar, M., et al. (Oct. 2021). *scikit-optimize/scikit-optimize*. Version v0.9.0. doi: [10.5281/zenodo.5565057](https://doi.org/10.5281/zenodo.5565057).
- Heckman, T. M. (July 1980). ‘An Optical and Radio Survey of the Nuclei of Bright Galaxies - Activity in the Normal Galactic Nuclei’. In: A&A 87, p. 152.
- Heckman, T. M. and Best, P. N. (Aug. 2014). ‘The Coevolution of Galaxies and Supermassive Black Holes: Insights from Surveys of the Contemporary Universe’. In: ARA&A 52, pp. 589–660. doi: [10.1146/annurev-astro-081913-035722](https://doi.org/10.1146/annurev-astro-081913-035722).
- Helfand, D. J., White, R. L., and Becker, R. H. (Mar. 2015). ‘The Last of FIRST: The Final Catalog and Source Identifications’. In: ApJ 801.1, 26, p. 26. doi: [10.1088/0004-637X/801/1/26](https://doi.org/10.1088/0004-637X/801/1/26).
- Helou, G., Soifer, B. T., and Rowan-Robinson, M. (Nov. 1985). ‘Thermal infrared and nonthermal radio : remarkable correlation in disks of galaxies.’ In: ApJ 298, pp. L7–L11. doi: [10.1086/184556](https://doi.org/10.1086/184556).
- Hernán-Caballero, A., Varela, J., et al. (Oct. 2021). ‘The miniJPAS survey: Photometric redshift catalogue’. In: A&A 654, A101, A101. doi: [10.1051/0004-6361/202141236](https://doi.org/10.1051/0004-6361/202141236).
- Hickox, R. C. and Alexander, D. M. (Sept. 2018). ‘Obscured Active Galactic Nuclei’. In: ARA&A 56, pp. 625–671. doi: [10.1146/annurev-astro-081817-051803](https://doi.org/10.1146/annurev-astro-081817-051803).
- Hildebrand, R. H. (Sept. 1983). ‘The determination of cloud masses and dust characteristics from submillimetre thermal emission.’ In: QJRAS 24, pp. 267–282.
- Hildebrandt, H., Arnouts, S., et al. (Nov. 2010). ‘PHAT: PHoto-z Accuracy Testing’. In: A&A 523, A31, A31. doi: [10.1051/0004-6361/201014885](https://doi.org/10.1051/0004-6361/201014885).
- Hill, G. J., Gebhardt, K., et al. (Oct. 2008). ‘The Hobby-Eberly Telescope Dark Energy Experiment (HETDEX): Description and Early Pilot Survey Results’. In: *Panoramic Views of Galaxy Formation and Evolution*. Ed. by T. Kodama, T. Yamada, and K. Aoki. Vol. 399. Astronomical Society of the Pacific Conference Series, p. 115.
- Hoaglin, D., Mosteller, F., et al. (1983). *Understanding Robust and Exploratory Data Analysis*. Wiley Series in Probability and Statistics: Probability and Statistics Section Series. John Wiley & Sons. ISBN: 9780471097778.
- Hodge, J. A., Becker, R. H., et al. (July 2011). ‘High-resolution Very Large Array Imaging of Sloan Digital Sky Survey Stripe 82 at 1.4 GHz’. In: AJ 142.1, 3, p. 3. doi: [10.1088/0004-6256/142/1/3](https://doi.org/10.1088/0004-6256/142/1/3).
- Hoffer, R. M. and Fleming, M. D. (1978). ‘Mapping vegetative cover by computer-aided analysis of satellite data’. In: *USDA Forest Service Gen. Tech. Rep. RM-55*, pp. 227–237.
- Hogg, D. W. (May 1999). ‘Distance measures in cosmology’. In: *arXiv e-prints*, astro-ph/9905116, astro-ph/9905116. doi: [10.48550/arXiv.astro-ph/9905116](https://doi.org/10.48550/arXiv.astro-ph/9905116).
- Hoyle, B., Gruen, D., et al. (July 2018). ‘Dark Energy Survey Year 1 Results: redshift distributions of the weak-lensing source galaxies’. In: MNRAS 478.1, pp. 592–610. doi: [10.1093/mnras/sty957](https://doi.org/10.1093/mnras/sty957).
- Huertas-Company, M. and Lanusse, F. (Jan. 2023). ‘The Dawes Review 10: The impact of deep learning for the analysis of galaxy surveys’. In: PASA 40, e001, e001. doi: [10.1017/pasa.2022.55](https://doi.org/10.1017/pasa.2022.55).

- Hunter, J. D. (2007). ‘Matplotlib: A 2D graphics environment’. In: *Computing in Science & Engineering* 9.3, pp. 90–95. doi: [10.1109/MCSE.2007.55](https://doi.org/10.1109/MCSE.2007.55).
- Huterer, D., Takada, M., et al. (Feb. 2006). ‘Systematic errors in future weak-lensing surveys: requirements and prospects for self-calibration’. In: MNRAS 366.1, pp. 101–114. doi: [10.1111/j.1365-2966.2005.09782.x](https://doi.org/10.1111/j.1365-2966.2005.09782.x).
- Ibar, E., Ivison, R. J., et al. (Jan. 2010). ‘Deep multi-frequency radio imaging in the Lockman Hole - II. The spectral index of submillimetre galaxies’. In: MNRAS 401.1, pp. L53–L57. doi: [10.1111/j.1745-3933.2009.00786.x](https://doi.org/10.1111/j.1745-3933.2009.00786.x).
- İkiz, T., Peletier, R. F., et al. (Aug. 2020). ‘Infrared-detected AGNs in the local Universe’. In: A&A 640, A68, A68. doi: [10.1051/0004-6361/201935971](https://doi.org/10.1051/0004-6361/201935971).
- Ilbert, O., Arnouts, S., et al. (Oct. 2006). ‘Accurate photometric redshifts for the CFHT legacy survey calibrated using the VIMOS VLT deep survey’. In: A&A 457.3, pp. 841–856. doi: [10.1051/0004-6361:20065138](https://doi.org/10.1051/0004-6361:20065138).
- Ilbert, O., Capak, P., et al. (Jan. 2009). ‘Cosmos Photometric Redshifts with 30-Bands for 2-deg²’. In: ApJ 690.2, pp. 1236–1249. doi: [10.1088/0004-637X/690/2/1236](https://doi.org/10.1088/0004-637X/690/2/1236).
- Inayoshi, K., Visbal, E., and Haiman, Z. (Aug. 2020). ‘The Assembly of the First Massive Black Holes’. In: ARA&A 58, pp. 27–97. doi: [10.1146/annurev-astro-120419-014455](https://doi.org/10.1146/annurev-astro-120419-014455).
- IPCC (2022). *Climate Change 2022: Mitigation of Climate Change. Contribution of Working Group III to the Sixth Assessment Report of the Intergovernmental Panel on Climate Change*. Ed. by P. Shukla, J. Skea, et al. Cambridge, UK and New York, NY, USA: Cambridge University Press. doi: [10.1017/9781009157926](https://doi.org/10.1017/9781009157926).
- Ivezić, Ž., Kahn, S. M., et al. (Mar. 2019). ‘LSST: From Science Drivers to Reference Design and Anticipated Data Products’. In: ApJ 873.2, 111, p. 111. doi: [10.3847/1538-4357/ab042c](https://doi.org/10.3847/1538-4357/ab042c).
- James, G., Witten, D., et al. (2023). *An Introduction to Statistical Learning: with Applications in Python*. Springer Texts in Statistics. Springer International Publishing. ISBN: 9783031387470.
- Jarrett, T. H., Cluver, M. E., et al. (Feb. 2017). ‘Galaxy and Mass Assembly (GAMA): Exploring the WISE Web in G12’. In: ApJ 836.2, 182, p. 182. doi: [10.3847/1538-4357/836/2/182](https://doi.org/10.3847/1538-4357/836/2/182).
- Jarvis, M., Taylor, R., et al. (Jan. 2016). ‘The MeerKAT International GHz Tiered Extragalactic Exploration (MIGHTEE) Survey’. In: *MeerKAT Science: On the Pathway to the SKA*, 6, p. 6. doi: [10.22323/1.277.0006](https://doi.org/10.22323/1.277.0006).
- Jia, P., Jia, Q., et al. (June 2023). ‘Observation Strategy Optimization for Distributed Telescope Arrays with Deep Reinforcement Learning’. In: AJ 165.6, 233, p. 233. doi: [10.3847/1538-3881/accceb](https://doi.org/10.3847/1538-3881/accceb).
- Jiang, L., Fan, X., et al. (July 2014). ‘The Sloan Digital Sky Survey Stripe 82 Imaging Data: Depth-optimized Co-adds over 300 deg² in Five Filters’. In: ApJS 213.1, 12, p. 12. doi: [10.1088/0067-0049/213/1/12](https://doi.org/10.1088/0067-0049/213/1/12).
- Jiang, T., Gradus, J. L., et al. (Feb. 2021). ‘Addressing Measurement Error in Random Forests Using Quantitative Bias Analysis’. In: *American Journal of Epidemiology* 190.9, pp. 1830–1840. ISSN: 0002-9262. doi: [10.1093/aje/kwab010](https://doi.org/10.1093/aje/kwab010).
- Johnson, J., Douze, M., and Jégou, H. (2019). ‘Billion-scale similarity search with GPUs’. In: *IEEE Transactions on Big Data* 7.3, pp. 535–547.
- Johnson, N. and Leone, F. (1964). *Statistics and Experimental Design in Engineering and the Physical Sciences*. Vol. 2. Wiley, p. 125. ISBN: 9780471444893.

REFERENCES

- Jonas, J. and MeerKAT Team (Jan. 2016). ‘The MeerKAT Radio Telescope’. In: *MeerKAT Science: On the Pathway to the SKA*, 1, p. 1. doi: [10.22323/1.277.0001](https://doi.org/10.22323/1.277.0001).
- Josse, J., Prost, N., et al. (Feb. 2019). ‘On the consistency of supervised learning with missing values’. In: *arXiv e-prints*, arXiv:1902.06931, arXiv:1902.06931. doi: [10.48550/arXiv.1902.06931](https://doi.org/10.48550/arXiv.1902.06931).
- Josse, J. and Reiter, J. P. (2018). ‘Introduction to the Special Section on Missing Data’. In: *Statistical Science* 33.2, pp. 139–141. doi: [10.1214/18-STS332IN](https://doi.org/10.1214/18-STS332IN).
- Kalton, G. and Kasprzyk, D. (1982). ‘Imputing for missing survey responses’. In: *Proceedings of the section on survey research methods, American Statistical Association*. Vol. 22. American Statistical Association Cincinnati, p. 31.
- Kamiran, F. and Calders, T. (Oct. 2012). ‘Data preprocessing techniques for classification without discrimination’. In: *Knowledge and Information Systems* 33.1, pp. 1–33. issn: 0219-3116. doi: [10.1007/s10115-011-0463-8](https://doi.org/10.1007/s10115-011-0463-8).
- Karniadakis, G. E., Kevrekidis, I. G., et al. (June 2021). ‘Physics-informed machine learning’. In: *Nature Reviews Physics* 3.6, pp. 422–440. issn: 2522-5820. doi: [10.1038/s42254-021-00314-5](https://doi.org/10.1038/s42254-021-00314-5).
- Katz, H., Kimm, T., et al. (Aug. 2018). ‘A Census of the LyC photons that form the UV background during reionization’. In: *MNRAS* 478.4, pp. 4986–5005. doi: [10.1093/mnras/sty1225](https://doi.org/10.1093/mnras/sty1225).
- (Feb. 2019). ‘Tracing the sources of reionization in cosmological radiation hydrodynamics simulations’. In: *MNRAS* 483.1, pp. 1029–1041. doi: [10.1093/mnras/sty3154](https://doi.org/10.1093/mnras/sty3154).
- Kauffmann, G., Heckman, T. M., et al. (Dec. 2003). ‘The host galaxies of active galactic nuclei’. In: *MNRAS* 346.4, pp. 1055–1077. doi: [10.1111/j.1365-2966.2003.07154.x](https://doi.org/10.1111/j.1365-2966.2003.07154.x).
- Ke, G., Meng, Q., et al. (2017). ‘LightGBM: A Highly Efficient Gradient Boosting Decision Tree’. In: *Advances in Neural Information Processing Systems*. Ed. by I. Guyon, U. V. Luxburg, et al. Vol. 30. Curran Associates, Inc. URL: <https://proceedings.neurips.cc/paper/2017/file/6449f44a102fde848669bdd9eb6b76fa-Paper.pdf>.
- Kennicutt Robert C., J., Hao, C.-N., et al. (Oct. 2009). ‘Dust-corrected Star Formation Rates of Galaxies. I. Combinations of H α and Infrared Tracers’. In: *ApJ* 703.2, pp. 1672–1695. doi: [10.1088/0004-637X/703/2/1672](https://doi.org/10.1088/0004-637X/703/2/1672).
- Kewley, L. J., Dopita, M. A., et al. (July 2001). ‘Theoretical Modeling of Starburst Galaxies’. In: *ApJ* 556.1, pp. 121–140. doi: [10.1086/321545](https://doi.org/10.1086/321545).
- Kewley, L. J., Groves, B., et al. (Nov. 2006). ‘The host galaxies and classification of active galactic nuclei’. In: *MNRAS* 372.3, pp. 961–976. doi: [10.1111/j.1365-2966.2006.10859.x](https://doi.org/10.1111/j.1365-2966.2006.10859.x).
- Khrabtsov, V., Spiniello, C., et al. (July 2021). ‘VEXAS: VISTA EXtension to Auxiliary Surveys. Data Release 2: Machine-learning based classification of sources in the Southern Hemisphere’. In: *A&A* 651, A69, A69. doi: [10.1051/0004-6361/202040131](https://doi.org/10.1051/0004-6361/202040131).
- Kim, J.-Y., Krichbaum, T. P., et al. (Aug. 2020). ‘Event Horizon Telescope imaging of the archetypal blazar 3C 279 at an extreme 20 microarcsecond resolution’. In: *A&A* 640, A69, A69. doi: [10.1051/0004-6361/202037493](https://doi.org/10.1051/0004-6361/202037493).
- Kim, S. J., Lee, H. M., et al. (Dec. 2012). ‘The North Ecliptic Pole Wide survey of AKARI: a near- and mid-infrared source catalog’. In: *A&A* 548, A29, A29. doi: [10.1051/0004-6361/201219105](https://doi.org/10.1051/0004-6361/201219105).

- King, A. and Pounds, K. (Aug. 2015). ‘Powerful Outflows and Feedback from Active Galactic Nuclei’. In: ARA&A 53, pp. 115–154. doi: [10.1146/annurev-astro-082214-122316](https://doi.org/10.1146/annurev-astro-082214-122316).
- Kirkpatrick, A., Alberts, S., et al. (Nov. 2017). ‘The AGN-Star Formation Connection: Future Prospects with JWST’. In: ApJ 849.2, 111, p. 111. doi: [10.3847/1538-4357/aa911d](https://doi.org/10.3847/1538-4357/aa911d).
- Kirkpatrick, A., Pope, A., et al. (Nov. 2012). ‘GOODS-Herschel: Impact of Active Galactic Nuclei and Star Formation Activity on Infrared Spectral Energy Distributions at High Redshift’. In: ApJ 759.2, 139, p. 139. doi: [10.1088/0004-637X/759/2/139](https://doi.org/10.1088/0004-637X/759/2/139).
- Kluyver, T., Ragan-Kelley, B., et al. (2016). ‘Jupyter Notebooks – a publishing format for reproducible computational workflows’. In: *Positioning and Power in Academic Publishing: Players, Agents and Agendas*. Ed. by F. Loizides and B. Schmidt. IOS Press, pp. 87–90.
- Kohavi, Ron and John, G. H. (1997). ‘Wrappers for feature subset selection’. In: *Artificial Intelligence* 97.1. Relevance, pp. 273–324. issn: 0004-3702. doi: [10.1016/S0004-3702\(97\)00043-X](https://doi.org/10.1016/S0004-3702(97)00043-X).
- Kollmeier, J. A., Zasowski, G., et al. (Nov. 2017). ‘SDSS-V: Pioneering Panoptic Spectroscopy’. In: *arXiv e-prints*, arXiv:1711.03234, arXiv:1711.03234. doi: [10.48550/arXiv.1711.03234](https://doi.org/10.48550/arXiv.1711.03234).
- Kondapally, R., Best, P. N., et al. (July 2022). ‘Cosmic evolution of low-excitation radio galaxies in the LOFAR two-metre sky survey deep fields’. In: MNRAS 513.3, pp. 3742–3767. doi: [10.1093/mnras/stac1128](https://doi.org/10.1093/mnras/stac1128).
- Kormendy, J. and Ho, L. C. (Aug. 2013). ‘Coevolution (Or Not) of Supermassive Black Holes and Host Galaxies’. In: ARA&A 51.1, pp. 511–653. doi: [10.1146/annurev-astro-082708-101811](https://doi.org/10.1146/annurev-astro-082708-101811).
- Koshida, S., Minezaki, T., et al. (June 2014). ‘Reverberation Measurements of the Inner Radius of the Dust Torus in 17 Seyfert Galaxies’. In: ApJ 788.2, 159, p. 159. doi: [10.1088/0004-637X/788/2/159](https://doi.org/10.1088/0004-637X/788/2/159).
- Koshida, S., Yoshii, Y., et al. (Aug. 2009). ‘Variation of Inner Radius of Dust Torus in NGC4151’. In: ApJ 700.2, pp. L109–L113. doi: [10.1088/0004-637X/700/2/L109](https://doi.org/10.1088/0004-637X/700/2/L109).
- Kovács, O. E., Bogdán, Á., et al. (Feb. 2019). ‘Detection of the Missing Baryons toward the Sightline of H1821+643’. In: ApJ 872.1, 83, p. 83. doi: [10.3847/1538-4357/aaef78](https://doi.org/10.3847/1538-4357/aaef78).
- Krumpe, M., Miyaji, T., and Coil, A. L. (Nov. 2014). ‘Clustering Measurements of broad-line AGNs: Review and Future’. In: *Multifrequency Behaviour of High Energy Cosmic Sources*, pp. 71–78. doi: [10.14311/APP.2014.01.0071](https://doi.org/10.14311/APP.2014.01.0071).
- Kulkarni, G., Worseck, G., and Hennawi, J. F. (Sept. 2019). ‘Evolution of the AGN UV luminosity function from redshift 7.5’. In: MNRAS 488.1, pp. 1035–1065. doi: [10.1093/mnras/stz1493](https://doi.org/10.1093/mnras/stz1493).
- Kull, M., Filho, T. M. S., and Flach, P. (2017a). ‘Beyond sigmoids: How to obtain well-calibrated probabilities from binary classifiers with beta calibration’. In: *Electronic Journal of Statistics* 11.2, pp. 5052–5080. doi: [10.1214/17-EJS1338SI](https://doi.org/10.1214/17-EJS1338SI).
- Kull, M., Filho, T. S., and Flach, P. (Apr. 2017b). ‘Beta calibration: a well-founded and easily implemented improvement on logistic calibration for binary classifiers’. In: *Proceedings of the 20th International Conference on Artificial Intelligence and Statistics*. Ed. by A. Singh and J. Zhu. Vol. 54. Proceedings of Machine Learning Research. PMLR, pp. 623–631. url: <https://proceedings.mlr.press/v54/kull17a.html>.
- Kunsági-Máté, S., Beck, R., et al. (Oct. 2022). ‘Photometric redshifts for quasars from WISE-PS1-STRM’. In: MNRAS 516.2, pp. 2662–2670. doi: [10.1093/mnras/stac2411](https://doi.org/10.1093/mnras/stac2411).

REFERENCES

- Kurtz, M. J. and Mink, D. J. (Aug. 1998). ‘RVSAO 2.0: Digital Redshifts and Radial Velocities’. In: PASP 110.750, pp. 934–977. doi: [10.1086/316207](https://doi.org/10.1086/316207).
- Kuźmicz, A. and Jamrozy, M. (Mar. 2021). ‘Giant Radio Quasars: Sample and Basic Properties’. In: ApJS 253.1, 25, p. 25. doi: [10.3847/1538-4365/abd483](https://doi.org/10.3847/1538-4365/abd483).
- Lacerda, E. A. D., Sánchez, S. F., et al. (Nov. 2022). ‘pyFIT3D and pyPipe3D - The new version of the integral field spectroscopy data analysis pipeline’. In: New A 97, 101895, p. 101895. doi: [10.1016/j.newast.2022.101895](https://doi.org/10.1016/j.newast.2022.101895).
- Lacy, M., Baum, S. A., et al. (Mar. 2020). ‘The Karl G. Jansky Very Large Array Sky Survey (VLASS). Science Case and Survey Design’. In: PASP 132.1009, 035001, p. 035001. doi: [10.1088/1538-3873/ab63eb](https://doi.org/10.1088/1538-3873/ab63eb).
- Lacy, M., Petric, A. O., et al. (Jan. 2007). ‘Optical Spectroscopy and X-Ray Detections of a Sample of Quasars and Active Galactic Nuclei Selected in the Mid-Infrared from Two Spitzer Space Telescope Wide-Area Surveys’. In: AJ 133.1, pp. 186–205. doi: [10.1086/509617](https://doi.org/10.1086/509617).
- Lacy, M., Ridgway, S. E., et al. (Oct. 2013). ‘The Spitzer Mid-infrared Active Galactic Nucleus Survey. I. Optical and Near-infrared Spectroscopy of Obscured Candidates and Normal Active Galactic Nuclei Selected in the Mid-infrared’. In: ApJS 208.2, 24, p. 24. doi: [10.1088/0067-0049/208/2/24](https://doi.org/10.1088/0067-0049/208/2/24).
- Lacy, M., Storrie-Lombardi, L. J., et al. (Sept. 2004). ‘Obscured and Unobscured Active Galactic Nuclei in the Spitzer Space Telescope First Look Survey’. In: ApJS 154.1, pp. 166–169. doi: [10.1086/422816](https://doi.org/10.1086/422816).
- Lacy, M., Surace, J. A., et al. (Feb. 2021). ‘A Spitzer survey of Deep Drilling Fields to be targeted by the Vera C. Rubin Observatory Legacy Survey of Space and Time’. In: MNRAS 501.1, pp. 892–910. doi: [10.1093/mnras/staa3714](https://doi.org/10.1093/mnras/staa3714).
- Lacy, M. and Sajina, A. (Apr. 2020). ‘Active galactic nuclei as seen by the Spitzer Space Telescope’. In: *Nature Astronomy* 4, pp. 352–363. doi: [10.1038/s41550-020-1071-x](https://doi.org/10.1038/s41550-020-1071-x).
- Lal, D. V. (July 2021). ‘The Discovery of a Remnant Radio Galaxy in A2065 Using GMRT’. In: ApJ 915.2, 126, p. 126. doi: [10.3847/1538-4357/ac042d](https://doi.org/10.3847/1538-4357/ac042d).
- LaMassa, S. M., Urry, C. M., et al. (Feb. 2016). ‘The 31 Deg² Release of the Stripe 82 X-Ray Survey: The Point Source Catalog’. In: ApJ 817.2, 172, p. 172. doi: [10.3847/0004-637X/817/2/172](https://doi.org/10.3847/0004-637X/817/2/172).
- Lang, D. (May 2014). ‘unWISE: Unblurred Coadds of the WISE Imaging’. In: AJ 147.5, 108, p. 108. doi: [10.1088/0004-6256/147/5/108](https://doi.org/10.1088/0004-6256/147/5/108).
- Langeroodi, D. and Hjorth, J. (Apr. 2023). ‘PAH Emission from Star-forming Galaxies in JWST Mid-infrared Imaging of the Lensing Cluster SMACS J0723.3-7327’. In: ApJ 946.2, L40, p. L40. doi: [10.3847/2041-8213/acc1e0](https://doi.org/10.3847/2041-8213/acc1e0).
- Langley, P. (1977). ‘BACON: A Production System That Discovers Empirical Laws’. In: *International Joint Conference on Artificial Intelligence*. URL: <https://api.semanticscholar.org/CorpusID:2320342>.
- (1979). ‘Rediscovering Physics with BACON.3’. In: *Proceedings of the 6th International Joint Conference on Artificial Intelligence - Volume 1*. IJCAI’79. Tokyo, Japan: Morgan Kaufmann Publishers Inc., pp. 505–507. ISBN: 0934613478.
- Langley, P., Bradshaw, G. L., and Simon, H. A. (1981). ‘BACON.5: The Discovery of Conservation Laws’. In: *Proceedings of the 7th International Joint Conference on Artificial Intelligence - Volume 1*. IJCAI’81. Vancouver, BC, Canada: Morgan Kaufmann Publishers Inc., pp. 121–126.

- Langley, P. and Zytkow, J. M. (1990). ‘Data-Driven Approaches to Empirical Discovery’. In: *Machine Learning: Paradigms and Methods*. USA: Elsevier North-Holland, Inc., pp. 283–312. ISBN: 0262530880.
- Lansbury, G. B., Banerji, M., et al. (Jan. 2020). ‘X-ray observations of luminous dusty quasars at $z > 2$ ’. In: MNRAS 495.3, pp. 2652–2663. doi: [10.1093/mnras/staa1220](https://doi.org/10.1093/mnras/staa1220).
- Latimer, C. J., Reines, A. E., et al. (June 2021). ‘A Chandra and HST View of WISE-selected AGN Candidates in Dwarf Galaxies’. In: ApJ 914.2, 133, p. 133. doi: [10.3847/1538-4357/abfe0c](https://doi.org/10.3847/1538-4357/abfe0c).
- Lazio, J. W., Kimball, A., et al. (Feb. 2014). ‘Radio Astronomy in LSST Era’. In: PASP 126.936, p. 196. doi: [10.1086/675262](https://doi.org/10.1086/675262).
- Le Fèvre, O., Tasca, L. A. M., et al. (Apr. 2015). ‘The VIMOS Ultra-Deep Survey: ~10 000 galaxies with spectroscopic redshifts to study galaxy assembly at early epochs $2 < z \approx 6$ ’. In: A&A 576, A79, A79. doi: [10.1051/0004-6361/201423829](https://doi.org/10.1051/0004-6361/201423829).
- Lee, H. M., Kim, S. J., et al. (Feb. 2009). ‘North Ecliptic Pole Wide Field Survey of AKARI: Survey Strategy and Data Characteristics’. In: PASJ 61, p. 375. doi: [10.1093/pasj/61.2.375](https://doi.org/10.1093/pasj/61.2.375).
- Lehmer, B. D., Brandt, W. N., et al. (Nov. 2005). ‘The Extended Chandra Deep Field-South Survey: Chandra Point-Source Catalogs’. In: ApJS 161.1, pp. 21–40. doi: [10.1086/444590](https://doi.org/10.1086/444590).
- Leja, J., Johnson, B. D., et al. (June 2019). ‘An Older, More Quiescent Universe from Panchromatic SED Fitting of the 3D-HST Survey’. In: ApJ 877.2, 140, p. 140. doi: [10.3847/1538-4357/ab1d5a](https://doi.org/10.3847/1538-4357/ab1d5a).
- Lichtenstein, S., Fischhoff, B., and Phillips, L. D. (1982). ‘Calibration of probabilities: The state of the art to 1980’. In: *Judgment under Uncertainty: Heuristics and Biases*. Ed. by D. Kahneman, P. Slovic, and A. Tversky. Cambridge University Press, pp. 306–334. doi: [10.1017/CBO9780511809477.023](https://doi.org/10.1017/CBO9780511809477.023).
- Lima, E. V. R., Sodré, L., et al. (Jan. 2022). ‘Photometric redshifts for the S-PLUS Survey: Is machine learning up to the task?’ In: *Astronomy and Computing* 38, 100510, p. 100510. doi: [10.1016/j.ascom.2021.100510](https://doi.org/10.1016/j.ascom.2021.100510).
- Linardatos, P., Papastefanopoulos, V., and Kotsiantis, S. (2021). ‘Explainable AI: A Review of Machine Learning Interpretability Methods’. In: *Entropy* 23.1. ISSN: 1099-4300. doi: [10.3390/e23010018](https://doi.org/10.3390/e23010018).
- Lira, P., Arévalo, P., et al. (Aug. 2011). ‘Optical and near-IR long-term monitoring of NGC 3783 and MR 2251-178: evidence for variable near-IR emission from thin accretion discs’. In: MNRAS 415.2, pp. 1290–1303. doi: [10.1111/j.1365-2966.2011.18774.x](https://doi.org/10.1111/j.1365-2966.2011.18774.x).
- Lira, P., Arévalo, P., et al. (Nov. 2015). ‘Long-term monitoring of the archetype Seyfert galaxy MCG-6-30-15: X-ray, optical and near-IR variability of the corona, disc and torus’. In: MNRAS 454.1, pp. 368–379. doi: [10.1093/mnras/stv1945](https://doi.org/10.1093/mnras/stv1945).
- Lisenfeld, U. and Völk, H. J. (Feb. 2000). ‘On the radio spectral index of galaxies’. In: A&A 354, pp. 423–430.
- Liske, J., Baldry, I. K., et al. (Sept. 2015). ‘Galaxy And Mass Assembly (GAMA): end of survey report and data release 2’. In: MNRAS 452.2, pp. 2087–2126. doi: [10.1093/mnras/stv1436](https://doi.org/10.1093/mnras/stv1436).
- Little, R. and Rubin, D. (2014). *Statistical Analysis with Missing Data*. Wiley Series in Probability and Statistics. Wiley. ISBN: 9781118625880.
- Liu, D., Lang, P., et al. (Oct. 2019). ‘Automated Mining of the ALMA Archive in the COSMOS Field (A^3 COSMOS). I. Robust ALMA Continuum Photometry Catalogs and Stellar Mass and Star Formation Properties for ~700 Galaxies at $z = 0.5\text{--}6$ ’. In: ApJS 244.2, 40, p. 40. doi: [10.3847/1538-4365/ab42da](https://doi.org/10.3847/1538-4365/ab42da).

REFERENCES

- Lochner, M. and Bassett, B. A. (July 2021). ‘ASTRONOMALY: Personalised active anomaly detection in astronomical data’. In: *Astronomy and Computing* 36, 100481, p. 100481. doi: [10.1016/j.ascom.2021.100481](https://doi.org/10.1016/j.ascom.2021.100481).
- Loeb, A. and Furlanetto, S. R. (2013). *The First Galaxies in the Universe*. Princeton Series in Astrophysics. Princeton University Press. ISBN: 9780691144924.
- Loh, E. D. and Spillar, E. J. (Apr. 1986). ‘Photometric Redshifts of Galaxies’. In: *ApJ* 303, p. 154. doi: [10.1086/164062](https://doi.org/10.1086/164062).
- Louppe, G., Wehenkel, L., et al. (2013). ‘Understanding variable importances in forests of randomized trees’. In: *Advances in Neural Information Processing Systems*. Ed. by C. J. C. Burges, L. Bottou, et al. Vol. 26. Curran Associates, Inc. URL: <https://proceedings.neurips.cc/paper/2013/file/e3796ae838835da0b6f6ea37bcf8bcb7-Paper.pdf>.
- LSST Science Collaboration, Abell, P. A., et al. (Dec. 2009). ‘LSST Science Book, Version 2.0’. In: *arXiv e-prints*, arXiv:0912.0201, arXiv:0912.0201. doi: [10.48550/arXiv.0912.0201](https://doi.org/10.48550/arXiv.0912.0201).
- Luken, K. J., Norris, R. P., et al. (Apr. 2022). ‘Estimating galaxy redshift in radio-selected datasets using machine learning’. In: *Astronomy and Computing* 39, 100557, p. 100557. doi: [10.1016/j.ascom.2022.100557](https://doi.org/10.1016/j.ascom.2022.100557).
- Luken, K. J., Norris, R. P., and Park, L. A. F. (Oct. 2019). ‘Preliminary Results of Using k-Nearest Neighbors Regression to Estimate the Redshift of Radio-selected Data Sets’. In: *PASP* 131.1004, p. 108003. doi: [10.1088/1538-3873/aaea17](https://doi.org/10.1088/1538-3873/aaea17).
- Lukic, V., Brüggen, M., et al. (Aug. 2019). ‘Morphological classification of radio galaxies: capsule networks versus convolutional neural networks’. In: *MNRAS* 487.2, pp. 1729–1744. doi: [10.1093/mnras/stz1289](https://doi.org/10.1093/mnras/stz1289).
- Lundberg, S. M. and Lee, S.-I. (2017). ‘A Unified Approach to Interpreting Model Predictions’. In: *Advances in Neural Information Processing Systems 30*. Ed. by I. Guyon, U. V. Luxburg, et al. Curran Associates, Inc., pp. 4765–4774. URL: <http://papers.nips.cc/paper/7062-a-unified-approach-to-interpreting-model-predictions.pdf>.
- Lundberg, S. M., Erion, G., et al. (2020). ‘From local explanations to global understanding with explainable AI for trees’. In: *Nature Machine Intelligence* 2.1, pp. 2522–5839.
- Lyu, J., Alberts, S., et al. (Dec. 2022). ‘AGN Selection and Demographics in GOODS-S/HUDF from X-Ray to Radio’. In: *ApJ* 941.2, 191, p. 191. doi: [10.3847/1538-4357/ac9e5d](https://doi.org/10.3847/1538-4357/ac9e5d).
- Lyu, J. and Rieke, G. (May 2022). ‘Infrared Spectral Energy Distribution and Variability of Active Galactic Nuclei: Clues to the Structure of Circumnuclear Material’. In: *Universe* 8.6, 304, p. 304. doi: [10.3390/universe8060304](https://doi.org/10.3390/universe8060304).
- Ma, S. and Tourani, R. (Aug. 2020). ‘Predictive and Causal Implications of using Shapley Value for Model Interpretation’. In: *Proceedings of the 2020 KDD Workshop on Causal Discovery*. Vol. 127. Proceedings of Machine Learning Research. PMLR, pp. 23–38. URL: <https://proceedings.mlr.press/v127/ma20a.html>.
- Ma, Z., Xu, H., et al. (Feb. 2019). ‘A Machine Learning Based Morphological Classification of 14,245 Radio AGNs Selected from the Best-Heckman Sample’. In: *ApJS* 240.2, 34, p. 34. doi: [10.3847/1538-4365/aaf9a2](https://doi.org/10.3847/1538-4365/aaf9a2).
- Maccacaro, T., della Ceca, R., et al. (June 1991). ‘The Properties of X-Ray-selected Active Galactic Nuclei. I. Luminosity Function, Cosmological Evolution, and Contribution to the Diffuse X-Ray Background’. In: *ApJ* 374, p. 117. doi: [10.1086/170102](https://doi.org/10.1086/170102).

- Machado, D. P., Leonard, A., et al. (Dec. 2013). ‘Darth Fader: Using wavelets to obtain accurate redshifts of spectra at very low signal-to-noise’. In: *A&A* 560, A83, A83. doi: [10.1051/0004-6361/201219857](https://doi.org/10.1051/0004-6361/201219857).
- Machado Poletti Valle, L. F., Avestruz, C., et al. (Oct. 2021). ‘SHAPing the gas: understanding gas shapes in dark matter haloes with interpretable machine learning’. In: *MNRAS* 507.1, pp. 1468–1484. doi: [10.1093/mnras/stab2252](https://doi.org/10.1093/mnras/stab2252).
- Madau, P. and Dickinson, M. (Aug. 2014). ‘Cosmic Star-Formation History’. In: *ARA&A* 52, pp. 415–486. doi: [10.1146/annurev-astro-081811-125615](https://doi.org/10.1146/annurev-astro-081811-125615).
- Madau, P. and Haardt, F. (Nov. 2015). ‘Cosmic Reionization after Planck: Could Quasars Do It All?’ In: *ApJ* 813.1, L8, p. L8. doi: [10.1088/2041-8205/813/1/L8](https://doi.org/10.1088/2041-8205/813/1/L8).
- Madau, P., Haardt, F., and Rees, M. J. (Apr. 1999). ‘Radiative Transfer in a Clumpy Universe. III. The Nature of Cosmological Ionizing Sources’. In: *ApJ* 514.2, pp. 648–659. doi: [10.1086/306975](https://doi.org/10.1086/306975).
- Magliocchetti, M., Lutz, D., et al. (July 2014). ‘The PEP survey: infrared properties of radio-selected AGN’. In: *MNRAS* 442.1, pp. 682–693. doi: [10.1093/mnras/stu863](https://doi.org/10.1093/mnras/stu863).
- Magliocchetti, M. (Dec. 2022). ‘Hosts and environments: a (large-scale) radio history of AGN and star-forming galaxies’. In: *A&A Rev.* 30.1, 6, p. 6. doi: [10.1007/s00159-022-00142-1](https://doi.org/10.1007/s00159-022-00142-1).
- Magliocchetti, M., Maddox, S. J., et al. (June 2002). ‘The 2dF Galaxy Redshift Survey: the population of nearby radio galaxies at the 1-mJy level’. In: *MNRAS* 333.1, pp. 100–120. doi: [10.1046/j.1365-8711.2002.05386.x](https://doi.org/10.1046/j.1365-8711.2002.05386.x).
- Magorrian, J., Tremaine, S., et al. (June 1998). ‘The Demography of Massive Dark Objects in Galaxy Centers’. In: *AJ* 115.6, pp. 2285–2305. doi: [10.1086/300353](https://doi.org/10.1086/300353).
- Mainzer, A., Bauer, J., et al. (Apr. 2011). ‘Preliminary Results from NEOWISE: An Enhancement to the Wide-field Infrared Survey Explorer for Solar System Science’. In: *ApJ* 731.1, 53, p. 53. doi: [10.1088/0004-637X/731/1/53](https://doi.org/10.1088/0004-637X/731/1/53).
- Mainzer, A., Bauer, J., et al. (Sept. 2014). ‘Initial Performance of the NEOWISE Reactivation Mission’. In: *ApJ* 792.1, 30, p. 30. doi: [10.1088/0004-637X/792/1/30](https://doi.org/10.1088/0004-637X/792/1/30).
- Maitra, C., Haberl, F., et al. (Feb. 2019). ‘Identification of AGN in the XMM-Newton X-ray survey of the SMC’. In: *A&A* 622, A29, A29. doi: [10.1051/0004-6361/201833663](https://doi.org/10.1051/0004-6361/201833663).
- Mandal, S., Prandoni, I., et al. (Apr. 2021). ‘Extremely deep 150 MHz source counts from the LoTSS Deep Fields’. In: *A&A* 648, A5, A5. doi: [10.1051/0004-6361/202039998](https://doi.org/10.1051/0004-6361/202039998).
- Marchesi, S., Civano, F., et al. (Jan. 2016). ‘The Chandra COSMOS Legacy survey: optical/IR identifications’. In: *ApJ* 817.1, 34, p. 34. doi: [10.3847/0004-637X/817/1/34](https://doi.org/10.3847/0004-637X/817/1/34).
- Marocco, F., Eisenhardt, P. R. M., et al. (Mar. 2021). ‘The CatWISE2020 Catalog’. In: *ApJS* 253.1, 8, p. 8. doi: [10.3847/1538-4365/abd805](https://doi.org/10.3847/1538-4365/abd805).
- Martocchia, S., Piconcelli, E., et al. (Dec. 2017). ‘The WISSH quasars project. III. X-ray properties of hyper-luminous quasars’. In: *A&A* 608, A51, A51. doi: [10.1051/0004-6361/201731314](https://doi.org/10.1051/0004-6361/201731314).
- Mateos, S., Alonso-Herrero, A., et al. (Nov. 2012). ‘Using the Bright Ultrahard XMM-Newton survey to define an IR selection of luminous AGN based on WISE colours’. In: *MNRAS* 426.4, pp. 3271–3281. doi: [10.1111/j.1365-2966.2012.21843.x](https://doi.org/10.1111/j.1365-2966.2012.21843.x).

REFERENCES

- Mathews, E. P., Leja, J., et al. (Sept. 2023). ‘As Simple as Possible but No Simpler: Optimizing the Performance of Neural Net Emulators for Galaxy SED Fitting’. In: ApJ 954.2, 132, p. 132. doi: [10.3847/1538-4357/ace720](https://doi.org/10.3847/1538-4357/ace720).
- Matsuoka, Y., Strauss, M. A., et al. (Dec. 2018). ‘Subaru High-z Exploration of Low-luminosity Quasars (SHELLQs). V. Quasar Luminosity Function and Contribution to Cosmic Reionization at $z = 6$ ’. In: ApJ 869.2, 150, p. 150. doi: [10.3847/1538-4357/aaee7a](https://doi.org/10.3847/1538-4357/aaee7a).
- Matthews, B. W. (1975). ‘Comparison of the predicted and observed secondary structure of T4 phage lysozyme’. In: *Biochimica et Biophysica Acta (BBA) - Protein Structure* 405.2, pp. 442–451. ISSN: 0005-2795. doi: [10.1016/0005-2795\(75\)90109-9](https://doi.org/10.1016/0005-2795(75)90109-9).
- Mauch, T., Cotton, W. D., et al. (Jan. 2020). ‘The 1.28 GHz MeerKAT DEEP2 Image’. In: ApJ 888.2, 61, p. 61. doi: [10.3847/1538-4357/ab5d2d](https://doi.org/10.3847/1538-4357/ab5d2d).
- Mauch, T. and Sadler, E. M. (Mar. 2007). ‘Radio sources in the 6dFGS: local luminosity functions at 1.4 GHz for star-forming galaxies and radio-loud AGN’. In: MNRAS 375.3, pp. 931–950. doi: [10.1111/j.1365-2966.2006.11353.x](https://doi.org/10.1111/j.1365-2966.2006.11353.x).
- McAlpine, K., Jarvis, M. J., and Bonfield, D. G. (Dec. 2013). ‘Evolution of faint radio sources in the VIDEO-XMM3 field’. In: MNRAS 436.2, pp. 1084–1095. doi: [10.1093/mnras/stt1638](https://doi.org/10.1093/mnras/stt1638).
- McConnell, D., Hale, C. L., et al. (Nov. 2020). ‘The Rapid ASKAP Continuum Survey I: Design and first results’. In: PASA 37, e048, e048. doi: [10.1017/pasa.2020.41](https://doi.org/10.1017/pasa.2020.41).
- McConnell, N. J. and Ma, C.-P. (Feb. 2013). ‘Revisiting the Scaling Relations of Black Hole Masses and Host Galaxy Properties’. In: ApJ 764.2, 184, p. 184. doi: [10.1088/0004-637X/764/2/184](https://doi.org/10.1088/0004-637X/764/2/184).
- McGreer, I. D., Becker, R. H., et al. (Nov. 2006). ‘Discovery of a $z = 6.1$ Radio-Loud Quasar in the NOAO Deep Wide Field Survey’. In: ApJ 652.1, pp. 157–162. doi: [10.1086/507767](https://doi.org/10.1086/507767).
- McHardy, I. M., Connolly, S. D., et al. (May 2016). ‘The origin of UV-optical variability in AGN and test of disc models: XMM-Newton and ground-based observations of NGC 4395’. In: *Astronomische Nachrichten* 337.4-5, p. 500. doi: [10.1002/asna.201612337](https://doi.org/10.1002/asna.201612337).
- McKinney, W. (2010). ‘Data Structures for Statistical Computing in Python’. In: *Proceedings of the 9th Python in Science Conference*. Ed. by S. van der Walt and J. Millman, pp. 56–61. doi: [10.25080/Majora-92bf1922-00a](https://doi.org/10.25080/Majora-92bf1922-00a).
- Mead, R. A. and Meyer, M. P. (1977). ‘Landsat digital data application to forest vegetation and land use classification in Minnesota’. In: *LARS Symposia*, p. 220.
- Meiksin, A. (Jan. 2005). ‘Constraints on the ionization sources of the high-redshift intergalactic medium’. In: MNRAS 356.2, pp. 596–606. doi: [10.1111/j.1365-2966.2004.08481.x](https://doi.org/10.1111/j.1365-2966.2004.08481.x).
- Meisner, A. M., Lang, D., et al. (Dec. 2019). ‘unWISE Coadds: The Five-year Data Set’. In: PASP 131.1006, p. 124504. doi: [10.1088/1538-3873/ab3df4](https://doi.org/10.1088/1538-3873/ab3df4).
- Meisner, A. M., Lang, D., et al. (Sept. 2022). ‘9-yr Deep Sky unWISE Coadds’. In: *Research Notes of the American Astronomical Society* 6.9, 188, p. 188. doi: [10.3847/2515-5172/ac913e](https://doi.org/10.3847/2515-5172/ac913e).
- Menzel, M. .-, Merloni, A., et al. (Mar. 2016). ‘A spectroscopic survey of X-ray-selected AGNs in the northern XMM-XXL field’. In: MNRAS 457.1, pp. 110–132. doi: [10.1093/mnras/stv2749](https://doi.org/10.1093/mnras/stv2749).

- Merlin, E., Castellano, M., et al. (May 2021). ‘The ASTRODEEP-GS43 catalogue: New photometry and redshifts for the CANDELS GOODS-South field’. In: A&A 649, A22, A22. doi: [10.1051/0004-6361/202140310](https://doi.org/10.1051/0004-6361/202140310).
- Messias, H., Afonso, J., et al. (Aug. 2012). ‘A New Infrared Color Criterion for the Selection of $0 < z < 7$ AGNs: Application to Deep Fields and Implications for JWST Surveys’. In: ApJ 754.2, 120, p. 120. doi: [10.1088/0004-637X/754/2/120](https://doi.org/10.1088/0004-637X/754/2/120).
- Michailidis, M. (2017). ‘Investigating machine learning methods in recommender systems’. PhD thesis. University College London, UK. URL: <https://discovery.ucl.ac.uk/id/eprint/10031000>.
- Michelucci, U. and Venturini, F. (2023). ‘New metric formulas that include measurement errors in machine learning for natural sciences’. In: *Expert Systems with Applications* 224, p. 120013. issn: 0957-4174. doi: [10.1016/j.eswa.2023.120013](https://doi.org/10.1016/j.eswa.2023.120013).
- Mickaelian, A. M. (Dec. 2020). ‘Big Data in Astronomy: Surveys, Catalogs, Databases and Archives’. In: *Communications of the Byurakan Astrophysical Observatory* 67, pp. 159–180. doi: [10.52526/25792776-2020.67.2-159](https://doi.org/10.52526/25792776-2020.67.2-159).
- Miley, G. and De Breuck, C. (Feb. 2008). ‘Distant radio galaxies and their environments’. In: A&A Rev. 15.2, pp. 67–144. doi: [10.1007/s00159-007-0008-z](https://doi.org/10.1007/s00159-007-0008-z).
- Miller, S. T., Lindner, J. F., et al. (2020). ‘The scaling of physics-informed machine learning with data and dimensions’. In: *Chaos, Solitons & Fractals: X* 5, p. 100046. issn: 2590-0544. doi: [10.1016/j.csfx.2020.100046](https://doi.org/10.1016/j.csfx.2020.100046).
- Mingo, B., Watson, M. G., et al. (Nov. 2016). ‘The MIXR sample: AGN activity versus star formation across the cross-correlation of WISE, 3XMM, and FIRST/NVSS’. In: MNRAS 462.3, pp. 2631–2667. doi: [10.1093/mnras/stw1826](https://doi.org/10.1093/mnras/stw1826).
- Mitra, S., Choudhury, T. R., and Ferrara, A. (Jan. 2018). ‘Cosmic reionization after Planck II: contribution from quasars’. In: MNRAS 473.1, pp. 1416–1425. doi: [10.1093/mnras/stx2443](https://doi.org/10.1093/mnras/stx2443).
- Miyaji, T., Hasinger, G., and Schmidt, M. (Apr. 2001). ‘Soft X-ray AGN luminosity function from ROSAT surveys. II. Table of the binned soft X-ray luminosity function’. In: A&A 369, pp. 49–56. doi: [10.1051/0004-6361:20010102](https://doi.org/10.1051/0004-6361:20010102).
- Mo, W., Gonzalez, A., et al. (Oct. 2020). ‘The Massive and Distant Clusters of WISE Survey. VIII. Radio Activity in Massive Galaxy Clusters’. In: ApJ 901.2, 131, p. 131. doi: [10.3847/1538-4357/abb08d](https://doi.org/10.3847/1538-4357/abb08d).
- Mohale, K. and Lochner, M. (Nov. 2023). ‘Enabling Unsupervised Discovery in Astronomical Images through Self-Supervised Representations’. In: *arXiv e-prints*, arXiv:2311.14157, arXiv:2311.14157. doi: [10.48550/arXiv.2311.14157](https://doi.org/10.48550/arXiv.2311.14157).
- Mohan, N. and Rafferty, D. (Feb. 2015). *PyBDSF: Python Blob Detection and Source Finder*. Astrophysics Source Code Library, record ascl:1502.007.
- Morabito, L. K., Sweijen, F., et al. (Oct. 2022). ‘Identifying active galactic nuclei via brightness temperature with sub-arcsecond international LOFAR telescope observations’. In: MNRAS 515.4, pp. 5758–5774. doi: [10.1093/mnras/stac2129](https://doi.org/10.1093/mnras/stac2129).
- Morrissey, P., Conrow, T., et al. (Dec. 2007). ‘The Calibration and Data Products of GALEX’. In: ApJS 173.2, pp. 682–697. doi: [10.1086/520512](https://doi.org/10.1086/520512).

REFERENCES

- Mostert, R. I. J., Duncan, K. J., et al. (Jan. 2021). ‘Unveiling the rarest morphologies of the LOFAR Two-metre Sky Survey radio source population with self-organised maps’. In: A&A 645, A89, A89. doi: [10.1051/0004-6361/202038500](https://doi.org/10.1051/0004-6361/202038500).
- Moya, A. and López-Sastre, R. J. (July 2022). ‘Stellar mass and radius estimation using artificial intelligence’. In: A&A 663, A112, A112. doi: [10.1051/0004-6361/202142930](https://doi.org/10.1051/0004-6361/202142930).
- Naidoo, K., Johnston, H., et al. (Feb. 2023). ‘Euclid: Calibrating photometric redshifts with spectroscopic cross-correlations’. In: A&A 670, A149, A149. doi: [10.1051/0004-6361/202244795](https://doi.org/10.1051/0004-6361/202244795).
- Nakoneczny, S. J., Bilicki, M., et al. (May 2021). ‘Photometric selection and redshifts for quasars in the Kilo-Degree Survey Data Release 4’. In: A&A 649, A81, A81. doi: [10.1051/0004-6361/202039684](https://doi.org/10.1051/0004-6361/202039684).
- Netzer, H. (Aug. 2015). ‘Revisiting the Unified Model of Active Galactic Nuclei’. In: ARA&A 53, pp. 365–408. doi: [10.1146/annurev-astro-082214-122302](https://doi.org/10.1146/annurev-astro-082214-122302).
- Newman, J. A., Abate, A., et al. (Mar. 2015). ‘Spectroscopic needs for imaging dark energy experiments’. In: *Astroparticle Physics* 63, pp. 81–100. doi: [10.1016/j.astropartphys.2014.06.007](https://doi.org/10.1016/j.astropartphys.2014.06.007).
- Newman, J. A. and Gruen, D. (Aug. 2022). ‘Photometric Redshifts for Next-Generation Surveys’. In: ARA&A 60, pp. 363–414. doi: [10.1146/annurev-astro-032122-014611](https://doi.org/10.1146/annurev-astro-032122-014611).
- Nicastro, F., Kaastra, J., et al. (June 2018). ‘Observations of the missing baryons in the warm-hot intergalactic medium’. In: Nature 558.7710, pp. 406–409. doi: [10.1038/s41586-018-0204-1](https://doi.org/10.1038/s41586-018-0204-1).
- Nicastro, F., Krongold, Y., et al. (Mar. 2017). ‘A decade of warm hot intergalactic medium searches: Where do we stand and where do we go?’ In: *Astronomische Nachrichten* 338.281, pp. 281–286. doi: [10.1002/asna.201713343](https://doi.org/10.1002/asna.201713343).
- Niculescu-Mizil, A. and Caruana, R. (2005). ‘Predicting Good Probabilities with Supervised Learning’. In: *Proceedings of the 22nd International Conference on Machine Learning*. ICML ’05. Bonn, Germany: Association for Computing Machinery, pp. 625–632. ISBN: 1595931805. doi: [10.1145/1102351.1102430](https://doi.org/10.1145/1102351.1102430).
- Norris, R. P. (June 2017). ‘Astroinformatics Challenges from Next-generation Radio Continuum Surveys’. In: *Astroinformatics*. Ed. by M. Brescia, S. G. Djorgovski, et al. Vol. 325, pp. 103–113. doi: [10.1017/S1743921316012825](https://doi.org/10.1017/S1743921316012825).
- Norris, R. P., Hopkins, A. M., et al. (Aug. 2011). ‘EMU: Evolutionary Map of the Universe’. In: PASA 28.3, pp. 215–248. doi: [10.1071/AS11021](https://doi.org/10.1071/AS11021).
- Norris, R. P., Marvil, J., et al. (Sept. 2021). ‘The Evolutionary Map of the Universe pilot survey’. In: PASA 38, e046, e046. doi: [10.1017/pasa.2021.42](https://doi.org/10.1017/pasa.2021.42).
- Norris, R. P., Salvato, M., et al. (Oct. 2019). ‘A Comparison of Photometric Redshift Techniques for Large Radio Surveys’. In: PASP 131.1004, p. 108004. doi: [10.1088/1538-3873/ab0f7b](https://doi.org/10.1088/1538-3873/ab0f7b).
- Nour, D. and Sriram, K. (Jan. 2023). ‘Association of optical, ultraviolet, and soft X-ray excess emissions in AGNs’. In: MNRAS 518.4, pp. 5705–5717. doi: [10.1093/mnras/stac3505](https://doi.org/10.1093/mnras/stac3505).
- Obrić, M., Ivezić, Ž., et al. (Aug. 2006). ‘Panchromatic properties of 99000 galaxies detected by SDSS, and (some by) ROSAT, GALEX, 2MASS, IRAS, GB6, FIRST, NVSS and WENSS surveys’. In: MNRAS 370.4, pp. 1677–1698. doi: [10.1111/j.1365-2966.2006.10675.x](https://doi.org/10.1111/j.1365-2966.2006.10675.x).
- Ochsenbein, F., Bauer, P., and Marcout, J. (Apr. 2000). ‘The VizieR database of astronomical catalogues’. In: A&AS 143, pp. 23–32. doi: [10.1051/aas:2000169](https://doi.org/10.1051/aas:2000169).

- Oke, J. B. and Sandage, A. (Oct. 1968). ‘Energy Distributions, K Corrections, and the Stebbins-Whitford Effect for Giant Elliptical Galaxies’. In: *ApJ* 154, p. 21. doi: [10.1086/149737](https://doi.org/10.1086/149737).
- Oliver, S., Rowan-Robinson, M., et al. (Aug. 2000). ‘The European Large Area ISO Survey - I. Goals, definition and observations’. In: *MNRAS* 316.4, pp. 749–767. doi: [10.1046/j.1365-8711.2000.03550.x](https://doi.org/10.1046/j.1365-8711.2000.03550.x).
- Opitz, D. and Maclin, R. (July 1999). ‘Popular Ensemble Methods: An Empirical Study’. In: *J. Artif. Int. Res.* 11.1, pp. 169–198. issn: 1076-9757.
- Osorio-Clavijo, N., Gonzalez-Martín, O., et al. (July 2023). ‘AGNs in the CALIFA survey: X-ray detection of nuclear sources’. In: *MNRAS* 522.4, pp. 5788–5804. doi: [10.1093/mnras/stad1262](https://doi.org/10.1093/mnras/stad1262).
- Osterbrock, D. E. (Oct. 1981). ‘Seyfert galaxies with weak broad H alpha emission lines’. In: *ApJ* 249, pp. 462–470. doi: [10.1086/159306](https://doi.org/10.1086/159306).
- Pacifici, C., Iyer, K. G., et al. (Feb. 2023). ‘The Art of Measuring Physical Parameters in Galaxies: A Critical Assessment of Spectral Energy Distribution Fitting Techniques’. In: *ApJ* 944.2, 141, p. 141. doi: [10.3847/1538-4357/acacff](https://doi.org/10.3847/1538-4357/acacff).
- Padovani, P., Alexander, D. M., et al. (Aug. 2017). ‘Active galactic nuclei: what’s in a name?’ In: *A&A Rev.* 25.1, 2, p. 2. doi: [10.1007/s00159-017-0102-9](https://doi.org/10.1007/s00159-017-0102-9).
- Padovani, P. (Sept. 2016). ‘The faint radio sky: radio astronomy becomes mainstream’. In: *A&A Rev.* 24.1, 13, p. 13. doi: [10.1007/s00159-016-0098-6](https://doi.org/10.1007/s00159-016-0098-6).
- (Nov. 2017). ‘Active Galactic Nuclei at all wavelengths and from all angles’. In: *Frontiers in Astronomy and Space Sciences* 4, 35, p. 35. doi: [10.3389/fspas.2017.00035](https://doi.org/10.3389/fspas.2017.00035).
- Page, M. J. and Carrera, F. J. (Jan. 2000). ‘An improved method of constructing binned luminosity functions’. In: *MNRAS* 311.2, pp. 433–440. doi: [10.1046/j.1365-8711.2000.03105.x](https://doi.org/10.1046/j.1365-8711.2000.03105.x).
- Palanque-Delabrouille, N., Magneville, C., et al. (Mar. 2016). ‘The extended Baryon Oscillation Spectroscopic Survey: Variability selection and quasar luminosity function’. In: *A&A* 587, A41, A41. doi: [10.1051/0004-6361/201527392](https://doi.org/10.1051/0004-6361/201527392).
- Pasquato, M., Trevisan, P., et al. (Oct. 2023). ‘Interpretable machine learning for finding intermediate-mass black holes’. In: *arXiv e-prints*, arXiv:2310.18560, arXiv:2310.18560. doi: [10.48550/arXiv.2310.18560](https://doi.org/10.48550/arXiv.2310.18560).
- Pearl, A. N., Zentner, A. R., et al. (Sept. 2023). ‘The DESI One-Percent Survey: Evidence for Assembly Bias from Low-Redshift Counts-in-Cylinders Measurements’. In: *arXiv e-prints*, arXiv:2309.08675, arXiv:2309.08675. doi: [10.48550/arXiv.2309.08675](https://doi.org/10.48550/arXiv.2309.08675).
- Pearson, K. and Galton, F. (1895). ‘VII. Note on regression and inheritance in the case of two parents’. In: *Proceedings of the Royal Society of London* 58.347-352, pp. 240–242. doi: [10.1098/rspl.1895.0041](https://doi.org/10.1098/rspl.1895.0041).
- Pedregosa, F., Varoquaux, G., et al. (2011). ‘Scikit-learn: Machine Learning in Python’. In: *Journal of Machine Learning Research* 12, pp. 2825–2830.
- Pepinsky, T. B. (2018). ‘A Note on Listwise Deletion versus Multiple Imputation’. In: *Political Analysis* 26.4, pp. 480–488. doi: [10.1017/pan.2018.18](https://doi.org/10.1017/pan.2018.18).
- Pérez-Torres, M., Mattila, S., et al. (Dec. 2021). ‘Star formation and nuclear activity in luminous infrared galaxies: an infrared through radio review’. In: *A&A Rev.* 29.1, 2, p. 2. doi: [10.1007/s00159-020-00128-x](https://doi.org/10.1007/s00159-020-00128-x).
- Perger, K., Frey, S., et al. (Aug. 2017). ‘A catalogue of active galactic nuclei from the first 1.5 Gyr of the Universe’. In: *Frontiers in Astronomy and Space Sciences* 4, 9, p. 9. doi: [10.3389/fspas.2017.00009](https://doi.org/10.3389/fspas.2017.00009).

REFERENCES

- Planck Collaboration, Aghanim, N., et al. (Sept. 2020). ‘Planck 2018 results. VI. Cosmological parameters’. In: *A&A* 641, A6, A6. doi: [10.1051/0004-6361/201833910](https://doi.org/10.1051/0004-6361/201833910).
- Poisot, T. (2023). ‘Guidelines for the prediction of species interactions through binary classification’. In: *Methods in Ecology and Evolution* 14.5, pp. 1333–1345. doi: [10.1111/2041-210X.14071](https://doi.org/10.1111/2041-210X.14071).
- Poliszczuk, A., Pollo, A., et al. (July 2021). ‘Active galactic nuclei catalog from the AKARI NEP-Wide field’. In: *A&A* 651, A108, A108. doi: [10.1051/0004-6361/202040219](https://doi.org/10.1051/0004-6361/202040219).
- Porqueres, N., Jasche, J., et al. (Apr. 2018). ‘Imprints of the large-scale structure on AGN formation and evolution’. In: *A&A* 612, A31, A31. doi: [10.1051/0004-6361/201732141](https://doi.org/10.1051/0004-6361/201732141).
- Portegies Zwart, S. (Sept. 2020). ‘The ecological impact of high-performance computing in astrophysics’. In: *Nature Astronomy* 4, pp. 819–822. doi: [10.1038/s41550-020-1208-y](https://doi.org/10.1038/s41550-020-1208-y).
- Pouliasis, E. (Feb. 2020). ‘Identification of Active Galactic Nuclei through different selection techniques’. PhD thesis. IAASARS, National Observatory of Athens.
- Pracy, M. B., Ching, J. H. Y., et al. (July 2016). ‘GAMA/WiggleZ: the 1.4 GHz radio luminosity functions of high- and low-excitation radio galaxies and their redshift evolution to $z = 0.75$ ’. In: *MNRAS* 460.1, pp. 2–17. doi: [10.1093/mnras/stw910](https://doi.org/10.1093/mnras/stw910).
- Prandoni, I., Gregorini, L., et al. (Jan. 2001). ‘The ATESP radio survey. III. Source counts’. In: *A&A* 365, pp. 392–399. doi: [10.1051/0004-6361:20000142](https://doi.org/10.1051/0004-6361:20000142).
- Prandoni, I., Guglielmino, G., et al. (Dec. 2018). ‘The Lockman Hole Project: new constraints on the sub-mJy source counts from a wide-area 1.4 GHz mosaic’. In: *MNRAS* 481.4, pp. 4548–4565. doi: [10.1093/mnras/sty2521](https://doi.org/10.1093/mnras/sty2521).
- Prandoni, I. and Seymour, N. (Apr. 2015). ‘Revealing the Physics and Evolution of Galaxies and Galaxy Clusters with SKA Continuum Surveys’. In: *Advancing Astrophysics with the Square Kilometre Array (AASKA14)*, 67, p. 67.
- Prestage, R. M. and Peacock, J. A. (July 1983). ‘Optical identifications of Parkes radio sources using UK Schmidt plates.’ In: *MNRAS* 204, pp. 355–364. doi: [10.1093/mnras/204.2.355](https://doi.org/10.1093/mnras/204.2.355).
- Prokhorenkova, L., Gusev, G., et al. (2018). ‘CatBoost: unbiased boosting with categorical features’. In: *Advances in Neural Information Processing Systems*. Ed. by S. Bengio, H. Wallach, et al. Vol. 31. Curran Associates, Inc. URL: https://proceedings.neurips.cc/paper_files/paper/2018/file/14491b756b3a51daac41c24863285549-Paper.pdf.
- Radcliffe, J. F., Barthel, P. D., et al. (May 2021a). ‘Nowhere to hide: Radio-faint AGN in the GOODS-N field. II. Multi-wavelength AGN selection techniques and host galaxy properties’. In: *A&A* 649, A27, A27. doi: [10.1051/0004-6361/202038591](https://doi.org/10.1051/0004-6361/202038591).
- Radcliffe, J. F., Barthel, P. D., et al. (May 2021b). ‘The radio emission from active galactic nuclei’. In: *A&A* 649, L9, p. L9. doi: [10.1051/0004-6361/202140791](https://doi.org/10.1051/0004-6361/202140791).
- Radcliffe, J. F., Garrett, M. A., et al. (Nov. 2018). ‘Nowhere to Hide: Radio-faint AGN in GOODS-N field. I. Initial catalogue and radio properties’. In: *A&A* 619, A48, A48. doi: [10.1051/0004-6361/201833399](https://doi.org/10.1051/0004-6361/201833399).
- Rajagopal, M., Marchesi, S., et al. (June 2021). ‘Identifying the 3FHL Catalog. V. Results of the CTIO-COSMOS Optical Spectroscopy Campaign 2019’. In: *ApJS* 254.2, 26, p. 26. doi: [10.3847/1538-4365/abf656](https://doi.org/10.3847/1538-4365/abf656).

- Rasmussen, C. E. and Williams, C. K. I. (Nov. 2005). *Gaussian Processes for Machine Learning*. The MIT Press.
isbn: 9780262256834. doi: [10.7551/mitpress/3206.001.0001](https://doi.org/10.7551/mitpress/3206.001.0001).
- Ratner, B. (June 2009). ‘The correlation coefficient: Its values range between +1/-1, or do they?’ In: *Journal of Targeting, Measurement and Analysis for Marketing* 17.2, pp. 139–142. issn: 1479-1862. doi: [10.1057/jt.2009.5](https://doi.org/10.1057/jt.2009.5).
- Rawlings, S. (Sept. 2003). ‘High-redshift radio galaxies: at the crossroads’. In: *New A Rev.* 47.4-5, pp. 397–404. doi: [10.1016/S1387-6473\(03\)00056-3](https://doi.org/10.1016/S1387-6473(03)00056-3).
- Reis, I., Rotman, M., et al. (2021). ‘Effectively using unsupervised machine learning in next generation astronomical surveys’. In: *Astronomy and Computing* 34, p. 100437. issn: 2213-1337. doi: [10.1016/j.ascom.2020.100437](https://doi.org/10.1016/j.ascom.2020.100437).
- Reis, I., Baron, D., and Shahaf, S. (Jan. 2019). ‘Probabilistic Random Forest: A Machine Learning Algorithm for Noisy Data Sets’. In: *AJ* 157.1, 16, p. 16. doi: [10.3847/1538-3881/aaf101](https://doi.org/10.3847/1538-3881/aaf101).
- Ricci, C., Trakhtenbrot, B., et al. (Dec. 2017). ‘BAT AGN Spectroscopic Survey. V. X-Ray Properties of the Swift/BAT 70-month AGN Catalog’. In: *ApJS* 233.2, 17, p. 17. doi: [10.3847/1538-4365/aa96ad](https://doi.org/10.3847/1538-4365/aa96ad).
- Richards, G. T., Strauss, M. A., et al. (June 2006). ‘The Sloan Digital Sky Survey Quasar Survey: Quasar Luminosity Function from Data Release 3’. In: *AJ* 131.6, pp. 2766–2787. doi: [10.1086/503559](https://doi.org/10.1086/503559).
- Richter, G. A. (Jan. 1975). ‘Search for Optical Identifications in the 5C3 Radio Survey. II. Statistical Treatment and Results’. In: *Astronomische Nachrichten* 296.2, p. 65. doi: [10.1002/asna.19752960203](https://doi.org/10.1002/asna.19752960203).
- Robertson, B. E. (Aug. 2022). ‘Galaxy Formation and Reionization: Key Unknowns and Expected Breakthroughs by the James Webb Space Telescope’. In: *ARA&A* 60, pp. 121–158. doi: [10.1146/annurev-astro-120221-044656](https://doi.org/10.1146/annurev-astro-120221-044656).
- Rodrigo, C. and Solano, E. (July 2020). ‘The SVO Filter Profile Service’. In: *XIV.0 Scientific Meeting (virtual) of the Spanish Astronomical Society*, 182, p. 182.
- Rodrigo, C., Solano, E., and Bayo, A. (Oct. 2012). *SVO Filter Profile Service Version 1.0*. IVOA Working Draft 15 October 2012. doi: [10.5479/ADS/bib/2012ivoa.rept.1015R](https://doi.org/10.5479/ADS/bib/2012ivoa.rept.1015R).
- Rohde, D. J., Drinkwater, M. J., et al. (June 2005). ‘Applying machine learning to catalogue matching in astrophysics’. In: *MNRAS* 360.1, pp. 69–75. doi: [10.1111/j.1365-2966.2005.08930.x](https://doi.org/10.1111/j.1365-2966.2005.08930.x).
- Rohde, D. J., Gallagher, M. R., et al. (June 2006). ‘Matching of catalogues by probabilistic pattern classification’. In: *MNRAS* 369.1, pp. 2–14. doi: [10.1111/j.1365-2966.2006.10304.x](https://doi.org/10.1111/j.1365-2966.2006.10304.x).
- Roscher, R., Bohn, B., et al. (2020a). ‘Explainable Machine Learning for Scientific Insights and Discoveries’. In: *IEEE Access* 8, pp. 42200–42216. doi: [10.1109/ACCESS.2020.2976199](https://doi.org/10.1109/ACCESS.2020.2976199).
- (2020b). ‘Explainable Machine Learning for Scientific Insights and Discoveries’. In: *IEEE Access* 8, pp. 42200–42216. doi: [10.1109/ACCESS.2020.2976199](https://doi.org/10.1109/ACCESS.2020.2976199).
- Ross, N. P. and Cross, N. J. G. (May 2020). ‘The near and mid-infrared photometric properties of known redshift $z \geq 5$ quasars’. In: *MNRAS* 494.1, pp. 789–803. doi: [10.1093/mnras/staa544](https://doi.org/10.1093/mnras/staa544).
- Ross, N. P., McGreer, I. D., et al. (Aug. 2013). ‘The SDSS-III Baryon Oscillation Spectroscopic Survey: The Quasar Luminosity Function from Data Release Nine’. In: *ApJ* 773.1, 14, p. 14. doi: [10.1088/0004-637X/773/1/14](https://doi.org/10.1088/0004-637X/773/1/14).

REFERENCES

- Rubin, D. (1987). *Multiple Imputation for Nonresponse in Surveys*. Wiley Series in Probability and Statistics. Wiley. ISBN: 9780471087052.
- Rubin, D. B. (Dec. 1976). ‘Inference and missing data’. In: *Biometrika* 63.3, pp. 581–592. ISSN: 0006-3444. doi: [10.1093/biomet/63.3.581](https://doi.org/10.1093/biomet/63.3.581).
- Rybicki, G. B. and Lightman, A. P. (2008). *Radiative Processes in Astrophysics*. Physics textbook. Wiley. ISBN: 9783527618187.
- Saarela, M. and Jauhainen, S. (Feb. 2021). ‘Comparison of feature importance measures as explanations for classification models’. In: *SN Applied Sciences* 3.2, p. 272. ISSN: 2523-3971. doi: [10.1007/s42452-021-04148-9](https://doi.org/10.1007/s42452-021-04148-9).
- Sabater, J., Best, P. N., et al. (Feb. 2019). ‘The LoTSS view of radio AGN in the local Universe. The most massive galaxies are always switched on’. In: *A&A* 622, A17, A17. doi: [10.1051/0004-6361/201833883](https://doi.org/10.1051/0004-6361/201833883).
- Sajina, A., Lacy, M., and Pope, A. (June 2022). ‘The Past and Future of Mid-Infrared Studies of AGN’. In: *Universe* 8.7, p. 356. doi: [10.3390/universe8070356](https://doi.org/10.3390/universe8070356).
- Salpeter, E. E. (Jan. 1955). ‘The Luminosity Function and Stellar Evolution.’ In: *ApJ* 121, p. 161. doi: [10.1086/145971](https://doi.org/10.1086/145971).
- Salvato, M., Buchner, J., et al. (Feb. 2018). ‘Finding counterparts for all-sky X-ray surveys with NWAY: a Bayesian algorithm for cross-matching multiple catalogues’. In: *MNRAS* 473.4, pp. 4937–4955. doi: [10.1093/mnras/stx2651](https://doi.org/10.1093/mnras/stx2651).
- Salvato, M., Ilbert, O., et al. (Dec. 2011). ‘Dissecting Photometric Redshift for Active Galactic Nucleus Using XMM- and Chandra-COSMOS Samples’. In: *ApJ* 742.2, 61, p. 61. doi: [10.1088/0004-637X/742/2/61](https://doi.org/10.1088/0004-637X/742/2/61).
- Salvato, M., Ilbert, O., and Hoyle, B. (June 2019). ‘The many flavours of photometric redshifts’. In: *Nature Astronomy* 3, pp. 212–222. doi: [10.1038/s41550-018-0478-0](https://doi.org/10.1038/s41550-018-0478-0).
- Samuel, A. L. (1959). ‘Some Studies in Machine Learning Using the Game of Checkers’. In: *IBM Journal of Research and Development* 3.3, pp. 210–229. doi: [10.1147/rd.33.0210](https://doi.org/10.1147/rd.33.0210).
- Sánchez, S. F., Avila-Reese, V., et al. (Apr. 2018). ‘SDSS IV MaNGA - Properties of AGN Host Galaxies’. In: *Rev. Mexicana Astron. Astrofis.* 54, pp. 217–260. doi: [10.48550/arXiv.1709.05438](https://doi.org/10.48550/arXiv.1709.05438).
- Sánchez-Sáez, P., Reyes, I., et al. (Mar. 2021). ‘Alert Classification for the ALeRCE Broker System: The Light Curve Classifier’. In: *AJ* 161.3, 141, p. 141. doi: [10.3847/1538-3881/abd5c1](https://doi.org/10.3847/1538-3881/abd5c1).
- Sandage, A. (Sept. 1962). ‘The Change of Redshift and Apparent Luminosity of Galaxies due to the Deceleration of Selected Expanding Universes.’ In: *ApJ* 136, p. 319. doi: [10.1086/147385](https://doi.org/10.1086/147385).
- Santos, M. S., Abreu, P. H., et al. (Dec. 2022). ‘On the joint-effect of class imbalance and overlap: a critical review’. In: *Artificial Intelligence Review* 55.8, pp. 6207–6275. ISSN: 1573-7462. doi: [10.1007/s10462-022-10150-3](https://doi.org/10.1007/s10462-022-10150-3).
- Sartori, L. F., Schawinski, K., et al. (Dec. 2015). ‘The search for active black holes in nearby low-mass galaxies using optical and mid-IR data’. In: *MNRAS* 454.4, pp. 3722–3742. doi: [10.1093/mnras/stv2238](https://doi.org/10.1093/mnras/stv2238).
- Saz Parkinson, P. M., Xu, H., et al. (Mar. 2016). ‘Classification and Ranking of Fermi LAT Gamma-ray Sources from the 3FGL Catalog using Machine Learning Techniques’. In: *ApJ* 820.1, 8, p. 8. doi: [10.3847/0004-637X/820/1/8](https://doi.org/10.3847/0004-637X/820/1/8).

- Schapire, R. E. (June 1990). ‘The strength of weak learnability’. In: *Machine Learning* 5.2, pp. 197–227. issn: 1573-0565. doi: [10.1007/BF00116037](https://doi.org/10.1007/BF00116037).
- Schapire, R. E., Freund, Y., et al. (1998). ‘Boosting the Margin: A New Explanation for the Effectiveness of Voting Methods’. In: *The Annals of Statistics* 26.5, pp. 1651–1686. issn: 00905364. url: <http://www.jstor.org/stable/120016> (visited on 05/12/2023).
- Schawinski, K., Thomas, D., et al. (Dec. 2007). ‘Observational evidence for AGN feedback in early-type galaxies’. In: MNRAS 382.4, pp. 1415–1431. doi: [10.1111/j.1365-2966.2007.12487.x](https://doi.org/10.1111/j.1365-2966.2007.12487.x).
- Schechter, P. (Jan. 1976). ‘An analytic expression for the luminosity function for galaxies.’ In: ApJ 203, pp. 297–306. doi: [10.1086/154079](https://doi.org/10.1086/154079).
- Schmidt, M. (Feb. 1968). ‘Space Distribution and Luminosity Functions of Quasi-Stellar Radio Sources’. In: ApJ 151, p. 393. doi: [10.1086/149446](https://doi.org/10.1086/149446).
- Schneider, P. C., Freund, S., et al. (May 2022). ‘The eROSITA Final Equatorial-Depth Survey (eFEDS). The Stellar Counterparts of eROSITA sources identified by machine learning and Bayesian algorithms’. In: A&A 661, A6, A6. doi: [10.1051/0004-6361/202141133](https://doi.org/10.1051/0004-6361/202141133).
- Schuecker, P. (Jan. 1993). ‘Automated Galaxy Redshift Measurements from Very Low Dispersion Objective Prism Schmidt Plates’. In: ApJS 84, p. 39. doi: [10.1086/191744](https://doi.org/10.1086/191744).
- Scoville, N., Aussel, H., et al. (Sept. 2007). ‘The Cosmic Evolution Survey (COSMOS): Overview’. In: ApJS 172.1, pp. 1–8. doi: [10.1086/516585](https://doi.org/10.1086/516585).
- Secrest, N. J., Dudik, R. P., et al. (Nov. 2015). ‘Identification of 1.4 Million Active Galactic Nuclei in the Mid-Infrared using WISE Data’. In: ApJS 221.1, 12, p. 12. doi: [10.1088/0067-0049/221/1/12](https://doi.org/10.1088/0067-0049/221/1/12).
- Selina, R. J., Murphy, E. J., et al. (Dec. 2018). ‘The ngVLA Reference Design’. In: *Science with a Next Generation Very Large Array*. Ed. by E. Murphy. Vol. 517. Astronomical Society of the Pacific Conference Series, p. 15. doi: [10.48550/arXiv.1810.08197](https://doi.org/10.48550/arXiv.1810.08197).
- Selina, R., Murphy, E., and Beasley, A. (Jan. 2023). ‘The ngVLA: A Technical Overview’. In: *American Astronomical Society Meeting Abstracts*. Vol. 55. American Astronomical Society Meeting Abstracts, 357.02, p. 357.02.
- Sen, S., Agarwal, S., et al. (Feb. 2022). ‘Astronomical big data processing using machine learning: A comprehensive review’. In: *Experimental Astronomy* 53.1, pp. 1–43. doi: [10.1007/s10686-021-09827-4](https://doi.org/10.1007/s10686-021-09827-4).
- Shakura, N. I. and Sunyaev, R. A. (Jan. 1973). ‘Black holes in binary systems. Observational appearance.’ In: A&A 24, pp. 337–355.
- Shapley, L. S. (1953). ‘A Value for n-Person Games’. In: *Contributions to the Theory of Games (AM-28), Volume II*. Vol. 1. Princeton University Press, pp. 307–318. doi: [10.1515/9781400881970-018](https://doi.org/10.1515/9781400881970-018).
- Shen, X., Hopkins, P. F., et al. (Jan. 2020). ‘The bolometric quasar luminosity function at z = 0–7’. In: MNRAS 495.3, pp. 3252–3275. doi: [10.1093/mnras/staa1381](https://doi.org/10.1093/mnras/staa1381).
- Shimwell, T. W., Röttgering, H. J. A., et al. (Feb. 2017). ‘The LOFAR Two-metre Sky Survey. I. Survey description and preliminary data release’. In: A&A 598, A104, A104. doi: [10.1051/0004-6361/201629313](https://doi.org/10.1051/0004-6361/201629313).
- Shimwell, T. W., Tasse, C., et al. (Feb. 2019). ‘The LOFAR Two-metre Sky Survey. II. First data release’. In: A&A 622, A1, A1. doi: [10.1051/0004-6361/201833559](https://doi.org/10.1051/0004-6361/201833559).

REFERENCES

- Shy, S., Tak, H., et al. (July 2022). ‘Incorporating Measurement Error in Astronomical Object Classification’. In: AJ 164.1, 6, p. 6. doi: [10.3847/1538-3881/ac6e64](https://doi.org/10.3847/1538-3881/ac6e64).
- Silva, L., Schurer, A., et al. (Jan. 2011). ‘Modelling the spectral energy distribution of galaxies: introducing the artificial neural network’. In: MNRAS 410.3, pp. 2043–2056. doi: [10.1111/j.1365-2966.2010.17580.x](https://doi.org/10.1111/j.1365-2966.2010.17580.x).
- Silva Filho, T., Song, H., et al. (Sept. 2023). ‘Classifier calibration: a survey on how to assess and improve predicted class probabilities’. In: *Machine Learning* 112.9, pp. 3211–3260. ISSN: 1573-0565. doi: [10.1007/s10994-023-06336-7](https://doi.org/10.1007/s10994-023-06336-7).
- Simpson, C., Rawlings, S., et al. (Apr. 2012). ‘Radio imaging of the Subaru/XMM-Newton Deep Field- III. Evolution of the radio luminosity function beyond $z=1$ ’. In: MNRAS 421.4, pp. 3060–3083. doi: [10.1111/j.1365-2966.2012.20529.x](https://doi.org/10.1111/j.1365-2966.2012.20529.x).
- Singh, V., Beelen, A., et al. (Sept. 2014). ‘Multiwavelength characterization of faint ultra steep spectrum radio sources: A search for high-redshift radio galaxies’. In: A&A 569, A52, A52. doi: [10.1051/0004-6361/201423644](https://doi.org/10.1051/0004-6361/201423644).
- Sipple, J. and Lidz, A. (Jan. 2024). ‘The Star Formation Efficiency during Reionization as Inferred from the Hubble Frontier Fields’. In: ApJ 961.1, 50, p. 50. doi: [10.3847/1538-4357/ad06a7](https://doi.org/10.3847/1538-4357/ad06a7).
- Skrutskie, M. F., Cutri, R. M., et al. (Feb. 2006). ‘The Two Micron All Sky Survey (2MASS)’. In: AJ 131.2, pp. 1163–1183. doi: [10.1086/498708](https://doi.org/10.1086/498708).
- Šlaus, B., Smolcic, V., et al. (Dec. 2023). ‘The XXL survey LII : The evolution of radio AGN luminosity function determined via parametric methods from GMRT, ATCA, VLA and Cambridge interferometer observations’. In: *arXiv e-prints*, arXiv:2312.14683, arXiv:2312.14683. doi: [10.48550/arXiv.2312.14683](https://doi.org/10.48550/arXiv.2312.14683).
- Šlaus, B., Smolčić, V., et al. (June 2020). ‘The XXL Survey. XLI. Radio AGN luminosity functions based on the GMRT 610 MHz continuum observations’. In: A&A 638, A46, A46. doi: [10.1051/0004-6361/201937258](https://doi.org/10.1051/0004-6361/201937258).
- Slob, M. M., Callingham, J. R., et al. (Dec. 2022). ‘Extragalactic peaked-spectrum radio sources at low frequencies are young radio galaxies’. In: A&A 668, A186, A186. doi: [10.1051/0004-6361/202244651](https://doi.org/10.1051/0004-6361/202244651).
- Smolčić, V., Novak, M., et al. (June 2017). ‘The VLA-COSMOS 3 GHz Large Project: Cosmic evolution of radio AGN and implications for radio-mode feedback since $z \approx 5$ ’. In: A&A 602, A6, A6. doi: [10.1051/0004-6361/201730685](https://doi.org/10.1051/0004-6361/201730685).
- Snyder, J. (1987). *Map Projections—a Working Manual*. Professional paper. U.S. Government Printing Office. ISBN: 9780318235622.
- (1997). *Flattening the Earth: Two Thousand Years of Map Projections*. University of Chicago Press. ISBN: 9780226767475.
- Sola, J. and Sevilla, J. (1997). ‘Importance of input data normalization for the application of neural networks to complex industrial problems’. In: *IEEE Transactions on Nuclear Science* 44.3, pp. 1464–1468. doi: [10.1109/23.589532](https://doi.org/10.1109/23.589532).
- Sollich, P. and Krogh, A. (1995). ‘Learning with ensembles: How overfitting can be useful’. In: *Advances in Neural Information Processing Systems*. Ed. by D. Touretzky, M. Mozer, and M. Hasselmo. Vol. 8. MIT Press.

URL: https://proceedings.neurips.cc/paper_files/paper/1995/file/1019c8091693ef5c5f55970346633f92-Paper.pdf.

- Sommer, M. W., Basu, K., et al. (May 2011). ‘Redshift evolution of the 1.4 GHz volume averaged radio luminosity function in clusters of galaxies’. In: A&A 529, A124, A124. doi: [10.1051/0004-6361/201016150](https://doi.org/10.1051/0004-6361/201016150).
- Sørensen, T. (1948). *A Method of Establishing Groups of Equal Amplitude in Plant Sociology Based on Similarity of Species Content*. Biologiske skrifter. I kommission hos E. Munksgaard.
- Sravan, N., Graham, M. J., et al. (July 2023). ‘Machine-directed gravitational-wave counterpart discovery’. In: arXiv e-prints, arXiv:2307.09213, arXiv:2307.09213. doi: [10.48550/arXiv.2307.09213](https://doi.org/10.48550/arXiv.2307.09213).
- Steidel, C. C., Adelberger, K. L., et al. (July 1999). ‘Lyman-Break Galaxies at $z > \sim 4$ and the Evolution of the Ultraviolet Luminosity Density at High Redshift’. In: ApJ 519.1, pp. 1–17. doi: [10.1086/307363](https://doi.org/10.1086/307363).
- Steidel, C. C., Giavalisco, M., et al. (May 1996a). ‘Spectroscopic Confirmation of a Population of Normal Star-forming Galaxies at Redshifts $Z > 3$ ’. In: ApJ 462, p. L17. doi: [10.1086/310029](https://doi.org/10.1086/310029).
- Steidel, C. C., Giavalisco, M., et al. (Aug. 1996b). ‘Spectroscopy of Lyman Break Galaxies in the Hubble Deep Field’. In: AJ 112, p. 352. doi: [10.1086/118019](https://doi.org/10.1086/118019).
- Steidel, C. C. and Hamilton, D. (Sept. 1992). ‘Deep Imaging of redshift QSO Fields Below the Lyman Limit. I. The Field of Q0000-263 and galaxies at $Z = 3.4$ ’. In: AJ 104, p. 941. doi: [10.1086/116287](https://doi.org/10.1086/116287).
- Stern, D. (July 2015). ‘The X-Ray to Mid-infrared Relation of AGNs at High Luminosity’. In: ApJ 807.2, 129, p. 129. doi: [10.1088/0004-637X/807/2/129](https://doi.org/10.1088/0004-637X/807/2/129).
- Stern, D., Assef, R. J., et al. (July 2012). ‘Mid-infrared Selection of Active Galactic Nuclei with the Wide-Field Infrared Survey Explorer. I. Characterizing WISE-selected Active Galactic Nuclei in COSMOS’. In: ApJ 753.1, 30, p. 30. doi: [10.1088/0004-637X/753/1/30](https://doi.org/10.1088/0004-637X/753/1/30).
- Stern, D., Eisenhardt, P., et al. (Sept. 2005). ‘Mid-Infrared Selection of Active Galaxies’. In: ApJ 631.1, pp. 163–168. doi: [10.1086/432523](https://doi.org/10.1086/432523).
- Stone, M. (1974). ‘Cross-Validatory Choice and Assessment of Statistical Predictions’. In: *Journal of the Royal Statistical Society: Series B (Methodological)* 36.2, pp. 111–133. doi: [10.1111/j.2517-6161.1974.tb00994.x](https://doi.org/10.1111/j.2517-6161.1974.tb00994.x).
- Storey-Fisher, K., Hogg, D. W., et al. (June 2023). ‘Quaia, the Gaia-unWISE Quasar Catalog: An All-Sky Spectroscopic Quasar Sample’. In: arXiv e-prints, arXiv:2306.17749, arXiv:2306.17749. doi: [10.48550/arXiv.2306.17749](https://doi.org/10.48550/arXiv.2306.17749).
- Storey-Fisher, K., Huertas-Company, M., et al. (Dec. 2021). ‘Anomaly detection in Hyper Suprime-Cam galaxy images with generative adversarial networks’. In: MNRAS 508.2, pp. 2946–2963. doi: [10.1093/mnras/stab2589](https://doi.org/10.1093/mnras/stab2589).
- Stoughton, C., Lupton, R. H., et al. (Jan. 2002). ‘Sloan Digital Sky Survey: Early Data Release’. In: AJ 123.1, pp. 485–548. doi: [10.1086/324741](https://doi.org/10.1086/324741).
- Suganuma, M., Yoshii, Y., et al. (Mar. 2006). ‘Reverberation Measurements of the Inner Radius of the Dust Torus in Nearby Seyfert 1 Galaxies’. In: ApJ 639.1, pp. 46–63. doi: [10.1086/499326](https://doi.org/10.1086/499326).
- Surana, S., Wadadekar, Y., et al. (Apr. 2020). ‘Predicting star formation properties of galaxies using deep learning’. In: MNRAS 493.4, pp. 4808–4815. doi: [10.1093/mnras/staa537](https://doi.org/10.1093/mnras/staa537).

REFERENCES

- Sutherland, W. and Saunders, W. (Dec. 1992). ‘On the likelihood ratio for source identification.’ In: MNRAS 259, pp. 413–420. doi: [10.1093/mnras/259.3.413](https://doi.org/10.1093/mnras/259.3.413).
- Sweijen, F., van Weeren, R. J., et al. (Jan. 2022). ‘Deep sub-arcsecond wide-field imaging of the Lockman Hole field at 144 MHz’. In: *Nature Astronomy* 6, pp. 350–356. doi: [10.1038/s41550-021-01573-z](https://doi.org/10.1038/s41550-021-01573-z).
- Tacchella, S., Conroy, C., et al. (Feb. 2022). ‘Fast, Slow, Early, Late: Quenching Massive Galaxies at $z \sim 0.8$ ’. In: ApJ 926.2, 134, p. 134. doi: [10.3847/1538-4357/ac449b](https://doi.org/10.3847/1538-4357/ac449b).
- Tanaka, M., Coupon, J., et al. (Jan. 2018). ‘Photometric redshifts for Hyper Suprime-Cam Subaru Strategic Program Data Release 1’. In: PASJ 70, S9, S9. doi: [10.1093/pasj/pss077](https://doi.org/10.1093/pasj/pss077).
- Taylor, M. B. (Dec. 2005). ‘TOPCAT & STIL: Starlink Table/VOTable Processing Software’. In: *Astronomical Data Analysis Software and Systems XIV*. Ed. by P. Shopbell, M. Britton, and R. Ebert. Vol. 347. Astronomical Society of the Pacific Conference Series, p. 29.
- Thomas, N., Davé, R., et al. (May 2021). ‘The radio galaxy population in the SIMBA simulations’. In: MNRAS 503.3, pp. 3492–3509. doi: [10.1093/mnras/stab654](https://doi.org/10.1093/mnras/stab654).
- Thorne, J. E., Robotham, A., et al. (Mar. 2022a). *AGN Unification Diagram*. doi: [10.5281/zenodo.6381013](https://doi.org/10.5281/zenodo.6381013).
- Thorne, J. E., Robotham, A. S. G., et al. (Feb. 2022b). ‘Deep Extragalactic VIIsible Legacy Survey (DEVILS): identification of AGN through SED fitting and the evolution of the bolometric AGN luminosity function’. In: MNRAS 509.4, pp. 4940–4961. doi: [10.1093/mnras/stab3208](https://doi.org/10.1093/mnras/stab3208).
- Toba, Y., Oyabu, S., et al. (June 2014). ‘Luminosity and Redshift Dependence of the Covering Factor of Active Galactic Nuclei viewed with WISE and Sloan Digital Sky Survey’. In: ApJ 788.1, 45, p. 45. doi: [10.1088/0004-637X/788/1/45](https://doi.org/10.1088/0004-637X/788/1/45).
- Tonry, J. and Davis, M. (Oct. 1979). ‘A survey of galaxy redshifts. I. Data reduction techniques.’ In: AJ 84, pp. 1511–1525. doi: [10.1086/112569](https://doi.org/10.1086/112569).
- Toth, M. J., Goran, M. I., et al. (1993). ‘Examination of data normalization procedures for expressing peak VO₂ data’. In: *Journal of applied physiology* 75.5, pp. 2288–2292.
- Trenti, M. and Stiavelli, M. (Apr. 2008). ‘Cosmic Variance and Its Effect on the Luminosity Function Determination in Deep High-z Surveys’. In: ApJ 676.2, pp. 767–780. doi: [10.1086/528674](https://doi.org/10.1086/528674).
- Tripodi, R., Feruglio, C., et al. (Sept. 2022). ‘Black hole and host galaxy growth in an isolated $z \sim 6$ QSO observed with ALMA’. In: A&A 665, A107, A107. doi: [10.1051/0004-6361/202243920](https://doi.org/10.1051/0004-6361/202243920).
- Troyer, J., Starkey, D., et al. (Mar. 2016). ‘Correlated X-ray/ultraviolet/optical variability in NGC 6814’. In: MNRAS 456.4, pp. 4040–4050. doi: [10.1093/mnras/stv2862](https://doi.org/10.1093/mnras/stv2862).
- Tulio Ribeiro, M., Singh, S., and Guestrin, C. (Feb. 2016). ‘“Why Should I Trust You?”: Explaining the Predictions of Any Classifier’. In: *arXiv e-prints*, arXiv:1602.04938, arXiv:1602.04938. doi: [10.48550/arXiv.1602.04938](https://doi.org/10.48550/arXiv.1602.04938).
- U, V. (July 2022). ‘The Role of AGN in Luminous Infrared Galaxies from the Multiwavelength Perspective’. In: *Universe* 8.8, 392, p. 392. doi: [10.3390/universe8080392](https://doi.org/10.3390/universe8080392).
- Ulmer-Moll, S., Santos, N. C., et al. (Oct. 2019). ‘Beyond the exoplanet mass-radius relation’. In: A&A 630, A135, A135. doi: [10.1051/0004-6361/201936049](https://doi.org/10.1051/0004-6361/201936049).

- Urry, C. (June 2004). ‘AGN Unification: An Update’. In: *AGN Physics with the Sloan Digital Sky Survey*. Ed. by G. T. Richards and P. B. Hall. Vol. 311. Astronomical Society of the Pacific Conference Series, p. 49. doi: [10.48550/arXiv.astro-ph/0312545](https://doi.org/10.48550/arXiv.astro-ph/0312545).
- Urry, C. M. and Padovani, P. (Sept. 1995). ‘Unified Schemes for Radio-Loud Active Galactic Nuclei’. In: PASP 107, p. 803. doi: [10.1086/133630](https://doi.org/10.1086/133630).
- Uttley, P., Edelson, R., et al. (Feb. 2003). ‘Correlated Long-Term Optical and X-Ray Variations in NGC 5548’. In: ApJ 584.2, pp. L53–L56. doi: [10.1086/373887](https://doi.org/10.1086/373887).
- Uzgil, B. D., Oesch, P. A., et al. (May 2021). ‘The ALMA Spectroscopic Survey in the HUDF: A Search for [C II] Emitters at $6 \leq z \leq 8$ ’. In: ApJ 912.1, 67, p. 67. doi: [10.3847/1538-4357/abe86b](https://doi.org/10.3847/1538-4357/abe86b).
- Van Calster, B., McLernon, D. J., et al. (Dec. 2019). ‘Calibration: the Achilles heel of predictive analytics’. In: *BMC Medicine* 17.1, p. 230. ISSN: 1741-7015. doi: [10.1186/s12916-019-1466-7](https://doi.org/10.1186/s12916-019-1466-7).
- van den Busch, J. L., Hildebrandt, H., et al. (Oct. 2020). ‘Testing KiDS cross-correlation redshifts with simulations’. In: A&A 642, A200, A200. doi: [10.1051/0004-6361/202038835](https://doi.org/10.1051/0004-6361/202038835).
- van der Velden, E. (Feb. 2020). ‘CMasher: Scientific colormaps for making accessible, informative and ’cmashing’ plots’. In: *The Journal of Open Source Software* 5.46, 2004, p. 2004. doi: [10.21105/joss.02004](https://doi.org/10.21105/joss.02004).
- van der Vlugt, D., Algera, H. S. B., et al. (Jan. 2021). ‘An Ultradeep Multiband VLA Survey of the Faint Radio Sky (COSMOS-XS): Source Catalog and Number Counts’. In: ApJ 907.1, 5, p. 5. doi: [10.3847/1538-4357/abcaa3](https://doi.org/10.3847/1538-4357/abcaa3).
- van der Vlugt, D., Hodge, J. A., et al. (Dec. 2022). ‘An Ultra-deep Multiband Very Large Array (VLA) Survey of the Faint Radio Sky (COSMOS-XS): New Constraints on the Cosmic Star Formation History’. In: ApJ 941.1, 10, p. 10. doi: [10.3847/1538-4357/ac99db](https://doi.org/10.3847/1538-4357/ac99db).
- van Haarlem, M. P., Wise, M. W., et al. (July 2013). ‘LOFAR: The LOw-Frequency ARray’. In: A&A 556, A2, A2. doi: [10.1051/0004-6361/201220873](https://doi.org/10.1051/0004-6361/201220873).
- van Rijsbergen, C. J. (1979). *Information Retrieval*. 2nd. USA: Butterworth-Heinemann. ISBN: 0408709294.
- Vanden Berk, D. E., Wilhite, B. C., et al. (Feb. 2004). ‘The Ensemble Photometric Variability of ~25,000 Quasars in the Sloan Digital Sky Survey’. In: ApJ 601.2, pp. 692–714. doi: [10.1086/380563](https://doi.org/10.1086/380563).
- Vanschoren, J. (2019). ‘Meta-Learning’. In: *Automated Machine Learning: Methods, Systems, Challenges*. Ed. by F. Hutter, L. Kotthoff, and J. Vanschoren. Cham: Springer International Publishing, pp. 35–61. ISBN: 978-3-030-05318-5. doi: [10.1007/978-3-030-05318-5_2](https://doi.org/10.1007/978-3-030-05318-5_2).
- Vanzella, E., Cristiani, S., et al. (Aug. 2004). ‘Photometric redshifts with the Multilayer Perceptron Neural Network: Application to the HDF-S and SDSS’. In: A&A 423, pp. 761–776. doi: [10.1051/0004-6361:20040176](https://doi.org/10.1051/0004-6361:20040176).
- Vapnik, V. (1995). *The Nature of Statistical Learning Theory*. Springer. ISBN: 9780387945590.
- Vardoulaki, E., Jiménez Andrade, E. F., et al. (Apr. 2021). ‘FR-type radio sources at 3 GHz VLA-COSMOS: Relation to physical properties and large-scale environment’. In: A&A 648, A102, A102. doi: [10.1051/0004-6361/202039488](https://doi.org/10.1051/0004-6361/202039488).
- Veilleux, S. and Osterbrock, D. E. (Feb. 1987). ‘Spectral Classification of Emission-Line Galaxies’. In: ApJS 63, p. 295. doi: [10.1086/191166](https://doi.org/10.1086/191166).
- Véron-Cetty, M. -., and Véron, P. (July 2010). ‘A catalogue of quasars and active nuclei: 13th edition’. In: A&A 518, A10, A10. doi: [10.1051/0004-6361/201014188](https://doi.org/10.1051/0004-6361/201014188).

REFERENCES

- Villaescusa-Navarro, F., Anglés-Alcázar, D., et al. (July 2021). ‘The CAMELS Project: Cosmology and Astrophysics with Machine-learning Simulations’. In: *ApJ* 915.1, 71, p. 71. doi: [10.3847/1538-4357/abf7ba](https://doi.org/10.3847/1538-4357/abf7ba).
- Vuttipittayamongkol, P., Elyan, E., and Petrovski, A. (2021). ‘On the class overlap problem in imbalanced data classification’. In: *Knowledge-Based Systems* 212, p. 106631. ISSN: 0950-7051. doi: [10.1016/j.knosys.2020.106631](https://doi.org/10.1016/j.knosys.2020.106631).
- Wagstaff, K. L., Huff, E., and Rebbapragada, U. (July 2022). ‘Machine-Assisted Discovery Through Identification and Explanation of Anomalies in Astronomical Surveys’. In: *Astronomical Society of the Pacific Conference Series*. Ed. by J. E. Ruiz, F. Pierfedereci, and P. Teuben. Vol. 532. Astronomical Society of the Pacific Conference Series, p. 183.
- Walcher, J., Groves, B., et al. (Jan. 2011). ‘Fitting the integrated spectral energy distributions of galaxies’. In: *Ap&SS* 331, pp. 1–52. doi: [10.1007/s10509-010-0458-z](https://doi.org/10.1007/s10509-010-0458-z).
- Wasleske, E. J. and Baldassare, V. F. (Aug. 2023). ‘X-Ray Emission of Ultraviolet Variable Active Galactic Nucleus Candidates’. In: *AJ* 166.2, 64, p. 64. doi: [10.3847/1538-3881/ace16b](https://doi.org/10.3847/1538-3881/ace16b).
- Wenzl, L., Schindler, J.-T., et al. (Aug. 2021). ‘Random Forests as a Viable Method to Select and Discover High-redshift Quasars’. In: *AJ* 162.2, 72, p. 72. doi: [10.3847/1538-3881/ac0254](https://doi.org/10.3847/1538-3881/ac0254).
- Werner, M. W., Roellig, T. L., et al. (Sept. 2004). ‘The Spitzer Space Telescope Mission’. In: *ApJS* 154.1, pp. 1–9. doi: [10.1086/422992](https://doi.org/10.1086/422992).
- Whittam, I. H., Prescott, M., et al. (Jan. 2024). ‘MIGHTEE: Multi-wavelength counterparts in the COSMOS field’. In: *MNRAS* 527.2, pp. 3231–3245. doi: [10.1093/mnras/stad3307](https://doi.org/10.1093/mnras/stad3307).
- Wilber, A. G., Dabbech, A., et al. (July 2023). ‘Scalable precision wide-field imaging in radio interferometry - II. AIRI validated on ASKAP data’. In: *MNRAS* 522.4, pp. 5576–5587. doi: [10.1093/mnras/stad1353](https://doi.org/10.1093/mnras/stad1353).
- Williams, W. L., Calistro Rivera, G., et al. (Apr. 2018). ‘LOFAR-Boötes: properties of high- and low-excitation radio galaxies at $0.5 < z < 2.0$ ’. In: *MNRAS* 475.3, pp. 3429–3452. doi: [10.1093/mnras/sty026](https://doi.org/10.1093/mnras/sty026).
- Williams, W. L. and Röttgering, H. J. A. (June 2015). ‘Radio-AGN feedback: when the little ones were monsters’. In: *MNRAS* 450.2, pp. 1538–1545. doi: [10.1093/mnras/stv692](https://doi.org/10.1093/mnras/stv692).
- Willott, C. J., Rawlings, S., et al. (Apr. 2001). ‘The radio luminosity function from the low-frequency 3CRR, 6CE and 7CRS complete samples’. In: *MNRAS* 322.3, pp. 536–552. doi: [10.1046/j.1365-8711.2001.04101.x](https://doi.org/10.1046/j.1365-8711.2001.04101.x).
- Witten, I., Frank, E., and Hall, M. (2011). *Data Mining: Practical Machine Learning Tools and Techniques*. The Morgan Kaufmann Series in Data Management Systems. Elsevier Science. ISBN: 9780080890364.
- Wolpert, D. H. (1992). ‘Stacked generalization’. In: *Neural Networks* 5.2, pp. 241–259. ISSN: 0893-6080. doi: [10.1016/S0893-6080\(05\)80023-1](https://doi.org/10.1016/S0893-6080(05)80023-1).
- Wolstencroft, R. D., Savage, A., et al. (Nov. 1986). ‘The identification of IRAS point sources- I. A 304 deg² field centred on the South Galactic Pole.’ In: *MNRAS* 223, pp. 279–302. doi: [10.1093/mnras/223.2.279](https://doi.org/10.1093/mnras/223.2.279).
- Wright, E. L., Eisenhardt, P. R. M., et al. (Dec. 2010). ‘The Wide-field Infrared Survey Explorer (WISE): Mission Description and Initial On-orbit Performance’. In: *AJ* 140.6, pp. 1868–1881. doi: [10.1088/0004-6256/140/6/1868](https://doi.org/10.1088/0004-6256/140/6/1868).
- Wu, C., Wong, O. I., et al. (Jan. 2019). ‘Radio Galaxy Zoo: CLARAN - a deep learning classifier for radio morphologies’. In: *MNRAS* 482.1, pp. 1211–1230. doi: [10.1093/mnras/sty2646](https://doi.org/10.1093/mnras/sty2646).

- Xue, Y. Q., Luo, B., et al. (July 2011). ‘The Chandra Deep Field-South Survey: 4 Ms Source Catalogs’. In: ApJS 195.1, 10, p. 10. doi: [10.1088/0067-0049/195/1/10](https://doi.org/10.1088/0067-0049/195/1/10).
- Yan, L., Donoso, E., et al. (Mar. 2013). ‘Characterizing the Mid-infrared Extragalactic Sky with WISE and SDSS’. In: AJ 145.3, 55, p. 55. doi: [10.1088/0004-6256/145/3/55](https://doi.org/10.1088/0004-6256/145/3/55).
- Yan, W., Brandt, W. N., et al. (July 2023). ‘The Most Obscured AGNs in the XMM-SERVS Fields’. In: ApJ 951.1, 27, p. 27. doi: [10.3847/1538-4357/accea6](https://doi.org/10.3847/1538-4357/accea6).
- Yang, J. (Sept. 2021). ‘Fast TreeSHAP: Accelerating SHAP Value Computation for Trees’. In: *arXiv e-prints*, arXiv:2109.09847, arXiv:2109.09847. doi: [10.48550/arXiv.2109.09847](https://doi.org/10.48550/arXiv.2109.09847).
- Yang, Q. and Shen, Y. (Jan. 2023). ‘A Southern Photometric Quasar Catalog from the Dark Energy Survey Data Release 2’. In: ApJS 264.1, 9, p. 9. doi: [10.3847/1538-4365/ac9ea8](https://doi.org/10.3847/1538-4365/ac9ea8).
- Ye, H., Sweijen, F., et al. (Sept. 2023). ‘1-arcsecond imaging strategy for the LoTSS survey using the International LOFAR Telescope’. In: *arXiv e-prints*, arXiv:2309.16560, arXiv:2309.16560. doi: [10.48550/arXiv.2309.16560](https://doi.org/10.48550/arXiv.2309.16560).
- Yeo, I.-K. and Johnson, R. A. (Dec. 2000). ‘A new family of power transformations to improve normality or symmetry’. In: *Biometrika* 87.4, pp. 954–959. issn: 0006-3444. doi: [10.1093/biomet/87.4.954](https://doi.org/10.1093/biomet/87.4.954).
- Yerushalmy, J. (1947). ‘Statistical Problems in Assessing Methods of Medical Diagnosis, with Special Reference to X-Ray Techniques’. In: *Public Health Reports (1896-1970)* 62.40, pp. 1432–1449. issn: 00946214. url: <http://www.jstor.org/stable/4586294> (visited on 10/08/2022).
- York, D. G., Adelman, J., et al. (Sept. 2000). ‘The Sloan Digital Sky Survey: Technical Summary’. In: AJ 120.3, pp. 1579–1587. doi: [10.1086/301513](https://doi.org/10.1086/301513).
- Yuan, Z., Jarvis, M. J., and Wang, J. (May 2020). ‘A Flexible Method for Estimating Luminosity Functions via Kernel Density Estimation’. In: ApJS 248.1, 1, p. 1. doi: [10.3847/1538-4365/ab855b](https://doi.org/10.3847/1538-4365/ab855b).
- Yuan, Z. and Wang, J. (June 2013). ‘A graphical analysis of the systematic error of classical binned methods in constructing luminosity functions’. In: Ap&SS 345.2, pp. 305–313. doi: [10.1007/s10509-013-1402-9](https://doi.org/10.1007/s10509-013-1402-9).
- Yuan, Z., Zhang, X., et al. (May 2022). ‘A Flexible Method for Estimating Luminosity Functions via Kernel Density Estimation. II. Generalization and Python Implementation’. In: ApJS 260.1, 10, p. 10. doi: [10.3847/1538-4365/ac596a](https://doi.org/10.3847/1538-4365/ac596a).
- Yule, G. U. (1912). ‘On the Methods of Measuring Association Between Two Attributes’. In: *Journal of the Royal Statistical Society* 75.6, pp. 579–652. issn: 09528385. url: <http://www.jstor.org/stable/2340126>.
- Zajaček, M., Busch, G., et al. (Oct. 2019). ‘Radio spectral index distribution of SDSS-FIRST sources across optical diagnostic diagrams’. In: A&A 630, A83, A83. doi: [10.1051/0004-6361/201833388](https://doi.org/10.1051/0004-6361/201833388).
- Zammit, M. A. and Adami, K. Z. (Nov. 2023). ‘Machine Learning Applications in Jupiter-host Star Classification using Stellar Spectra’. In: MNRAS. doi: [10.1093/mnras/stad3668](https://doi.org/10.1093/mnras/stad3668).
- Zeraatgari, F. Z., Hafezianzadeh, F., et al. (Jan. 2024). ‘Machine learning-based photometric classification of galaxies, quasars, emission-line galaxies, and stars’. In: MNRAS 527.3, pp. 4677–4689. doi: [10.1093/mnras/stad3436](https://doi.org/10.1093/mnras/stad3436).
- Zhang, Y. and Zhao, Y. (May 2015). ‘Astronomy in the Big Data Era’. In: *Data Science Journal* 14, p. 11. doi: [10.5334/dsj-2015-011](https://doi.org/10.5334/dsj-2015-011).

REFERENCES

- Zheng, A. and Casari, A. (2018). *Feature Engineering for Machine Learning: Principles and Techniques for Data Scientists*. O'Reilly. ISBN: 9781491953242.
- Zitlau, R., Hoyle, B., et al. (Aug. 2016). ‘Stacking for machine learning redshifts applied to SDSS galaxies’. In: MNRAS 460.3, pp. 3152–3162. doi: [10.1093/mnras/stw1454](https://doi.org/10.1093/mnras/stw1454).
- Zou, H., Gao, J., et al. (May 2019). ‘Photometric Redshifts and Stellar Masses for Galaxies from the DESI Legacy Imaging Surveys’. In: ApJS 242.1, 8, p. 8. doi: [10.3847/1538-4365/ab1847](https://doi.org/10.3847/1538-4365/ab1847).

Appendices

This page intentionally left blank.

A

Luminosity function formulation

As presented in Sect. 1.1, fluxes (F) can be used to obtain an estimate of the luminosities (L) emitted by an astrophysical source.

The initial formula to obtain luminosities (L) from fluxes as presented by, for example, Carroll and Ostlie (2017) is:

$$F = \frac{L}{4\pi r^2} \quad (\text{A.1})$$

with r being the distance from the observer to the emitting source. This expression does not take any change in the path of the light into account and assumes no interactions of it with intervening materials. Rearranging its terms, the luminosity can be then written as

$$L = 4\pi r^2 F. \quad (\text{A.2})$$

The first modification that can be applied is related to the distance at which the source is from the observer. Thus, a correction for its redshift must be applied (e.g. Sandage, 1962). Additionally, a term with the correction for the difference between the waveband of the detector and that of the observed source can be included (K-correction; Oke and Sandage, 1968). For the specific case of radio bands, it is possible to assume their continuum spectra can be modelled as a power law in the form $S_\nu \propto \nu^\alpha$ (Sommer et al., 2011), with α , the spectral index, typically taking values around $\alpha \sim -0.7$. Then, and taking into account the mentioned corrections, Eq. A.2 can be written as:

$$L_\nu = 4\pi D_L^2 S_\nu \frac{\mathcal{K}}{(1+z)}, \quad (\text{A.3})$$

in which D_L represents the luminosity distance to the source (Hogg, 1999) and \mathcal{K} stands for the aforementioned K-correction. For the radio emission, the K-correction can take the form $(1+z)^{-\alpha}$ (Condon et al., 2002; Radcliffe et al., 2018; Cochrane et al., 2023), with α being the same spectral index, and then, Eq. A.3 leads to:

APPENDIX A. LF FORMULATION

$$L_\nu = \frac{4\pi D_L^2}{(1+z)^{1+\alpha}} S_\nu. \quad (\text{A.4})$$

Considering that the radio emission has been assumed to have the shape of a power law, it is possible to use this fact to transform luminosities in different frequencies without complex procedures (Delhaize et al., 2017). If a luminosity is measured at a frequency ν_a , the way to convert it into the luminosity at frequency ν_b , using the spectral index, α , is through:

$$L_{\nu_b} = \frac{4\pi D_L^2}{(1+z)^{1+\alpha}} \left(\frac{\nu_b}{\nu_a}\right)^\alpha S_{\nu_a}. \quad (\text{A.5})$$

LFs can provide a measure of the evolution of the density of sources in different bins.

Define (radio) luminosity functions

It is possible to define the LF using a differential approach. In this way, the LF, ϕ , the number of sources per unit luminosity, L , and unit volume, V , can be defined as:

$$\phi(L, z) = \frac{d^2 d}{dV dL}(L, z), \quad (\text{A.6})$$

in which d corresponds to the number of objects with luminosity between L and $L + dL$ and in a volume of range V and $V + dV$ (which is a function of the redshift z). Equation A.6 can also be written using the logarithm of the luminosity as:

$$\phi(\log_{10} L, z) = \frac{d^2 d}{dV d(\log_{10} L)}. \quad (\text{A.7})$$

Using a sample of measured luminosities, it is possible to estimate the LF using different methods that take into account the general properties of the observations from which the measurements were obtained (e.g. the survey depth and the area it covers). One way in which LFs can be quantified is by the use of the $\langle V/V_{\max} \rangle$ method (Schmidt, 1968). An application of this method is the $1/V_{\max}$ technique (e.g. Avni and Bahcall, 1980; Maccacaro et al., 1991; Ellis et al., 1996). The $1/V_{\max}$ technique has been devised to measure the space number density ($d d d V$) via the small interval approximation:

$$\frac{d d}{dV} \approx \sum_{i=1}^{d} \frac{1}{V_a(i)}, \quad (\text{A.8})$$

where $V_a(i)$ corresponds to the volume in which the object i , with luminosity $L(i)$ might have been still detected in the redshift bin Δz (Page and Carrera, 2000). With this approximation, the

luminosity function can be estimated as:

$$\phi_{1/V_a}(L, z) = \frac{1}{\Delta L} \sum_{i=1}^{\text{d}} \frac{1}{V_a(i)}. \quad (\text{A.9})$$

Another technique for the estimation of the **LF** values is called binned approximation. First described by Page and Carrera (2000), it refines the region in which each step of the **LF** is calculated as assuming a dependence on the redshift of the sources (as originally presented in the definition of **LF**, Eq. A.6), concept which the $1/V_{\max}$ technique omits.

For the binned **LF**, it is assumed that the plane $L - z$ is divided into bins limited by fixed redshift values and luminosity values that depend on the conditions of the studied survey (i.e. the minimum luminosity at which a source can be detected). Therefore, the **LF** can be approximated as:

$$\phi \approx \phi_{\text{binned}} = \frac{\text{d}}{\int_{z_{\min}}^{z_{\max}} \int_{L_{\min}(L)}^{L_{\max}} \frac{dV}{dz} dz dL}, \quad (\text{A.10})$$

where d corresponds to the number of sources in each bin. In this case, Eq. A.10 needs to be calculated for the central point of each relevant bin of the plane $L - z$.

Finally, further methods to estimate the values of the **LF** can consider more complex mathematical expressions. That is the case of its calculation using a **kernel density estimation (KDE)** approach (Abramson, 1982; Davies et al., 2018b). As presented by Yuan et al. (2020) and Yuan et al. (2022), its implementation incorporates the addition of several kernels (one per source in the sample). Then, its complexity arises at the determination of the bandwidths (and additional parameters) of the kernels. The final expression of the **KDE-based LF** is then:

$$\phi \approx \phi_{\text{KDE}} = \frac{\text{d} (z_2 - z_1) \hat{f}(x, y | h_1, h_2)}{(z - z_1) (z_2 - z) \Omega \frac{dV}{dz}}, \quad (\text{A.11})$$

where z_1 and z_2 are the redshift limits of the studied sample, $\hat{f}(x, y | h_1, h_2)$ corresponds to the density function of the pair (x, y) which is the equivalent of (z, L) in the **KDE** space, and d is the size of such sample.

As expected, all the previous methods allow to count the sources that are located in a specific area of the sky. However, this count might be biased by the conditions of the measurements in the used catalogues. A selection function, \mathcal{P} , is used to correct the sources

APPENDIX A. LF FORMULATION

count. \mathcal{P} summarises the corrections that the distribution of sources must suffer in order to be as close as possible to our best guess of their real distribution. In this way, d becomes d_{eff} , the effective number of sources in the sample.

All the previous methods are non-parametric, meaning that they do not assume any analytic form or shape of the studied LF. Contrary to that, several parametric models have been developed to determine an expression for the LF. **List parametric LF formulations**

B

Sample of predicted radio-detectable AGN

The columns shown in the prediction results for sources in both **HETDEX** and **S82** fields are described in Table B.1. Full datasets and models from prediction pipeline can be obtained from Carvajal et al. (2023b) at <https://zenodo.org/doi/10.5281/zenodo.10220008>.

APPENDIX B. PREDICTED RADIO-DETECTABLE AGN

Table B.1: Table columns descriptions.

ID	Internal identification number
RA_ICRS	Right Ascension (in degrees) of source in CW
DE_ICRS	Declination (in degrees) of source in CW
Name	Name of source as it appears in CW catalogue
band_num	Number of non-radio bands with valid measurement per source (cf. Sect. 2.5)
class	1 if source is confirmed AGN by MQC . 0 if spectroscopically confirmed as SFG in SDSS-DR16 . Sources with no value do not have spectroscopic classification in this catalogue
Sint_LOFAR Fint_VLAS82) ^a	(or Imputed integrated flux (in mJy) of source from LOFAR or VLAS82
Sint_LOFAR_non_imp Fint_VLAS82_non_imp) ^a	(or Non imputed integrated flux (in mJy) of source from LOFAR or VLAS82
W1magPM	Imputed W1 magnitude of source
W2magPM	Imputed W2 magnitude of source
gmag	Imputed g magnitude of source
rmag	Imputed r magnitude of source
imag	Imputed i magnitude of source
zmag	Imputed z magnitude of source
ymag	Imputed y magnitude of source
W3mag	Imputed W3 magnitude of source
W4mag	Imputed W4 magnitude of source
Jmag	Imputed J magnitude of source
Hmag	Imputed H magnitude of source
Kmag	Imputed Ks magnitude of source
Score_AGN	Score from meta AGN-SFG classifier to be AGN
Prob_AGN	Probability from calibrated meta AGN-SFG classifier AGN
LOFAR_detect	1 if source has been detected on LoTSS-DR1 or in analogue surveys for different fields (see Sects. 2.1 and 2.2). 0 otherwise
Score_radio_AGN	Score from meta radio detection model to be detected in radio
Prob_radio_AGN	Probability from calibrated radio detection model to be detected in radio
radio_AGN	$\text{class} \times \text{LOFAR_detect}$. 1 if source is AGN and has been detected in radio. 0 otherwise
Score_rAGN	$\text{Score_AGN} \times \text{Score_radio}$. Score of source to be AGN detected in radio
Prob_rAGN	$\text{Prob_AGN} \times \text{Prob_radio}$. Probability of source to be AGN detected in radio
Z	Spectroscopic redshift as listed by the MQC (if available)
pred_Z	Redshift value predicted by our model

^a Sources from [HETDEX](#) field have columns with LOFAR suffix. Sources from [VLAS82](#) have VLAS82 suffix.

Table B.2: Predicted and original properties for 20 sources in testing subset with highest redshift predicted radio AGN. Sources sorted by decreasing predicted redshift.

ID	RA_ICRS	DE_ICRS	band_num	class	Score_AGN	Prob_AGN	LOFAR_detect	Score_radio	Prob_rAGN	z	pred_z
	(deg)	(deg)									
9898	717 203.016 113.55.518 097	9	1.0	0.500 082	0.954 114	0	0.390 861	0.375 122	0.195 462	0.357 909	4.738 4.3679
168	686 164.769 135.45.806 320	8	1.0	0.500 048	0.858 157	0	0.450 279	0.418 719	0.225 161	0.359 326	4.893 4.1733
14437	074 213.226 517.54.236 343	9	1.0	0.500 090	0.965 187	0	0.251 632	0.263 746	0.125 839	0.254 564	4.326 4.0475
10408	176 188.163 651.52.880 898	9	1.0	0.500 012	0.622 448	0	0.604 838	0.526 003	0.302 426	0.327 410	4.340 3.9553
12612	753 227.216 370.51.941 029	9	1.0	0.500 055	0.887 909	0	0.364 423	0.355 080	0.182 231	0.315 278	3.795 3.8797
5283	988 210.532 974.49.500 351	9	1.0	0.500 095	0.971 223	0	0.188 993	0.207 802	0.094 514	0.201 822	3.800 3.8733
6005	721 188.469 818.47.834 412	9	1.0	0.500 045	0.845 762	0	0.221 281	0.237 188	0.110 651	0.200 604	3.795 3.7482
13284	852 218.364 182.48.398 373	9	1.0	0.500 086	0.961 052	0	0.340 675	0.336 683	0.170 367	0.322 570	3.892 3.7222
12308	398 222.563 293.49.665 272	8	1.0	0.500 061	0.906 658	1	0.385 996	0.371 466	0.193 021	0.336 793	2.059 3.7173
8147	562 200.292 435.50.367 386	9	1.0	0.500 090	0.965 431	1	0.406 555	0.386 820	0.203 314	0.373 448	3.711 3.6748
4433	144 215.540 436.46.992 298	9	1.0	0.500 085	0.958 811	1	0.363 854	0.354 644	0.181 958	0.340 036	3.812 3.6541
12285	636 221.428 192.49.046 921	12	1.0	0.500 037	0.803 828	1	0.254 536	0.266 237	0.127 277	0.214 009	3.880 3.5737
8170	701 200.040 466.50.849 586	9	1.0	0.500 040	0.818 872	0	0.232 864	0.247 439	0.116 441	0.202 620	3.827 3.5436
12118	249 223.858 124.48.950 409	9	1.0	0.500 049	0.862 100	1	0.280 344	0.288 020	0.140 186	0.248 302	3.501 3.5381
1537	357 177.051 697 52.934 574	9	1.0	0.500 015	0.645 263	0	0.240 127	0.253 793	0.120 067	0.163 763	3.885 3.5037
10731	551 190.228 714.54.614 464	9	1.0	0.500 055	0.887 182	1	0.277 223	0.285 418	0.138 627	0.253 218	3.938 3.4858
8721	103 203.096 924.50.575 378	9	1.0	0.500 093	0.969 007	0	0.267 817	0.277 525	0.133 933	0.268 924	3.832 3.4604
10679	277 190.777 359.53.089 466	9	1.0	0.500 104	0.978 721	1	0.323 977	0.323 506	0.162 022	0.316 622	3.575 3.3764
8434	867 194.881 256.52.609 665	9	1.0	0.500 066	0.920 703	0	0.811 700	0.672 552	0.405 903	0.619 221	0.374 3.1584
10314	475 188.218 765.51.662 666	9	1.0	0.500 109	0.982 703	0	0.545 364	0.485 399	0.272 741	0.477 003	2.157 3.0701

DRAFT - MACC 15, 2024 - DRATE

APPENDIX B. PREDICTED RADIO-DETECTABLE AGN

Table B.3: Properties for the 20 sources in S82 with highest predicted redshift on labelled sources predicted to be radio AGN. Sources sorted by decreasing predicted redshift.

ID	RA_ICRS (deg)	DE_ICRS (deg)	band_num	class	Score_AGN	Prob_AGN	radio_detect	Score_radio	Prob_radio	Score_rAGN	Prob_rAGN	z	pred_z
1406323	32.679794	-0.305035	6	1.0	0.500050	0.866373	1	0.185842	0.204867	0.092930	0.177491	4.650	4.4986
326139	33.580879	-1.121398	8	1.0	0.500040	0.822622	0	0.208769	0.225946	0.104393	0.185868	4.600	4.3785
633752	12.526446	-0.888660	9	1.0	0.500035	0.793882	0	0.206182	0.223600	0.103098	0.177512	4.310	4.2946
2834844	344.101440	0.789000	7	1.0	0.500062	0.909395	0	0.375735	0.363709	0.187891	0.330756	4.099	4.0635
3191865	31.881712	1.063655	9	1.0	0.500087	0.962260	0	0.264210	0.274477	0.132128	0.264118	3.841	4.0509
834857	21.023815	-0.735512	9	1.0	0.500080	0.951495	0	0.270463	0.279754	0.135253	0.266185	4.073	4.0476
927403	30.860348	-0.664943	9	1.0	0.500086	0.960503	0	0.237843	0.251800	0.118942	0.241855	4.158	3.9690
1760668	343.580109	-0.031951	9	1.0	0.500088	0.962655	0	0.262341	0.272891	0.131193	0.262700	3.710	3.9594
1539341	35.058613	-0.202904	5	1.0	0.500028	0.746304	0	0.243109	0.256385	0.121561	0.191341	3.712	3.9175
794288	21.752874	-0.766390	12	1.0	0.500044	0.838993	0	0.830699	0.687772	0.415386	0.577036	4.105	3.8631
201543	18.192499	-1.218799	9	1.0	0.500062	0.909994	0	0.383420	0.369525	0.191734	0.336265	3.589	3.7324
2705463	27.703466	0.690627	12	1.0	0.500092	0.968344	0	0.284506	0.291475	0.142279	0.282248	3.685	3.6814
567008	13.804744	-0.939195	9	1.0	0.500114	0.985173	0	0.473856	0.435550	0.236982	0.429092	3.622	3.5531
2610655	334.937775	0.618921	9	1.0	0.500107	0.981287	0	0.201475	0.219309	0.100759	0.215205	3.531	3.5031
2972720	341.585175	0.894723	9	1.0	0.500087	0.961458	0	0.752861	0.628400	0.376496	0.604180	3.676	3.4776
315550	342.345581	-1.129457	9	1.0	0.500070	0.930942	0	0.485239	0.443596	0.242653	0.412962	3.989	3.4724
2774066	21.015764	0.742418	12	1.0	0.500045	0.843852	0	0.642026	0.551288	0.321042	0.465205	3.836	3.4492
3301527	346.665192	1.148655	9	1.0	0.500045	0.846709	0	0.305069	0.308323	0.152548	0.261060	3.648	3.4407
1926483	22.206123	0.095463	9	1.0	0.500117	0.986782	0	0.427273	0.402055	0.213687	0.396741	3.746	3.4282
211079	31.115847	-1.211047	9	1.0	0.500106	0.980813	0	0.455339	0.422351	0.227718	0.414247	3.940	3.3345

Table B.4: Predicted and original properties for the 20 sources in [HETDEX](#) field with highest predicted redshift on the unlabelled sources predicted to be radio AGN.

ID	RA_ICRS	DE_ICRS	band_num	Score_AGN	Prob_AGN	radio_detect	Score_radio	Prob_radio	Score_rAGN	Prob_rAGN	pred_z
	(deg)	(deg)									(deg)
9 544 254 201.309 235 53.746 429	6	0.500 007	0.578 804	0	0.351 672	0.345 250	0.175 838	0.199 832	4.711 14		
12 355 845 220.838 120 50.319 016	5	0.500 007	0.578 804	0	0.937 123	0.794 128	0.468 568	0.459 644	4.606 4		
13 814 216 219.839 142 52.660 328	7	0.500 015	0.650 248	0	0.213 846	0.230 529	0.106 926	0.149 901	4.562 2		
6 698 239 184.694 901 49.063 766	5	0.499 995	0.467 527	0	0.799 085	0.662 753	0.399 538	0.309 855	4.548 3		
2 951 011 175.882 446 55.497 799	5	0.500 008	0.589 419	0	0.823 295	0.681 768	0.411 654	0.401 847	4.532 0		
7 281 571 202.589 035 47.134 212	9	0.500 032	0.773 522	0	0.567 045	0.500 257	0.283 541	0.386 960	4.522 0		
8 634 951 206.688 446 51.339 924	7	0.499 981	0.349 392	0	0.289 692	0.295 758	0.144 841	0.103 336	4.511 1		
5 075 789 207.003 540 48.740 067	7	0.499 998	0.492 974	0	0.400 019	0.381 966	0.200 009	0.188 299	4.508 7		
12 750 738 222.945 663 52.196 320	7	0.500 009	0.593 819	0	0.238 322	0.252 219	0.119 163	0.149 772	4.506 4		
1 775 496 163.331 070 47.809 532	7	0.500 032	0.772 884	0	0.764 361	0.636 758	0.382 205	0.492 140	4.493 0		
14 577 806 213.842 804 56.349 747	8	0.500 047	0.856 822	0	0.615 253	0.533 082	0.307 656	0.456 756	4.466 3		
9 817 016 198.035 965 55.984 398	5	0.500 010	0.603 443	0	0.466 084	0.430 028	0.233 047	0.259 497	4.443 8		
12 429 128 226.345 795 49.744 789	7	0.500 007	0.581 465	0	0.485 468	0.443 757	0.242 737	0.258 029	4.443 8		
14 500 121 211.942 429 55.213 791	7	0.500 008	0.587 655	0	0.809 995	0.671 214	0.405 004	0.394 443	4.435 5		
2 166 668 163.079 010 53.084 713	7	0.500 010	0.605 185	0	0.743 381	0.621 584	0.371 698	0.376 173	4.435 3		
7 077 234 181.246 124 53.378 967	7	0.500 012	0.623 304	0	0.264 222	0.274 486	0.132 114	0.171 088	4.420 9		
14 074 782 218.186 417 54.400 047	7	0.500 019	0.681 823	0	0.396 363	0.379 240	0.198 189	0.258 574	4.406 5		
5 789 667 187.343 811 47.441 658	8	0.500 023	0.706 552	0	0.725 299	0.608 743	0.362 666	0.430 109	4.402 7		
11 070 539 183.812 180 54.915 974	7	0.500 012	0.621 592	0	0.202 662	0.220 393	0.101 333	0.136 995	4.395 9		
8 943 186 202.578 445 53.892 410	7	0.499 983	0.362 751	0	0.331 269	0.329 286	0.165 629	0.119 449	4.395 1		

DRAFT - MACC 15, 2024 - DRATE

APPENDIX B. PREDICTED RADIO-DETECTABLE AGN

Table B.5: Predicted and original properties for the 20 sources in S82 with highest predicted redshift on the unlabelled sources predicted to be radio AGN.

ID	RA_ICRS (deg)	DE_ICRS (deg)	band_num	Score_AGN	Prob_AGN	radio_detect	Score_radio	Prob_radio	Score_rAGN	Prob_rAGN	pred_z
3 244 450	26.276 423	1.104 065	7	0.500 002	0.531 172	0	0.542 061	0.483 128	0.271 031	0.256 624	4.3938
1 062 270	11.744 675	-0.562 642	7	0.499 982	0.356 043	0	0.196 326	0.214 586	0.098 159	0.076 402	4.3563
3 261 269	28.882 526	1.117 103	7	0.500 011	0.608 660	0	0.354 936	0.347 777	0.177 472	0.211 678	4.3153
1 466 227	18.157 259	-0.258 997	5	0.500 013	0.630 968	0	0.456 207	0.422 973	0.228 110	0.266 882	4.3146
1 134 866	11.304 936	-0.507 943	7	0.500 011	0.616 439	0	0.226 178	0.241 539	0.113 091	0.148 894	4.3140
1 726 140	29.144 888	-0.058 600	7	0.499 984	0.369 512	0	0.261 730	0.272 373	0.130 861	0.100 645	4.3125
220 011 331.973 877	-1.203 849	7	0.500 016	0.656 024	0	0.734 737	0.615 421	0.367 380	0.403 731	4.3098	
2 005 587	30.130 974	0.155 751	7	0.500 017	0.665 006	0	0.828 544	0.686 014	0.414 286	0.456 203	4.2972
1 058 229 344.614 166	-0.565 701	5	0.500 015	0.645 263	0	0.394 774	0.378 052	0.197 393	0.243 943	4.2899	
2 914 632 344.342 316	0.850 049	7	0.500 009	0.594 697	0	0.601 936	0.524 030	0.300 973	0.311 639	4.2767	
1 255 517	20.319 715	-0.418 364	7	0.500 012	0.625 012	0	0.210 549	0.227 556	0.105 277	0.142 226	4.2711
762 162 340.426 544	-0.790 798	7	0.500 014	0.638 566	0	0.671 060	0.571 113	0.335 539	0.364 693	4.2687	
1 167 955	21.433 058	-0.483 463	8	0.500 016	0.659 303	0	0.776 046	0.645 368	0.388 036	0.425 493	4.2652
1 160 900	35.526 070	-0.488 795	7	0.500 013	0.630 119	0	0.614 667	0.532 684	0.307 341	0.335 654	4.2516
706 252 332.367 462	-0.833 645	5	0.500 013	0.630 119	0	0.517 853	0.466 400	0.258 933	0.293 888	4.2481	
510 569	10.896 913	-0.981 369	7	0.500 016	0.651 903	0	0.192 197	0.210 775	0.096 102	0.137 405	4.2472
2 512 910 333.612 640	0.544 506	5	0.500 014	0.636 883	0	0.388 904	0.373 653	0.194 457	0.237 974	4.2471	
840 809 341.886 383	-0.730 991	7	0.500 042	0.827 874	0	0.212 097	0.228 954	0.106 057	0.189 545	4.2433	
2 932 746 35.531 948	0.863 913	8	0.500 013	0.631 815	0	0.917 725	0.770 169	0.458 874	0.486 604	4.2421	
325 442 344.384 644	-1.121 920	7	0.500 035	0.793 285	0	0.624 086	0.539 086	0.312 065	0.427 649	4.2353	

Extended prediction pipeline

For some of the calculations in Chapter 6, a new instance of the prediction pipeline was trained and implemented. Its steps were kept similar to its original definition (Sect. 1.4) with some relevant differences. The first change is in the overall structure of the pipeline. The prediction for radio-detected **AGN** works as presented in Fig. 1.8, but a new branch has been added for the treatment of radio-detected **SFGs** (i.e. extragalactic sources without indications of **AGN** emission). This new branch replicates the steps of the original process and its stages are presented, graphically, in the flowchart of Fig. C.1.

The difference in the processing of the candidates start when sources are predicted to be **SFGs** (i.e. not **AGN**). Instead of being discarded, they are subject to a series of models that replicate the process for predicted **AGN**. Thus, a new step that predicts their likelihood of being radio detectable is applied. The predicted radio-detectable **SFGs** have, then, their photometric redshifts predicted. Finally, the results from both branches, **AGN** and **SFGs**, are compiled into one single catalogue of source candidates.

The internal processing of each model remains the same as described in Chapter 5 and Fig. 2.6. The only difference can be found in the data collection. In particular, the cross-match of the **CW**-detected sources with the radio detections (for the training stages, from LoTSS-DR1). Instead of using a search radius of $1''1$ (as it is maintained for all the remaining ancillary catalogues), sources are cross-matched with a radius of $6''$ with the radio catalogue. This increase of more than five times in distance (and close to 30 times in area) can be explained by the need of obtaining a larger fraction of sources with a radio counterpart (as the results of the cross-match itself are to be assessed in Sect. 6.3). A modified version of Table 2.3, with the new search radius for radio counterparts, is shown in Table C.1.

As expected, the number of non-radio counterparts remains the same. In contrast, the number of radio cross-matches has grown by more than a 100 % from the use of a $1''1$ search radius. This change can, in turn, alter the metrics for the radio detection models and those of the redshift predictions as well given the modification of the distribution of values of the feature

APPENDIX C. EXTENDED PREDICTION PIPELINE

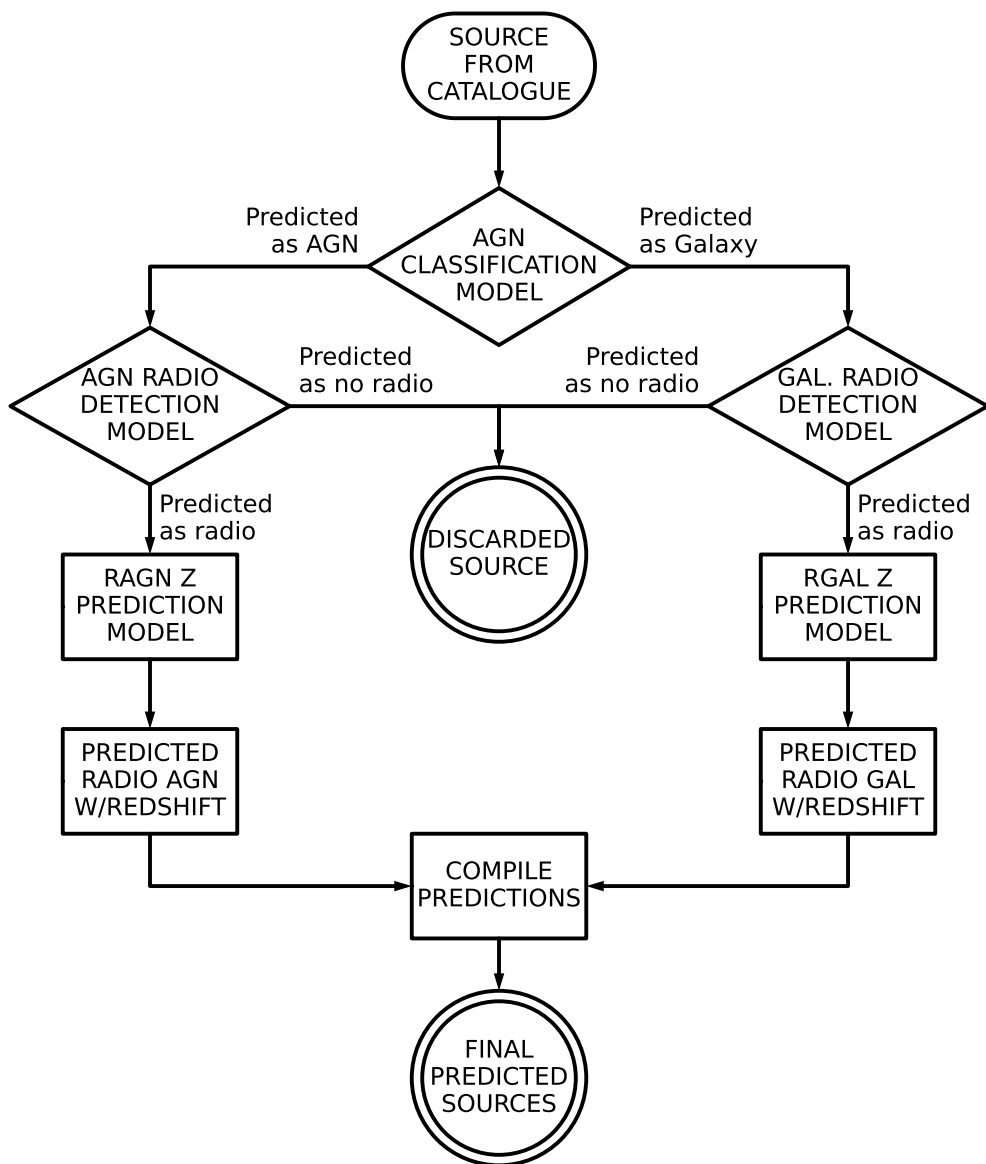


Figure C.1: Flowchart representing the proposed extended prediction pipeline used to predict the presence of radio-detected AGN and SFGs and their redshift values from IR-detected sources.

Table C.1: Composition of initial catalogue and number of cross matches with additional surveys and catalogues for training of updated pipeline

Survey	HETDEX	Stripe82
CatWISE2020	15 136 878	3 590 306
AllWISE	5 955 123	1 424 576
Pan-STARRS	4 837 580	1 346 915
2MASS	566 273	214 445
LoTSS (6'')	382 431	...
VLAS82 (6'')	...	17 706
MQC (AGN)	50 538	17 743
SDSS (SFG)	68 196	4085

`radio_detect`. For our purposes, the differences in the metrics for this new set of models do not imply a degradation of the results they provide given that they have been corrected for these differences when needed.

C.1 Training and model selection

Results and metrics of the `AGN-SFG` classification model have not changed with the extension of the prediction pipeline and the inclusion of a larger number of radio counterparts. This prediction stage does not use any form of radio information for its training and predictions. We refer, then, the reader to Chapter 6 and Sect. 4.1 for the analysis of its results for the prediction of `AGN`.

The model for the classification of radio-detectable `AGN` is modified by the change in the distribution of values in its target feature, `radio_detect`. Nevertheless, the features selected for training remain the same as with the original model (i.e. `band_num`, `W4mag`, `g_r`, `g_i`, `r_i`, `r_z`, `i_z`, `z_y`, `z_W1`, `y_J`, `y_W1`, `J_H`, `H_K`, `K_W3`, `K_W4`, `W1_W2`, and `W2_W3`). For the selection of the meta and base models, `XGBoost` was adopted as the meta learner while `GBC`, `RF`, `CatBoost`, and `ET` have been used as base learners. The results of such selection are displayed in Table C.2.

The training of the model for the prediction of radio detectability in predicted `SFGs` led to the use of 18 features (`W4mag`, `Kmag`, `g_r`, `g_W2`, `r_i`, `r_y`, `i_z`, `i_y`, `z_y`, `z_W2`, `y_J`, `y_W2`, `J_H`, `H_K`, `H_W3`, `W1_W2`, `W1_W3`, and `W3_W4`) together with its target, `radio_detect`. Additionally, and as seen in Table C.3, `RF` was selected as meta learner and `CatBoost`, `XGBoost`, `ET`, and `GBC`, as base models.

APPENDIX C. EXTENDED PREDICTION PIPELINE

Table C.2: Best performing modified models the radio detection classification for **AGN**

Model	F_β ($\times 100$)	MCC ($\times 100$)	Precision ($\times 100$)	Recall ($\times 100$)	Rank
XGBoost	36.41 ± 1.82	34.47 ± 2.16	61.93 ± 3.18	27.18 ± 1.53	3.25
GBC	36.98 ± 2.20	36.39 ± 2.26	66.47 ± 3.39	27.10 ± 1.99	1.25
RF	36.74 ± 1.99	35.90 ± 1.90	65.48 ± 1.91	26.98 ± 1.78	2.25
CatBoost	36.18 ± 1.64	35.21 ± 1.68	64.60 ± 2.46	26.55 ± 1.48	3.50
ET	35.08 ± 1.09	34.32 ± 1.48	64.22 ± 2.48	25.52 ± 0.83	4.75
No-skill	15.29 ± 0.76	0.00 ± 0.91	15.29 ± 0.76	15.29 ± 0.76	6.00

^a Values and uncertainties as in Table 3.1.

Table C.3: Best performing modified models the radio detection classification for **SFGs**

Model	F_β ($\times 100$)	MCC ($\times 100$)	Precision ($\times 100$)	Recall ($\times 100$)	Rank
RF	39.39 ± 2.49	41.69 ± 2.36	76.09 ± 2.42	28.19 ± 2.12	1.25
CatBoost	39.24 ± 2.36	41.53 ± 2.39	75.90 ± 2.69	28.06 ± 1.97	2.25
XGBoost	38.64 ± 1.98	40.38 ± 2.23	73.55 ± 2.87	27.76 ± 1.57	4.00
ET	38.35 ± 2.57	40.69 ± 2.50	75.28 ± 2.78	27.31 ± 2.17	4.00
GBC	37.69 ± 2.32	40.83 ± 2.40	77.39 ± 3.01	26.49 ± 1.89	3.50
No-skill	14.22 ± 1.13	0.00 ± 1.32	14.22 ± 1.14	14.22 ± 1.12	6.00

^a Values and uncertainties as in Table 3.1.

The model for the prediction of photometric redshifts of radio-detectable **AGN** is also modified but, in this case, by the change in number of sources in the training set, which is increased (by the larger search radius for radio-detected sources). Thus, the features selected for training are 17 (i.e. `band_num`, `W4mag`, `g_r`, `g_W1`, `r_i`, `r_z`, `i_z`, `i_y`, `z_y`, `y_J`, `y_W1`, `J_H`, `H_K`, `K_W3`, `K_W4`, `W1_W2`, and `W1_W3`). Despite three algorithms having the same mean rank, the algorithm selected to be meta learner is **RF** given that it presents the best value of σ_{NMAD} , which is the metric to be optimised during training. Its metrics (together with those from the base models) are presented in Table C.4.

The model for the prediction of photometric redshifts of radio-detectable **SFGs** is also modified and selects 14 features for its training: `W4mag`, `g_r`, `r_i`, `r_z`, `i_z`, `i_y`, `z_y`, `y_J`, `y_W2`, `J_H`, `H_K`, `K_W3`, `W1_W2`, and `W1_W3`. The selected algorithm to be meta learner is **ET** (again, because it presents the best value of σ_{NMAD}) and its metrics (together with those from the base models and an no-skill prediction) are presented in Table C.5.

For the sake of completeness, Table C.6 presents the optimised hyperparameters for all the five stacked models of the new prediction pipeline.

C.2. APPLICATION OF STACKED MODELS

Table C.4: Results of initial fit for redshift value prediction on predicted radio detectable AGN

Model	σ_{MAD} ($\times 100$)	σ_{NMAD} ($\times 100$)	σ_z ($\times 100$)	σ_z^N ($\times 100$)	η ($\times 100$)	Rank
RF	17.54 ± 1.24	7.70 ± 0.34	41.55 ± 4.38	19.63 ± 2.57	18.30 ± 1.60	2.0
ET	18.79 ± 1.22	8.32 ± 0.39	40.81 ± 3.25	18.29 ± 1.86	19.56 ± 1.78	2.0
CatBoost	21.07 ± 1.15	9.97 ± 0.25	39.65 ± 2.52	18.06 ± 1.57	21.14 ± 2.17	2.2
XGBoost	22.92 ± 1.20	10.49 ± 0.54	42.16 ± 3.85	19.36 ± 2.16	23.53 ± 1.62	3.8
GBR	28.33 ± 1.48	13.24 ± 0.73	44.77 ± 3.59	20.21 ± 1.93	29.90 ± 1.82	5.0
No-skill	97.06 ± 4.52	39.95 ± 1.89	86.78 ± 1.92	48.17 ± 1.10	72.49 ± 1.96	6.0

^a Algorithms sorted by increasing σ_{MAD} values.

^b Uncertainties as in Table 3.1.

Table C.5: Results of initial fit for redshift value prediction on predicted radio detectable SFGs

Model	σ_{MAD} ($\times 100$)	σ_{NMAD} ($\times 100$)	σ_z ($\times 100$)	σ_z^N ($\times 100$)	η ($\times 100$)	Rank
ET	3.85 ± 0.25	2.81 ± 0.18	9.89 ± 0.81	7.03 ± 1.06	2.91 ± 0.77	2.0
RF	3.89 ± 0.12	2.86 ± 0.12	9.78 ± 0.88	6.98 ± 1.10	3.08 ± 0.88	2.0
CatBoost	4.01 ± 0.20	2.96 ± 0.12	9.75 ± 0.72	6.99 ± 1.01	2.78 ± 0.56	2.0
XGBoost	4.31 ± 0.27	3.16 ± 0.17	9.98 ± 0.90	7.05 ± 1.05	3.13 ± 0.73	4.2
GBR	4.81 ± 0.16	3.54 ± 0.08	9.96 ± 0.76	7.05 ± 0.99	3.45 ± 1.05	4.6
No-skill	33.51 ± 1.86	21.70 ± 1.31	26.74 ± 0.67	20.94 ± 0.42	49.08 ± 1.93	6.0

^a Algorithms sorted by increasing σ_{MAD} values.

^b Uncertainties as in Table 3.1.

C.2 Application of stacked models

As stated in Sect. C.1, the model for the classification between AGN and SFGs has not suffered any change from the modifications of the new prediction pipeline. However, if the focus of the analyses is changed towards the prediction of SFGs, new metrics can be obtained from the same model. These values are presented in Table C.7.

After the hyperparameter optimisation and probability calibration, new metrics were obtained for both radio detection models in the test subset and in the labelled sources in the S82 field. These values are presented, jointly, in Tables C.10 and C.10 for sources in the test subset and in the S82 labelled sources, respectively.

Metrics from the application of the redshift prediction models to sources in our test subset and the labelled sources in the S82 field are presented in Table C.9.

As in the main text, we also provide a measure of the base status of the data as to assess the improvement given by our modified pipeline in the prediction of sources. In particular, Table presents the no-skill metrics for the three classification steps.

APPENDIX C. EXTENDED PREDICTION PIPELINE

Table C.6: Hyper-parameters values for meta-learners in modified pipeline after tuning.

AGN-SFG model (CatBoost)			
Parameter	Value	Parameter	Value
learning_rate	0.0075	random_strength	0.1
depth	6	l2_leaf_reg	10
Radio detection model for AGN (GradientBoosting)			
Parameter	Value	Parameter	Value
n_estimators	187	min_samples_leaf	2
learning_rate	0.0560	max_depth	9
subsample	0.3387	max_features	0.5248
min_samples_split	5		
Radio detection model for SFGs (RF)			
Parameter	Value	Parameter	Value
n_estimators	17	max_depth	6
min_impurity_decrease	0.0000	max_features	0.4280
bootstrap	False	criterion	gini
class_weight	balanced_subsample	min_samples_split	10
min_samples_leaf	3		
Redshift prediction model for rAGN (RF)			
Parameter	Value	Parameter	Value
n_estimators	187	max_depth	9
min_impurity_decrease	0.0000	max_features	0.6346
bootstrap	False	criterion	mae
min_samples_split	3	min_samples_leaf	5
Redshift prediction model for rGal (ET)			
Parameter	Value	Parameter	Value
n_estimators	100	criterion	mse
max_depth	None	min_impurity_decrease	0.0000
max_features	auto	bootstrap	False
min_samples_split	2	min_samples_leaf	1

^a This table shows the parameters which were subject to tuning.

^b Remaining hyper-parameters used their default values as defined by their developers.

Table C.7: Resulting metrics of **SFG-AGN** classification model for the test subset and the labelled sources in S82 using two different threshold values. Opposite to Table 4.1, the results of this table are focused on the prediction of **SFGs** and are only shown for the **PR**-based thresholds.

Subset	Threshold	F_β ($\times 100$)	MCC ($\times 100$)	Precision ($\times 100$)	Recall ($\times 100$)
HETDEX-test	PR	96.43 ± 0.33	91.85 ± 0.70	97.15 ± 0.31	95.84 ± 0.52
S82-label	PR	76.36 ± 1.37	70.67 ± 1.71	74.95 ± 1.90	77.60 ± 1.83

^a All metrics have been multiplied by 100.

^b Uncertainties show standard deviation of metrics obtained across all 10 training folds (cf. Sect. 3.5)

C.2. APPLICATION OF STACKED MODELS

Table C.8: Resulting metrics of radio detection prediction model for the [AGN](#) and [SFG](#) branch of our modified pipeline. Models have been applied to the test subset and the labelled sources in [S82](#) using the [PR](#) threshold values.

Branch	Subset	Threshold	F_β ($\times 100$)	MCC ($\times 100$)	Precision ($\times 100$)	Recall ($\times 100$)
AGN	HETDEX-test	PR	46.46 ± 3.25	34.86 ± 3.90	43.37 ± 3.18	49.46 ± 3.95
	S82-label	PR	23.46 ± 1.84	20.92 ± 2.51	13.55 ± 1.09	59.43 ± 4.59
	HETDEX-pipe	PR	44.82 ± 2.97	33.85 ± 3.67	42.34 ± 3.27	47.19 ± 3.28
	S82-pipe	PR	22.22 ± 1.99	20.25 ± 2.53	12.81 ± 1.24	56.63 ± 3.73
SFG	HETDEX-test	PR	45.88 ± 2.54	36.67 ± 3.08	46.23 ± 3.21	45.66 ± 2.62
	S82-label	PR	9.86 ± 5.64	9.90 ± 8.21	5.28 ± 3.00	35.00 ± 20.81
	HETDEX-pipe	PR	46.22 ± 3.11	36.73 ± 3.89	47.17 ± 3.94	45.51 ± 2.71
	S82-pipe	PR	23.17 ± 3.50	20.96 ± 4.68	13.72 ± 2.00	54.12 ± 9.71

^a All metrics have been multiplied by 100.

^b Uncertainties show standard deviation of metrics obtained across all 10 training folds (cf. Sect. 3.5)

Table C.9: Redshift prediction metrics for the test subset from [HETDEX](#) and [S82](#) labelled sources as discussed in Sect. 4.4

Branch	Subset	σ_{MAD} ($\times 100$)	σ_{NMAD} ($\times 100$)	σ_z ($\times 100$)	σ_z^N ($\times 100$)	η ($\times 100$)
AGN	HETDEX-test	14.78 ± 2.09	6.65 ± 0.70	38.63 ± 4.54	17.97 ± 2.90	16.58 ± 2.72
	S82-label	18.17 ± 2.73	8.81 ± 0.72	51.01 ± 3.41	22.98 ± 3.36	21.99 ± 1.88
	HETDEX-pipe	14.56 ± 2.34	6.65 ± 0.65	36.85 ± 5.90	23.04 ± 6.00	17.00 ± 3.08
	S82-pipe	17.92 ± 1.56	8.57 ± 0.72	43.59 ± 3.41	25.34 ± 3.36	21.77 ± 1.88
SFG	HETDEX-test	3.90 ± 0.34	2.93 ± 0.25	10.38 ± 1.06	7.01 ± 1.03	2.79 ± 0.97
	S82-label	6.77 ± 2.81	4.41 ± 1.61	14.27 ± 9.19	9.75 ± 7.97	5.54 ± 6.80
	HETDEX-pipe	3.55 ± 0.34	2.85 ± 0.30	14.35 ± 7.55	7.57 ± 1.61	2.79 ± 1.07
	S82-pipe	6.59 ± 1.32	4.85 ± 0.75	35.67 ± 16.66	11.91 ± 2.56	8.77 ± 2.73

^a Values and uncertainties as in Table 4.1.

Table C.10: Results of no-skill selection of sources in different stages of pipeline to the labelled sources in the [HETDEX](#) test subset

Branch	Prediction ($\times 100$)	F_β ($\times 100$)	MCC ($\times 100$)	Precision ($\times 100$)	Recall
AGN	AGN	42.57	0.00	42.57	42.57
	Radio-label	16.46	0.00	16.46	16.46
	Radio-pipe	15.51	0.00	15.51	15.51
	Radio AGN	14.64	0.00	14.64	14.64
SFG	SFG	57.43	0.00	57.43	57.43
	Radio-label	14.69	0.00	14.69	14.69
	Radio-pipe	15.40	0.00	15.40	15.40
	Radio SFG	14.23	0.00	14.23	14.23

^a All metrics have been multiplied by 100.

APPENDIX C. EXTENDED PREDICTION PIPELINE

Table C.11: Results of no-skill selection of sources in different stages of pipeline to the labelled sources in the [S82](#) labelled sources

Branch	Prediction	F_β	MCC	Precision	Recall
	($\times 100$)	($\times 100$)	($\times 100$)	($\times 100$)	
AGN	AGN	81.29	0.00	81.29	81.29
	Radio-label	4.92	0.00	4.92	4.92
	Radio-pipe	4.32	0.00	4.32	4.32
	Radio AGN	4.29	0.00	4.29	4.29
SFG	SFG	18.71	0.00	18.71	18.71
	Radio-label	1.74	0.00	1.74	1.74
	Radio-pipe	4.32	0.00	4.32	4.32
	Radio SFG	1.54	0.00	1.54	1.54

^a All metrics have been multiplied by 100.